Kinetic Property and SS 316/Alloy 617 Corrosion Study in Molten Chloride and Fluoride Salts

Qiufeng Yang

Dissertation submitted to the faculty of the Virginia Polytechnic Institute and State University

In partial fulfillment of the requirements for the degree of

Doctor of Philosophy

In

Nuclear Engineering

Jinsuo Zhang, Chair

Mark Pierson, Member

Yang Liu, Member

Xianming Bai, Member

August 11th, 2022

Blacksburg, VA

Keywords: molten salts, kinetic property, multicomponent system, corrosion study, galvanic corrosion

Kinetic Property and SS 316/Alloy 617 Corrosion Study in Molten Chloride and Fluoride Salts

Qiufeng Yang

Abstract

This study focused on the kinetic data measurements, such as diffusion coefficient D and exchange current density i_0 of the electrochemical reactions of corrosion products (Fe, Cr and Ni ions) and corrosive species (OH^-), and corrosion studies of structural materials (SS 316H and Alloy 617), including static corrosion and galvanic corrosion, in molten $MgCl_2$-NaCl-KCl and/or NaF-KF-UF_4-UF_3 salts in a temperature range of 600 to 800°C. The study applied the semi-differential (SD) analysis method and innovative fitting method for the kinetic property data measurements in the multicomponent system of NaF-KF-UF_4-UF_3 salts. In molten $MgCl_2$-NaCl-KCl salts, the measured D_{OH^-} has the largest value followed by $D_{Cr^{2+}}$, $D_{Fe^{2+}}$, $D_{Cr^{3+}}$ and $D_{Ni^{2+}}$ at the studied temperatures, and none of the diffusion coefficients depends on the ion concentration in the studied concentration range and all of them followed the Arrhenius law. At the same temperature, the measured $D_{Fe^{2+}}$ and $D_{Cr^{2+}}$ values in molten NaF-KF-UF_4-UF_3 salts were slightly smaller than those obtained in molten $MgCl_2$-NaCl-KCl salts. The non-linear curve fitting technique was applied to determine the exchange current density i_0, charge transfer coefficient α, limiting current density i_L and standard rate constant k^0 values. i_0 and k^0 followed the Arrhenius law. The obtained fundamental data can be applied to corrosion models which make the corrosion rate prediction possible in a static system from the experimental kinetic data.

Corrosion studies of SS 316H and Alloy 617 in thermal purified molten NaF-KF-UF_4-UF_3 salts were performed for 120 hours. Based on the post-test analysis, the major metal species corrosion products were Cr, Fe and Mn in SS 316H tests, and Cr, Co, Ni in Alloy 617 tests. The measured UF_4/UF_3 ratio increased after corrosion tests because some of the U^{3+} was oxidized to U^{4+} by corrosive impurities and corrosion products during tests. Cr depletion and salt penetration were observed at grain boundaries (GBs) for both SS 316H and Alloy 617. For Alloy 617 specimens, the corroded area could be divided into two parts: the first part (near the surface) where Cr was completely depleted, and the second part (underneath the first part) where Cr was partially depleted. For SS 316H specimens, the average attack depth was larger than that of Alloy 617. Mo segregation was observed in the matrix of SS 316H specimens but was found to be enriched at GBs in the second part of Alloy 617 specimens. The corrosion study of Alloy 617 with time was also conducted for 72 hours and 32 hours, respectively. A thin layer composed of Fe, Co, Ni and Mo was found on the surface of the specimen, which was different from the previous 120-hour tests. In the salt, the concentration of Cr kept increasing with time, while for the other identified corroded elements, i.e., Fe, Co, Ni and Mo, their concentrations increased first, then decreased until becoming zero or stable.

In the galvanic corrosion study of Alloy 617/graphite in molten NaF-KF-UF_4-UF_3 salts, the galvanic corrosion rate of Alloy 617 at 750°C was about four times of that at 650°C in the 2-hour

tests, which indicated that temperature has a significant effect on the galvanic effect. In the 120-hour galvanic corrosion test, the galvanic corrosion rate became slightly larger with time in the studied system. Similar to the previous 120-hour Alloy 617 corrosion test, the corroded area of the post-test specimen was divided into two parts. The measured attack depth in both parts were much smaller compared with that in the 120-hour Alloy 617 test. This was because of the lower corrosive impurity concentrations in the salt used in the test. The salt in the galvanic corrosion test has been used in the previous corrosion test, during which the corrosive impurities were consumed, which made the salt less corrosive.

Finally, it is necessary to point out that all the salts used in the present work were only thermally purified, which is effective in the removal of moisture but not in the removal of oxide impurities. Therefore, further studies are needed to understand the oxides' impacts on the corrosion behavior, especially on the salt penetration.

Kinetic Property and SS 316/Alloy 617 Corrosion Study in Molten Chloride and Fluoride Salts

Qiufeng Yang

General Audience Abstract

Molten salt is a promising candidate that can be used as fuel and coolant in the molten salt reactors (MSRs). Besides, it can also be used as thermal energy storage, heat transfer fluid in the concentrated solar power plants, because it has high heat capacity, low vapor pressure, and high thermal conductivity. However, materials corrosion is a key concern of molten salt applications, and it is known that the corrosion by molten salts is mainly impurity driven. The impurities, such as moisture in the salts, can make the salt more oxidized, thus becoming more corrosive to corrode the structural materials. The present work focus on the kinetic property of metal specie corrosion products and non-metal impurity in the molten fluoride and chloride salts, which were directly related to the mass transfer and charge transfer process during the corrosion. Especially in the measurements of fluoride salts, innovative methods were applied which were confirmed to perform well in the multicomponent system (Fe and Cr ions coexisted). The static corrosion tests of SS 316H and Alloy 617 were conducted in molten fluoride salt at high temperatures. The main purpose was to study their corrosion behavior and understand the corrosion mechanisms. The corrosion rate of SS 316H was also estimated, which could be a crucial criterion in the material selection. In addition, the corrosion of Alloy 617 with time was also investigated. The metal specie corrosion product concentration change trends were obtained, and the corrosion behavior over the different corrosion stages was analyzed. Different corrosion phenomenon was observed in different corrosion test. Thus, they shed lights on the study of how the corrosion was developed during the corrosion process. Moreover, galvanic corrosion was another major corrosion type when two or more dissimilar materials were electrically contacted. The galvanic corrosion of Alloy 617/graphite was studied in the molten fluoride salts. The galvanic corrosion rate increased with the rise of temperature, which verified that temperature was a key factor that affected the galvanic corrosion. And the galvanic effect was also turned out to increase with time in the present study.

Acknowledgement

I'd like to thank God to love me unconditionally. He mends me and heals my soul. He pulls me out from a bottomless pit and sends me back to the colorful world where I'm living right now. I can't image how I would have been without Him.

I'd like to thank my husband, Vince Wang, who is always considerate. He made me happy, and I have become more open-minded, confident, and passionate since we got married. I believe it's God who send him to me.

I'd like to thank my parents who always support me and stand firmly behind me no matter what happens. They gave me a happy childhood even under those harsh living conditions when I was young.

I'd like to thank my elder brother who is always my support. As a first-born son, he took the responsibility for the whole family and took care of our parents perfectly well when I was absent. He is absolutely a real and strong man.

I'd like to thank my committee members, Dr. Mark Pierson, Dr. Yang Liu and Dr. Xianming Bai. They spent effort to review my dissertation and provide me valuable suggestions.

I'd like to thank one of my best friends, Amanda Leong. She has become one of my important family members in the past five years.

I'd like to thank my colleagues, Dr Weiqian Zhuo, Dr Brendan D'Souza, Dr Huali Wu, Mingyang Zhang, Nagihan Karakaya, Kelly Sullivan, Emily Meilus, Brent Davis, Jaewoo Park, in NMFC at Virginia tech. They gave me lots of valuable suggestions on my research.

I'd like to thank Stephen McCartney, Dr Xu Feng, and Dr Weinan Leng for their technical support on the SEM and XPS analysis.

Special thanks to my advisor, Dr Jinsuo Zhang. He supported my research work over the past five years. He led me to explore the unknown fields in the molten salts and shown me how to be a good researcher. He taught me how to think independently and search an appropriate solution to a problem. He shaped me as a scientific researcher.

Attribution

Several colleagues and researchers have contributed to this work, whose contributions are specified as follows.

For all the work described in this dissertation, Dr Jinsuo Zhang advised and guided the whole project direction, and provided valuable suggestions on the experimental designs and data analysis methods.

For the work described in Chapter 2, I conducted the experiments and corresponding electrochemical, ICP-MS and XRD data analysis with the assistance of Dr Jianbang Ge. Dr Xu Feng helped to perform the XPS analysis. Some of the ICP-MS analysis were conducted by Jeffrey Parks.

For the work described in Chapter 3, I conducted the corrosion tests and corresponding salt and specimen analysis. Dr Brendan D'Souza advised me on the salt purification. Stephen McCartney, Amanda Leong, Jaewoo Park, Dr Huali Wu and Dr Weinan Leng gave me suggestions on SEM and XPS analysis.

For the work described in Chapter 4, I conducted the galvanic corrosion tests and corresponding salt and specimen analysis, including ICP-MS and SEM analysis.

Table of Contents

1 Introduction 1

1.1 Background 1

1.1.1 Molten Salts Application 1

1.1.2 Material Corrosion in Molten Salts 2

1.2 Research Gap and Motivation 20

2 Corrosion Kinetic Properties in Molten Salts 23

2.1 Experiment 23

2.2 Results and Discussion 26

2.2.1 Kinetic Parameters in Molten $MgCl_2$-NaCl-KCl Salts 26

2.2.2 Kinetic Parameters in Molten NaF-KF-UF_4-UF_3 Salts 49

2.2.3 Corrosion Rate Prediction Model Using Kinetic Parameters 59

2.3 Conclusions 63

3 Corrosion Study of SS 316H and Alloy 617 in Molten Salts 65

3.1 Experiment 65

3.1.1 Material Preparation 65

3.1.2 Experimental Setup 71

3.2 Results and Discussions 73

3.2.1 SS 316H Corrosion Study (120 hours) 73

3.2.2 Alloy 617 Corrosion Study (120 hours) 81

3.2.3 Alloy 617 Corrosion Study with Time (72 hours & 32 hours) 93

3.3 Conclusions 105

4 Galvanic Corrosion Study of Alloy 617/Graphite in Molten NaF-KF-UF_4-UF_3 Salts 107

4.1 Experiment 107

4.2 Results and Discussion 108

4.2.1 Alloy 617/Graphite Galvanic Corrosion Study (2 hours) 108

4.2.2 Alloy 617/Graphite Galvanic Corrosion Study (120 hours) 111

4.3 Conclusions 116

5 Summary 118

6 References 121

List of Figures

Figure 1-1 Galvanic corrosion coupling 4

Figure 1-2 Impurity-driven corrosion process in molten salts..... 5

Figure 2-1 Electrochemical Test Setup: 1. Working electrode 2. Reference electrode 3. Counter electrode 4. Quartz tube 5. Salt container 6. Liquid salt level 7. Alumina safety dish..... 25

Figure 2-2 $Ni/NiCl_2$ thermodynamic reference electrode setup 26

Figure 2-3 (a) Cyclic voltammetry at 600 ºC with scan rate of 200mV/s in $MgCl_2$-KCl-NaCl blank salts, working electrode surface area: 0.4562cm^2; and in salts with 1.53×10^{-4} mol cm^{-3} $FeCl_2$ addition, working electrode surface area: 0.7843cm^2, and in salts with 1.50×10^{-4} mol cm^{-3} $NiCl_2$ addition, working electrode surface area: 0.5432cm^2; (b) Plot of reduction peak potential Ep versus scan rate v, Ep - v in $MgCl_2$-KCl-NaCl-1.53×10^{-4} mol cm^{-3} $FeCl_2$ (and -1.50×10^{-4} mol cm^{-3} $NiCl_2$) at 600 ºC. 27

Figure 2-4 Cyclic voltammetry in $MgCl_2$-KCl-NaCl-1.53×10^{-4} mol cm^{-3} $FeCl_2$ at 650 ºC, working electrode surface area: 0.7843cm^2; (b) Chronopotentiometry in $MgCl_2$-KCl-NaCl-1.50×10^{-4} mol cm^{-3} $NiCl_2$ at 800 ºC, working electrode surface area: 0.5608 cm^2; (c) log D-1/ T plots of Fe^{2+}, Ni^{2+}, Cr^{2+} and Cr^{3+} at the concentration of 1.53×10^{-4} mol cm^{-3} $FeCl_2$, 1.50×10^{-4} mol cm^{-3} $NiCl_2$ and 1.58×10^{-4} mol cm^{-3} $CrCl_2$. 29

Figure 2-5 XPS spectra of Cr $2p_{3/2}$ in $MgCl_2$-KCl-NaCl-1.58×10^{-4} mol cm^{-3} $CrCl_2$ at 700ºC before electrochemical tests 31

Figure 2-6 (a) Cyclic voltammetry in $MgCl_2$-KCl-NaCl-1.58×10^{-4} mol cm^{-3} $CrCl_2$ at 650 ºC, working electrode surface area: 0.7653cm^2; (b) Chronopotentiometry in $MgCl_2$-KCl-NaCl-1.58×10^{-4} mol cm^{-3} $CrCl_2$ at 650 ºC, working electrode surface area: 0.5412 cm^2; (c) Cyclic voltammetry of Cr^{3+}/Cr^{2+} reaction in $MgCl_2$-KCl-NaCl-1.58×10^{-4} mol cm^{-3} $CrCl_2$ at 650 ºC, working electrode surface area: 0.7843 cm^2; (d) Cyclic voltammetry of Cr^{2+}/Cr reaction in $MgCl_2$-KCl-NaCl-1.58×10^{-4} mol cm^{-3} $CrCl_2$ at 650 ºC, working electrode surface area: 0.6423 cm^2. ... 32

Figure 2-7 (a) Three identical scans in $MgCl_2$-KCl-NaCl-9.17×10^{-5} mol cm^{-3} $FeCl_2$ at 650 ºC with a scan rate of 5mV/s; (b) Measured and fitted potentiodynamic polarization curves in $MgCl_2$-KCl-NaCl-1.53×10^{-6}, 9.17×10^{-5} and 1.53×10^{-4} mol cm^{-3} $FeCl_2$ at 650 ºC with a scan rate of 5mV/s; (c) $i0$ measured in $MgCl_2$-KCl-NaCl-1.53×10^{-6} $FeCl_2$ at each temperature; (d) The exponential relation of $i0$ and Fe^{2+} bulk concentration $CFe2 + b$ fitted from Eq(9). 37

Figure 2-8 (a) log$i0$ – 1/T plots measured in $MgCl_2$-KCl-NaCl-1.53×10^{-4} mol cm^{-3} $FeCl_2$ (1.50×10^{-4} mol cm^{-3} $NiCl_2$ or 1.58×10^{-4} mol cm^{-3} $CrCl_2$); (b) lgk^0 – 1/T plots fitted at each temperature.. 38

Figure 2-9 Precipitates on the bottom in $MgCl_2$-NaCl-KCl-NaOH at 600 ºC..... 40

Figure 2-10 (a) XRD analysis of salt melt on the top in $MgCl_2$-NaCl-KCl-NaOH at 600 ºC (b). XRD analysis of precipitates and salt melt in $MgCl_2$-NaCl-KCl-NaOH. Salt 1 on the bottom: precipitate at 600 ºC; salt 2 on the top: salt melt at 650 ºC; salt 1 on the top: salt melt at 600 ºC; salt 3 on the top: salt melt at 700 ºC. 41

Figure 2-11 (a) Mg^{2+} wt.% in $MgCl_2$-NaCl-KCl-NaOH at 650 ºC before and after NaOH added (b). Mg^{2+} wt.% in $MgCl_2$-NaCl-KCl-NaOH at 700 ºC before and after NaOH added. 43

Figure 2-12 (a) CV scan in $MgCl_2$-NaCl-KCl at 650 ºC before and after NaOH added. WE: tungsten, CE: graphite, RE: Ni/$NiCl_2$ (b). CV scan of redox couple OH^-/H_2 in $MgCl_2$-NaCl-KCl at 650 ºC after NaOH added. WE: tungsten, CE: graphite, RE: Ni/$NiCl_2$..... 44

Figure 2-13(a) Relation of Ip vs. v in $MgCl_2$-NaCl-KCl-NaOH at 650 ºC. WE: tungsten, CE: graphite, RE: Ni/$NiCl_2$. (b) Plot of ln$D$ vs. 1/T at different temperatures in $MgCl_2$-NaCl-KCl-NaOH 45

Figure 2-14 Potentiodynamic scans of OH- in $MgCl_2$-NaCl-KCl at different temperatures, scan rate: 5mV/s. WE: tungsten, CE: graphite, RE: Ni/$NiCl_2$. 47

Figure 2-15 Measured and fitted potentiodynamic polarization curves in $MgCl_2$-KCl-NaCl-NaOH with a scan rate of 5mV/s. WE: tungsten, CE: graphite, RE: Ni/$NiCl_2$: (a) 600 ºC; (b) 700 ºC... 48

Figure 2-16 Ln k^0 – 1/T plots fitted at each temperature. 49

Figure 2-17 CV scan in molten NaF-KF-UF_4-UF_3 salts at 800 ºC, WE: tungsten, CE: graphite, RE: Pt. 51

Figure 2-18 CV scans of Cr^{2+}/Cr and Fe^{2+}/Fe at different scan rates in molten NaF-KF-UF_4-UF_3 salts at at 800 ºC, WE: tungsten, CE: graphite, RE: Pt. 52

Figure 2-19 CV and SD transformation of CV in molten NaF-KF-UF_4-UF_3 salts at 800 ºC..... 53

Figure 2-20 LnD-$1/T$ relation of Fe^{2+} and Cr^{2+} in molten NaF-KF-UF_4-UF_3 salts, (a) SD method, (b) CV method 54

Figure 2-21 PD scans in molten NaF-KF-UF_4-UF_3 salts at 700 ºC, (a) log i vs. V (b) i vs. V..... 56

Figure 2-22 PD scan within different potential range in molten NaF-KF-UF_4-UF_3 salts at 700 ºC 57

Figure 2-23 Deterination of actural PD curve of Cr^{3+}/Cr^{2+} in molten NaF-KF-UF_4-UF_3 salts at 700 ºC..... 57

Figure 2-24 Deterination of actural PD curve of Cr^{2+}/Cr in molten NaF-KF-UF_4-UF_3 salts at 700 ºC..... 58

Figure 2-25 Measured and fitted PD curves of Fe^{2+}/Fe in NaF-KF-UF_4-UF_3 salts at 700 ºC with a scan rate of 5mV/s. WE: tungsten, CE: graphite, RE: Pt..... 58

Figure 2-26 Ln i_0 – 1/T plots of Fe^{2+}, Cr^{2+} and Cr^{3+} at 700 ºC, 750 ºC and 800 ºC in molten NaF-KF-UF_4-UF_3 salts..... 59

Figure 2-27 Metal dissolution and mass transfer process..... 61

Figure 3-1 Specimen dimension used in the tests..... 67

Figure 3-2 (a) Mapping scan on the surface of SS 316H; (b) Mapping scan on the surface of SS Alloy 617. 68

Figure 3-3 (a) Mapping scan on the cross-Section of SS 316H; (b) Mapping scan on the cross-section of Alloy 617..... 69

Figure 3-4 UF_4/UF_3 ratio fitting from the HR scan using XPS 70

Figure 3-5 Static corrosion test Setup. 1: Boron nitride tube, 2: Nickel lid, 3. Nickel wire, 4: Molten salt liquid level, 5: Glassy carbon crucible, 6: Specimen. 72

Figure 3-6 Alloy 617 corroison test setup: 1. Ni wire 2. Clip 3. Quartz tube 4. Furnace 5. Glassy carbon crucible 6. Liquid salt level 7. Nickel safety crucible 8. Alloy 617 72
Figure 3-7 Cross-section of post-test salt 74
Figure 3-8 SS 316H-post-test-specimen overview 76
Figure 3-9 SEM image of 1003-post-test SS 316H specimen, Mag 200× 78
Figure 3-10 Mapping scan of corroded area of 1003-post-test SS 316H specimen, Mag 2000× 79
Figure 3-11 Line scan of black spots on the 1003-post-test SS 316H specimen, Mag 2000× 80
Figure 3-12 Line scan of bright line on the 1003-post-test SS 316H specimen, Mag 2000× 80
Figure 3-13 Line scan of GB of corroded area on the 1003-post-test SS 316H specimen, Mag 4500× 81
Figure 3-14 Line scan of GB of uncorroded area on the 1003-post-test SS 316H specimen, Mag 2200× 81
Figure 3-15 Outside surface and cross-section of post-test salt in test 2001 82
Figure 3-16 Overview of Alloy 617 post-test specimens in test 2001 84
Figure 3-17 SEM image of 2001-post-test specimen cross-section 85
Figure 3-18 SEM mapping scan of 1st part on the 2001-post-test specimen cross-section 85
Figure 3-19 SEM line scan of 1st part on the 2001-post-test specimen cross-section 86
Figure 3-20 SEM mapping scan of 2nd part on the 2001-post-test specimen cross-section 87
Figure 3-21 SEM line scan across GBs in the 2nd part on the 2001-post-test specimen cross-section 88
Figure 3-22 SEM line scan of black line-shaped material in the 2nd part on the 2001-post-test specimen cross-section 89
Figure 3-23 SEM line scan across GBs in the 3rd part on the 2001-post-test specimen cross-section 90
Figure 3-24 Carbides present at GBs in the 3rd part on the 2001-post-test specimen cross-section 91
Figure 3-25 Metal specie corrosion products concentration change trend: (a) S001, (b) S002, (c) S001 & S002 95
Figure 3-26 (a) Outside surface of S001-post-test salt, (b) Outside surface of S002-post-test salt, (c) Inner surface of glassy carbon crucible after S002 test 96
Figure 3-27 SEM image of S001 post-test specimen cross-section 97
Figure 3-28 SEM line scan in the 1st part of test S001 99
Figure 3-29 SEM mapping scan in the 1st part of test S001 100
Figure 3-30 SEM line scan in the 2nd part of test S001 100
Figure 3-31 SEM line scan across the specimen surface in test S001 102

Figure 3-32 SEM mapping scan of black spots observed in test S001 102

Figure 3-33 SEM line scan of black spots observed in test S001 103

Figure 3-34 SEM line scan across GBs in the uncorroded area of test S001 104

Figure 4-1 Alloy 617 Corroison test setup: 1. Ni wire working electrode 2. Pt wire reference electrode 3. Ni wire counter electrode 4. Quartz tube 5. Ni crucbile 6. Liquid salt level 7. Alloy 617 specimen 8. Alumina safety dish 9. Furnace power switch 10. Furnace display 11. Graphite Specimen 108

Figure 4-2 Galvanic current density of Alloy 617/graphite couple in molten NaF-KF-UF_4-UF_3 salts at 650 and 750 °C for 2 hours 110

Figure 4-3 SEM surface images of the Alloy 617 specimen after the galvanic corrosion tests in the molten NaF-KF-UF_4-UF_3 salts, (a) 650 °C , and (b) 750 °C. 110

Figure 4-4 SEM cross-section images of the Alloy 617 specimen after the galvanic corrosion tests in the molten NaF-KF-UF_4-UF_3 salts, (a) 650 °C , and (b) 750 °C. 111

Figure 4-5 (a) Galvanic current density of Alloy 617/graphite couple (b) OCP of Alloy 617 in molten NaF-KF-UF_4-UF_3 salts at 650 and 750 °C over 120 hours test duration 112

Figure 4-6 SEM image on the cross-section of post-test specimen in test GU002 113

Figure 4-7 SEM mapping scan of the 1^{st} part and 2^{nd} part in test GU002 114

Figure 4-8 SEM line scan from the 1^{st} part to the 2^{nd} part in test GU002 114

Figure 4-9 SEM line scan across the specimen surface in test GU002 115

Figure 4-10 SEM line scan of the 1^{st} part in test GU002 115

Figure 4-11 Outside surface of the post-test salt in test GU002 116

List of Tables

Table 1-1 SS 316H composition specification 5

Table 1-2 Alloy 617 chemical composition 5

Table 1-3 Diffusion coefficient calculation using CV method 7

Table 1-4 Available diffusion coefficient data of Fe^{2+}, Ni^{2+}, Cr^{2+}, Cr^{3+} and OH^- 8

Table 1-5 Available exchange current density data of Fe^{2+}, Ni^{2+}, Cr^{2+}, Cr^{3+} and OH^- 12

Table 2-1 Temperature profile used for thermal purification of salts 24

Table 2-2 Electrochemical test profiles in molten chloride and fluoride salts 26

Table 2-3 Reduction peak potential Ep of Fe^{2+}/Fe and Ni^{2+}/Ni in $MgCl_2$-KCl-NaCl-1.53×10^{-4} mol cm^{-3} $FeCl_2$ and $MgCl_2$-KCl-NaCl-1.50×10^{-4} mol cm^{-3} $NiCl_2$ at 600 ºC 27

Table 2-4 Calculated $DFe2+$ and $DNi2+$ from CV and CP tests at different concentrations and temperatures 30

Table 2-5 Averaged ratio of Cr^{3+}/Cr^{2+} in molten $MgCl_2$-KCl-NaCl salts measured by XPS at different temperatures 31

Table 2-6 Reduction peak potential Ep of Cr^{3+}/ Cr^{2+} and Cr^{2+}/Cr in $MgCl_2$-KCl-NaCl-1.58×10^{-4} mol cm^{-3} $CrCl_2$ at 650 ºC 32

Table 2-7 α values of Cr^{3+}/Cr^{2+} calculated from CV and potentiodynamic scans 34

Table 2-8 Calculated $DCr3+$ and $DCr2+$ using CV technique in $MgCl_2$-KCl-NaCl at different concentrations and temperatures 35

Table 2-9 Calculated $i0$, α and iL of Fe^{2+}, Ni^{2+}, Cr^{2+} and Cr^{3+}in $MgCl_2$-KCl-NaCl-1.53×10^{-4} mol cm^{-3} $FeCl_2$ (1.50×10^{-4} mol cm^{-3} $NiCl_2$ or 1.58×10^{-4} mol cm^{-3} $CrCl_2$) at 600, 650, 700. 750, 800 ºC 38

Table 2-10 Calculated $k0$ and Ea of Fe^{2+}/Fe, Ni^{2+}/Ni, Cr^{2+}/Cr and Cr^{3+}/ Cr^{2+} at different temperatures 39

Table 2-11 Gibbs energy formation of reaction calculation using HSC 10.0 40

Table 2-12 $COH-$ Measurement Test Design 42

Table 2-13 Equilibrated $COH-$ in $MgCl_2$-NaCl-KCl-2wt.% at different temperature 43

Table 2-14 Reaction potential ΔE (vs. Cl^-/Cl_2) calculation using HSC 10.0 at 600 ºC 45

Table 2-15 Calculated $DOH-$ in $MgCl_2$-NaCl-KCl-NaOH at different temperatures 45

Table 2-16 Electrochemical reactions of OH^-/H_2 in $MgCl_2$-NaCl-KCl 48

Table 2-17 Fitted $i0$, α, iL and $k0$ of OH^- in $MgCl_2$-KCl-NaCl at 600, 650, 700, 750, 800 ºC 49

Table 2-18 Standard reduction potential of Fe, Cr and U ions 52

Table 2-19 Calacualted elenctron transfer number of Fe^{2+}/Fe and Cr^{2+}/Cr 52

Table 2-20 Diffusion coefficient of Fe^{2+} and Cr^{2+} in molten salts at different temperatures 53

Table 2-21 Fitted $i0$, α, and iL of Fe^{2+}, Cr^{2+} and Cr^{3+} in NaF-KF-UF_4-UF_3 salts at 700 ºC, 750 ºC and 800 ºC 59
Table 3-1 Overview of performed corrosion tests in molten NaF-KF-UF_4-UF_3 salts 65
Table 3-2 Chemical composition of SS 316H 66
Table 3-3 Chemical composition of Alloy 617 67
Table 3-4 Purity check results from ICP-MS and XPS analysis 71
Table 3-5 UF_4/UF_3 Ratio check in pre-test NaF-KF-UF_4-UF_3 salts 71
Table 3-6 Salt samples collection schedule of test S001 and test S002 73
Table 3-7 Metal specie concentration in SS 316H-post-test salts measured using ICP-MS 75
Table 3-8 Measured UF_4/UF_3 ratio of SS 316H-post-test salt using XPS 75
Table 3-9 Estimated corrosion rate of SS 316H in molten NaF-KF-UF_4-UF_3 salt 76
Table 3-10 SEM point scan on bright particles in salts, Mag 200× 78
Table 3-11 Specimen attack depth in test 1001, 1002, 1003 79
Table 3-12 Point scans of silver material in test 2001 82
Table 3-13 Metal species concentration in the post-test salt of test 2001 83
Table 3-14 Thickness of Alloy 617 in the 2001-pre-test and 2001-post-test 91
Table 3-15 Attack depth and maximum attack depth of Alloy 617 in test 2001 92
Table 3-16 Point scans of 1st part on the 2001-post-test specimen cross-section 92
Table 3-17 Cr, Co and Ni concentration at the end of test 2001, S001 and S002 95
Table 3-18 UF_4/UF_3 ratio in the post-test salt of test S001 and S002 96
Table 3-19 SEM point scan in the 1st part of test S001 98
Table 3-20 Thickness of pre-test and post-test Alloy 617 specimen in test S001 and S002 104
Table 3-21 Attack depth of the 1st part and 2nd part in test S001 and S002 105
Table 4-1 Electrochemical scan profile in test GU002 at 650 °C 108
Table 4-2 Calcualted galvnic corroisn rate and average corrosion rate molten NaF-KF-UF_4-UF_3 salts at 650 and 750 °C 111
Table 4-3 Thickness of pre-test and post-test Alloy 617 specimen in test GU002 116
Table 4-4 Attack depth of the 1st part and 2nd part in test GU002 116

List of Abbreviations

MSRs	Molten Salt Reactors	ASME	American Society of Mechanical Engineers
TES	Thermal Energy Storage	ICP-MS	Inductively Coupled Plasma-Mass Spectroscopy
HTF	Heat Transfer Fluid	XPS	X-ray Photoelectron Spectroscopy
SS	Stainless Steel	XRD	X-Ray Diffraction
wt.%	Weight Percent	SEM	Scanning Electron Microscopy
Mag.	Magnitude	mol %	Molar Fraction
GB	Grain Boundary	DSC	Differential Scanning Calorimetry
ASTM	American Society for Testing and Materials	°C	Degree-Celsius
CSP	Concentrated Solar Power Plant	Ln	Natural Logarithm
Lg	Base 10 Logarithm		

1 Introduction

1.1 Background

1.1.1 Molten Salts Application

In general, a salt is solid at a standard temperature and pressure but becomes liquid phase (molten salt), when the temperature is above the salt melting temperature[1]. There are varieties of molten salt, such as nitrate, carbonate, chloride, and fluoride molten salt, which has been widely applied in nuclear power plants and solar power plants. In the nuclear power energy field, the molten salt reactor (MSR) concept is one of the advanced Gen IV reactor concepts. A MSR is a nuclear fission reactor in which the primary coolant and/or fuel is a molten salt mixture. It is designed to operate at a high temperature in the range of 700-800 ºC. In a liquid fuel MSR, the nuclear fuel is dissolved in a molten salt mixture. Heat generated in the core is transferred to a secondary coolant and the lower temperature molten salt is pumped back to the reactor core to start a new power cycle. In case of accident, the molten salt will be drained into a tank, thus the reactor shuts down. MSRs have two excellent advantages: minimum disposal of radioactive waste and maximum usage of raw fuel materials[2].

Molten salt plays a crucial role in the development of MSRs. One of the molten fluoride salts, NaF-KF-UF_4, has been proposed as a promising candidate to be used as fuel and coolant salt in MSRs, because it has high heat capacity (about 1kJ/kg/K), low vapor pressure (< 1bar), and high thermal conductivity (about 0.44 w/m/K)[127]. Moreover, this salt mixture doesn't contain enriched ^{7}LiF for economic and technological reasons associated with tritium control and irradiation defects. However, UF_4 in a liquid fluoride mixture intrinsically oxidizes to dissolve Cr as the most vulnerable constitution of the structural material to result in CrF_2 and form UF_3[3]. This challenge to be addressed for a UF_4 fueled molten salt reactor was overcome by keeping UF_4/UF_3 ratio no less than a specific value with constant monitoring of CrF_2 concentration. Therefore, the quaternary salt NaF-KF-UF_4-UF_3 is proposed instead to be used in MSRs and UF_3 serves as redox buffer to mitigate the corrosion induced by UF_4.

Furthermore, molten salts also have significant applications in molten salt extraction (MSE) process. As is known, reactor-grade plutonium metal contains isotopes, such as ^{238}Pu, ^{239}Pu, ^{240}Pu, ^{241}Pu and ^{242}Pu [4]. The decay of ^{241}Pu results in its daughter product ^{241}Am, which is an alpha emitter with a half-life of 13.2 years. ^{241}Am can further decay to its daughter product ^{237}Np, which is a gamma emitter with a half-life of 458 years[5]. The radiation emission presents a health hazard to personnel. Americium must be removed from plutonium, which can be conducted through a MSE process. MSE separates americium from plutonium metal by a pyrochemical oxidation reaction followed by molten salt solvent extraction. One of molten salts composed of $MgCl_2$-NaCl-KCl has been used as a solvent salt to extract americium from plutonium. In the study by Knighton et al., it was found that approximately 90% of americium could be extracted by increasing the $MgCl_2$ concentration in the $MgCl_2$-NaCl-KCl salt mixture to 30 wt. % [6]. Besides, molten NaCl-KCl-$MgCl_2$ salts were also used in the reprocessing of the liquid metal fuel, which was composed of bismuth, uranium and fission products at Brookhaven National Laboratory (BNL) in the 1950s as part of the liquid metal reactor experiment (LMR)[7].

What's more, molten salts also play a critical role in the solar power plants, which can act as heat transfer fluid (HTF) and thermal energy storage (TES) fluids. Among them, molten nitrate salts $NaNO_3$-KNO_3 have been widely used as TES fluids in the solar thermal energy (STE) plants, because of their good thermophysical properties (high heat capacity, low melting point, and high thermal conductivity), low prices and good corrosion performance of alloys up to about 620 ºC which is the practical upper temperature limit. However, at a temperature higher than the threshold temperature, nitrate salt will begin to decompose and become unstable, which has limited the application of nitrate salt at higher temperatures [8]. Due to this, researchers have spent lots of efforts to find the other candidate that meet the high temperature stability requirement. As a result, carbonate salt Li_2CO_3-Na_2CO_3-K_2CO_3 is proposed as a potential candidate for high-temperature STE applications though it has a high melting temperature. Comparing nitrate salt, carbonate salts have moderate melting points (>390 ºC), high thermal stability temperature (>650 ºC) and high heat capacities, but high prices due to utilization of expensive Li_2CO_3 for lowering the melting point [9]. To compromise the high-temperature thermal stability and commercial price, another salt composed of 44.7 mol.% $MgCl_2$-29.4 mol.% NaCl-25.8 mol.% KCl (Mgnak) has attracted more and more of researcher's attention. It must be emphasized that the salt composition is different from that used in molten salt extraction due to different purposes. Alkali metal chloride salts like KCl and NaCl have high heat capacities, low vapor pressures at high temperatures, weak hygroscopic and low prices, but high melting temperatures (>750 ºC). The melting temperatures of single alkali metal chloride salts can be significant reduced by mixing with alkaline earth metal chlorides, such as $MgCl_2$. $MgCl_2$/KCl mixture has a relatively low melting temperature around 426 ºC, low vapor pressure at high temperatures and low prices about 0.35 US $/kg[10]. Moreover, the thermal physical properties of the salts can be further improved by adding inexpensive NaCl to lower the melting temperature to about 385 ºC, reduce cost, increase heat capacity and obtain excellent thermal stability at high temperatures such as 800 ºC. Thus, $MgCl_2$-NaCl-KCl is a promising chloride mixture as a high-temperature TES/HTF material in the next generation concentrated solar power (CSP) plants.

1.1.2 Material Corrosion in Molten Salts

In general, the pure molten salt is non-corrosive, or the induced corrosion is low. Corrosion in molten salts is driven by a variety of factors, such as thermodynamics of corrosion reactions, impurities, and galvanic contact, etc.

When applied in a high-temperature environment, the corrosion resistance in material is achieved through the formation of stable and protective oxide layer on the surface of alloys. For example, Cr in the alloys may form a self-healing protective oxide film on the surface which acts as a diffusion barrier to reduce further oxidation and corrosion. However, material corrosion in molten salt is more challenging than the traditional waterpower systems due to the unstable protective oxide layer. In molten halide (fluoride or chloride) salts, the oxide film will get dissolved by the fluxing action of molten salts, thus through which, no reliable corrosion protection can be provided[11]. The corrosion will proceed by attacking the most reactive components exposed to the surface once the oxide film is removed. Even in some cases that the oxide formation is thermodynamically favored[12], the halide ions may destabilize the passive oxide layer on the surface which leads to less protective.

The thermodynamic free energies of the formation of metal fluorides that make up the salts such as NaF-KF-UF_4, LiF-NaF-KF and $MgCl_2$-NaCl-KCl are more negative than the fluorides of the common components of structural alloys[13,14], with Cr being the most prone to attack among Ni, Co, Fe or Cr. Thus, little corrosion should occur when structural alloys are in contact with pure molten salts without impurities. The contaminants in salts are primarily oxygen-based or moisture-based, which depends on the nature of the salt, i.e., hygroscopic salts, such as $MgCl_2$ and UF_4, can easily attract and absorb water without bonding. The impurities introduced by ingress of OH^-, moisture or oxygen will make the salt more oxidizing, thus becoming much more corrosive. It may result in the corrosion of transition metals such as Fe, Ni, or Cr which are the typical components of the structure materials [15]. The corrosion in molten salts is, to a great extent, driven by impurities in the salt, such as, H_2O, OH^-, O_2 and H^+. Especially the presence of moisture can result in the formation of HCl or HF with its significant effects on corrosion.

Moreover, galvanic corrosion is another common corrosion type in molten salt. It's an enhanced corrosion that occurs when two or more dissimilar metals (or graphite) are electrically contacted, either directly or through an external path, in the presence of conductive medium[16]. The galvanic corrosion coupling is illustrated in Figure 1-1. In nuclear reactors or solar power plants, the components may be manufactured using different alloys due to different specification requirements[17,18,19,20]. And in thermal MSRs, it's known that many components are fabricated from Graphite, such as the moderator and reflector[21]. During the operation of power plants, it's highly possible that different materials (metal/graphite) may have electrical contact, thereby resulting in galvanic corrosion. The motivating force of galvanic corrosion is the potential difference which leads to the current flow between the anodic and cathodic materials. It increases the corrosion rate of the anodic material (with a more negative potential) and reduces the corrosion rate of cathodic material (with a more positive potential). When coupled together, the material with a more negative potential undergoes anodic dissolution, while on the surface of material with a more positive potential, the excess electrons are consumed by cathodic reactions. The extent of galvanic corrosion depends on various factors, such as effective surface area ratio of cathode/anode, temperature, potential difference, cathodic efficiency, and polarization characteristics of the more noble material.

The material corrosion has been a major concern in the successful fruition of the MSR and CSP technology[22,23]. It is of significant importance to study and understand the corrosion mechanism and behavior of structural materials in molten salts. In both MSRs and CSPs, structural components, such as piping and ducting are machined and fabricated from various structural materials. To apply a structural material in the nuclear or solar power plants, one must have excellent stability at high temperatures, superior mechanical strength and low cost which has potential to be widely used in industry. Among various structural material alloys, stainless steel 316H and Alloy 617 have been proposed to be good candidates, because of their excellent performance in previous studies[24,25,26,27,28,29].

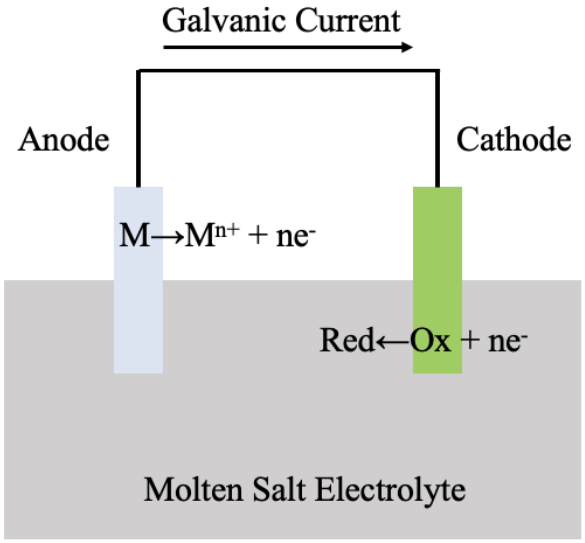

Figure 1-1 Galvanic corrosion coupling

Stainless steel 316H (SS 316H) is a high carbon modification of stainless steel 316 developed for use in elevated temperature services. It is a Fe-C-Ni-Cr alloy, where Cr is added for corrosion resistance and Ni is added to counteract the ferritic stabilizing nature of Cr and stabilize the austenite phase. It has high strength at elevated temperatures and is used for structural pressure vessel applications at temperatures above 500 ºC. This steel has the advantage of ASME Section III Division 5 code certifiable for mechanical properties at 700°C. The higher carbon content also delivers higher tensile and yields higher strength. It is often used in process streams containing halides. It exhibits adequate long-term creep rupture strength at elevated temperatures and displays good corrosion resistance in purified molten salts. SS 316H is non-magnetic in the annealed condition. It cannot be hardened by heat treatment; however, the material will be hardened due to cold working. The common composition specification of SS 316H is given in Table 1-1.

Besides, nickel-based alloys are among few alloys that can remain stable in molten salts for long term. One of them is Alloy 617, which is a solid-solution strengthened nickel-based superalloy introduced in the early 1970s. Alloy 617 is well known for its good oxidation and corrosion resistance at temperatures up to 1093 ºC and high creep-rupture strength at temperatures from 649 ºC to 1093 ºC [30.] The common limiting chemical composition of Alloy 617 is listed in Table 1-2. The alloy has excellent resistance to a wide range of corrosive environments, and it is readily formed and welded by conventional techniques. The high nickel and chromium contents make the alloy resistant to a variety of both reducing and oxidizing media. The aluminum, in conjunction with the chromium, provides oxidation resistance at high temperatures. Solid-solution strengthening is imparted by the cobalt and molybdenum. The combination of high strength and oxidation resistance at temperatures over 980 ºC makes Alloy 617 an attractive material for components applied at high temperatures. It has been identified as one of the candidate materials for Gen IV nuclear reactor system components operating in the temperature range of 760 ºC to 1000 ºC [31].

Table 1-1 SS 316H composition specification

Elements	Cr	Ni	Mo	C	Mn	S	Si	Fe	Others
wt.%	16-18	10-14	2-3	0.04-0.1	2	0.03	0.75	Balance	P, N...

Table 1-2 Alloy 617 chemical composition

Elements	Ni	Cr	Co	Mo	Fe	Mn	Al	C	Others
wt.%	≥44.5	22.20	12.50	9.64	1.21	0.04	1.06	0.08	Ti, S...

1.1.2.1 Fundamental Kinetic Parameters

The impurity-driven corrosion on the interface of structural material and molten salt involves three processes as given in Figure 1-2: first, the impurities reactant, such as O_2, OH^- or H_2O, are transported from the molten salt bulk solution to the interface; second, the corrosion reaction happens at the interface resulting in the electron exchange, in which, the impurities are reduced to O^{2-} or H^0, yet the transition metals in the structural materials, such as Fe, Ni and Cr, are oxidized to Fe^{2+}, Ni^{2+}, Cr^{2+} or Cr^{3+}; third, the corrosion products (Fe^{2+}, Ni^{2+}, Cr^{2+} or Cr^{3+}) are transported from the interface back to the molten salt. During the whole corrosion process, kinetic property data, such as diffusion coefficient, exchange current density, charge transfer coefficient, limiting current density, and standard rate constant are vital. The first and third parts are related to material transport which are determined by diffusion coefficient D, while the second part involves the electron exchange which is governed by the exchange current density i_0, charge transfer coefficient α, and limiting current density i_l. Therefore, the kinetic data measurements of corrosion products (Fe^{2+}, Ni^{2+}, Cr^{2+} or Cr^{3+}) and impurities (e.g. OH^-) are significant to further understand the electrochemical behavior of corrosion products and impurities, as well as understand the corrosion mechanisms of structural material in the molten salts.

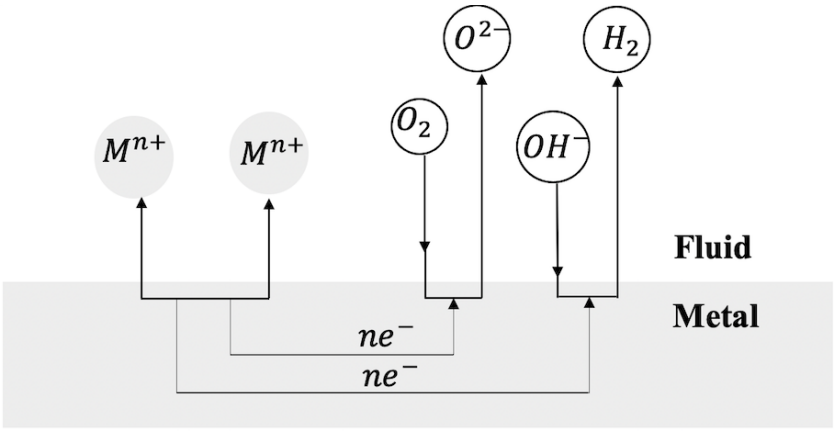

Figure 1-2 Impurity-driven corrosion process in molten salts

1.1.2.1.1 Diffusion Coefficient Measurement

There have been a variety of methods developed to measure diffusion coefficient. These methods, including but not limited to, cyclic voltammetry (CV), chronopotentiometry (CP), chronoamperometry (CA), rotating disc electrode (RDE), have been applied in the study of electrochemistry using a typical three-electrode (working, counter, and reference electrode) system. CV and CP are the most commonly used techniques among them.

1.1.2.1.1.1 Cyclic Voltammetry

Cyclic voltammetry is an electrochemical technique which is performed by cycling the potential on the working electrode and measuring the resulting current in the forward and reverse directions once or several times. The working electrode potential ramps linearly versus time. And the obtained CV curves gives the relation between the current and applied potential. The applied potential range varies depending on the interested redox reaction on the working electrode, and the reference electrode applied in the experiment. The static electrode and unstirred solution make the diffusion controlled peak possible. However, the steady-state solution may lead to a certain amount of analyte species to remain on the electrode after reduction and oxidation. This deposition layer may insulate the electrode surface and affect the subsequence scans. Therefore, it's suggested to perform electrode conditioning (or cleaning) after each scan by applying an appropriate constant potential to remove the layer on the electrode surface.

When using the CV technique, different scan rates are applied in the experiments and the diffusion coefficient is calculated from the relation between the peak current density and scan rate. As for different redox reaction types, such as, soluble-soluble or soluble-insoluble, reversible, quasi-reversible, or irreversible reaction, appropriate equations are applied as given in Table 1-3, where I is cathodic peak current, n is electron transfer number, F is Faraday constant, A is electrode surface area, v is scan rate, R is gas constant, C is specie concentration, and T is temperature.

Table 1-3 Diffusion coefficient calculation using CV method

Reaction Type		Equation	
Soluble-Soluble	Reversible	Randles-Sevcik[32,33,34]	$I = 0.446nFAC\sqrt{\frac{nFDv}{RT}}$
	Quasi-Reversible		$I = 0.436nFAC\sqrt{\frac{nFDv}{RT}}$
	Irreversible		$I = 0.496\sqrt{\alpha n}nFAC\sqrt{\frac{nFDv}{RT}}$
Soluble-Insoluble		Berzins-Delahay[35]	$I = 0.611nFAC\sqrt{\frac{nFDv}{RT}}$

1.1.2.1.1.2 Chronopotentiometry

In chronopotentiometry, a current pulse is applied on the working electrode and the resulting potential is recorded against the reference electrode as a function of time. Species will be reduced or oxidized at the working electrode surface when a constant current is applied. The electrode potential varies with time as the concentration of reactants changes at the electrode surface. After the reactant concentration drops to zero at the interface, the reactant cannot accept the electrons forced by current. Thereby, the potential will have a sharp change until to a plateau. Transition time τ is a crucial parameter in the measurement, which can be used in the calculation of diffusion coefficient D. The relation of applied constant current I, transition time τ and diffusion coefficient D is given by Sand's equation[36].

$$\frac{I\tau^{1/2}}{C} = \frac{nAFD^{1/2}\pi^{1/2}}{2} \qquad 1\text{-}1$$

Here, I is the applied constant current, τ is the transition time, n is the charge transfer number, A is the electrode surface area, D is the diffusion coefficient, C is the concentration of interested specie. One of the major issues related to CP technique is the determination of transition time. One must be extremely careful to obtain an accurate transition time to ensure accuracy of diffusion coefficient.

1.1.2.1.2 Available Diffusion Coefficient Data

In the present work, studies were conducted in molten NaF-KF-UF_4-UF_3 and $MgCl_2$-NaCl-KCl salts. And the diffusion coefficient of corrosion products (Fe^{2+}, Ni^{2+}, Cr^{2+} and Cr^{3+}) in both molten chloride and fluoride salts, and impurity (OH^-) in molten chloride salt is of interest. A variety of

studies have been conducted in the past several decades though perhaps in different salts, which may still shed a light on the present study.

Table 1-4 summarizes the available diffusion coefficient data of Fe^{2+}, Ni^{2+}, Cr^{2+}, Cr^{3+} and OH^- in molten salts.

Table 1-4 Available diffusion coefficient data of Fe^{2+}, Ni^{2+}, Cr^{2+}, Cr^{3+} and OH^-

Diffusion Coefficient ($cm^2\ s^{-1}$)		Molten Salt	Temperature (ºC)	References
Fe^{2+}	1.40×10^{-5}	KCl-LiCl-NaCl	550	Khalaghi et al.[38]
	1×10^{-6}	LiF-NaF-KF	500	D. Manning et al.[44]
	5×10^{-6}	$LiF\text{-}BeF_2$		
Fe^{3+}	3.8×10^{-6}	LiF-NaF-KF	600	H. Peng et al.[37]
	4.38×10^{-6}			
Ni^{2+}	$0.1 - 0.6 \times10^{-6}$	LiCl-KCl	500	Horvath et al. [39]
	5×10^{-6}	LiF-NaF-KF	470 - 540	Inoue et al.[43]
Cr^{2+}	1.53×10^{-5}	LiCl-KCl	500	Inman et al.[40]
	$(0.62 \pm 0.37) \times10^{-5}$	LiCl-KCl	429	Cotarta et al.[41]
	$(1.92 - 2.71) \times10^{-5}$	$KCl\text{-}CrCl_3$	800 - 900	Elizarov et al.[42]
	$(3.68 \pm 0.09) \times10^{-6}$	LiF-NaF-KF	700	Wu et al.[45]
	$(1.2 \pm 0.2) \times10^{-5}$	$LiF\text{-}BeF_2$	600 - 650	W. Doniger et al.[46]
	$(0.36 – 1.84) \times10^{-6}$	LiF-NaF-KF	612 - 983	Yoko et al.[47]
Cr^{3+}	0.55×10^{-5}	LiCl-KCl	500	Inman et al.[40]
	$1.53 - 2.33\times10^{-5}$	$KCl\text{-}CrCl_3$	800 - 900	Elizarova et al.[42]
	$(9.56 \pm 0.57) \times10^{-7}$	LiF-NaF-KF	700	Wu et al.[45]
H^+	2.1×10^{-4}	LiCl-KCl	450	Kanzaki et al.[49]
	$0.7 - 2.8 \times10^{-4}$	$LiCl\text{-}KCl\text{-}ZnCl_2$	450	Minh et al.[50]
OH^-	1.7×10^{-5}	$LiOH\text{-}LiClO_4$	25	Littauer et al.[51]
O^{2-}	2.1×10^{-6}	$LiCl\text{-}KCl\text{-}CsCl\text{-}Li_2O$	500	Kado et al.[52]

Khalaghi et al. [38] conducted an electrochemical study of Fe^{2+} in KCl-LiCl-NaCl at 550 ºC using CV technique. The calculated diffusion coefficient of Fe^{2+} was 1.40×10^{-5} cm^2 s^{-1}. Peng et al. investigated the electrochemical behavior of Fe^{3+} in molten FLiNaK salt at 600 ºC. Fe^{3+} was initially reduced to Fe^{2+} followed by reduction of Fe^{2+} to Fe and both reduction processes were diffusion controlled. The diffusion coefficient of Fe^{3+} was 3.8×10^{-6} cm^2 s^{-1} from CV measurement and 4.38×10^{-6} cm^2 s^{-1} from CP measurement. Horvath et al.[39] measured the diffusion coefficient of Ni^{2+} in LiCl-KCl eutectic at 500 ºC, with a value ranging from 0.1 - 0.6 $\times10^{-6}$ cm^2 s^{-1} at different concentrations. Studies have confirmed that both Cr^{2+} and Cr^{3+} were stable ion states in molten chloride salts. Inman et al. [40] employed steady-state voltammetry and chronopotentiometry techniques to study the electroreduction process of Cr^{3+}/Cr^{2+} and Cr^{2+}/Cr in molten LiCl-KCl at 500 ºC, in which Cr^{2+} was introduced in situ by the anodic dissolution of Cr metal at a constant current. The calculated averaged diffusion coefficient of Cr^{2+} using the adsorption model in Inman et al.'s study was 1.53×10^{-5} cm^2 s^{-1}, while the value of Cr^{3+} was 0.55×10^{-5} cm^2 s^{-1}. In the study by Cotarta et al.,[41] the diffusion coefficient of Cr^{2+} calculated based on CP scans using Sand's law yielded values of $(0.62 \pm 0.37)\times10^{-5}$ cm^2 s^{-1} at 429 ºC in molten LiCl-KCl salts. Moreover, Elizarova[42] proposed a hypothesis about the formation of polynuclear chromium complex in KCl-$CrCl_3$ melts. The measured diffusion coefficient of Cr ions was 1.53 - 2.33×10^{-5} cm^2 s^{-1} for Cr^{3+} and 1.92 - 2.71×10^{-5} cm^2 s^{-1} for Cr^{2+} in the temperature range of 800 - 900 ºC, respectively. Inoue et al. [43] measured the diffusion coefficient of Ni^{2+} in molten LiF-NaF-KF (FLiNaK) salts using CV technique. The electrochemical measurements were conducted at temperatures between 470 and 540 ºC. In this study, it confirmed that redox reaction of Ni^{2+}/Ni was a reversible two-electron reaction. The measured diffusion coefficient of Ni^{2+} was 5×10^{-6} cm^2 s^{-1} and the corresponding activation energy was $(5.86 \pm 1.67)\times10^{-4}$ J mol^{-1}. D. L. Manning et al.[44]conducted voltametric and chronopotentiometric study of Fe^{2+} in molten LiF-NaF-KF and LiF-BeF_2 salt at 500 ºC. The CV curves were obtained at the scan rates range from 50 mV/min to 10 V/min. The calculated diffusion coefficient was approximately 1×10^{-6} cm^2 s^{-1} in LiF-NaF-KF and 5×10^{-6} cm^2 s^{-1} in LiF-BeF_2 salt, respectively. Wu et al.[45] studied the kinetic properties of Cr^{3+} in molten FLiNaK salts at 700 ºC using CV and square wave voltammetry (SWV). It indicated that the reduction of Cr^{3+} to Cr is a two-steps reaction, which involved a reversible single-electron exchange redox reaction of Cr^{3+}/Cr^{2+} and a quasi-reversible two-electron exchange reaction of Cr^{2+}/Cr. In the study, the diffusion coefficients of Cr^{3+} and Cr^{2+} were calculated to $(9.56 \pm 0.57)\times10^{-7}$ cm^2 s^{-1} and $(3.68 \pm 0.09)\times10^{-6}$ cm^2 s^{-1}, respectively. W. Doniger et al.[46] investigated electrochemical behavior of Cr^{2+} in molten 2LiF-BeF_2 (FLiBe) salt at temperatures ranging from 500 ºC to 700 ºC using CV and linear sweep voltammetry (LSV). The measured diffusion coefficient of Cr^{2+} was $(1.2 \pm 0.2)\times10^{-5}$ cm^2 s^{-1}. By relating faradaic cathodic peak current density to Cr^{2+} concentration at 600 ºC and 650 ºC, a model was developed for predicting Cr^{2+} concentration and its diffusion coefficient. Yoko et al.[47] studied the reduction mechanism of Cr^{3+} in molten FLiNaK using CV and CP over a temperature range of 612 ºC - 983 ºC. Cr^{3+} was reduced to Cr^{2+} followed by a two-electron reduction of Cr^{2+} to Cr and both reduction processes were quasi-reversible. The measured diffusion coefficient of Cr^{3+} were 1.84×10^{-6} cm^2 s^{-1} at 983 ºC, 1.19×10^{-6} cm^2 s^{-1} at 893 ºC, 0.95×10^{-6} cm^2 s^{-1} at 804 ºC, 0.59×10^{-6} cm^2 s^{-1} at 716 ºC, and 0.36×10^{-6} cm^2 s^{-1} at 612 ºC.

In the diffusion coefficient measurement of OH^-, Swain et al.[48] investigated the redox behavior of moisture in LiCl-KCl eutectic melts using CV technique. Complicated voltammetric features were

observed that were attributed to the cathodic reduction of H_2O to form OH^-, adsorption of OH^- on the tungsten electrode, and cathodic reduction of OH^- to form O^{2-}. However, no quantitative estimation of diffusion coefficient was demonstrated. Kanzaki et al.[49] observed the hydrogen evolution reaction of OH^- in LiCl-KCl eutectic. The CV scans showed that the redox reaction of OH^-/H_2 was a reversible one-electron transfer reaction. Unfortunately, the diffusion coefficient of OH^- was not able to be measured, because the cathodic peak of OH^-/H_2 was close to the current rise due to the deposition of lithium metal. But the diffusion coefficient of H^+ at 450 ºC was calculated from cathodic peak current density, which was 2.1×10^{-4} cm^2/s. Minh et al.[50] studied the cathodic reduction of HCl dissolved in molten LiCl-KCl-$ZnCl_2$ at 450 ºC using CV and CP techniques. The calculated diffusion coefficient ranged from 0.7 to 2.8×10^{-4} cm^2/s at different concentrations of $ZnCl_2$. Littauer et al.[51] conducted a study on the diffusion coefficient of OH^- in aqueous LiOH-$LiClO_4$ electrolyte by utilizing RDE technique. The measured diffusion coefficient was 1.7×10^{-5} cm^2/s in 0.5 M LiOH solution at 25 ºC. Kado et al.[52] investigated the diffusion coefficient of O^{2-} in LiCl-KCl-CsCl-0.5 mol% Li_2O eutectic melt using boron-doped diamond (BDD) and glassy carbon (GC) electrodes. O_2 evolution on the BDD electrode and CO_2 evolution on the GC electrode were reversible and irreversible, respectively. The estimated diffusion coefficient of O^{2-} using CV technique was 2.1×10^{-6} cm^2/s at 500 ºC. Xie et al.[53] investigated the dissolution of steam in molten LiCl, and the electrochemical behavior of dissolve species at 660 ºC. An obvious cathodic current was detected in the steam dissolved molten LiCl salt, which was not observed in the blank LiCl salt. There was no corresponding anodic peak in the cyclic voltammetry scan. It demonstrated that the redox reaction of H^+/H_2 was irreversible. In addition, the electro-chemical reduction of dissolve H^+ was confirmed to be diffusion-controlled process. Lithium was found to be deposited at a more positive potential in the moisturized LiCl salt, which was attributed to the formation of LiH intermediate compound. Unfortunately, the kinetic property data was not measured or included in the scope of the study.

1.1.2.1.3 Exchange Current Density Measurement

In general, three conventional techniques are available to measure the exchange current density i_0, charge transfer coefficient α, and limiting current density i_l: Tafel plot, linear polarization resistance (LPR), and electrochemical impedance spectroscopy (EIS)[54]. These techniques have been widely used in aqueous solution. However, the electrode reaction rate is much faster in molten salts. Thus, it can be limited by mass transfer of reactants from the bulk solution to the electrode surface. Significant errors may be introduced by using techniques without considering the mass transfer effect[64]. Therefore, a modified Butler-Volmer equation was applied as given in Eq. 1-2 or Eq. 1-3. It involves charge transfer process at the electrode-electrolyte interface and the mass transfer process of the reactant and product to/away from the electrode surface[64].

$$i = i_0 \left\{ exp\left[\frac{(1-\alpha)nF}{RT}\eta\right] - \frac{C_{M^{n+}}^{s}}{C_{M^{n+}}^{b}} exp\left[\frac{-\alpha nF}{RT}\eta\right]\right\} \quad 1\text{-}2$$

$$i = \frac{i_0 \left\{ exp\left[\frac{(1-\alpha)nF}{RT}\eta\right] - exp\left[\frac{-\alpha nF}{RT}\eta\right]\right\}}{1 - \frac{i_0}{i_L} exp\left[\frac{-\alpha nF}{RT}\eta\right]} \quad 1\text{-}3$$

Where, i is the current density, n is the number of exchange electrons; F is the Faraday constant, α is the charge transfer coefficient; overpotential $\eta = E - E_{eq}$; E and E_{eq} are the electrode potential and the equilibrium potential respectively; i_0 is the exchange current density; $C^s_{M^{n+}}$ and $C^b_{M^{n+}}$ are the concentration of M^{n+} at the electrode surface and bulk solution respectively; i_L is limiting diffusion current density.

1.1.2.1.3.1 Tafel Plot

At larger overpotentials[54,64], Eq. 1-3 can be simplified as Eq. 1-4.

$$\log|i| = \log|i_0| + b\eta \quad 1\text{-}4$$

Where $b = \frac{(1-\alpha)nF}{2.3RT}, \eta > 0$; $b = \frac{\alpha nF}{2.3RT}, \eta < 0$.

Tafel plot method is based on Eq. 1-4, which indicates a linear correlation of the $\log|i|$ and η in the Tafel regions. Thus, i_0 can be determined by extrapolating the linear portions of curve to the equilibrium potential.

1.1.2.1.3.2 Linear Polarization Resistance

At very small overpotentials[54,64], the relation of $i - \eta$ can be simplified as Eq. 1-5. It indicates i is linearly related to η within small overpotential range. Hence, the value of i_0 can be determined from the slope of $i - \eta$ curve near the equilibrium potential.

$$i = i_0 \frac{nF}{RT}\eta \quad 1\text{-}5$$

1.1.2.1.3.3 Electrochemical Impedance Spectroscopy

In an EIS scan, a small sinusoidal potential with a fixed frequency is applied to the electrode, and the response of the current is measured. This behavior will repeat for a wide range of frequencies. The electrochemical reaction can be described by the electrical equivalent circuit that contains a double layer capacitor, in parallel with a faradaic impedance z_f. If the mass transfer effect is involved in the electrode kinetics, the faradaic impedance can be expressed by Eq. 1-6, where R_{ct} is charge transfer resistance and z_w is the mass transfer impedance. i_0 is estimated using Eq. 1-7 in EIS measurements[54,64].

$$z_f = R_{ct} + z_w \quad 1\text{-}6$$

$$R_{ct} = \frac{RT}{nFi_0} \quad 1\text{-}7$$

1.1.2.1.3.4 Curve Fitting Technique

Potentiodynamic scans are performed to obtain the relation of $i - \eta$. The value of i_0, α, and i_l are calculated by fitting the measured current density i and overpotential η using Eq. 1-3. In the present study, a recently developed technique — non-linear curve fitting, which was based on Guo et al.'s study[64], was applied in the calculation. Comparing with Guo et al.'s method, it improved the efficiency of the curve fitting with the assistance of built-in solver function in Excel. The procedures of the non-linear curve fitting technique are summarized as: (1) assign appropriate initial values to the unknown parameters including i_0, α, and i_l; (2) calculate square of deviation between the values of measured i_0, α, and i_l and computed i_0, α, and i_l; (3) repeat Step (2) until obtain the least squared deviation, which corresponds to optimized values of i_0, α, and i_l.

1.1.2.1.4 Available Exchange Current Density Data

A few studies have been conducted on the exchange current density measurements of Fe^{2+}, Ni^{2+}, Cr^{2+}, Cr^{3+} and OH^- in molten salts. The available data is given in Table 1-5.

Table 1-5 Available exchange current density data of Fe^{2+}, Ni^{2+}, Cr^{2+}, Cr^{3+} and OH^-

Exchange Current Density		Molten Salt	Temperature	References
mA/cm^2			(ºC)	
Fe^{2+}	1.89-6.18	FLiNaK	600 - 750	Wu et al.[63]
Ni^{2+}	0.064 - 0.196	$LiF-BeF_2-ZrF_4$	500	Jenkins[56]
Cr^{2+}	0.15-0.88	FLiNaK	600 - 750	Wu et al.[63]
H^+	$10^{-2.6}$-$10^{-3.1}$	H_2SO_4	25	Seri[65]
OH^-	0.10-0.11	0.1 mol/L KOH	25	Tang et al.[67]
Standard Rate Constant		Molten Salt	Temperature	References
cm/s			(ºC)	
Cr^{3+}	0.02-0.08	$NaCl-KCl-CrCl_3$	700-850	Stulov et al.[61]
Cr^{3+}	0.005-0.05	$NaCl-KCl-K_3CrF_6$		

Manning et al.[55] investigated the voltammetry of Fe^{2+} in molten FLiNaK over the temperature range of 470-545 ºC. The current-potential curves were recorded for relatively slow scan rates in the range of 25 to 150 mV/min using platinum as working, counter, and reference electrodes. The redox reactions of Fe^{2+}/Fe and Fe^{3+}/Fe^{2+} were reversible in the experimental conditions. The limiting current of cathodic wave was proportional to the concentration of iron in the molten salts. The activation energy calculated from the limiting current of Fe^{2+}/Fe was 12 kcal mol^{-1}. Jenkins[56] conducted a kinetic property study of Ni^{2+}/Ni in $LiF-BeF_2-ZrF_4$ at 500 ºC using a voltage-step

method. The measurements were performed at different concentrations of Ni^{2+}/Ni in a range of 2.43×10^{-6} to 1.45×10^{-5} mol/cm^3. The measured i_0 of Ni^{2+}/Ni was in the range of 0.064-0.196 mA/cm^2, and it didn't show dependence on concentration in the study. The fitted values of α using equation $i_0 = nFk^0C^{(1-\alpha)}$ ranged from 0.32 to 0.55, while the corresponding calculated k^0 was 1.6×10^{-4} to 2.3×10^{-3} cm/s. Lim et al.[57] conducted a study on the exchange current density of neodymium chlorides in LiCl-KCl molten salt at 500 ºC using Tafel plot method. The two-step reaction of Nd^{3+} to Nd^{2+} and Nd^{2+} to Nd were confirmed by potentiodynamic scan, since two peaks were observed in the Tafel curves, which couldn't be observed in the cyclic voltammetry scan because of close reaction potential of Nd^{3+}/Nd^{2+} and Nd^{2+}/Nd couples. The measured i_0 of Nd^{3+}/Nd^{2+} and Nd^{2+}/Nd were 1.48± 0.24 and 18.38±0.64 mA cm^{-2}. However, the i_0 values showed significant differences from the data reported by Kim et al.[58] and Wu[59]. In another study by Lim et al.[60], the exchange current density and transfer coefficient of uranium in molten LiCl-KCl were measured using Tafel plot and linear polarization resistance methods. The temperature dependency of exchange current density followed Arrhenius' law in the temperature range from 450 to 500 ºC. The calculated averaged cathodic transfer coefficient was 0.22±0.01, which was quite different from the value 0.5 assumed in most electrochemical modeling study. In the study by Stulov et al.[61], cyclic voltammetry was applied to determine standard rate constants of charge transfer at a glassy carbon electrode for the Cr^{3+}/Cr^{2+} redox couple in the NaCl-KCl-$CrCl_3$ and NaCl-KCl-K_3CrF_6 in the temperature range of 700-900 ºC. According to the theory of elementary charge transfer act, the smaller complexes need more energy in the reorganization before the electron transfer process, thus, the electrode reaction proceeds at a lower rate. As expected, the calculated standard rate constant in NaCl-KCl-$CrCl_3$ was less than that in NaCl-KCl-K_3CrF_6. And the standard rate constants in both molten salts increased with temperature and followed Arrhenius Law. In the study by Yoon et al.[62] electrochemical impedance spectroscopy, linear polarization resistance, Tafel plot and cyclic voltammetry measurement were conducted to measure exchange current density of U^{3+}/U reaction in molten LiCl-KCl salt at different UCl_3 concentrations and temperatures. In the measurements using the EIS method, a minimum overpotential from equilibrium potential was applied and fitted to an appropriate equivalent circuit to obtain the exchange current density. When using Tafel plot and LPR methods, linear fitting was conducted at small and large overpotential range of the current-potential curves to determine the exchange current density. According to Yoon et al.'s results, all calculated i_0 have the linear trend with concentration and temperature. But i_0 calculated using EIS method was the most consistent and accurate in comparison to those from LP, Tafel plot and CV methods.

Recently, another new method was developed as well, in which i_0 was obtained by fitting the potentiodynamic scan curve using the electrode kinetic equation. Wu et al.[63] estimated i_0 and charge transfer coefficient α of Cr^{2+}/Cr and Fe^{2+}/Fe couple in the molten FLiNaK eutectic at temperatures ranging from 600 to 750 ºC using an optimized fitting method, Tafel plot, and LPR techniques, respectively. The values obtained from the three techniques were in good agreement, while optimized fitting methods gave smaller uncertainty. The calculated exchange current density using optimized fitting methos is in the range of 0.15-0.88 mA cm^{-2} for Cr^{2+}/Cr, and 1.89-6.18 mA cm^{-2} for Fe^{2+}/Fe, respectively. As for the charge transfer coefficient α, it was in the range of 0.22-0.42 for Cr^{2+}/Cr and 0.09-0.13 for Fe^{2+}/Fe. Both i_0 of Cr^{2+}/Cr and Fe^{2+}/Fe increased with

temperature. The calculated α of Cr^{2+}/Cr decreased with temperature, while α of Fe^{2+}/Fe showed little temperature dependence. Based on the study by Wu et al.[63], the curve fitting technique might have been probably the best option to obtain more reliable i_0 and α. However, all these techniques are developed based on the simplified Butler-Volmer equation, in which mass transfer is not taken into consideration. In the experiments involving molten salts, the reaction on the electrode is faster, thus the reaction rate on the electrode surface could be limited by the mass transfer rate of reactants from the bulk solution to the electrode surface. Therefore, significant error may be introduced by using Tafel plot, LPR and EIS methods. On that account, Guo et al.[64] conducted an electrochemical study of Gd^{3+}/Gd in molten LiCl-KCl salts at different concentrations (1-9 wt. %) and temperatures (450-550 ºC). In the study, three conventional techniques, i.e., Tafel plot, LPR and EIS, and one newly developed technique, i.e., optimized fitting technique using non-simplified Butler-Volmer equation which has considered the mass transfer effect, were applied in the measurements of exchange current density, charge transfer coefficient, limiting current density and standard rate constant. It showed that optimized fitting method could give more reliable values of i_0. Because the values of i_0 calculated from the optimized methods followed the theoretical power law with the concentration of Gd^{3+}/Gd, and the fitted values of α from the relation of exchange current density and concentration using the optimized fitting technique keeps consistent with that fitted using the Butler-Volmer equation. While the fitted values of α using the other three conventional techniques are either negative or zero which was unrealistic. Moreover, the standard rate constant k^0 was also calculated using optimized fitting technique, which was in the range of 4.93-9.13$\times 10^{-5}$ cm/s at the studied temperatures.

As for the exchange current density of OH^- in molten salts, no related study has been reported to the best of my knowledge. However, there is still study available in aqueous solution which may shed some light to the present study. Seri[65] estimated the exchange current density of hydrogen evolution on Titanium in sulfuric acid solution. The value of exchange current density was $10^{-2.6}$-$10^{-3.1}$ mA/cm^2 calculated using the Tafel extrapolation method and 10^{-3} mA/cm^2 using the differential polarization method. In comparison, differential polarization method gave a more accurate value, which can be applied to eliminate the undesired physical factor such as oxide film and solution resistance. And the cathodic charge transfer coefficient was around 0.3. Vega et al.[66] investigated the hydrogen oxidation reaction using a polycrystalline platinum rotating disk electrode in hydroxide and carbonate aqueous electrolytes. Exchange current density was obtained using Tafel plot method by linear regression extrapolated to the reversible hydrogen potential. The measured exchange current density of hydrogen oxidation was 0.14 ± 0.01, 0.24 ± 0.09 and 0.32 ± 0.09 mA/cm^2 in 1M KOH, 0.3M Na_2CO_3-0.55M $NaClO_4$ and 0.5M Na_2CO_3-0.25M $NaClO_4$, respectively. The exchange current density was higher in the presence of carbonate compared to hydroxide. It attributed to a more exothermic process involving carbonate and hydrogen reaction, compared to hydroxide and hydrogen, which made the carbonate reaction thermodynamically favored. Moreover, mass transfer analysis was performed using Koutecky-Levich plots. It has been confirmed that the hydrogen oxidation reaction was a two-electron reaction. And the measured diffusion coefficient was 2.21, 2.31 and 2.08 $\times 10^{-5}$ cm^2/s. Tang et al.[67] investigated the hydrogen electrode reaction using a platinum rotating disk electrode in 0.1 mol/L KOH solution saturated with hydrogen. In this study, a new equation was derived for the hydrogen electrode reactions to

correct for both the change in effective equilibrium potential and in effective exchange current density. The exchange current density of hydrogen reactions on a Pt rotating disk electrode was 0.10-0.11 mA/cm^2 with an activation energy 33.5 kJ/mol.

1.1.2.2 Static Corrosion Study

Various structural materials used in MSRs or CSPs must be tested to verify conformation to quality standards. Such tests can provide useful information in order to make sound decisions regarding selection of materials, processing, and treatment. Among them, static immersion test is considered to be the most popular and simplest type of corrosion test, in which different materials that are subjected to particular conditions are assessed. It's a very versatile process which can be customized to meet specific needs regardless of application.

In static immersion tests, specimens are immersed in the solution at specific experimental conditions. At the end of tests, specimens are removed from the solution, followed by appropriate cleaning procedures before conducting further analysis. The measured weight loss of specimens can be used to estimate the corrosion rate, which is a crucial criterion in material selection[68,69]. To understand the corrosion mechanism of materials, the surface and/or cross-section of specimens are analyzed by scanning electron microscopy (SEM) and transmission electron microscope (TEM), from which, attack depth and corrosion behavior can be obtained.

Static immersion test has been widely applied in material corrosion studies [70,71,72,73,74,75,76]. This section only briefly reviewed the studies that are closely related to the present study. Dai et al.[77] studied the static corrosion of Incoloy 800H alloy with Nickel cladding in LiF-NaF-KF (FLiNaK) at 850 ºC. Results show that Cr and Fe are depleted from the alloys' surface and grain boundaries, where "diffusion paths" are formed. The corrosion process is mainly controlled by the redox reaction of impurity metal ions with Fe and Cr at the alloy surface. And Cr element is hardly depleted from Σ3 type grain boundaries (refers to grain boundaries between crystallites with twin orientation relationship). Ouyang et al.[78] investigated long-term corrosion behaviors of Ni-based Hastelloy-N and Hastelloy-B3 in the moisture-containing molten FLiNaK salts at 700 °C. The weight loss for the tested duration of 100-1000 h was caused by the aggregate dissolution of Cr and Mo into FLiNaK salts. The alleviated corrosion rate was due to the depletion of Cr and Mo near the surface of the alloys, and thus the long-term corrosion rate was controlled by diffusion of Cr and Mo outward to the alloy surface. The corrosion pattern tended to be intergranular corrosion at the early stage of corrosion test and then transferred to general corrosion for longer immersion hours. Danon et al.[79] assessed the molten salt corrosion performance of a Ni-Mo-Cr (GH3535) alloy weldment. Corrosion testing was performed in FLiNaK molten salt at 750 ºC for 500 h. Results suggest that large M_6C carbides present in the parent metal may contribute to corrosion attack through galvanic corrosion. In the study by Patel et al.[80], the corrosion tests of alloys, Inconel 718, Inconel C-276, and Nimonic 80A, were performed at 680 ºC in FLiNaK with an immersion period from 8 to 48 hours. Corrosion occurred predominantly by depletion of Cr near the surface. Cr-rich oxide layers were formed, which may retard further internal corrosion for longer immersion hours. Ouyang's group[81] conducted corrosion tests of Hastelloy-N, Hastelloy-B3, and Haynes 263 at 600 and 700 ºC in FLiNaK salt with different moisture contents. The mass loss of the tested alloys is primarily determined by the purity of FLiNaK salts. And the mass loss varied

linearly with original Cr content plus one-third of Mo content. Lei et al.[82] conducted an in-situ X-ray diffraction study of Inconel 617 corrosion in FLiNaK molten salts. Cr-rich $M_{23}C_6$ and Mo-rich M_6C were formed at the grain boundaries. These carbides at the grain boundary can form a galvanic couple with the matrix and lead to more serious loss of other elements and intergranular corrosion. And atoms exposed along the grain boundary were much easily diffused compared to those buried inside the matrix. X. Ye et al. [83] investigated the corrosion behavior of Hastelloy N alloy in molten FLiNaK at 850 ºC. It showed that Mo and Cr were depleted, and Fe-enriched layer was formed on the surface. The redox reaction between Fe ion and Cr controlled the corrosion process. The concentration-gradient between $M_{12}C$ and alloy matrix leaded to the loss of Mo and Cr in $M_{12}C$ carbide.

Hofmeister et al.[84] studied the corrosion behavior of low-carbon stainless steels X2CrNi18–9 and Ti-stabilised stainless steel X6CrNi-Ti18-10 in a ternary LiCl-KCl-CsCl molten salt. It has been concluded that the latter alloy was protected against intergranular corrosion by a Cr_2O_3 passive layer up to a temperature of approximately 500 °C and short exposure times. The passive protective layer is degraded at higher temperatures and longer exposure times. The corrosion mechanism was suggested to be based on a "chlorination–oxidation" mechanism already observed in other steels. Ren et al.[85] investigated carburized SS316 and SS316 in ternary NaCl-KCl-$MgCl_2$ salt at 700 ºC under argon atmosphere when adding Mg metal (1 wt%). It was concluded that residual water and oxygen in the salts greatly oxidize Fe, Cr, and Ni at the alloy surface in the initial stage of the corrosion process. Later, Fe and Cr at the alloy surface dissolved into salts through the redox reaction with metallic ion impurities such as Ni^{2+}, Fe^{2+}, and Fe^{3+} in the salts. Cr-rich carbides were formed and vulnerable to attack by molten chloride salts because Cr atoms in the carbides preferentially escape from the carbides and dissolve into salts, causing the decomposition of Cr-rich carbides and reducing the hardness of carburized SS316. In the study by Zheng et al.[86], corrosion tests of SS 316 were performed in FLiBe at 700 ºC. Chromium carbide particles were observed protruding from the grain boundaries. These particles were formed as inwardly diffusing carbon reacted with outwardly diffusing chromium. Doniger et al.[87] investigated the impurity-driven corrosion behavior of SS 316H in molten FLiBe salt by adding CrF_2 and FeF_2. The addition of CrF_2 decreased the apparent grain boundary attack depth. And in the salts with FeF_2 added, the specimens showed Cr deficient and Fe rich layer parallel to the exposed surface, which may occur through the reaction of $FeF_2 + Cr \leftrightarrow Fe + CrF_2$. Moreover, voltammetry techniques applied to determine the dilute species concentration demonstrate the ability to distinguish between common corrosion products, such as dissolved CrF_2 and FeF_2. Brendan et al.[147] conducted corrosion studies of ferrous-based alloys (stainless steel 316L) and nickel-based alloys (Inconel 718, Haynes 230 and Hastelloy C276) in molten KCl-MgCl2-NaCl salts (salts purified with Mg) at 800 ºC for 100 hours. The corroded surface of nickel-base alloy showed pitting, and Cr depletion was observed in the region near the surface. Similar corrosion behavior was also observed in ferrous-based alloys. Moreover, Mg and O deposits were observed to embed in the open pits or pores in the corroded nickel-based specimens. It indicated that the salts could continue to infiltrate into the alloy through the porous structure and attack the material until either the oxide and chloride species reached equilibrium in the salts, or most of the impurities in the salts have been consumed.

Sarvghad et al.[88] investigated the compatibility of SS 316 with eutectic mixtures of NaCl+Na_2CO_3 and NaCl + Na_2SO_4 at 700 °C and Li_2CO_3 + K_2CO_3 + Na_2CO_3 at 450 °C in the air for thermal energy storage. For the SS 316 specimen submerged for 120h in the molten chloride sulfate at 700 °C, SEM analysis indicated grain boundary (GB) de-alloying of Cr, Fe, and Mn followed by the formation of a Mo-Ni-S oxide along GBs. Deng et al.[89] investigated the grain boundary oxidation of proton-irradiated 304 nuclear-grade stainless steel in primary water of pressurized water reactor, using the atom probe tomography (APT) in conjunction with transmission electron microscope (TEM). Chromium oxide was observed at the GBs. A lower GB oxidation rate was observed in the 0.5-dpa irradiated specimen due to the lower Cr content in oxide, since a higher Cr content in oxide indicated a higher protectability of the oxide, which could mitigate further oxidation by decreasing oxygen diffusion rate through the oxide itself.

1.1.2.3 Galvanic Corrosion Study

When electrically conductive materials are ohmically coupled as given in Figure 1-1, galvanic corrosion of the coupling is susceptible. The electrode potential difference between the reactions at the two electrodes is the driving force for an accelerated attack on the anode. In studies of galvanic corrosion, an electrochemical technique — zero resistance ammeter (ZRA) technique is applied[90,91,92,93,94].

In the measuremen, ZRA controls two electrodes to be equal potential as though they were connected with a wire. When exposed to an electrolyte, one material (more active one) is corroded and protect the more noble one. The anode reaction is generally dissolution of metal, while on the cathode, corrosive species, such as HF, H_2O or O_2, are reduced. Galvanic current and potential are measured, in which the direction of measured galvanic current flow determines which electrode is active, and the magnitude of the current determines the level of activity[95]. The galvanic corrosion rate can be calculated using Eq. 1-8, which is derived based on Faraday's law[96,97].

$$CR = \frac{\int Idt}{nFAt} M_{alloy} \quad 1\text{-}8$$

Where CR is galvanic corrosion rate with a unit of $mg/(cm^2 \cdot h)$, A is anode surface area with a unit of cm^2, t is test duration time with a unit of hour, M_{alloy} is mass of alloy per mol with a unit of g/mol. In the calculation of M_{alloy}, only the major component elements in the alloy are considered, and the minor ones are ignored based on the standard practice described in ASTM-G102[98]. The calculation of M_{alloy} is given in Eq. 1-9 and Eq. 1-10 using SS 316H and Alloy 617 as examples.

$$M_{SS316H} = \frac{1}{\frac{C_{Fe}}{55.85} + \frac{C_{Ni}}{58.69} + \frac{C_{Cr}}{52.00}} \quad 1\text{-}9$$

$$M_{Alloy\ 617} = \frac{1}{\frac{C_{Co}}{58.93} + \frac{C_{Ni}}{58.69} + \frac{C_{Cr}}{52.00} + \frac{C_{Mo}}{95.95}} \quad 1\text{-}10$$

Where C is the weight percent of each element in the alloy.

A variety of studies have been conducted on the galvanic corrosion between different metal alloys, although most of them are performed in aqueous solution, and related studies in molten salts are scarce. Yoo et al.[99] conducted galvanic corrosion tests using Korean standard D 3504 steel/SS 304 couple and Korean standard D 3504 steel/copper couple in the Ca $(OH)_2$-NaCl solution. A galvanic sensor system was developed to detect the corrosion damage through the relationship between the galvanic current and the weight loss, which can be expressed by $Q = I \times t = \frac{nFw}{M}$, where Q is total coulombs, w is the weight loss and M is the atomic weight. Mansfeld et al.[100] performed galvanic corrosion tests by coupling Al alloy to Cu, SS 304L, 4130, Ti-6Al-4V, Cd or Zn in air-saturated 3.5% NaCl aqueous solution. Galvanic current and weight loss data were obtained for cathode and anode area ratio = 0.1, 1 and 10 in 24-hour tests. Moreover, since the measured galvanic current density represented the "galvanic effect", which is the increase of dissolution rates due to the galvanic coupling, it confirmed that theoretical calculations based on mixed potential theory, according to which the dissolution rate was linearly related to cathode/anode area ratio expressed by $r_A = K(1 + \frac{S_c}{S_a})$ in the case of diffusion control of the cathodic reaction. Yin et al.[101] investigated the galvanic corrosion associated with SM 80SS steel and Ni-based alloy G3 couples in NaCl solution. The effect of cathode/anode area ratio and temperature on galvanic corrosion was studied. The galvanic corrosion rates increased when the temperature and cathode/anode area ratio increased. SEM analysis was also applied to measure corrosion pits depth, which confirmed that the pitting corrosion aggravated with cathode/anode area ratio $\frac{S_c}{S_a}$. Okonkwo et al.[102] studied the galvanic corrosion between low alloy steel (LAS) A508 and 309/308L stainless steel (SS) in pressurized water reactor (PWR) simulated primary solution, using several electrochemical techniques, including potentiodynamic polarization scan, electrochemical impedance spectroscopy (EIS) and zero resistance ammeter (ZRA). From ZRA measurements, the estimated dissolution rate was slightly different from the measured ZRA galvanic corrosion rate. It signified that some factors such as metallic resistance and solution resistance played vital roles in the galvanic interaction of separated coupled metals. EIS analysis showed that oxide film formed on the surface as exposure time prolonged would suppress the galvanic corrosion rate. Jeon et al.[103] studied galvanic corrosion behavior between Alloy 690 and magnetite in alkaline aqueous solutions at 30 ºC and 60 ºC using the potentiodynamic polarization method and zero resistance ammeter. The current value in the galvanic couple was positive and the corrosion potential of Alloy 690 was relatively lower, which indicated that Alloy 690 acted as the anode. Galvanic effect between Alloy 690 and magnetite is proposed to be an additional factor accelerating the corrosion rate of Alloy 690 steam generator tubing in PWRs. And the extent of galvanic effect increased with the rise of the temperature. Fushimi et al.[104] investigated the galvanic corrosion of carbon steel welded with type-390 stainless steel in NaCl solutions. An innovative multi-channel electrode technique was applied, which allowed the working electrodes to join a galvanic couple and simultaneous measurement of current and open circuit potential as a function of immersion time. It turned out that difference between anodic and cathodic currents was larger at the initial stage of immersion in artificial sea water. Wang et al.[105] studied the galvanic corrosion Cr and GH 3535 caused by the temperature gradient. The results showed that temperature difference caused the different corrosion potentials between metals in the melt, which leaded to significant galvanic

corrosion. Both Cr and GH3535 suffered from galvanic corrosion when the same samples were electrically-contact in molten FLiNaK where temperature gradients existed. The samples at the high temperature sections acted as the anodes. The dissolved metal ions diffused to be reduced on the cold-section samples, resulting in the continued dissolution of the hot-end samples. The dissolution accelerated significantly at a higher temperature gradient. Li et al.[106] studied the galvanic effect between N80 carbon steel and 13Cr stainless steel in supercritical CO_2-containing formation water under static and dynamic conditions. Different electrochemical techniques were applied, including OCP, EIS and ZRA. In the study, it indicated that the galvanic effect accelerated the N80 carbon steel in both static and dynamic conditions. The flow fluid promoted the galvanic effect with higher galvanic current density. The galvanic current density decreased with the rise of immersion time because of the decreasing of potential difference and increasing of resistance. In static tests, the time at which the coupled potential positively shifted and then the galvanic current density sharply decreased was later than that in dynamic tests, probably because of earlier formation of $FeCO_3$ in dynamic tests. Gao et al.[107] performed a high-temperature corrosion behavior study of Inconel 617 with Ni-cladding in Molten FLiNaK salt. $FeNi_3$ layer was found to cover the Inconel 617 specimen surface. When the Ni cladding on the Inconel 617 was broken, the coupling of Ni cladding and Inconel 617 can accelerate the corrosion of Inconel 617 by galvanic corrosion. The dissolved Co in the salts were transferred to the Ni cladding and reduced to Co which formed Ni-Co alloy. This process was accelerated by the difference of Co activity in the galvanic coupled alloys. Wang et al.[108] investigated temperature gradient induced galvanic corrosion of Fe and SS 316L in molten FLiNaK with temperature gradient of 650/700 ºC and 600/700 ºC. It's found that the temperature difference is the cause of corrosion potential difference, thus leading to galvanic corrosion. The galvanic effect became larger when temperature gradient increased. Fe and SS 316L at 700 acted as the anodes and the corrosion was accelerated. Choi et al.[109] conducted corrosion tests of SS 316 in FLiNaK, and Haynes 230, SS 316L and Hastelloy C-22 in $MgCl_2$-NaCl-KCl at 500 ºC using ZRA. The measured ZRA current of SS 316L in FLiNaK was reduced after addition of Li metal, which indicated that corrosion has been mitigated due to redox control. The results kept consistent with the relative post-test examination of metal surfaces and salt samples. It has been concluded that electrochemical measurements using ZRA could be standard protocol in rapid assessments regarding the effect of salt composition and metal alloy characteristics on corrosion in molten salts.

As for the study of galvanic corrosion between alloy and graphite, abundant literature reports that the presence of graphite can accelerate alloy corrosion in the molten salts[110,111,112]. However, these studies are mainly from static corrosion tests conducted to study the impact of alloys/Graphite coupling in molten fluoride salts, and no quantitative analysis was performed. Zheng et al.[113] performed corrosion tests of SS 316 in FLiBe at 700 ºC for an exposure duration up to 3000h. Tests were performed in both 316 stainless steel and graphite capsules. The samples tested in the graphite capsules have more severe grain boundary attacks than those tested in SS 316, indicating that graphite accelerated the corrosion attack of SS 316. The graphite capsule was found to liberate carbon particles in the presence of salt even though it was cleaned and baked. Ai et al.[114] investigated the effects of graphite/alloy interaction on corrosion of Ni-Mo-Cr alloy in molten FLiNaK salt. The corrosion attack was more severe with more weight loss and a deeper Cr depletion layer in samples that were in electric contact with graphite than those isolated with

graphite. Galvanic corrosion between alloy and graphite was confirmed by electrochemical measurement. The corrosion in isolated tests was controlled by nonelectric transfer, and a thin silver-gray Cr_7C_3 film was identified on the graphite. A similar corrosion phenomenon was also reported by Qiu's group[115]. In Qiu's study, pure metal Cr corrosion tests were performed in molten FLiNaK salt at 700 ºC for 500 h using graphite crucible and Ni crucible. Results indicate that the container materials accelerated corrosion due to different potentials between metal Cr and the crucibles. The Cr-rich film on the graphite crucible was identified as Cr_7C_3 with a small amount of $Cr_{23}C_6$, while the Cr was deposited on the Ni crucible surface and formed Ni-Cr alloy by thermal diffusion mechanism. Seller et al.[116] investigated the corrosion of SS 316L in molten FLiNaK salt. When graphite was present in the system, 316L coupons have nearly double the weight loss in addition to larger void formations near the surface. This accelerated corrosion of 316L was caused by the nonelectric transfer of Cr, Fe, and Mo from 316L to graphite surface to form Cr_7C_3 and Mo_2C carbides.

There are limited reports on the quantitative analysis of galvanic corrosion between the candidate structural materials and graphite in molten salts. Qiu et al.[117] investigated the galvanic corrosion of SS 316L/graphite in molten FLiNaK salt. The graphite, with more positive potential, acted as the cathode and accelerates the corrosion of the steel. The galvanic current density increased with rise of cathode/anode area ratio. The corrosion rate was calculated, which increased linearly with the increase of cathode/anode area ratio, temperature, and moisture content in the studied system.

1.2 Research Gap and Motivation

In the present work, the material corrosion study in molten salts can be roughly divided into three parts: (1) fundamental corrosion kinetic data, (2) static corrosion, and (3) galvanic corrosion study. As discussed before, fundamental kinetic property data of metal corrosion products (Fe^{2+}, Ni^{2+}, Cr^{2+}, and Cr^{3+}) and non-metal impurities (OH^-), are of importance to understand their electrochemical behavior, and structural material corrosion mechanism in molten salts, since they determine the mass transfer and interface reaction during the corrosion process. In the measurements of kinetic parameters, i.e., diffusion coefficient and exchange current density, different electrochemical techniques, including CV, CP and PD, etc., have been widely applied in a variety of fields. However, most of the available studies on the kinetic data measurements of corrosion products were performed in the temperature range less than 600 °C, either in FLiNaK, LiCl-KCl or NaCl-KCl salts. The kinetic data varies in different salts. The available data definitely can't satisfy the design need of MSRs or CSPs, since their normal operation temperature always ranges from 600 °C to 800 °C and the salt mediums utilized are $MgCl_2$-NaCl-KCl or NaF-KF-UF_4-UF_3 in the present study. And the measured data showed large discrepancies in the different studies, which made it very difficult for researchers to apply them in industry. For example, the measured diffusion coefficient of Fe^{2+} by Khalaghi et al.[38] was ten times large than that measured by D. Manning et al[44]. Even though considering that the salts and temperatures used in the tests were slightly different, the data discrepancy was still unacceptable. Furthermore, although it's believed that the diffusion coefficient values are directly related to ion radius, which means that the larger the ion dimension is, the larger the diffusion coefficient, there hasn't no corresponding study which purposely compared the magnitude order of different ions.

For measurements of exchange current density, the available data for Fe^{2+}, Cr^{2+}, Cr^{3+} and Ni^{2+} were very scarce. And most of the available studies were conducted using three conventional techniques (Tafel plot, linear polarization resistance and EIS), which were based on a simplified Butler-Volmer equation and didn't consider the mass transfer effect. However, the electrode reaction in the molten salts was very fast comparing with aqueous solution, thus reaction rate could be limited by the mass transfer process[64]. The mass transfer effect was not negligible in molten salts. Moreover, Guo et al.'s[64] study has demonstrated that significant error would be introduced in the exchange current density calculation if mass transfer effect was not considered. Until now there haven't been available exchange current density data for Fe^{2+}, Cr^{2+}, Cr^{3+} and Ni^{2+} which were obtained by considering the mass transfer in the salts that the present study addressed.

As for the kinetic data measurements of the non-metal specie OH^-, the situation is even worse. Researchers have spent lots of effort to investigate its kinetic properties in aqueous solution, but the related study in molten salts at high temperatures is far from sufficient. The available investigation of OH^-/H_2 redox reaction in molten salts was performed several decades ago, which only focused on qualitive analysis, and the diffusion coefficient was not measured. When it comes to the OH^- exchange current density measurement in molten salts, to the best of my knowledge, there have been not any studies conducted yet until now. One of the major reasons is that it's not easy to obtain stable CV or potentiodynamic scans during the electrochemical tests since the redox reaction involves the production of H_2 gas bubbles on the electrode. Lots of fluctuation may be present in the curves, which makes the electrochemical data analysis impossible. Appropriate experiment parameters must be chosen and set carefully in electrochemical tests. Overall, more electrochemical study of corrosion products and non-metal impurity species are urgent to be performed to fill the gap in molten salts.

Besides, corrosion behavior of structural material, i.e., SS 316H and Alloy 617, is essential in the applications of MSRs. It can be investigated in a static corrosion study using static immersion test method, which has been widely applied in the corrosion field. However, most of available studies on SS 316H or Alloy 617 were conducted at temperatures less than 700 °C in FLiNaK. That is to say, the related study in NaF-KF-UF_4-UF_3 at high temperatures, such as 800 °C is still blank. Additionally, no repeated tests were performed to ensure data reliability in the previous studies. As for the post-test data analysis, most of the effort was put on the post-test specimens. And the post-test salts were not of much interest, thus useful information in the salts may have been missed. The observed corrosion behavior of post-test specimens was mainly Cr depletion at GBs, and there was seldom other interesting phenomenon reported. In some cases, the metal alloy specimens were even directly contacted with the salt container, without considering the possible galvanic effect on the corrosion. Moreover, there has not been an available study to investigate corrosion with time and how the corrosion product concentration changed during the corrosion test. Hence, to obtain more accurate and reliable data, the static immersion test design must be improved. It's crucial to conduct more static corrosion tests of SS 316H and Alloy 617.

And last but not least, galvanic corrosion is another important issue in MSRs or CSPs, since components are fabricated from different materials. The available studies on galvanic corrosion mainly aimed to demonstrate that the galvanic effect may accelerate anode material corrosion and

protect the cathode materials. The quantitative analysis, such as galvanic corrosion rate calculation, was not thoroughly understood. And the applied methods in different studies were not consistent, which made the calculations less convincing. Moreover, most of the studies were conducted in aqueous solution at room temperatures or high temperatures in FLiNaK. For the galvanic study of Alloy 617/graphite couple in NaF-KF-UF_4-UF_3, there hasn't been available studies conducted yet. Considering the fact that these three materials are essential in thermal MSRs, i.e., Alloy 617 is a good structural material candidate, graphite is used as a moderator and NaF-KF-UF_4-UF_3 acts as a fuel salt, it is important to perform studies on Alloy 617/graphite galvanic couples.

More comprehensive studies on material corrosion in molten salts is urgent to satisfy the need for the application of MSRs and CSPs. That is also the motivation of this research work. In the present study, the kinetic property data of metal species of corrosion products (Fe^{2+}, Cr^{2+}, Cr^{3+} and Ni^{2+}) and the non-metal specie OH^- were measured in $MgCl_2$-NaCl-KCl and NaF-KF-UF_4-UF_3 salts with a temperature ranging from 600 °C to 800 °C. The corrosion behavior of structural materials, i.e., SS 316H and Alloy 617 were studied at 800 °C in molten NaF-KF-UF_4-UF_3 salts. The galvanic corrosion tests of Alloy 617/graphite were performed at 650 °C and 750 °C to obtain the galvanic corrosion rate in molten NaF-KF-UF_4-UF_3 salts. The study will benefit the corrosion community in further understanding the corrosion mechanism in molten salts at high temperatures. Thus, appropriate methods may be developed to mitigate the corrosion issues in the operation of power plants.

2 Corrosion Kinetic Properties in Molten Salts

In the present study, the corrosion kinetic properties were investigated in molten chloride and fluoride salts, respectively. In molten $MgCl_2$-KCl-NaCl salts, the kinetic parameters, i.e., D, i_0, i_L and k^0, of metal species (Fe^{2+}, Ni^{2+}, Cr^{2+} and Cr^{3+}) and non-metal specie OH^- were measured. Considering that the corrosion product ions, i.e., Fe^{2+}, Ni^{2+}, Cr^{2+} and Cr^{3+}, that accumulated in the molten salts were always a very small amount, the fundamental data measurements were conducted at the concentrations of corrosion products as low as possible, such as 1.53×10^{-6} mol cm^{-3} Fe^{2+}. And a new method was developed to measure the actual concentration of OH^- in the molten salts, which was a crucial parameter in the calculation of D. In molten NaF-KF-UF_4-UF_3 salts, D, i_0, i_L and k^0, of metal species (Fe^{2+}, Cr^{2+} and Cr^{3+}) were calculated accordingly. All electrochemical tests were performed at high temperatures ranging from 600 - 800 ºC, which were the general operation temperatures of molten salts in MSRs and CSP plants. As for the measurements of i_0, the present study mainly focused on a recently developed technique – non-linear least squares curve fitting (NLS) – based on the kinetic equation with mass transfer effect, since it can give more accurate results in molten salts. Moreover, the standard rate constants k^0 of Fe^{2+}, Ni^{2+}, Cr^{2+} and Cr^{3+} in molten $MgCl_2$-KCl-NaCl salt were calculated based on the relationship with i_0, α and bulk concentration C^b of studied ions. By providing full integrated data of D, i_0, i_L and k^0, this work will definitely help to further understand the electrochemical behavior and fundamental corrosion mechanisms of Fe^{2+}/Fe, Ni^{2+}/Ni, Cr^{3+}/Cr^{2+}, Cr^{2+}/Cr and OH^-/H_2 in molten salts.

2.1 Experiment

The salt preparation and electrochemical tests were conducted in a glove box filled with circulating high-purity argon gas. During the tests, the oxygen and moisture level were strictly controlled at O_2 < 5ppm and H_2O <0.5ppm. In molten chloride tests, chemicals, i.e., $MgCl_2$ (BioUltra, ≥98.0%), KCl (ACS regent, ≥99.0%, Sigma-Aldrich), NaCl (ACS regent, ≥99.0%, Sigma-Aldrich) were mixed evenly in the proportion of 44.7 mol %, 25.8mol % and 29.4 mol %, then placed in an alumina crucible. An analytical balance (MS 105DU Mettler Toledo) with an accuracy of 10^{-4} g was used to weight salts. A muffle furnace with a temperature accuracy ± 2°C was used to heat and keep the salts at the target temperature. Considering the strong hydrophilicity of $MgCl_2$, the salt mixtures were purified to remove moisture impurities, following the thermal purification procedures as given in Table 2-1, which were developed in our lab based on the study by Vidal et al[118]. After thermal purification, a certain amount of $FeCl_2$ (≥99.9%, Sigma-Aldrich), $NiCl_2$ (≥99.9%, Sigma-Aldrich), $CrCl_2$ (≥99.9%, Sigma-Aldrich), or NaOH (95%, Sigma-Aldrich) was added into the purified salt melts to introduce Fe^{2+}, Ni^{2+}, Cr^{3+}, Cr^{2+} or OH^-, respectively. The added $FeCl_2$, $NiCl_2$, $CrCl_2$ and NaOH have been heated at 180 ºC for 10 hours to remove possible moisture contamination accumulated during storage. And only one single kind of ion was introduced at one time in the salts.

In molten fluoride salt tests, a nickel crucible was used as a molten salt container. To mimic the actual corrosion products of structural materials presented in the fuel salts of MSRs, the salt mixture NaF-KF-UF_4-UF_3 used in tests was the post-test salts from static corrosion tests as discussed in Section 3, in which the corrosion products of SS 316H, i.e., Fe and Cr ions, have been

produced after 120 hours of corrosion tests at 800 °C. Thereby, it ensured that the kinetic parameters measured in the tests can represent the actual parameters in MSRs, and saved lots of time which would have to be taken in salt fabrication. After salt mixtures were ready, they were heated at the target temperature to let the system reach equilibrium before any electrochemical tests.

Meanwhile, to determine the concentration of Fe, Ni, Cr, and OH ions in the salt melts, inductively coupled plasma mass spectrometry (ICP-MS) analysis was applied. Salt samples were taken from the electrolyte bath using a tungsten rod. The rod was inserted into the salt melts and then taken out immediately. The salts which adhered on the surface of the rod were then quenched in the glovebox in less than 5 seconds. ICP-MS samples were prepared by dissolving the salt samples into 20 ml 1M nitric acid (HNO_3) and diluted into appropriate concentration range accordingly. Three ICP-MS salt samples were prepared and analyzed to ensure data reliability. The measured concentration deviation of three salt samples were required to less than 10%, otherwise the data was invalid.

Table 2-1 Temperature profile used for thermal purification of salts

Temperature (ºC)	Dwell time (hours)	Notes
117	20	Stir the salt after 10 hours
180	20	Stir the salt after 10 hours
240	5	Stir the salt after 5 hours
300	2	\
400	2	\
Target Temperature	\	Heating ramp rate 2.5 ºC/min

A three-electrode cell system as shown in Figure 2-1 was applied to perform electrochemical tests. The working electrode was a tungsten rod (diameter 3.2/1.6mm, Midwest tungsten service), and the counter electrode was a graphite rod (diameter 3.0mm, Sigma-Aldrich) in both chloride and fluoride salts. A tungsten working electrode was applied in the electrochemistry tests, because tungsten is an inert metal and wouldn't form an alloy with Fe, Ni and Cr. Both Horvath et al.[39] and Yin et al.[119] have used a tungsten working electrode to conduct electrochemical behavior study of Ni^{2+} in the molten chloride salts. For the reference electrode, a platinum wire (diameter 1.0mm, Super Chemicals) was used in measurements of metal species. During measurements of the non-metal specie OH^-, oxygen may be produced in the electrochemical tests and reacted with the Pt wire on the surface, which made the Pt wire became unstable[120,121,122]. A thermodynamic $Ni/NiCl_2$ reference was developed as shown in Figure 2-2. An alumina tube (one end open, inner diameter 4.78mm, outer diameter 6.35mm) served as the container of bulk salt of reference electrode. The bulk salt was composed of $MgCl_2$-NaCl-KCl with 3 wt.% $NiCl_2$ added. The bottom of alumina tube was polished with a thickness less than 0.41mm to ensure good ionic conductivity. A Ni wire

(99.999%, Alfa Aesar) was immersed into the bulk salt of the reference electrode. To eliminate the interface and background noise of reference electrode, the whole reference electrode setup was placed into the electrochemical test salt without touching the alumina crucible bottom. Moreover, it was found that the liquid salt level in the alumina tube must be lower than that of electrochemical test salt in the alumina crucible, otherwise the reference electrode would fail due to severe background noise. All the electrodes, tubes and crucibles used in the tests were bathed in deionized water and cleaned in an ultrasonic machine for 40 min, then dried with a ceramic-stirring hotplate before use to remove possible contamination on the surface. For alumina tubes and crucibles, besides these general cleaning processes, they were also pre-heated at 650 ºC for 12 hours outside of the glovebox to remove easily oxidized impurities in them as much as possible.

The electrochemical tests were done at different temperatures and concentrations which are listed in Table 2-2. A Gamry interface 1000 controlled by a Gamry Instrument Framework software were used to conduct the measurements. Transient electrochemical techniques, i.e., CV and CP, were performed to determine D. During all the CV scans, five cycles were conducted in each scan to check the curve repetition. The relative standard deviation of the peak current value between different cycles should be less than 0.1% to ensure data reliability. As for the measurements of i_0, three identical potentiodynamic scans were conducted to check the data repetition. All three scan curves shall be overlapped, otherwise, the measurement was invalid. Furthermore, a stripping potential of 0.2V (vs. Pt) was applied for at least 1 min to clean the working electrode surface after each measurement. This clean process was checked by CV scans with 3 cycles. The good repetition of CV curves indicated that the working electrode has been well restored to its initial condition.

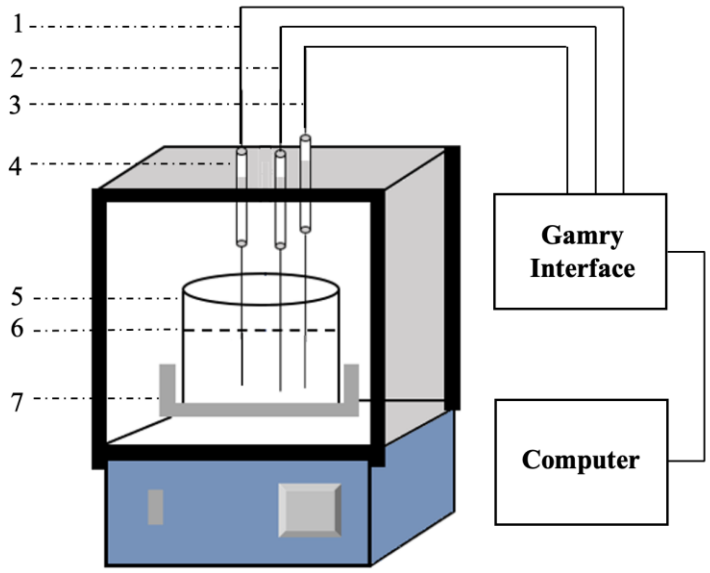

Figure 2-1 Electrochemical Test Setup: 1. Working electrode 2. Reference electrode 3. Counter electrode 4. Quartz tube 5. Salt container 6. Liquid salt level 7. Alumina safety dish

Figure 2-2 $Ni/NiCl_2$ thermodynamic reference electrode setup

Table 2-2 Electrochemical test profiles in molten chloride and fluoride salts

Molten Salt	Temperature (°C)	Metal and Non-metal Specie Concentration (mol cm^{-3})			
		Fe	Ni	Cr	OH^-
$MgCl_2$-NaCl-KCl	600, 650, 700, 750, 800	1.53×10^{-6}, 9.17×10^{-5}, 1.53×10^{-4}	1.50×10^{-4}, 4.49×10^{-4}, 7.48×10^{-4}	3.15×10^{-5}, 9.46×10^{-5}, 1.58×10^{-4}	Discussed in Section 2.2.1.2.1
NaF-KF-UF_4-UF_3	700, 750, 800	1.16×10^{-4}	N/A	8.59×10^{-5}	N/A

2.2 Results and Discussion

2.2.1 Kinetic Parameters in Molten $MgCl_2$-NaCl-KCl Salts

2.2.1.1 Metal Species Fe^{2+}, Ni^{2+}, Cr^{2+} and Cr^{3+} Measurements

2.2.1.1.1 Diffusion Coefficient of Fe^{2+} and Ni^{2+}

Figure 2-3(a) showed the typical CV curves obtained from the $MgCl_2$-KCl-NaCl melts before and after the addition of $FeCl_2$ or $NiCl_2$. Only one cathodic peak was observed in the blank salts, which corresponded to the deposition of magnesium. There were no other peaks shown before -1.14V (vs. Pt). After the addition of $FeCl_2$ or $NiCl_2$, one more cathodic peak was observed at -0.6V (vs. Pt) for $FeCl_2$ and -0.06V (vs. Pt) for $NiCl_2$, which corresponded to the one-step reduction reaction of Fe^{2+} to Fe and Ni^{2+} to Ni, respectively.

$$Fe^{2+} + 2e^- \leftrightarrow Fe \qquad 2\text{-}1$$

$$Ni^{2+} + 2e^- \leftrightarrow Ni \qquad 2\text{-}2$$

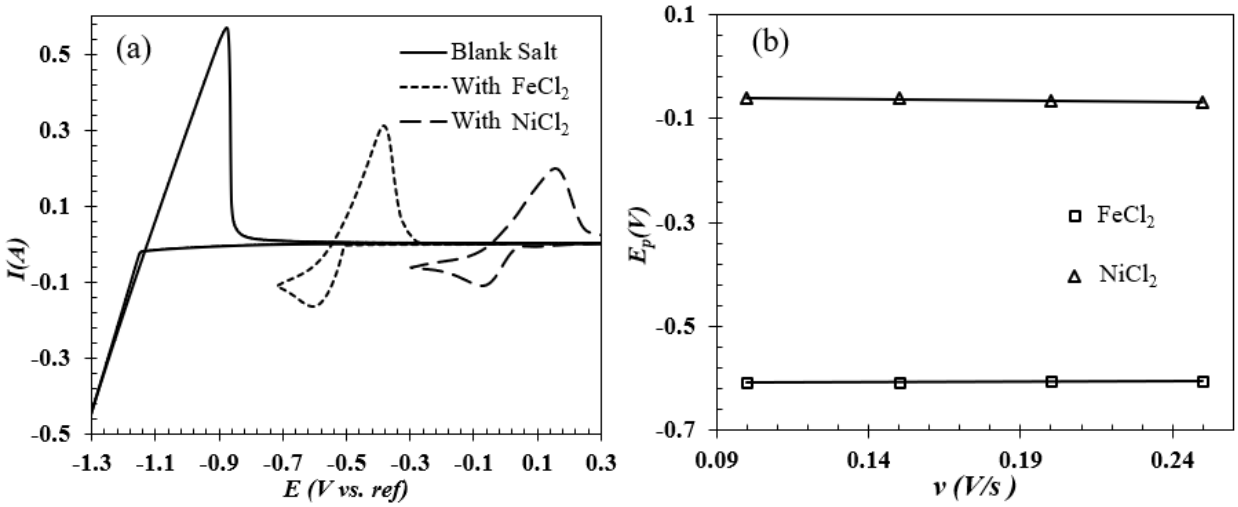

Figure 2-3 (a) Cyclic voltammetry at 600 ºC with scan rate of 200mV/s in $MgCl_2$-KCl-NaCl blank salts, working electrode surface area: 0.4562cm^2; and in salts with 1.53×10^{-4} mol cm^{-3} $FeCl_2$ addition, working electrode surface area: 0.7843cm^2, and in salts with 1.50×10^{-4} mol cm^{-3} $NiCl_2$ addition, working electrode surface area: 0.5432cm^2; (b) Plot of reduction peak potential E_p versus scan rate v, E_p - v in $MgCl_2$-KCl-NaCl-1.53×10^{-4} mol cm^{-3} $FeCl_2$ (and -1.50×10^{-4} mol cm^{-3} $NiCl_2$) at 600 ºC.

The reversibility of the redox reaction Fe^{2+}/Fe and Ni^{2+}/Ni were checked using CV scans with different scan rates in $MgCl_2$-KCl-NaCl-1.53×10^{-4} mol cm^{-3} $FeCl_2$ and 1.50×10^{-4} mol cm^{-3} $NiCl_2$ at 600 ºC, respectively. As given in Figure 2-4 and Table 2-3, the reduction peak potential was constant (about -0.6V vs. Pt for Fe^{2+}/Fe and -0.06V vs. Pt for Ni^{2+}/Ni) at scan rates up to 250mV s^{-1}. It displayed Nernstian behavior and demonstrated the characteristic of a reversible system[17].

Table 2-3 Reduction peak potential E_p of Fe^{2+}/Fe and Ni^{2+}/Ni in $MgCl_2$-KCl-NaCl-1.53×10^{-4} mol cm^{-3} $FeCl_2$ and $MgCl_2$-KCl-NaCl-1.50×10^{-4} mol cm^{-3} $NiCl_2$ at 600 ºC

	Scan rate v (V s^{-1})							
	0.1		0.15		0.2		0.25	
	Fe^{2+}/Fe	Ni^{2+}/Ni	Fe^{2+}/Fe	Ni^{2+}/Ni	Fe^{2+}/Fe	Ni^{2+}/Ni	Fe^{2+}/Fe	Ni^{2+}/Ni
E_p (V)	-0.6068	-0.0618	-0.6067	-0.0618	-0.6058	-0.0639	-0.6058	-0.0648

For a reversible soluble-insoluble reaction, the diffusion coefficient D can be calculated using CV technique based on Berzins-Delahay equation given in Eq 2-3,

$$I_p = 0.611\ nFSC\ (\frac{nF}{RT}vD)^{1/2} \qquad 2\text{-}3$$

Where I_p is peak current (A), S is the electrode area (cm^2), C is bulk concentration of studied ions (mol cm^{-3}), v is the scan rate (V s^{-1}), n is charge transfer number in the reaction and D is diffusion

coefficient (cm^2 s^{-1}). Figure 2-4(a) illustrated an example of CV scans in $MgCl_2$-KCl-NaCl-1.53×10^{-4} mol cm^{-3} $FeCl_2$ at 650 ºC. As shown in the inset of Figure 2-4(a), the cathodic peak current I_p was plotted versus the square root of scan rate $v^{1/2}$. The correlation of I_p-$v^{1/2}$ demonstrated good linearity, indicating that the reaction in the chosen scan rate range was diffusion control. The values of D can be calculated from the slope of I_p-$v^{1/2}$. In addition, CP scans were also conducted in the measurements of $NiCl_2$. A constant current was applied in the electrochemical system when using CP technique. Figure 2-4(b) illustrated typical CP scan curves in $MgCl_2$-KCl-NaCl-1.50×10^{-4} mol cm^{-3} $NiCl_2$ at 650 ºC. Two plateaus were observed which corresponded to the reduction of Ni^{2+} and Mg^{2+}. Considering that the redox reaction of Ni^{2+}/Ni was reversible, Sand's equation given in Eq. 2-4 was applied in the calculation of D.

$$\tau^{1/2} = \frac{nFA(\pi D)^{1/2}C}{2i} \qquad 2\text{-}4$$

Where τ is transition time (s) which can be determined in CP curves, i is applied constant current (A). Plot of $\tau^{1/2}$ – $1/i$ was given in the inset of Figure 2-4(b), which shown a good linear correlation. And the values of D were estimated from the slope of $\tau^{1/2}$ – $1/i$.

Table 2-4 listed the calculated D of Fe^{2+} and Ni^{2+} at different concentrations and temperatures using CV and CP techniques. The calculated D of Ni^{2+} from CV and CP techniques matched well. At the same temperature, the values of D had no significant difference at different concentrations. It indicated that the diffusion coefficients of Fe^{2+} and Ni^{2+} were independent of concentration in the studied systems. The relation of $logD$-$1/T$ at different temperatures were given in Figure 2-4(c). Both the plots of Fe^{2+} and Ni^{2+} demonstrated good linearity and followed Arrhenius law given in Eq. 2-5.

$$D = D_0 \exp\left(-\frac{E_a}{RT}\right) \qquad 2\text{-}5$$

Where D_0 is a pre-exponential constant, E_a is activation energy in the diffusion process. The values of R-squared between the fitted regression lines and experimental points were all greater than 0.98, which indicated a good fit to the data sets. The activation energy E_a of Fe^{2+} and Ni^{2+} calculated from the slope of $\log D$-$1/T$ were listed in Table 2-4 as well.

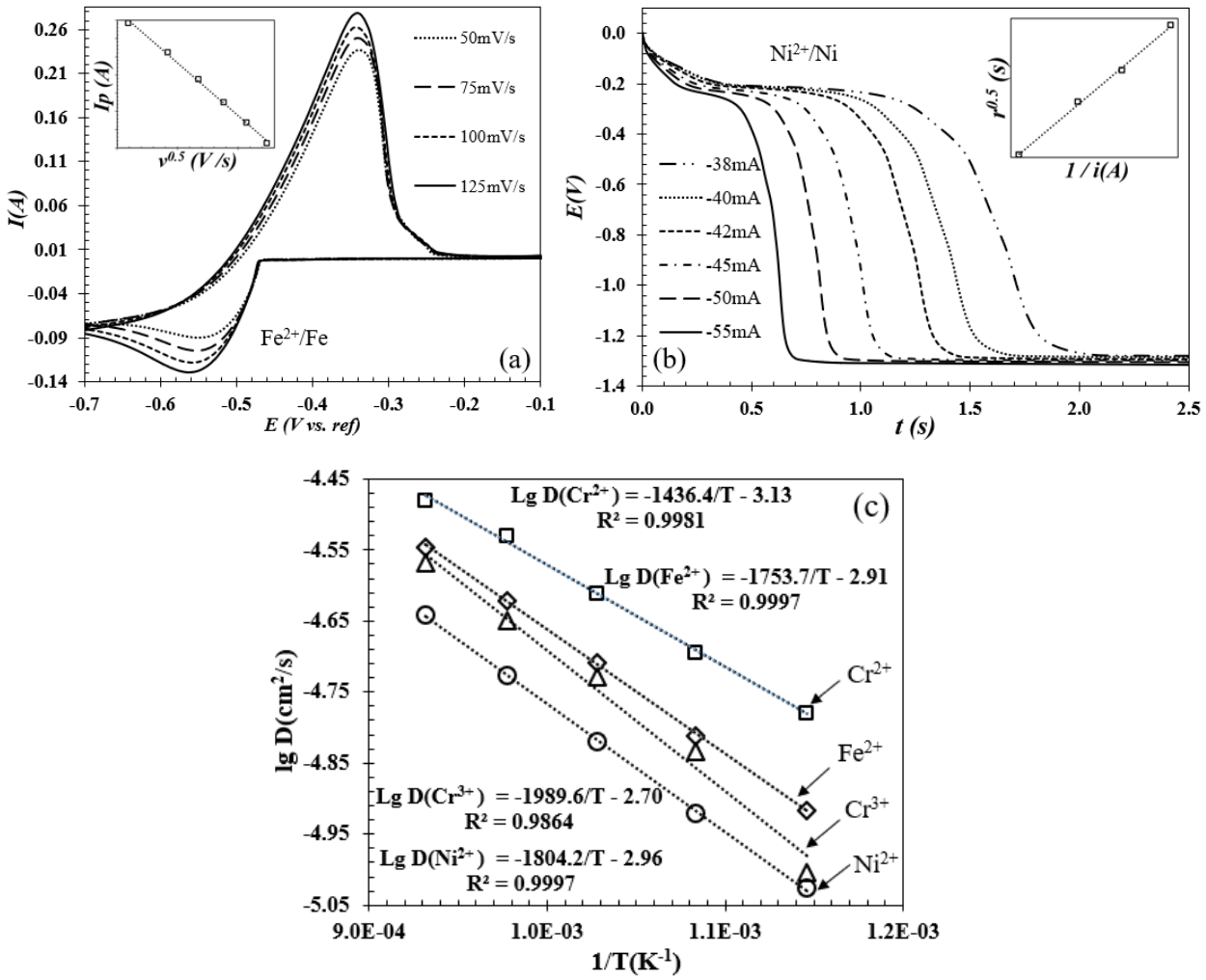

Figure 2-4 Cyclic voltammetry in $MgCl_2$-KCl-NaCl-1.53×10^{-4} mol cm^{-3} $FeCl_2$ at 650 ºC, working electrode surface area: 0.7843cm^2; (b) Chronopotentiometry in $MgCl_2$-KCl-NaCl-1.50×10^{-4} mol cm^{-3} $NiCl_2$ at 800 ºC, working electrode surface area: 0.5608 cm^2; (c) log D-1/ T plots of Fe^{2+}, Ni^{2+}, Cr^{2+} and Cr^{3+} at the concentration of 1.53×10^{-4} mol cm^{-3} $FeCl_2$, 1.50×10^{-4} mol cm^{-3} $NiCl_2$ and 1.58×10^{-4} mol cm^{-3} $CrCl_2$.

Table 2-4 Calculated $D_{Fe^{2+}}$ and $D_{Ni^{2+}}$ from CV and CP tests at different concentrations and temperatures

T (ºC)	Calculated $D_{Fe^{2+}}$ using CV technique					
	1.53×10^{-6} mol cm^{-3}		9.17×10^{-5} mol cm^{-3}		1.53×10^{-4} mol cm^{-3}	
	D (10^5 cm^2 s^{-1})	E_a (kJ mol^{-1})	D (10^5 cm^2 s^{-1})	E_a (kJ mol^{-1})	D (10^5 cm^2 s^{-1})	E_a (kJ mol^{-1})
600	1.17	34.3	1.20	33.6	1.21	33.5
650	1.49		1.52		1.54	
700	1.90		1.92		1.96	
750	2.36		2.37		2.39	
800	2.80		2.82		2.85	

T (ºC)	Calculated $D_{Ni^{2+}}$ using CV and CP techniques											
	1.50×10^{-4} mol cm^{-3}				4.49×10^{-4} mol cm^{-3}				7.48×10^{-4} mol cm^{-3}			
	CV		CP		CV		CP		CV		CP	
	D	E_a	D	E_a	D	E_a	D	E_a	D	E_a	D	E_a
600	0.94	34.5	0.91	36.1	0.91	35.7	0.89	37.2	0.93	34.9	0.88	36.6
650	1.20		1.25		1.13		1.12		1.10		1.19	
700	1.51		1.59		1.39		1.48		1.46		1.56	
750	1.88		1.86		1.82		1.88		1.83		1.88	
800	2.28		2.37		2.28		2.28		2.21		2.27	

Note: D is in the unit of 10^5 cm^2 s^{-1} and E_a is in the unit of kJ mol^{-1}.

2.2.1.1.2 Diffusion Coefficients of Cr^{3+} and Cr^{2+}

As for the fundamental data measurements of Cr ions, even though only a certain amount of $CrCl_2$ was added into the molten salts, based on the x-ray photoelectron spectroscopy (XPS) analysis, both Cr^{2+} and Cr^{3+} were identified in the melt before any electrochemical tests. It matched well with that reported by Park[8]. The XPS analysis result at 600 ºC was given as a demonstration in Figure 2-5. Table 2-5 listed the averaged ratio of Cr^{3+}/Cr^{2+} in the molten salts at different temperatures. The ratio became larger as temperature increased, probably because more Cr^{2+} tended to be converted to Cr^{3+} at higher temperatures.

To investigate the electrochemical behavior of Cr^{2+} and Cr^{3+}, CV scans were conducted in the blank salt and salt with $CrCl_2$ addition. As given in Figure 2-6(a), two pairs of redox peaks were observed after the addition of $CrCl_2$. Moreover, CP scans shown in Figure 2-6(b) were also conducted. As expected, three plateaus were observed in the CP curves, of which the corresponding potential coincided with that in the CV curves. And they represented the reduction reactions of Cr^{3+}, Cr^{2+} and Mg^{2+}, respectively.

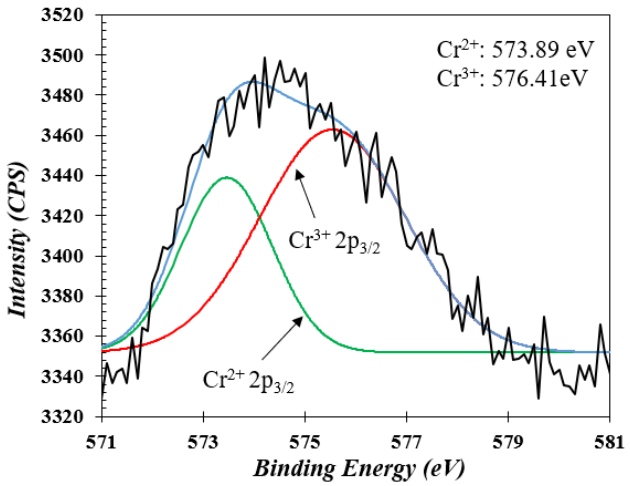

Figure 2-5 XPS spectra of Cr $2p_{3/2}$ in $MgCl_2$-KCl-NaCl-1.58×10^{-4} mol cm^{-3} $CrCl_2$ at 700ºC before electrochemical tests

Table 2-5 Averaged ratio of Cr^{3+}/Cr^{2+} in molten $MgCl_2$-KCl-NaCl salts measured by XPS at different temperatures

T/ºC	600	650	700	750	800
$\frac{Cr^{3+}}{Cr^{2+}}$	0.7892	1.1169	1.3987	1.7786	2.2041

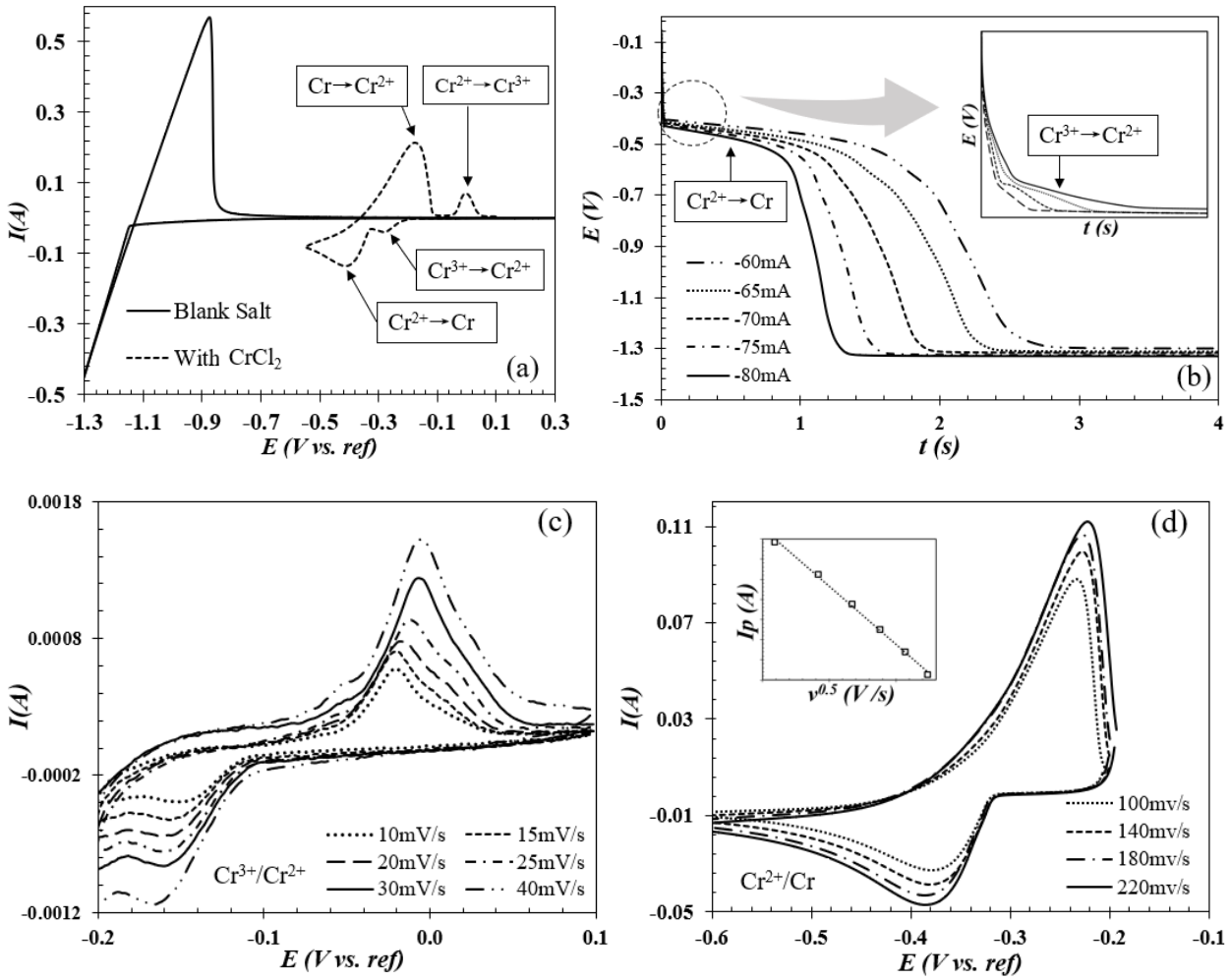

Figure 2-6 (a) Cyclic voltammetry in $MgCl_2$-KCl-NaCl-1.58×10^{-4} mol cm^{-3} $CrCl_2$ at 650 ºC, working electrode surface area: 0.7653cm^2; (b) Chronopotentiometry in $MgCl_2$-KCl-NaCl-1.58×10^{-4} mol cm^{-3} $CrCl_2$ at 650 ºC, working electrode surface area: 0.5412 cm^2; (c) Cyclic voltammetry of Cr^{3+}/Cr^{2+} reaction in $MgCl_2$-KCl-NaCl-1.58×10^{-4} mol cm^{-3} $CrCl_2$ at 650 ºC, working electrode surface area: 0.7843 cm^2; (d) Cyclic voltammetry of Cr^{2+}/Cr reaction in $MgCl_2$-KCl-NaCl-1.58×10^{-4} mol cm^{-3} $CrCl_2$ at 650 ºC, working electrode surface area: 0.6423 cm^2.

Table 2-6 Reduction peak potential E_p of Cr^{3+}/ Cr^{2+} and Cr^{2+}/Cr in $MgCl_2$-KCl-NaCl-1.58×10^{-4} mol cm^{-3} $CrCl_2$ at 650 ºC

	Scan rate v (V s^{-1})							
	0.02		0.06		0.12		0.18	
	Cr^{3+}/Cr^{2+}	Cr^{2+}/Cr	Cr^{3+}/Cr^{2+}	Cr^{2+}/Cr	Cr^{3+}/Cr^{2+}	Cr^{2+}/Cr	Cr^{3+}/Cr^{2+}	Cr^{2+}/Cr
E_p (V)	-0.2379	-0.3816	-0.2519	-0.3816	-0.2639	-0.3822	-0.2739	-0.3824

CV scans within the potential range from -0.2 to 0.1V (vs. Pt) were performed at different scan rates to study the redox reaction of Cr^{3+}/Cr^{2+} as given in Figure 2-6(c). In the scan rate range of 10 mV/s to 40mV/s, the peak potential difference ΔE_p ($\Delta E_p = |E_{pa} - E_{pc}|$) was close to the value of $2.3RT/nF$ (or 182mV) for a one-electron reaction at 650 ºC.

It was observed that the reduction peak potential shifted to more negative potentials as the applied scan rates increased. The values of E_p with scan rates up to 180mV/s are summarized in Table 2-6. The deviation of E_p for Cr^{3+}/Cr^{2+} was as large as 0.04V, which is the characteristic of a reaction limited by electron transfer. Considering the relatively large reduction peak potential shift within such small scan rates (20-180mV s^{-1}), and the different characteristics of CV scans from that of Fe^{2+}/Fe and Ni^{2+}/Ni, it's highly possible that the redox reaction of Cr^{3+}/Cr^{2+} is irreversible. More study is needed to further confirm this conclusion in the future.

In general, for a reversible soluble-soluble redox reaction, if only reactant or product presented initially, the diffusion coefficient D of studied ions can be calculated using Randles-Sevcik equation, otherwise the equation was not applicable. When both reactant and product existed in a reversible reaction, the theory developed by Keightley et al. can be adopted for the data analysis of CV scans[123]. Based on the theory, Guo et al. calculated the diffusion coefficient of Eu^{3+} and Eu^{2+} in FLiNaK[124]. The average values of $D_{Eu^{3+}}$ were 1.21×10^{-5}, 1.37×10^{-5} and 1.79×10^{-5} cm^2 s^{-1} at 650, 700 and 750ºC, while the values at the same temperature predicted calculated by Huang et al. using Randles-Sevcik equations were 2.59×10^{-5}, 3.37×10^{-5} and 4.29×10^{-5} cm^2 s^{-1}, respectively[125]. Comparing the results from the two studies (Ref. 124 and Ref. 125) using same salt components at same experiment temperatures, the inappropriate application of Randles-Sevcik equation could cause slight overestimation of diffusion coefficient, but the values were still in the reasonable magnitude (i.e., 10^{-5}). It indicated that the Randles-Sevcik equation may be applied in the estimation of diffusion coefficient to obtain rough values when both reactant and product presented in the studied system, if there were no other available analysis methods.

In an irreversible soluble-soluble system, for the calculation of diffusion coefficient using CV scans, the only available data analysis method is using Randles-Sevcik equation expressed by Eq. 2-6, which is derived for an irreversible reaction. Before any other new analysis theory has been proposed, the diffusion coefficient D of Cr^{3+} in the present study was calculated from Eq. 2-6. However, it needs to be stressed that, considering that Cr^{3+} and Cr^{2+} coexisted in the molten salts, which conflicted with the assumption when deriving Randles-Sevcik equation, certain deviation would be introduced in the calculation. The diffusion coefficient of Cr^{3+} obtained in the present study were estimated values to fill the blank of $D_{Cr^{3+}}$ values in molten $MgCl_2$-KCl-NaCl salts. The data reliability needs to be checked in a future study once a new theory is developed.

$$\mathrm{I_p} = 0.496(\alpha n')^{1/2}\ \mathrm{nFSC}\ (\frac{\mathrm{nF}}{\mathrm{RT}}\mathrm{vD})^{1/2} \qquad 2\text{-}6$$

As shown in Eq. 2-6, n is electron transfer number in the electrochemical reaction, C is concentration of Cr^{3+} in the bulk solution which is determined from the ratio of Cr^{3+}/Cr^{2+} given in Table 2-5, α is charge transfer coefficient, n' is the electron transfer number before the rate determining step. For irreversible systems, α can be estimated from the equation given by,

$$\left|E_{\mathrm{p}} - E_{\mathrm{P}/2}\right| = 1.857\,\frac{RT}{\alpha n' F} \qquad 2\text{-}7$$

Where E_{p} is peak potential and $E_{\mathrm{P}/2}$ is half-peak potential in the curve. Moreover, the values of α can also be obtained from the potentiodynamic scans, which would be discussed in detail in Section 2.2.1.1.3. Table 2-7 listed the value of α calculated from CV and potentiodynamic scan curves. There was no significant difference in the value of α when using these two completely different techniques, which further confirmed the data reliability of α. Here, $\alpha n'$ estimated from Eq. 2-7 was utilized in the calculations. The correlation of I_p - $v^{1/2}$ shown in the inset of Figure 2-6(c) demonstrated good linearity. And the slope of the I_p - $v^{1/2}$ plot was used to calculate the diffusion coefficient D.

As for the diffusion coefficient D of Cr^{2+}, CV scans were also conducted as shown in Figure 2-6(d). The peak current E_p were constant at different scan rates as given in Table 2-6. It indicated that the redox reaction of Cr^{2+}/Cr was a soluble-insoluble reversible reaction. Therefore, the diffusion coefficient D of Cr^{2+} can be calculated using the same techniques discussed in Section 2.2.1.1.1. However, it needs to be mentioned that the concentrations of Cr^{2+} used for the calculation of D in Eq. 2-3 were estimated by the XPS analysis. The calculated D of Cr^{3+} and Cr^{2+} at different concentrations and temperatures are summarized in Table 2-8. The results showed that the diffusion coefficient of Cr^{3+} and Cr^{2+} were independent of concentration of added $CrCl_2$ but increased with rise in temperature. The linear correlations of $\log D$-$1/T$ were illustrated in Figure 2-4(c), which followed Arrhenius law. The activation energy E_a related to the diffusion process of Cr^{3+} and Cr^{2+} were also calculated with an average value of 37.9 kJ mol^{-1} and 27.5 kJ mol^{-1}.

Table 2-7 α values of Cr^{3+}/Cr^{2+} calculated from CV and potentiodynamic scans

T/ºC	α	
	CV	Potentiodynamic
600	0.88	0.82
650	0.82	0.86
700	0.87	0.81
750	0.88	0.83
800	0.85	0.88

Table 2-8 Calculated $D_{Cr^{3+}}$ and $D_{Cr^{2+}}$ using CV technique in $MgCl_2$-KCl-NaCl at different concentrations and temperatures

T (°C)	Calculated $D_{Cr^{3+}}$ and $D_{Cr^{2+}}$ using CV technique											
	3.15×10^{-5} mol cm^{-3}				9.46×10^{-5} mol cm^{-3}				1.58×10^{-4} mol cm^{-3}			
	Cr^{2+}		Cr^{3+}		Cr^{2+}		Cr^{3+}		Cr^{2+}		Cr^{3+}	
	D	E_a	D	E_a	D	E_a	D	E_a	D	E_a	D	E_a
600	1.65		0.98		1.64		1.01		1.66		0.99	
650	2.00		1.49		2.04		1.48		2.02		1.47	
700	2.46	27.1	1.86	38.5	2.48	27.8	1.84	37.3	2.45	27.5	1.87	38.0
750	2.84		2.25		2.91		2.22		2.94		2.24	
800	3.29		2.73		3.33		2.72		3.31		2.70	

Note: D is in the unit of 10^5 cm^2 s^{-1} and E_a is in the unit of kJ mol^{-1}.

Comparing the D values of Fe^{2+}, Ni^{2+}, Cr^{3+} and Cr^{2+}, they were in the descending order of $D_{Cr^{2+}} > D_{Fe^{2+}} > D_{Cr^{3+}} > D_{Ni^{2+}}$. Both CV and CP techniques worked well in the calculations and the results from these two techniques were reasonably close as discussed before. All the diffusion coefficients of these four corrosion product ions (Fe^{2+}, Ni^{2+}, Cr^{3+} and Cr^{2+}) were independent of concentrations in the studied systems and demonstrated good linearity in terms of $\lg D$-$1/T$. The calculated activation energy E_a descended in the order of $E_{a,\,Fe^{2+}} > E_{a,\,Ni^{2+}} > E_{a,\,Cr^{2+}} > E_{a,\,Cr^{3+}}$ within the values range of 27.1 - 38.5 kJ mol^{-1}.

2.2.1.1.3 Exchange Current Density i_0, Charge Transfer Coefficient α, Limiting Current Density i_L and Standard Rate Constant k^0 Measurements

In general, the exchange current density of a redox couple is determined using the Butler-Volmer equation, in which only the charge transfer process is considered. However, for a reaction on the electrode surface in the molten salt, it always involves not only the charge transfer process at the interface of the electrode and electrolyte, but also the transfer process between the reactants and products on the electrode surface as mentioned before. Therefore, in the present study, a modified Butler-Volmer equation proposed by Guo et al.[64] was used to express the current density of a redox reaction on a tungsten electrode in molten $MgCl_2$-KCl-NaCl salts, which was given in Eq.2-8,

$$i = \frac{i_0\left\{exp\left[\frac{(1-\alpha)nF}{RT}\eta\right] - exp\left[-\frac{\alpha nF}{RT}\eta\right]\right\}}{1 - \frac{i_0}{i_L}exp\left[-\frac{\alpha nF}{RT}\eta\right]} \qquad 2\text{-}8$$

Where i is current density (A cm^{-2}); i_0 is exchange current density (A cm^{-2}); α is charge transfer coefficient; n is electron transfer number, F is Faraday constant, 96485 C mol^{-1}; η is overpotential

(V), which equals $E - E^{eq}$; E is applied potential and E^{eq} is equilibrium potential; i_L is limiting current density due to diffusion. The current-potential curves obtained from potentiodynamic scans can be fitted to Eq.2-8, through which the values of α, i_0 and i_L were calculated.

In the potentiodynamic scans, the potential was applied from cathodic (η<0) to anodic direction (η>0). When η<0, Fe^{2+}, Ni^{2+}, Cr^{2+} and Cr^{3+} ions were reduced to Fe, Ni, Cr and Cr^{2+} on the tungsten electrode surface. While for η>0, the dominant reaction on the working electrode surface was the oxidation of Fe, Ni, Cr and Cr^{2+}. The current density became larger as the applied overpotential increased. Typical potentiodynamic scan curves of Fe^{2+}/Fe were shown in Figure 2-7(a) as an example, in which three identical scans were conducted. The figure indicated good test repetition. A slight distortion was observed on the curves at the beginning of the cathodic scan as shown in Figure 2-7(a). This phenomenon may result from the initial formation of diffusion layers. Figure 2-7(b) gave the fitting results of the potentiodynamic scans. The dash lines were the fitted i-η curves using the non-linear least square fitting technique, while the solid lines were the experiment data sets. The fitted curves matched well with the experimental data at these three concentrations. In particular, Table 2-9 listed the optimized value of i_0, α and i_L of Fe^{2+}, Ni^{2+}, Cr^{2+} and Cr^{3+} with 1.53×10^{-4} mol cm^{-3} $FeCl_2$ ($NiCl_2$, $CrCl_2$) addition in $MgCl_2$-KCl-NaCl salts. The fitted α value of each redox couple kept consistent which was independent of temperature.

As one of the major parameters related to the kinetic properties, the standard rate constant k^0 is independent of concentration and only depends on temperature. k^0 is determined by Eq.2-9 which is given by,

$$i_0 = nFk^0{C_b}^{(1-\alpha)} = m{C_b}^{(1-\alpha)} \qquad 2\text{-}9$$

Where C_b is bulk concentration of studied ions (Fe^{2+}, Ni^{2+}, Cr^{2+} and Cr^{3+}) in the molten salts, m is a constant which equals nFk^0. The value of k^0 at a specific temperature can be calculated by fitting the measured i_0 to the bulk concentration C_b of different ions in the molten salts. As an example, shown in Figure 2-7(d), it illustrated the fitted exponential relation of i_0 and $C^b_{Fe^{2+}}$ at different temperatures. The fitted k^0 of Fe^{2+}, Ni^{2+}, Cr^{2+} and Cr^{3+} were listed in Table 2-10. The temperature dependence of i_0 and k^0 obeyed Arrhenius law as given in Figure 2-8(a) and (b). The calculated activation Energy E_a for i_0 were in the range of 22.7 - 46.5 kJ mol^{-1}, which varied at different concentrations. And the corresponding E_a for k^0 was calculated with values of 28.9 - 40.5 kJ mol^{-1}, which agreed well with the calculated values of E_a for i_0.

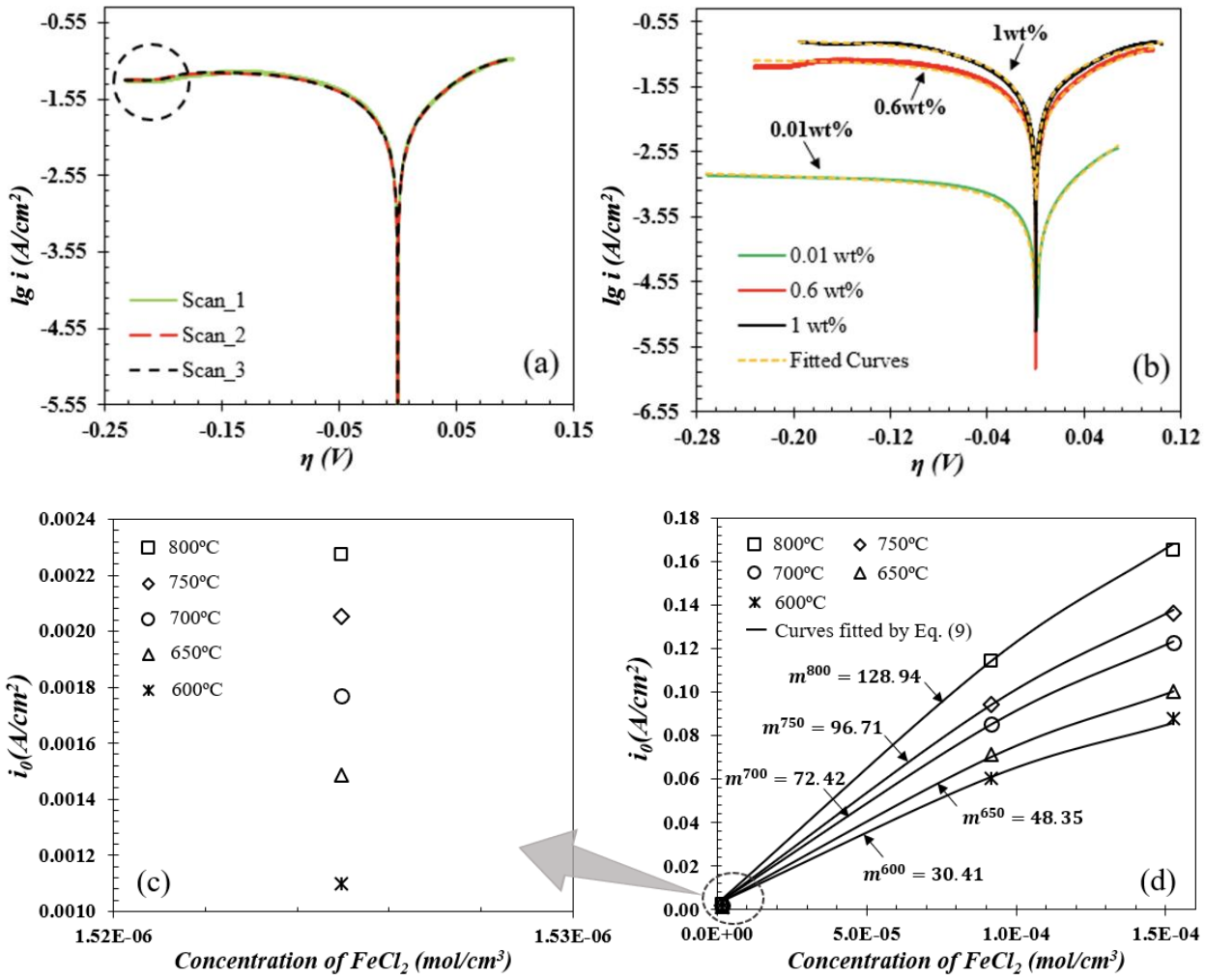

Figure 2-7 (a) Three identical scans in $MgCl_2$-KCl-NaCl-9.17×10^{-5} mol cm^{-3} $FeCl_2$ at 650 ºC with a scan rate of 5mV/s; (b) Measured and fitted potentiodynamic polarization curves in $MgCl_2$-KCl-NaCl-1.53×10^{-6}, 9.17×10^{-5} and 1.53×10^{-4} mol cm^{-3} $FeCl_2$ at 650 ºC with a scan rate of 5mV/s; (c) i_0 measured in $MgCl_2$-KCl-NaCl-1.53×10^{-6} $FeCl_2$ at each temperature; (d) The exponential relation of i_0 and Fe^{2+} bulk concentration $C_{Fe^{2+}}^{b}$ fitted from Eq(9).

Table 2-9 Calculated i_0, α and i_L of Fe^{2+}, Ni^{2+}, Cr^{2+} and Cr^{3+}in $MgCl_2$-KCl-NaCl-1.53×10^{-4} mol cm^{-3} $FeCl_2$ (1.50×10^{-4} mol cm^{-3} $NiCl_2$ or 1.58×10^{-4} mol cm^{-3} $CrCl_2$) at 600, 650, 700. 750, 800 ºC

T/ºC	Fe^{2+}/Fe			Ni^{2+}/Ni		
	i_0/ (A cm^{-2})	α	i_L/ (A cm^{-2})	i_0/ (A cm^{-2})	α	i_L/ (A cm^{-2})
600	0.0676	0.83	-0.1416	0.0508	0.79	-0.0866
650	0.1001	0.82	-0.1514	0.0789	0.62	-0.0892
700	0.1226	0.81	-0.1631	0.1023	0.82	-0.0938
750	0.1361	0.78	-0.1655	0.1125	0.72	-0.1075
800	0.1731	0.76	-0.2176	0.1359	0.79	-0.1167
T/ºC	Cr^{2+}/Cr			Cr^{3+}/Cr^{2+}		
	i_0/ (A cm^{-2})	α	i_L/ (A cm^{-2})	i_0/ (A cm^{-2})	α	i_L/ (A cm^{-2})
600	0.1162	0.88	-0.0617	8.13×10^{-4}	0.82	-6.65×10^{-4}
650	0.1573	0.85	-0.0647	1.04×10^{-3}	0.86	-7.83×10^{-4}
700	0.1938	0.86	-0.0758	1.43×10^{-3}	0.81	-8.52×10^{-4}
750	0.2327	0.88	-0.0855	1.64×10^{-3}	0.83	-9.36×10^{-4}
800	0.2801	0.85	-0.1037	1.88×10^{-3}	0.88	-9.94×10^{-4}

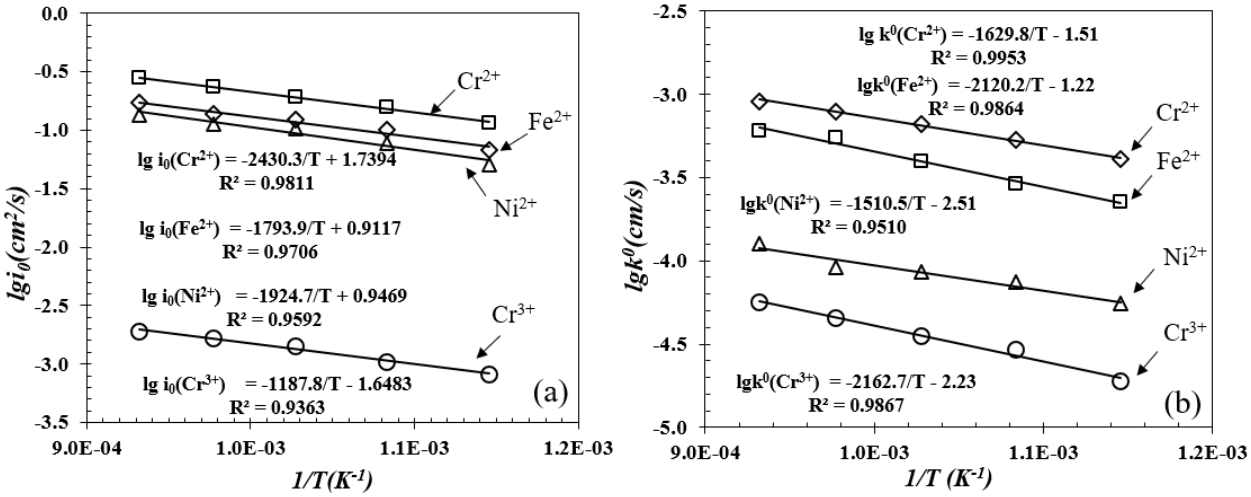

Figure 2-8 (a) logi_0 – 1/T plots measured in $MgCl_2$-KCl-NaCl-1.53×10^{-4} mol cm^{-3} $FeCl_2$ (1.50×10^{-4} mol cm^{-3} $NiCl_2$ or 1.58×10^{-4} mol cm^{-3} $CrCl_2$); (b) lgk^0 – 1/T plots fitted at each temperature.

Table 2-10 Calculated k^0 and E_a of Fe^{2+}/Fe, Ni^{2+}/Ni, Cr^{2+}/Cr and Cr^{3+}/ Cr^{2+} at different temperatures

T (ºC)	Calculated k^0 and E_a using curve fitting technique							
	Fe^{2+}/Fe		Ni^{2+}/Ni		Cr^{2+}/Cr		Cr^{3+}/ Cr^{2+}	
	k^0 (10^4 cm s^{-1})	E_a (kJ mol^{-1})	k^0 (10^5 cm s^{-1})	E_a (kJ mol^{-1})	k^0 (10^4 cm s^{-1})	E_a (kJ mol^{-1})	k^0 (10^5 cm s^{-1})	E_a (kJ mol^{-1})
600	2.28	40.5	5.53	28.9	4.08	31.2	1.88	39.9
650	2.91		7.43		5.31		2.93	
700	3.95		8.54		6.65		3.54	
750	5.47		9.15		7.87		4.55	
800	6.08		12.61		9.06		5.66	

2.2.1.2 Non-Metal Specie OH^- Measurements

2.2.1.2.1 OH^- Concentration

As mentioned before, all the salts used were thermally purified before tests. 2 wt.% NaOH was added into ternary salt mixture $MgCl_2$-NaCl-KCl, then heated to target temperature. Precipitates were found on the bottom of the crucible after 12 hours at 600 ºC, which was shown in Figure 2-9. The precipitates still presented even after heated at 800 ºC for 24 hours. To identify these precipitates and further understand its production mechanism, the Gibbs energy formation of reaction were calculated using HSC 10.0 as given in Table 2-11[126]. Gibbs energy formation of reaction $\Delta_r G^0$ at 600-800 ºC was less than 0, which indicated that both of the reactions were thermally favored and most probably happened in the molten salt system. To verify the assumption, salts samples of precipitates on the bottom and salt melt on the top were collected at 600 ºC, then quenched in 5 seconds in the Argon-filled glovebox. The salt samples were ground into fine powder and sealed in an air-tight sample holder for X-ray powder diffraction (XRD) analysis. XRD analysis was conducted using a PANalytical X'pert Pro X-ray diffractometer equipped with high power X-ray ceramic diffraction X-ray with copper anode. The analyzed XRD results were given in Figure 2-10. As shown in Figure 2-10(a), besides the major components, such as $KMgCl_3$, $NaMgCl_3$ and NaCl, $Mg(OH)_2$ were identified in the salt melt on the top. It indicated that reaction (1) given in Table 2-11 did happen after NaOH was added. In Figure 2-10(b), four XRD curves are given, among which one was the precipitate sample on the bottom at 600 ºC, the other three were different salt melt samples on the top at 600, 650 and 700 ºC. Multiple samples at different temperatures were collected to ensure data reliability. Peak related to MgO was identified in the XRD curve of the precipitate sample. Although efforts have been done to eliminate the interference of bulk salt when collecting precipitate samples, the main peaks of $KMgCl_3$, $NaMgCl_3$ and NaCl

still showed up in the curve. While in the three curves of salt melt on the top, the peaks for MgO were not observed. Therefore, it can be concluded that the precipitates on the bottom were mainly MgO and the reaction (2) given in Table 2-11 was confirmed as well.

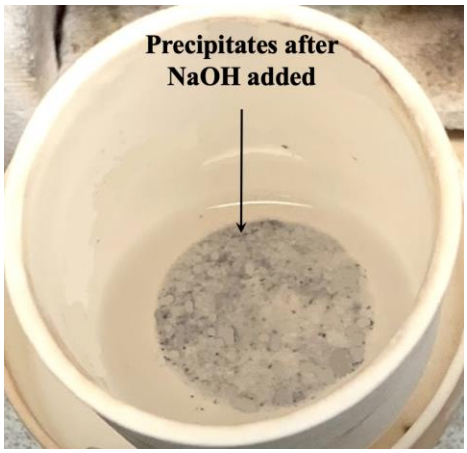

Figure 2-9 Precipitates on the bottom in $MgCl_2$-NaCl-KCl-NaOH at 600 ºC

Table 2-11 Gibbs energy formation of reaction calculation using HSC 10.0

	Chemical Reactions	$\Delta_r G^0$ at 600-800 ºC
(1)	$2NaOH_{(l)} + MgCl_{2(l)} = 2Mg(OH)_{2(l)} + 2NaCl_{(l)}$	$\Delta_r G^0 < 0$
(2)	$Mg(OH)_2 \leftrightarrow MgO_{(s)} + H_2O_{(g)}$	$\Delta_r G^0 < 0$

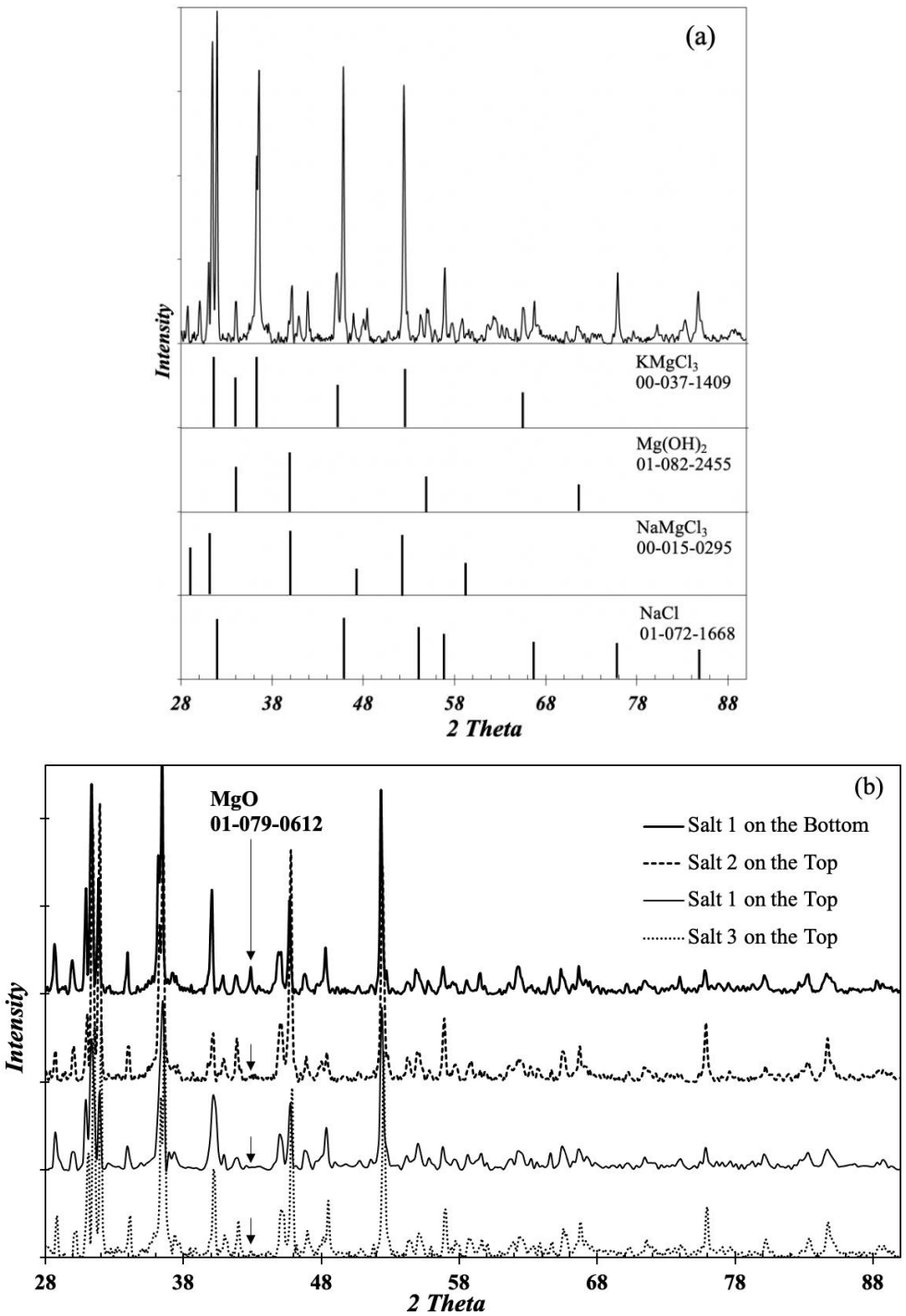

Figure 2-10 (a) XRD analysis of salt melt on the top in $MgCl_2$-NaCl-KCl-NaOH at 600 ºC (b). XRD analysis of precipitates and salt melt in $MgCl_2$-NaCl-KCl-NaOH. Salt 1 on the bottom: precipitate at 600 ºC; salt 2 on the top: salt melt at 650 ºC; salt 1 on the top: salt melt at 600 ºC; salt 3 on the top: salt melt at 700 ºC.

Since part of OH^- has been consumed to produce MgO, which has been deposited on the bottom, the real concentration of OH^- (C_{OH^-}) in the molten salts were not the original NaOH concentration added at the beginning. A test as given in Table 2-12 was designed to measure C_{OH^-} using ICP-

MS technique. $MgCl_2$-NaCl-KCl salt mixture was heated at target temperature for 2 days to let system stable. After that, 2 wt.% NaOH was added. Salts were heated for another 7 days for tests at 600 and 650 ºC, while 5 days for tests at 700, 750 and 800 ºC. With the assistance of ICP-MS analysis, first, the produced quantity of MgO was calculated from the quantity difference of Mg^{2+} in $MgCl_2$-NaCl-KCl before and after NaOH added; then the residual amount of OH^- was obtained according to reaction (2), since once 1 MgO was produced, 2 OH^- would have been consumed. The measured Mg^{2+} wt.% change before and after the addition of NaOH in the test at 650 ºC and 700 ºC were given in Figure 2-11. In the first 48 hours' heating before NaOH added, Mg^{2+} wt.% was stable. At 650 ºC, after NaOH was added, Mg^{2+} wt.% began to decrease and became stable again at the 84th hour, which indicated that the concentration of Mg^{2+} has reached equilibrium. While for the test at 700 ºC, the equilibrium was obtained at the 60th hour. Comparing these two figures, the system reached equilibrium much faster at higher temperature, because the reaction rate increased with the rise of temperature. The calculated C_{OH^-} at the equilibrium state was given in Table 2-13. The calculated C_{OH^-} decreased as the temperature increased since the forward reaction of reaction (2) was endothermic. The rise of temperature prompted the reaction to move forward, thus more MgO precipitates were produced, which meant that more OH^- was consumed and there was less residual OH^- in the molten salt.

Table 2-12 C_{OH^-} Measurement Test Design

T ºC	Heating duration	
	Before NaOH added	After NaOH added
600	2	7
650	2	7
700	2	5
750	2	5
800	2	5

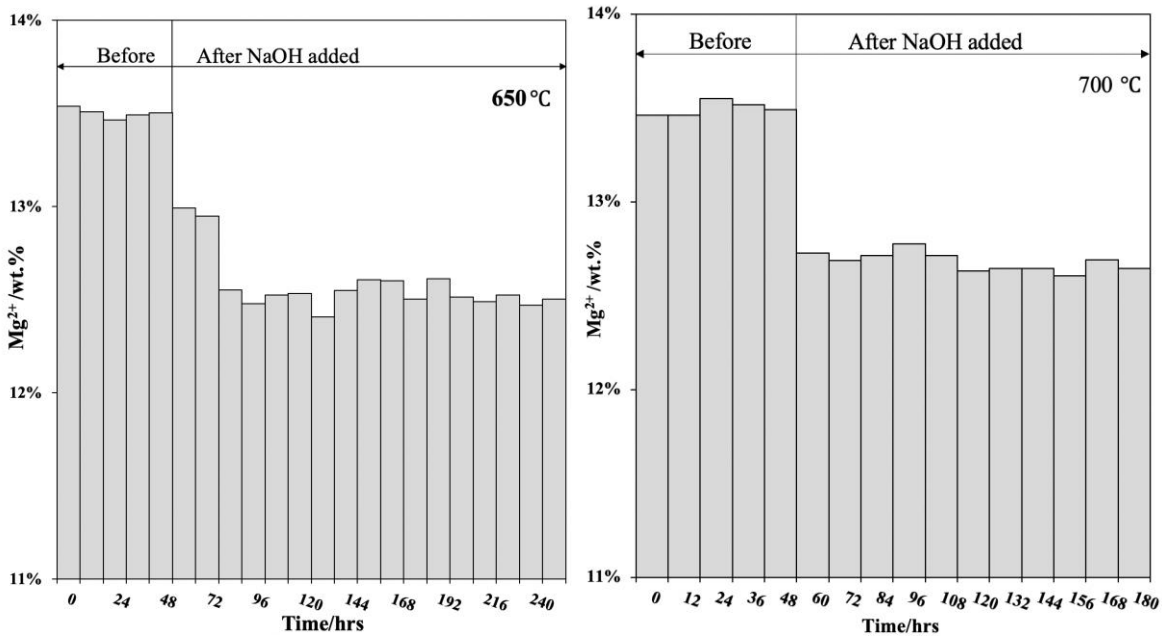

Figure 2-11 (a) Mg^{2+} wt.% in $MgCl_2$-NaCl-KCl-NaOH at 650 ºC before and after NaOH added (b). Mg^{2+} wt.% in $MgCl_2$-NaCl-KCl-NaOH at 700 ºC before and after NaOH added.

Table 2-13 Equilibrated C_{OH^-} in $MgCl_2$-NaCl-KCl-2wt.% at different temperature

T ºC	C_{OH^-} ($\times 10^{-6}$ mol cm^{-3})
600	4.11
650	3.73
700	3.46
750	3.19
800	2.84

2.2.1.2.2 Diffusion Coefficient *D*

CV technique was used to measure D_{OH^-} at different temperatures. To identify the peak position of OH^-/H_2 redox reaction, a CV scan was conducted between -1.8 V and -0.2 V as shown in Fig. 4(a). The peaks on the left were the redox peaks of Mg/Mg^{2+}. A new peak was observed after NaOH was added. To identify the peaks, the reaction potential ΔE (vs. Cl^-/Cl_2) was calculated as given in Table 2-14. The estimated reaction potential difference of redox couple Mg/Mg^{2+} and the redox couple to be identified was around 1V. It's close to the calculated value 1.01V as given in Table 2-14. Therefore, it can be concluded that the peak indicated by the arrow was the redox

peak of OH^-/H_2, among which the reduction peak was almost invisible due to its weak reduction peak current. CV scans in the range from -0.42V to -0.82V were conducted at different scan rates as given in Figure 2-12(b). In the scan rate range of 100 mV/s to 400mV/s, the peak potential difference ΔE_p ($\Delta E_p = |E_{pa} - E_{pc}|$) was close to the value of $2.3RT/nF$ (or 183mV) for a one-electron reaction at 650 ºC. Moreover, no obvious shift was observed in the reduction peak potential at different scan rates. Both of those characteristics indicated that the redox reaction of OH^-/H_2 was a one-electron reversible reaction. The same conclusion was also made in the study by Kanzaki et al[49]. Eq. 2-10 was applied in the calculation of diffusion coefficient D_{OH^-},

$$I_p = 0.4463nFAC\sqrt{\frac{nFDv}{RT}} \qquad 2\text{-}10$$

where I_p is peak current (A), n is electron transfer number, A is working electrode surface area (cm^2), C: OH^- concentration C_{OH^-} (mol/cm^3) and v is scan rate (v/s). D_{OH^-} was calculated by plotting I_p versus square root of v (I_p vs. $\sqrt{v}$). The relation of I_p and $\sqrt{v}$ demonstrated good linearity as shown in Figure 2-13(a), which characterized that the reaction was diffusion controlled and the value of D_{OH^-} can be obtained from the slope of plot. The calculated D_{OH^-} at different temperatures were summarized in Table 2-15. The value of D_{OH^-} increased with the rise of temperature. Comparing with diffusion coefficient of Fe^{2+}, Ni^{2+}, Cr^{2+} and Cr^{3+} in $MgCl_2$-NaCl-KCl at the same temperature calculated in Section 2.2.1.1, D_{OH^-} ranged from 2.46 to 4.48×10^{-4} cm^2/s, which were much larger as expected. $\ln D$ was linearly related to 1/T, which indicate that D_{OH^-} follows Arrhenius law. And the calculated activation energy E_a was 22.39 kJ/mol.

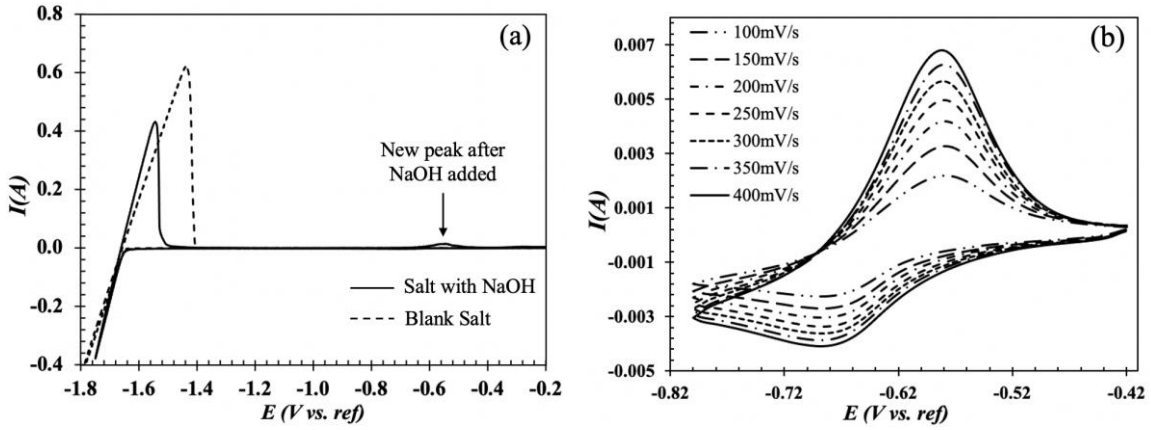

Figure 2-12 (a) CV scan in $MgCl_2$-NaCl-KCl at 650 ºC before and after NaOH added. WE: tungsten, CE: graphite, RE: $Ni/NiCl_2$ (b). CV scan of redox couple OH^-/H_2 in $MgCl_2$-NaCl-KCl at 650 ºC after NaOH added. WE: tungsten, CE: graphite, RE: $Ni/NiCl_2$.

Table 2-14 Reaction potential ΔE (vs. Cl^-/Cl_2) calculation using HSC 10.0 at 600 ºC

	Electrochemical Reactions	ΔE (vs. Cl^-/Cl_2)
(1)	$MgCl_2 = Mg + Cl_2$	$\Delta E_{Mg/Mg^{2+}}$ = -2.61V
(2)	$NaOH + MgCl_2 = H_2 + Cl_2 + Na_2O + MgO$	$\Delta E_{OH^-/H_2}$ = -1.60V
$\lvert \Delta E_{Mg/Mg^{2+}} - \Delta E_{OH^-/H_2} \rvert$ = 1.01V		

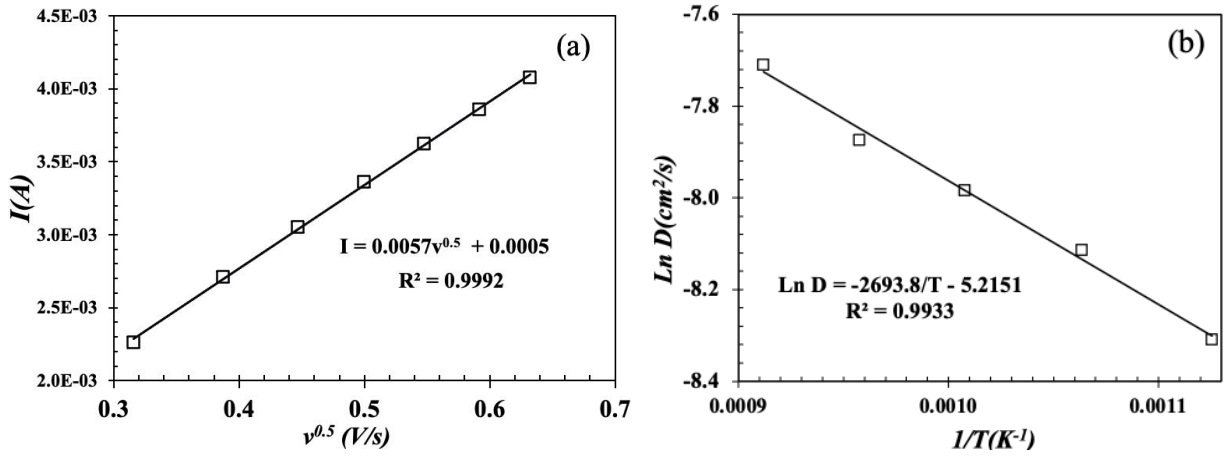

Figure 2-13(a) Relation of I_p vs. $\sqrt{v}$ in $MgCl_2$-NaCl-KCl-NaOH at 650 ºC. WE: tungsten, CE: graphite, RE: Ni/$NiCl_2$. (b) Plot of ln D vs. 1/T at different temperatures in $MgCl_2$-NaCl-KCl-NaOH

Table 2-15 Calculated D_{OH^-} in $MgCl_2$-NaCl-KCl-NaOH at different temperatures

T ºC	D_{OH^-} ($\times 10^{-4}$ cm^2 s^{-1})	E_a (kJ mol^{-1})
600	2.46	22.39
650	2.99	
700	3.41	
750	3.71	
800	4.48	

2.2.1.2.3 Exchange Current Density i_0, Charge Transfer Coefficient α, Limiting Current Density i_L and Standard Rate Constant k^0 Measurements

As mentioned before, the calculation of exchange current density must consider both the interface reaction and mass transfer process in the molten salt system. Therefore, the exchange current density can be calculated using the derived modified Butler-Volmer equation as given in Eq. 2-8. Potentiodynamic scans were conducted at different temperatures as given in Figure 2-14. Three identical scans were conducted in each test to check the data repetition and ensure data reliability. As shown in Figure 2-14, at the same overpotential η, current density increased with the rise of temperature. When overpotential η < 0, OH^- transported to the interface was reduced to H^0, eventually form H_2 gas, through the electrochemical reduction reactions as given in Table 2-16. The production rate of H_2 gas became faster as the temperature increased. As a result, it's possible that a certain amount of H_2 bubble formed on the electrode surface, thus leading to the fluctuation on the potentiodynamic curve. As observed in the curve at 800 ºC, the fluctuation was the strongest at η = 0, since the accumulated H_2 bubble reached maximum. When overpotential η > 0, H_2 bubble was consumed through the electrochemical oxidation reaction as given in Table 2-16. The curve became smooth and there was no obvious fluctuation. Figure 2-15 gave the fitting result of the potentiodynamic scan at 600 and 700 ºC. The dash line was the fitted i-η curve using the non-linear least square fitting technique, while the solid line was the experiment data sets. The fitted curves matched well with the experimental data. Table 2-17 listed the optimized value of i_0, α and i_L of OH^- in $MgCl_2$-KCl-NaCl salts at each temperature. The fitted α value kept consistent which was independent of temperature. The values of α were all less than 0.5, which was in the range from 0.25 to 0.27. In general, the value of α lied between 0 and 1. If the value was extremely close to 0 (or 1), it indicated that the transition state (or electrochemical reaction) was reactant-favored (or product-favored). In the present study, the small values of α which were close to 0 demonstrated a reactant-favored transition state.

The standard rate constant k^0 at each temperature was calculated by substituting the measured C_b of OH^-, fitted i_0 and α into Eq. 2-9. The calculated k^0 was in the range from 1.23 to 2.50×10^{-4} cm s^{-1} as given in Table 2-17. k^0 increased with the rise of temperature. The relation of $\ln k^0$ vs. $1/T$ demonstrated good linearity as shown in Figure 2-16, which indicated that k^0 followed Arrhenius law. The activation energy E_a calculated from k^0 was 28.71 kJ mol^{-1}. Moreover, the diffusion layer thickness δ was estimated using Eq. 2-11. The value of δ was within a reasonable range of 0.05 – 0.1mm, which further confirmed the data reliability.

$$i_L = -\frac{nFDC_b}{\delta} \qquad 2\text{-}11$$

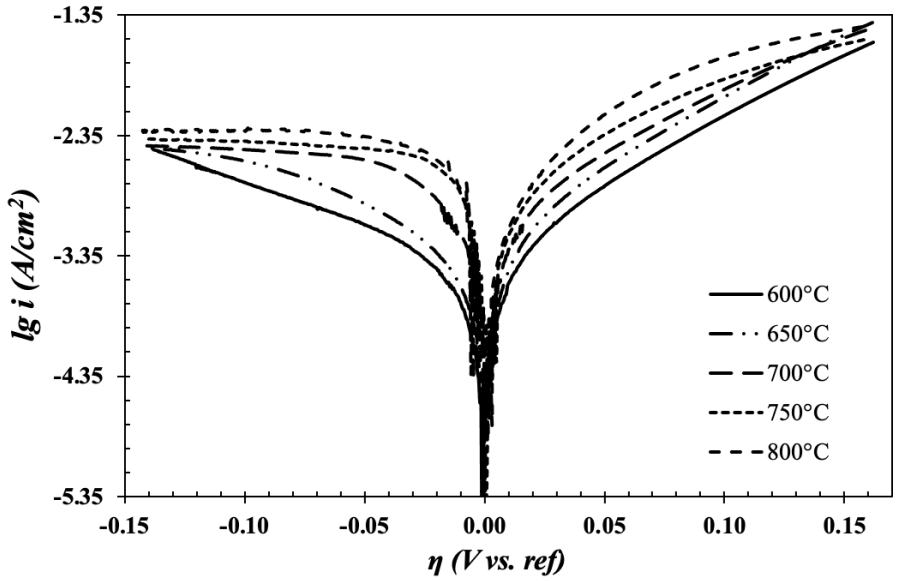

Figure 2-14 Potentiodynamic scans of OH- in $MgCl_2$-NaCl-KCl at different temperatures, scan rate: 5mV/s. WE: tungsten, CE: graphite, RE: $Ni/NiCl_2$.

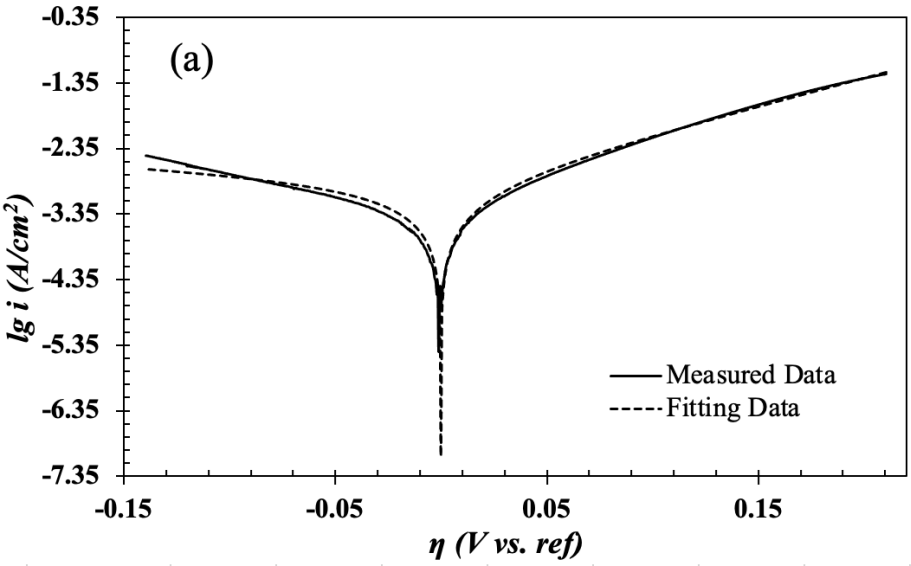

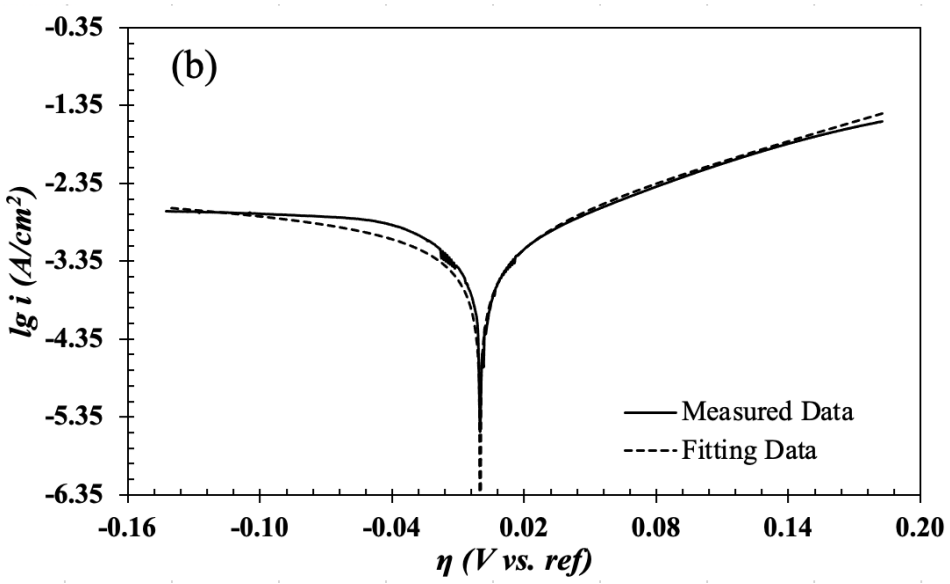

Figure 2-15 Measured and fitted potentiodynamic polarization curves in $MgCl_2$-KCl-NaCl-NaOH with a scan rate of 5mV/s. WE: tungsten, CE: graphite, RE: $Ni/NiCl_2$: (a) 600 ºC; (b) 700 ºC.

Table 2-16 Electrochemical reactions of OH^-/H_2 in $MgCl_2$-NaCl-KCl

Reaction Type	Electrochemical Reactions	Overpotential η
Reduction	$OH^- + e^- \rightarrow H + O^{2-}$ $H + H \rightarrow H_2$	$\eta < 0$
Oxidation	$H_2 + 2O^{2-} - 2e^- \rightarrow 2OH^-$	$\eta > 0$

Table 2-17 Fitted i_0, α, i_L and k^0 of OH^- in $MgCl_2$-KCl-NaCl at 600, 650, 700, 750, 800 ºC

T ºC	i_0 ($\times 10^{-3}$ A cm^{-2})	i_L ($\times 10^{-2}$ A cm^{-2})	α	k^0 ($\times 10^{-4}$ cm s^{-1})
600	1.08	-0.94	0.25	1.23
650	1.34	-1.98	0.27	1.28
700	1.47	-2.31	0.27	1.48
750	1.66	-2.71	0.26	2.01
800	1.89	-3.27	0.26	2.50

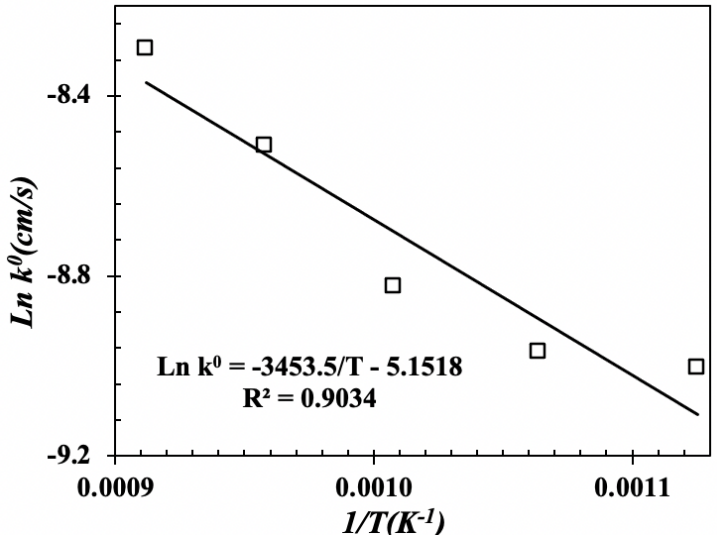

Figure 2-16 Ln k^0 – 1/T plots fitted at each temperature.

2.2.2 Kinetic Parameters in Molten NaF-KF-UF_4-UF_3 Salts

2.2.2.1 Diffusion Coefficient

The oxidation state of Fe and Cr needed to be identified in molten NaF-KF-UF_4-UF_3 salts for diffusion coefficient measurements. According to the previous studies in FLiNaK, NaF-ZrF_4 and LiF-BeF_2 salts[127,128,129], it's highly possible that the predominant oxidation states of Fe and Cr could be Fe^{2+}, Cr^{2+} and Cr^{3+}. To verify this hypothesis, CV and PD scans were conducted as given in Figure 2-17. Based on previous studies[130,131], the R3 and R4 peaks corresponded to the reduction reaction of redox couples U^{4+}/U^{3+} and U^{3+}/U. The other two reduction peaks R1 and R2 were related to reduction reactions of Fe^{2+}, Cr^{2+} or Cr^{3+}. Table 2-18 lists the calculated standard reduction potential of Fe, Cr and U ions using HSC 10.0 software[126]. The table showed that the difference between the reduction potential of Cr^{2+}/Cr and Fe^{2+}/Fe at 800°C was 0.42V, which matched well with the measured data (~0.45V) in CV scan shown in Figure 2-17. It confirmed that

R1 and R2 peak represent the reduction reactions of Fe^{2+}/Fe and Cr^{2+}/Cr couple, respectively. According to previous study[40,42,132], the redox reaction current signal of Cr^{3+}/ Cr^{2+} was always much smaller than Cr^{2+}/Cr in CV scans, which may make the redox peaks of Cr^{3+}/ Cr^{2+} invisible in the present study. More analysis is needed to verify the presence of Cr^{3+} in the salts.

When using CV technique to measure the diffusion coefficient in a multicomponent salt system, the baseline for the second or succeeding reduction peak was affected by the tail from the previous peak[133]. Therefore, the second peak current in the CV scan (see Figure 2-17.) was the combination of the second component Cr^{2+}/Cr reduction current and the tail from the preceding reduction peak of Fe^{2+}/Fe. The error associated with the Cr baseline determination could be significant at a high concentration of Fe^{2+}.

One option would be to make the measurement of the Cr peak current using the decaying current of the first wave as the baseline in the CV scans [36]. Since the reduction peaks of Cr^{3+}/ Cr^{2+} was not identified in the electrochemical tests, the current study only considered $D_{Fe^{2+}}$ and $D_{Cr^{2+}}$. CV scans of Fe^{2+}/Fe and Cr^{2+}/Cr at different scan rates were performed as shown in Figure 2-18. Assuming that the reduction peak potential of Cr^{2+}/Cr was not affected by the reduction reaction of Fe^{2+}/Fe, the electron transfer number n of redox couple Fe^{2+}/Fe and Cr^{2+}/Cr were calculated at different temperatures using $\Delta E_p = \left|E_{pa} - E_{pc}\right| = 2.3RT/nF$. The calculated values of n are given in Table 2-19, which further confirmed the two-electron transferred redox reactions. $D_{Fe^{2+}}$ and $D_{Cr^{2+}}$ were calculated using Eq. 2-3. The relation of I_p-$v^{1/2}$ shown in the inset of Figure 2-18(a) and Figure 2-18(b) demonstrated good linearity which indicated the diffusion-controlled redox reactions of Fe^{2+}/Fe and Cr^{2+}/Cr at the measured scan rates. The diffusion coefficient by CV at different temperatures is given in Table 2-20.

An effective method for solving the problem of baseline determination for a system containing multiple components is semi-differential (SD) analysis. It transforms a CV curve into a SD plot by the first semi-integration of the current-potential data and then take the first derivative with respect to potential[134,135,136,137,138]. For a soluble-insoluble reaction, an equation was derived to describe the relation of SD peak current and potential as given below[133,139,140]:

$$S_p = \frac{n^2F^2AC\sqrt{D}}{2RT} \qquad 2\text{-}12$$

An example of a SD plot is given in Figure 2-19. A Cr peak that is independent of the Fe peak is observed in the SD plot. It shows a better baseline resolution between the Cr and Fe peaks. The SD method has the advantages of high sensitivity and high resolvability for the species and provided a better baseline for Cr^{2+}/Cr peak in the multicomponent system.

To validate the SD method, the diffusion coefficient of Fe^{2+} was calculated using CV and SD as listed in Table 2-20. The values obtained from using both electro-analytical methods were in good agreement, which verified the validity of the SD method and the accuracy of the approach used in the method. The diffusion coefficient of Cr^{2+} was calculated using both CV and SD methods, as shown in Table 2-20. Although the SD method could give more accurate results as previously discussed, the calculated values of $D_{Cr^{2+}}$ using both methods were close. Therefore, considering

the low concentration of Fe^{2+} in the molten NaF-KF-UF_4-UF_3 salts, it was believed that the CV method in which using decay current of the first peak as the baseline could be applied in the diffusion coefficient measurement of the second component (refer to the second peak in the CV curve) at a low concentration of the first component (refer to the first peak in the CV curve), but it would introduce large errors in the measurement when used at a high concentration[133].

$D_{Fe^{2+}}$ and $D_{Cr^{2+}}$ calculated from both methods followed the Arrhenius law as shown in Figure 2-20. The activation energy of Fe^{2+} and Cr^{2+} diffusivity was estimated from the slope of ln D-$1/T$ curves, which were 39.47 kJ mol^{-1} (Fe^{2+}) and 30.98 kJ mol^{-1} (Cr^{2+}) for the CV method, and 36.72 kJ mol^{-1} (Fe^{2+}) and 31.08 kJ mol^{-1} (Cr^{2+}) for the SD method, respectively.

In general, the diffusion coefficient was determined by ion dimension, solution viscosity, pressure, density and temperature[141,142,143,144,145]. The value of $D_{Cr^{2+}}$ was slightly larger than that of $D_{Fe^{2+}}$ at the same temperature, which was consistent with that in $MgCl_2$-NaCl-KCl. Nevertheless, the measured $D_{Fe^{2+}}$ and $D_{Cr^{2+}}$ values in molten $MgCl_2$-NaCl-KCl tended to be larger than those in molten NaF-KF-UF_4-UF_3 salts as listed in Table 2-4 and Table 2-20. The higher density of NaF-KF-UF_4-UF_3 salts was believed to be one of the major causes of the difference.

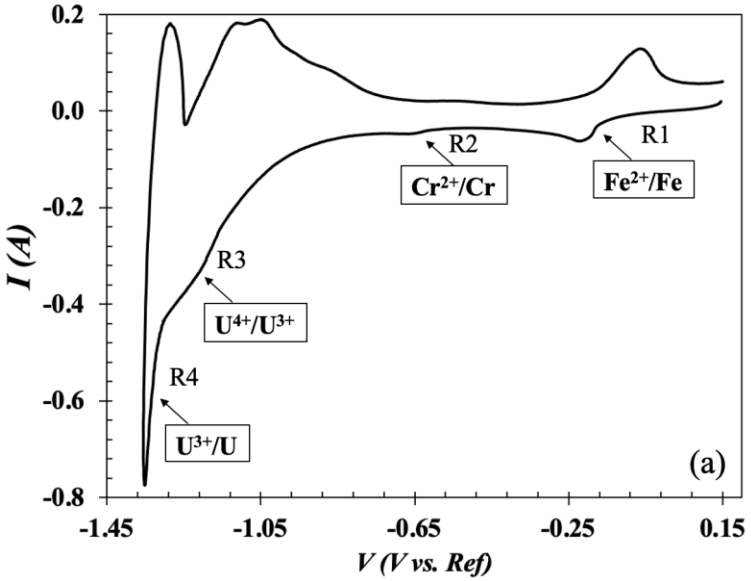

Figure 2-17 CV scan in molten NaF-KF-UF_4-UF_3 salts at 800 ºC, WE: tungsten, CE: graphite, RE: Pt.

Table 2-18 Standard reduction potential of Fe, Cr and U ions

T (℃)	$\Delta E\ vs.F_2$ (V)			
	U^{3+}/ U	U^{4+}/ U^{3+}	Cr^{2+}/Cr	Fe^{2+}/Fe
700	-4.44	-3.56	-3.38	-2.97
750	-4.40	-3.53	-3.35	-2.94
800	-4.37	-3.50	-3.32	-2.90

Table 2-19 Calacualted elenctron transfer number of Fe^{2+}/Fe and Cr^{2+}/Cr

T (℃)	Electron transfer number n	
	Fe^{2+}/Fe	Cr^{2+}/Cr
700	2.14	1.92
750	2.21	2.09
800	2.02	2.16

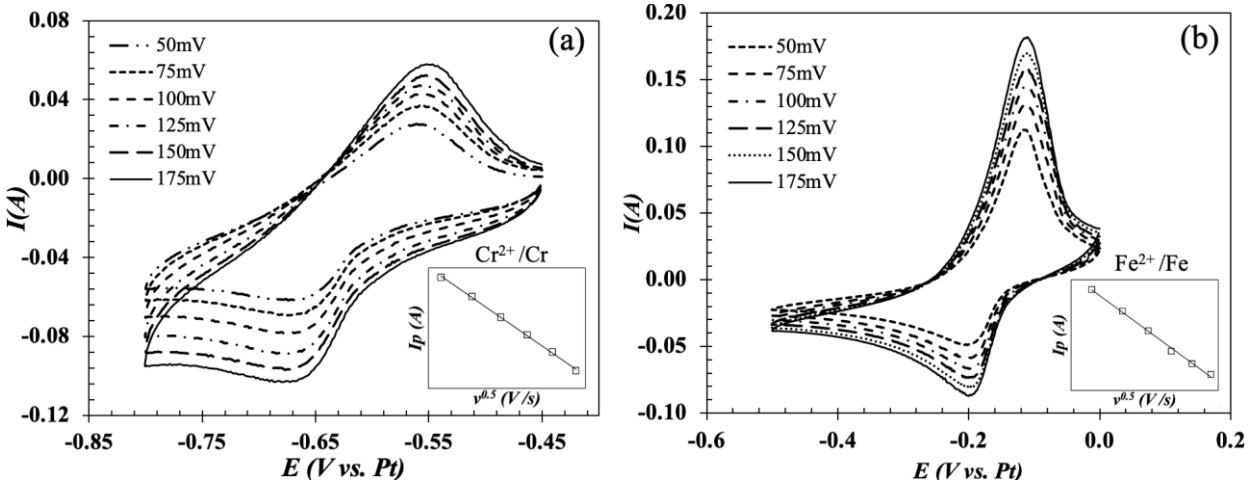

Figure 2-18 CV scans of Cr^{2+}/Cr and Fe^{2+}/Fe at different scan rates in molten NaF-KF-UF_4-UF_3 salts at at 800 ºC, WE: tungsten, CE: graphite, RE: Pt.

Table 2-20 Diffusion coefficient of Fe^{2+} and Cr^{2+} in molten salts at different temperatures

Temperature (ºC)	Fe^{2+}				Cr^{2+}			
	CV		SD		CV		SD	
	D	E_a	D	E_a	D	E_a	D	E_a
700	1.60	39.47	1.60	36.72	2.11	30.98	2.02	31.09
750	2.02		1.90		2.59		2.48	
800	2.52		2.45		3.01		2.90	

Note: D is in the unit of 10^5 cm^2 s^{-1} and E_a is in the unit of kJ mol^{-1}.

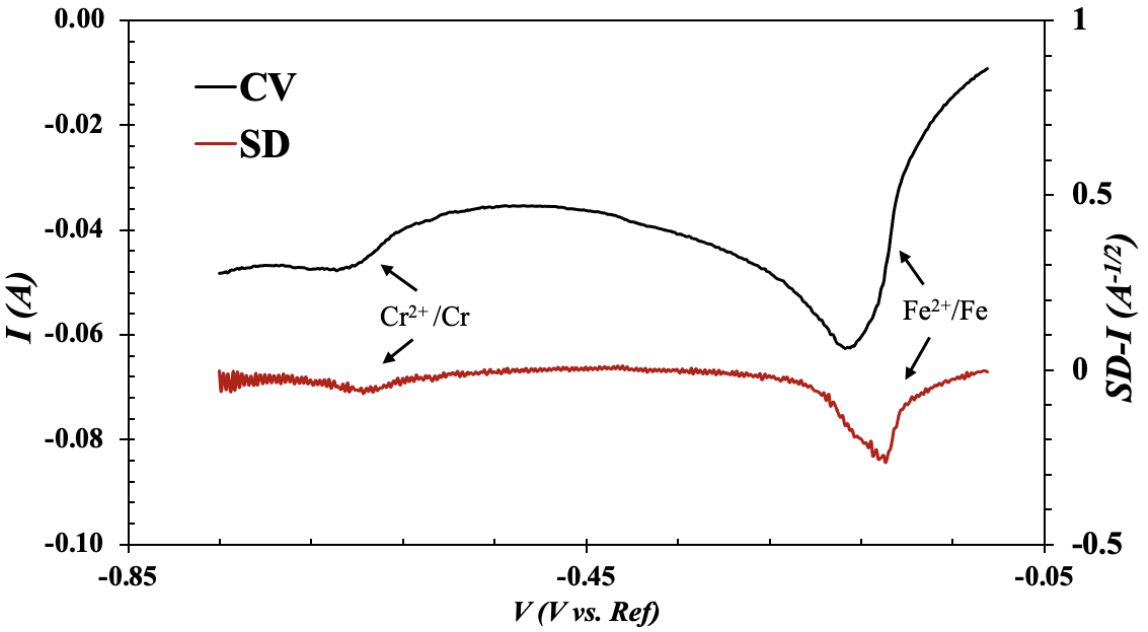

Figure 2-19 CV and SD transformation of CV in molten NaF-KF-UF_4-UF_3 salts at 800 ºC

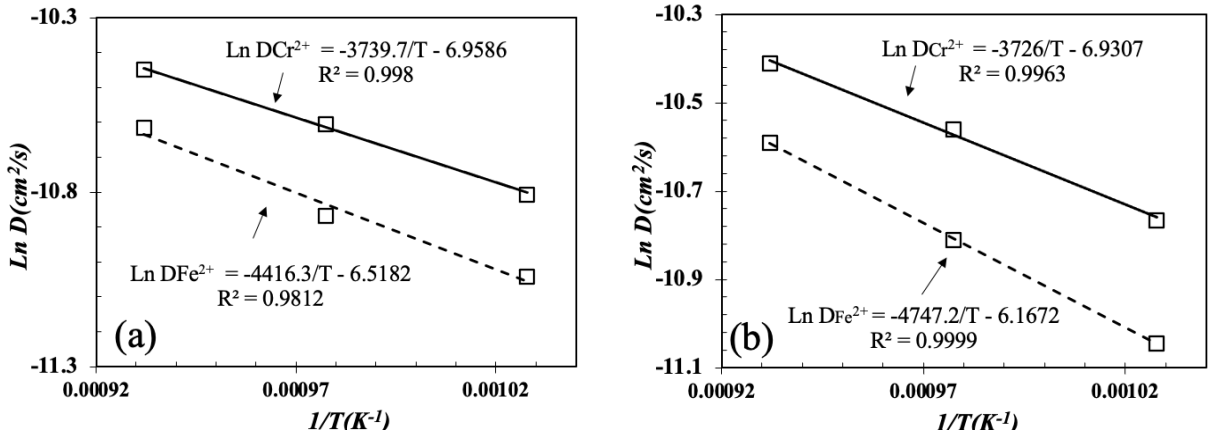

Figure 2-20 Ln D-$1/T$ relation of Fe^{2+} and Cr^{2+} in molten NaF-KF-UF_4-UF_3 salts, (a) SD method, (b) CV method

2.2.2.2 Exchange Current Density i_0, Charge Transfer Coefficient α, Limiting Current Density i_L

As shown in Figure 2-21(a), three peaks were observed in the PD curve which was in terms of lg i versus E, and scanned from -0.66 V to -0.05 V. In the PD scan, peaks such as P1, P2 and P3 would show up once the measured current was zero as shown in Figure 2-21(b). In a monocomponent system, such as $FeCl_2$ in the molten $MgCl_2$-NaCl-KCl salt as shown in Figure 2-7(a), when scanning from the negative to positive potential within the redox reaction potential of Fe^{2+}/Fe, a peak represented a shift between a reduction reaction and an oxidation reaction of Fe^{2+}/Fe, in which the reduction reaction with a negative current was within the negative overpotential, and the oxidation reaction with a positive current occurred over the positive overpotential range. However, the peaks observed in the PD curve were the combination of several reactions in the multicomponent system. Although the Cr^{3+}/Cr^{2+} peak was not identified in CV scans, the three peaks in the PD scan indicated the presence of Cr^{3+} in the salt. The reduction potential of Fe^{2+}, Cr^{2+} and Cr^{3+} descended in the order of Fe^{2+} > Cr^{3+} > Cr^{2+}. It meant that when scanning from a potential less than $E_{Cr^{2+}}$, some Fe may have been deposited on the electrode surface. In the left half part of P1, the reaction included the reduction of Fe^{2+} to Fe, Cr^{2+} to Cr and Cr^{3+} to Cr^{2+}, and in the right half part of P1, it included the oxidation of Cr to Cr^{2+}, and reduction of Fe^{2+} to Fe and Cr^{3+} to Cr^{2+}. For P2, the reactions included in the left part were the same as those in the right half of P1, but the current of each reaction contributed was different resulting in different current values. In the right half part of P2, the reactions were composed of the oxidation of Cr^{2+} to Cr^{3+}, Cr to Cr^{2+} and reduction of Fe^{2+} to Fe. For P3, the left half part included the oxidation reaction of Cr^{2+} to Cr^{3+} and reduction of Fe^{2+} to Fe, and right half part only included the oxidation reaction of Fe to Fe^{2+} and Cr^{2+} to Cr^{3+}.

To measure the exchange current density of Fe^{2+}, Cr^{2+} and Cr^{3+}, PD scans were conducted within different potential range as given in Figure 2-22. Assuming the PD scan of Fe^{2+} was not affected by Cr^{3+} and Cr^{2+}, the green PD curve in Figure 2-22 only included the Fe^{2+}/Fe redox peak. Therefore, i_0, α and i_L of Fe^{2+}/Fe was calculated by fitting the measured overpotential η and current density i to Eq. 2-8 using non-linear curve fitting technique as shown in Figure 2-25(a).

As for the measurement of Cr^{3+}/Cr^{2+}, the red PD curve that should include both Cr^{3+}/Cr^{2+} and Fe^{2+}/Fe redox peaks was applied. An innovative method was developed accordingly as follows: (1) the green PD curve including only Fe^{2+}/Fe was fitted; (2) the green PD curve was extrapolated using the Butler-Volmer equation until there was a cross-point with the red PD curve. This cross-point corresponded to the corrosion potential of Cr^{3+}/Cr^{2+} as given in Figure 2-23, which also confirmed that Cr^{3+} was present in the salts; (3) a new PD curve was obtained by using the red PD curve to subtract the new extrapolated green PD curve as given in Figure 2-25(c), and i_0, α and i_L of Cr^{3+} was obtained by fitting the new PD scan. In the measurement of Cr^{2+}/Cr, the black PD curve including Cr^{2+}/Cr, Cr^{3+}/Cr^{2+} and Fe^{2+}/Fe was used. Following the similar procedures applied in the measurement of Cr^{3+}/Cr^{2+}, a cross-point corresponding to the corrosion potential of Cr^{2+}/Cr was obtained as given in Figure 2-24. A new PD curve of Cr^{2+}/Cr can be obtained by using the black PD curve to subtract the new extrapolated red PD curve as shown in Figure 2-25(b), from which i_0, α and i_L of Cr^{2+} was obtained.

The fitting results of Fe^{2+}/Fe, Cr^{2+}/Cr and Cr^{3+}/Cr^{2+} matched well with the experimental data as given in Figure 2-25(a), (b) and (c). Table 2-21 lists the measured i_0, α and i_L values of Fe^{2+}/Fe, Cr^{2+}/Cr and Cr^{3+}/Cr^{2+} at 700 ºC, 750 ºC and 800 ºC. Both i_0 and i_L increased with a rise in temperature. α was consistent at different temperatures, with a value ranging from 0.23 to 0.32 for Fe^{2+} (reactant-favored reaction), 0.75-0.89 for Cr^{2+} and 0.74-0.91 for Cr^{3+} (product-favored reaction). i_0 of Fe^{2+}, Cr^{2+} and Cr^{3+} followed the Arrhenius law as shown in Figure 2-26. The activation energy of i_0 was calculated from the slope of Ln i_0 – 1/T plot, which were 56.56 kJ/mol (Fe^{2+}), 44.40 kJ/mol (Cr^{2+}) and 60.00 kJ/mol (Cr^{3+}), respectively.

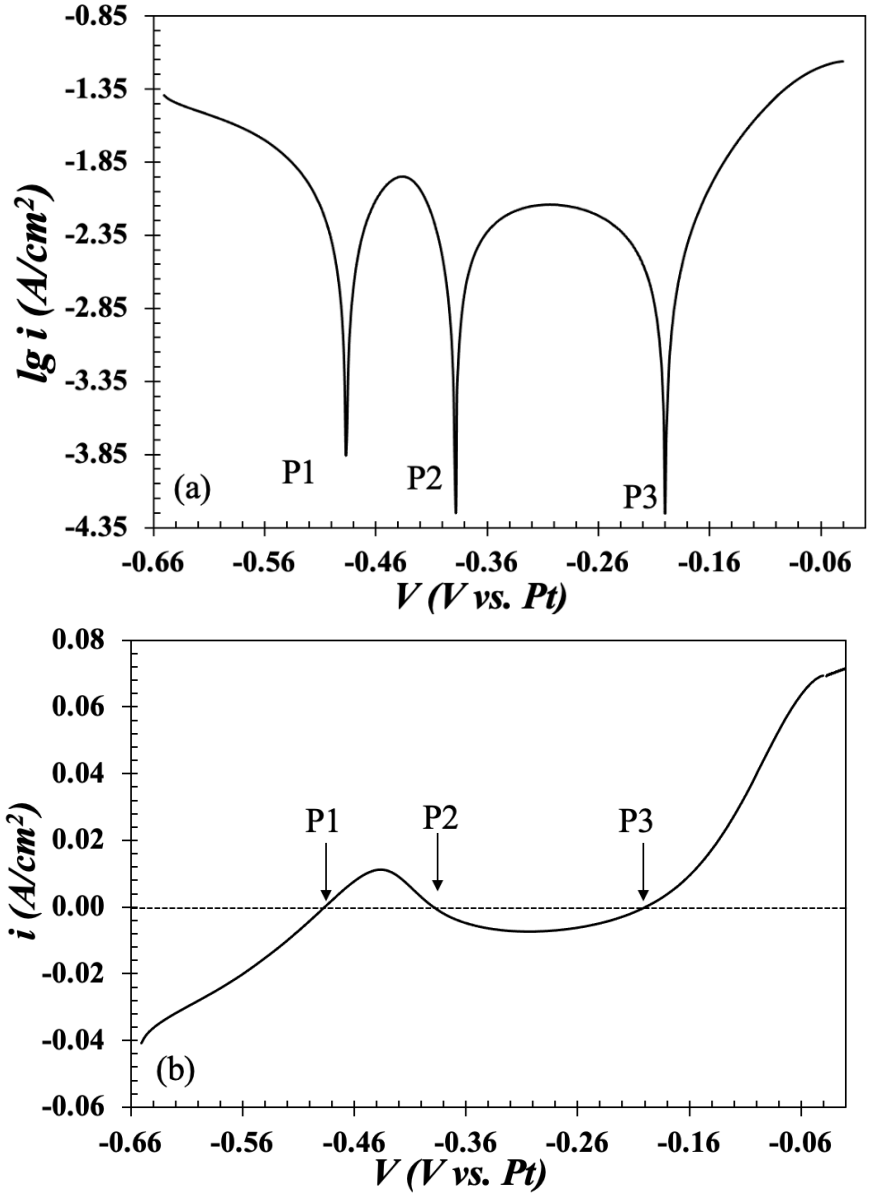

Figure 2-21 PD scans in molten NaF-KF-UF_4-UF_3 salts at 700 ºC, (a) lg i vs. V (b) i vs. V

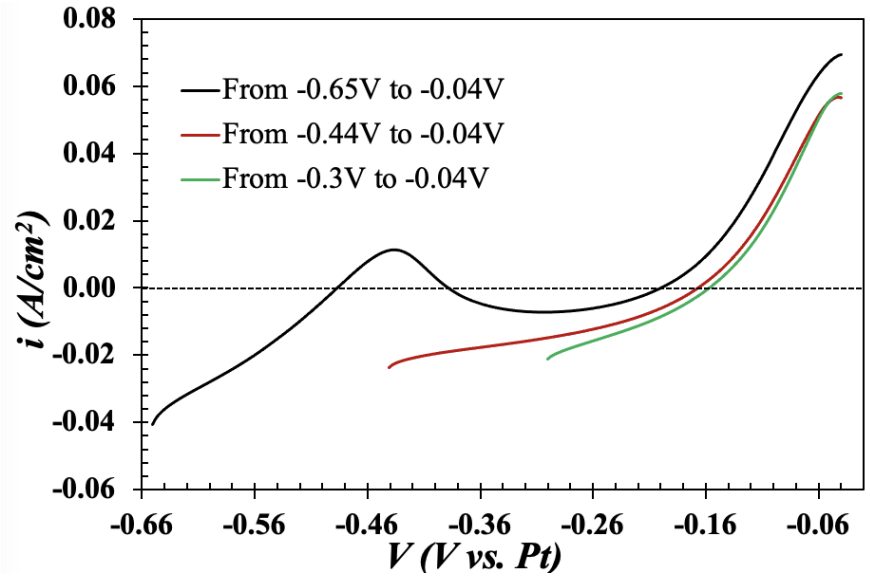

Figure 2-22 PD scan within different potential range in molten NaF-KF-UF_4-UF_3 salts at 700 ºC

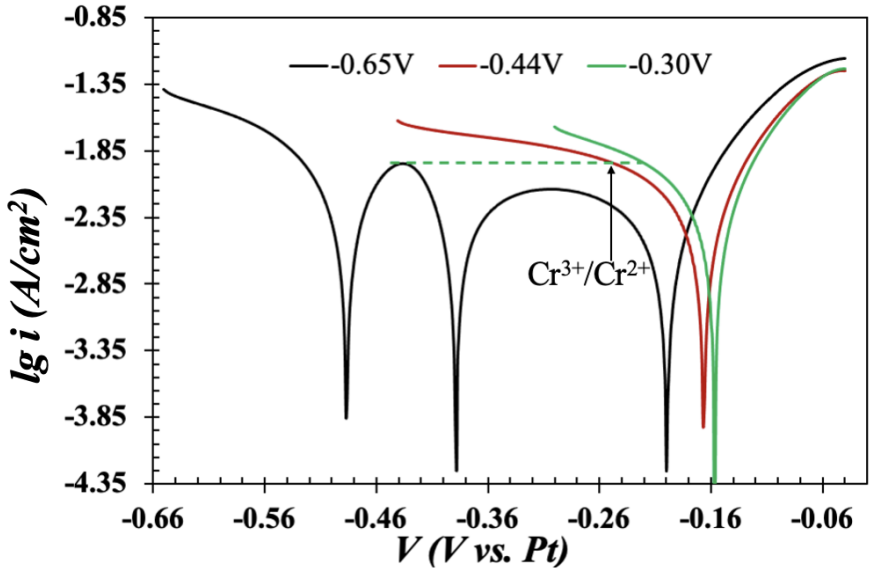

Figure 2-23 Deterination of actural PD curve of Cr^{3+}/Cr^{2+} in molten NaF-KF-UF_4-UF_3 salts at 700 ºC

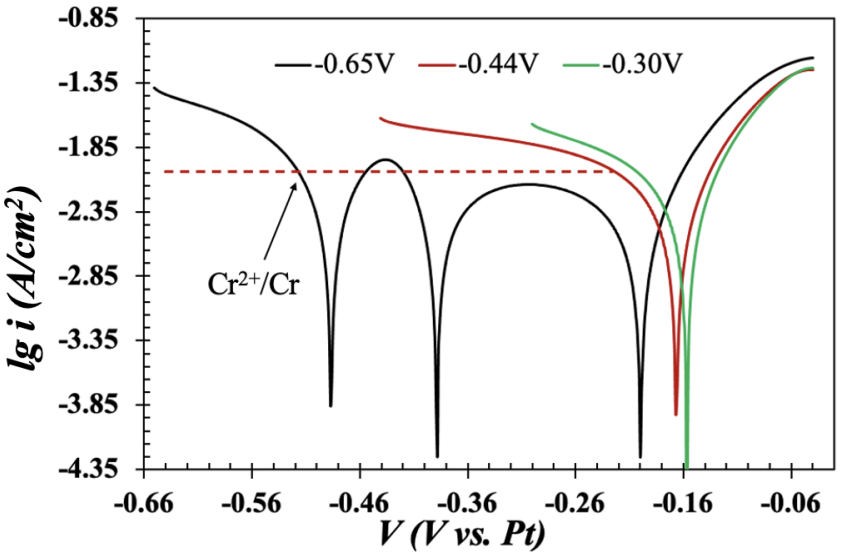

Figure 2-24 Deterination of actural PD curve of Cr^{2+}/Cr in molten NaF-KF-UF_4-UF_3 salts at 700 ºC

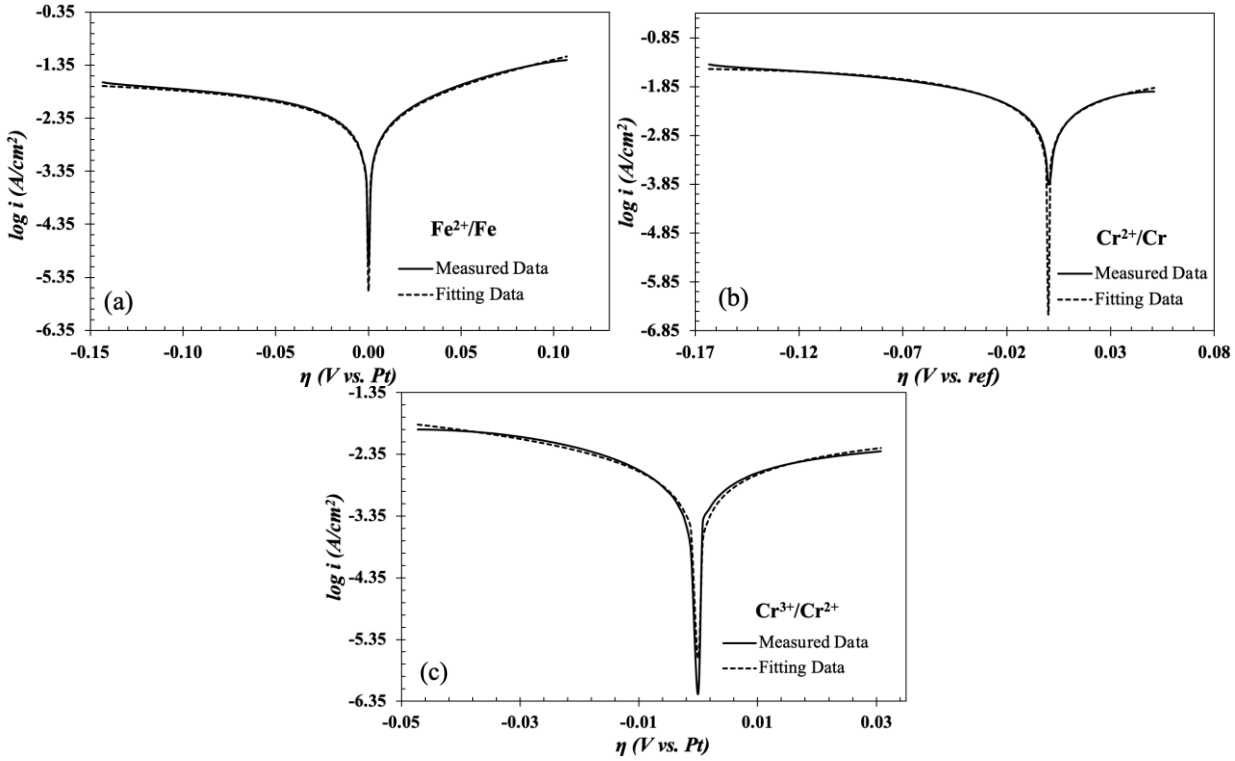

Figure 2-25 Measured and fitted PD curves of Fe^{2+}/Fe in NaF-KF-UF_4-UF_3 salts at 700 ºC with a scan rate of 5mV/s. WE: tungsten, CE: graphite, RE: Pt

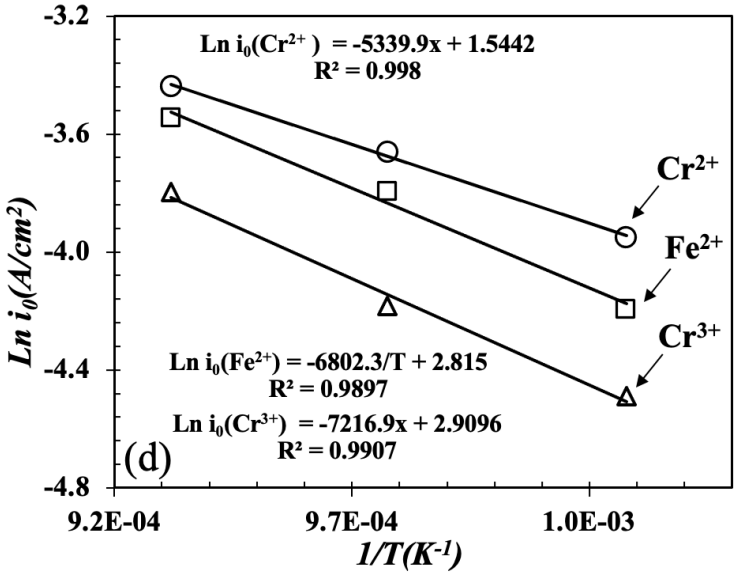

Figure 2-26 Ln i_0 – 1/T plots of Fe^{2+}, Cr^{2+} and Cr^{3+} at 700 ºC, 750 ºC and 800 ºC in molten NaF-KF-UF_4-UF_3 salts

Table 2-21 Fitted i_0, α, and i_L of Fe^{2+}, Cr^{2+} and Cr^{3+} in NaF-KF-UF_4-UF_3 salts at 700 ºC, 750 ºC and 800 ºC

Temperature (ºC)	i_0 (×10^{-2} A cm^{-2})			i_L (×10^{-2} A cm^{-2})			α		
	Fe^{2+}	Cr^{2+}	Cr^{3+}	Fe^{2+}	Cr^{2+}	Cr^{3+}	Fe^{2+}	Cr^{2+}	Cr^{3+}
700	1.51	1.93	1.12	-3.21	-3.52	-5.61	0.32	0.87	0.91
750	2.25	2.57	1.52	-8.82	-4.81	-7.38	0.23	0.89	0.74
800	2.89	3.21	2.25	-13.63	-8.02	-9.47	0.31	0.75	0.80

2.2.3 Applications of Kinetic Parameters

As mentioned before, a corrosion rate can be predicted once the kinetic parameters of corrosion products were obtained from the experiments.

Assume an electrode reaction of metal dissolution and deposition on the interface between the metal and liquid,

$$M - ne^- \underset{k_b}{\overset{k_f}{\rightleftharpoons}} M^{n+} \qquad 2\text{-}13$$

The dissolution rate R_{diss} is defined as,

$$R_{diss} = k_f X_M \quad \text{2-14}$$

Where, k_f is dissolution reaction constant, X_M is molar fraction of M in the solid, and for pure metal $X_M = 1$.

The deposition rate R_{depo} is defined as,

$$R_{depo} = k_b X_M^I \quad \text{2-15}$$

Where, k_b is deposition reaction constant, X_M^I is molar fraction of M^{n^+} at the interface of the metal and liquid.

Then the corrosion rate R_{corr} can be expressed with an equation given as,

$$R_{corr} = R_{diss} - R_{depo} = k_f X_M - k_b X_M^I \quad \text{2-16}$$

For a pure metal at the equilibrium state, the metal dissolution rate is equal to the deposition rate.

$$R_{corr} = k_f X_M - k_b X_M^I = k_f - k_b X_{M,e}^I = 0 \quad \text{2-17}$$

$$k_f = k_b X_{M,e}^I \quad \text{2-18}$$

Where, $X_{M,e}^I$ is equilibrium molar fraction of M^{n^+} at the interface of the metal and liquid.

Then, the corrosion rate can be expressed as:

$$R_{corr} = k_b (X_{M,e}^I - X_M^I) \quad \text{2-19}$$

The corrosion process involves mass transfer of corrosion product. Here, mass transfer rate is defined as,

$$R_m = -\rho D_{diff} \frac{\partial X_M}{\partial x} = \frac{\rho D_{diff}}{\delta} \left(X_M^I - X_M^b\right) = k_m \left(X_M^I - X_M^b\right) \quad \text{2-20}$$

Where, ρ is liquid density, D_{diff} is diffusion coefficient of M^{n^+}, δ is diffusion layer thickness, X_M^I is molar fraction of M^{n^+} at the interface of the metal and liquid, X_M^b is molar fraction of M^{n^+} in the bulk liquid, k_m is equal to $\frac{\rho D_{diff}}{\delta}$.

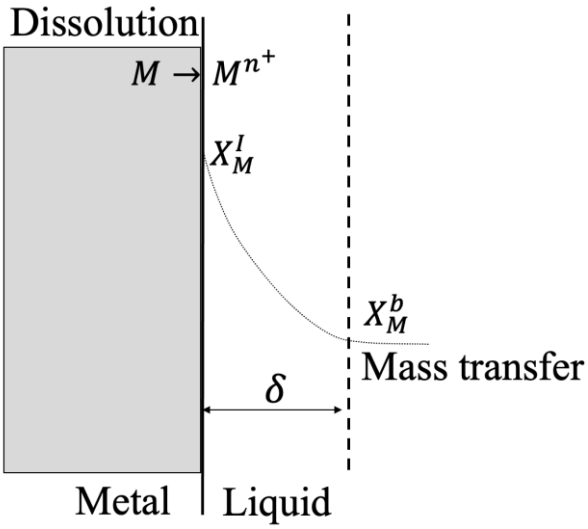

Figure 2-27 Metal dissolution and mass transfer process

Since the corrosion rate is equal to mass transfer rate,

$$R_m = R_{corr} \tag{2-21}$$

Then,

$$k_m\left(X_M^I - X_M^b\right) = k_b(X_{M,e}^I - X_M^I) \tag{2-22}$$

$$X_M^I = \frac{k_m X_M^b + k_b X_{M,e}^I}{k_m + k_b} \tag{2-23}$$

Therefore,

$$R_{corr} = \frac{k_m k_b}{k_m + k_b}\left(X_{M,e}^I - X_M^b\right) = k'(X_{M,e}^I - X_M^b) \tag{2-24}$$

Where, k' is equal to $\frac{k_m k_b}{k_m + k_b}$.

In a static container, the relation of $X_{M,e}^I$ and X_M^b can be expressed as

$$V\rho\frac{dX_M^b}{dt} = AR_{corr} = Ak'(X_{M,e}^I - X_M^b) \tag{2-25}$$

Where, V is the volume of liquid, A is the surface of the metal.

Therefore,

$$X_M^b(t) = X_{M,e}^I\left[1 - exp\left(-\frac{Ak'}{V\rho}t\right)\right] \tag{2-26}$$

By combining Eq. 2-24 and 2-26, the relation of corrosion rate and time in a static container is obtaind as given in

$$R_{corr} = k'\left(X_{M,e}^{I} - X_{M}^{b}\right) = k'\left(X_{M,e}^{I} - X_{M}^{b}(t)\right) = k' X_{M,e}^{I} exp\left(-\frac{Ak'}{V\rho}t\right) \quad 2\text{-}27$$

Or,

$$R_{corr} = k' X_{M,e}^{I} exp\left(-\frac{Ak'}{V\rho}t\right) \quad 2\text{-}28$$

As shown in Eq. 2-28, R_{corr} is directly related to k', which is equal to $\frac{k_m k_b}{k_m + k_b}$.

$$k' = \frac{k_m k_b}{k_m + k_b} \quad 2\text{-}29$$

k_m can be calculated from D_{diff} as shown in 2-30, which is one of the measured kinetic data in Section 2.2.1 and 2.2.2.

$$k_m = \frac{\rho D_{diff}}{\delta} \quad 2\text{-}30$$

In addition, k_b is related to k^0, which is also one of the measured kinetic data in the experiments.

For a electrode made of metal M or an inert electrode, a modified Butler-Volmer equation which is applied in the insoluble-soluble reactions is given in Eq.2-32[146]. The relation between k_b and k^0 can be obtained from the equations as follows,

$$R_{corr} = \frac{i_{corr}}{nFA} Z = k_b (X_{M,e}^{I} - X_{M}^{I}) \quad 2\text{-}31$$

$$i_{corr} = i_0 \left\{ \frac{C_M^I}{C_M^b} exp\left[\frac{-\alpha nF}{RT}\left(E_{corr} - E_{eq}\right)\right] - exp\left[\frac{(1-\alpha)nF}{RT}\left(E_{corr} - E_{eq}\right)\right] \right\} \quad 2\text{-}32$$

$$i_0 = nFk^0 C_b^{M^{(1-\alpha)}}$$

Where Z is molar mass of the metal, C_M^b and C_M^I are the concentration of M^{n^+} in the bulk concentration and the interface, unit mol/cm^3.

Or,

$$i_{corr} = P \times nFk^0 C_M^{b\,(1-\alpha)} \quad 2\text{-}33$$

Where,

$$P = \frac{C_M^I}{C_M^b} exp\left[\frac{-\alpha nF}{RT}\left(E_{corr} - E_{eq}\right)\right] - exp\left[\frac{(1-\alpha)nF}{RT}\left(E_{corr} - E_{eq}\right)\right] \quad 2\text{-}34$$

Therefore,

$$R_{corr} = \frac{i_{corr}}{nFA} Z = k_b \left(X_{M,e}^I - X_M^I \right) = \frac{PZk^0 {C_M^b}^{(1-\alpha)}}{A} \quad 2\text{-}35$$

Or,

$$k_b = \frac{PZk^0 {C_M^b}^{(1-\alpha)}}{A\left(X_{M,e}^I - X_M^I \right)} \quad 2\text{-}36$$

Therefore, the relation between k_b and k^0 is obtained and k_b can be calculated using Eq. 2-36, which means that the corrosion rate can be predicted used Eq. 2-28 once the kinetic data D_{diff} and k_b are measured from the experiments. However, Eq. 2-28 is only applied in a static system. For a flow pipe, the corrosion rate prediction is much more complicated, as the liquid is flowing in the pipe, which makes X_M^b varying along the pipe. More studies are needed to build another comprehensive model to predict the corrosion rate in a flowing system.

2.3 Conclusions

Cyclic voltammetry, chronopotentiometry, and potentiodynamic techniques were applied to measure the fundamental kinetic property parameters of Fe^{2+}, Ni^{2+}, Cr^{2+}, Cr^{3+} and OH^- in the molten $MgCl_2$-KCl-NaCl and NaF-KF-UF_4-UF_3 salt. The experiments were conducted at different concentrations (1.53×10^{-6} to 7.48×10^{-4} mol cm^{-3}) and temperatures (600 to 800ºC) to explore the concentration and temperature dependence of each parameter.

In both molten chloride and fluoride salts, the measured diffusion coefficient D of Fe^{2+}, Ni^{2+}, Cr^{2+}, Cr^{3+} and OH^- were independent of concentration and followed the Arrhenius law. The D values obtained using CV and CP technique were consistent. Non-linear curve fitting technique was applied to determine the i_0, α, i_L and k^0 values of Fe^{2+}, Ni^{2+}, Cr^{2+}, Cr^{3+} and OH^-. i_0 and k^0 followed the Arrhenius law. And i_0 varied with concentration which demonstrated positive correlation. i_0 and k^0 of Cr^{2+} has the largest value followed by Fe^{2+}, Ni^{2+}, and Cr^{3+} at the same concentration and temperature. And the absolute values of i_L became larger as the temperature increased.

In molten $MgCl_2$-KCl-NaCl salts, a new method using ICP-MS analysis was developed to measure actual OH^- concentration. The C_{OH^-} value decreased from 4.11 to 2.84×10^{-6} mol cm^{-3} as the temperature increased from 600 to 800ºC. The measured D values descended in the order of $D_{OH^-} > D_{Cr^{2+}} > D_{Fe^{2+}} > D_{Ni^{2+}} > D_{Cr^{3+}}$. i_0 of Fe^{2+}, Ni^{2+}, Cr^{2+}, and Cr^{3+} were in the range from 8.13×10^{-4} (Cr^{3+}) to 2.80×10^{-1} A cm^{-2} (Cr^{2+}) within 600-800 ºC at a concentration of 1.5×10^{-4} mol cm^{-3}. The calculated charge transfer coefficient α remained consistent at different concentrations and temperatures, which were 0.62-0.88 for Fe^{2+}, Ni^{2+}, Cr^{2+}, Cr^{3+} (product-favored reaction), and 0.25-0.27 for OH^- (reactant-favored reaction). The magnitude of α represented the electrochemical reaction type: a smaller value close to 0 indicated a reactant-favored reaction, and larger value close to 1 meant a product-favored reaction. Moreover, diffusion coefficient thickness δ was estimated in the OH^- measurements, which was within a reasonable range of 0.05 – 0.1mm.

In molten NaF-KF-UF_4-UF_3 salts, Fe^{2+}, Cr^{2+} and Cr^{3+} were confirmed to coexist in the present study. And the measurements were conducted in a multicomponent system. In the diffusion coefficient measurements, only Cr^{2+}/Cr and Fe^{2+}/Fe peaks were identified in the curves. SD and CV method were applied and gave close values. $D_{\mathrm{Cr}^{2+}}$ was larger than $D_{\mathrm{Fe}^{2+}}$ at the same temperature. The measured $D_{Fe^{2+}}$ and $D_{Cr^{2+}}$ values in molten $MgCl_2$-NaCl-KCl salts were slightly larger than those obtained in molten NaF-KF-UF_4-UF_3 salts, because of higher density of molten NaF-KF-UF_4-UF_3 salts. For the measurements of i_0, α and i_{L}, an innovative method was used to eliminate the effect of the first reaction on the second reaction in the PD curves of Fe^{2+}, Cr^{2+} and Cr^{3+}. At the same temperature and concentration of Fe^{2+}, Cr^{2+} and Cr^{3+}, i_0 calculated in NaF-KF-UF_4-UF_3 salts tended to be smaller than that in $MgCl_2$-NaCl-KCl salts, which perhaps is due to the lower electrode reaction rate in molten NaF-KF-UF_4-UF_3 salts. α was calculated at different temperatures, with a value ranging from 0.23 to 0.32 for Fe^{2+} (reactant-favored reaction), 0.75-0.89 for Cr^{2+} and 0.74-0.91 for Cr^{3+} (product-favored reaction).

Moreover, a corrosion model was developed in the present study. It made the corrosion rate prediction of a static system possible by using the measured kinetic parameter data in the experiments, which would definitely provide further insight in the corrosion study of molten salts.

3 Corrosion Study of SS 316H and Alloy 617 in Molten Salts

Structural material corrosion has been a major concern in the application of molten salts. SS 316H and Alloy 617 are two good structural material candidates in MSRs. Related corrosion studies of these two materials have been conducted in molten $MgCl_2$-NaCl-KCl salts by B. D'Souza in our group[147]. In the present work, corrosion study of SS 316H and Alloy 617 were performed in the thermally-purified molten NaF-KF-UF_4-UF_3 salt (UF_4/UF_3 initial ratio 12~14) at 800 °C. Multiple experiments were designed to study the corrosion mechanism, which included the SS 316H and Alloy 617 corrosion tests for 120 hours to compare the corrosion resistance of these two materials, and the Alloy 617 corrosion tests for 72 hours and 32 hours to investigate corrosion development with time.

3.1 Experiment

In the corrosion study of SS 316H and Alloy 617, corrosion tests listed in Table 3-1 were conducted. For SS 316H, the test was repeated for three times (test 1001, 1002 and 1003), and three identical specimens were used in each test to check the data reliability. For Alloy 617, one test was performed for 120 hours, in which three specimens were used. The other tests were performed for 72 hours and 32 hours respectively, in which one specimen was used.

Table 3-1 Overview of performed corrosion tests in molten NaF-KF-UF_4-UF_3 salts

Alloy Type	Test ID	Test Duration (hours)	Specimen Qty.
SS 316H	1001	120	3
	1002		
	1003		
Alloy 617	2001	120	3
	S001	72	1
	S002	32	1

3.1.1 Material Preparation

3.1.1.1 SS 316H and Alloy 617

SS 316H and Alloy 617 plates were procured from Sandmeyer Steel Company and High Temp Metals, respectively. The chemical composition provided by the suppliers is listed in Table 3-2 (SS 316H) and Table 3-3 (Alloy 617). Specimens of these two materials were machined using Electrical Discharge Machining (EDM). All specimens used in the tests have a length (22 ± 0.2) mm × width (12 ± 0.2) mm × thickness (2 ± 0.1) mm, as shown in Figure 3-1. Before corrosion tests, each specimen was polished using different grades of SiC polishing paper ranging from grade 240 to 1200, then polished with 1 μm diamond paste. After polishing, specimens were

ultrasonically cleaned in deionized water to remove surface debris and contamination. The cleaned specimens were quickly transferred into a glovebox and sealed in a sample bag for future use. SEM analysis was conducted on the surface of each specimen to ensure that the surface of the specimens were well polished and no significant oxide layers were formed before tests. Mapping scans of one SS 316H and one Alloy 617 specimen surface are given in Figure 3-2. The cross section of one spare specimen for each material (SS316H and Alloy 617) was also checked using SEM, which was used as a reference to compare with the post-test specimen results. Figure 3-3 demonstrates mapping scans on the specimen cross-sections of SS 316H and Alloy 617.

Table 3-2 Chemical composition of SS 316H

Chemical Composition (wt. %)										
	C	Mn	P	S	Si	Cr	Ni	Mo	Others	Fe
Target Values	0.04-0.1	≤2	≤0.045	≤0.03	≤0.75	16-18	10-14	2-3	…	Bal.
Measured Values	0.048	1.446	0.033	0.0006	0.425	16.92	10.2	2.009	N: 0.0463 Cu: 0.341 Co: 0.217 Ti: 0.003 Nb: 0.007 P+S: 0.0336	Bal.

Table 3-3 Chemical composition of Alloy 617

Chemical Composition (wt. %)										
	Al	C	Co	Cr	Fe	Mo	Si	Ti	Others	Ni
Target Values	0.8-1.5	0.05-0.15	10-15	20-24	3.0	8-10	1.0	0.6	…	44.5 (min)
Measured Values	1.06	0.08	12.5	22.2	1.21	9.64	0.13	0.4	B: 0.003 P: 0.004 S: <0.002 Cu: 0.02 Mn: 0.04	52.61

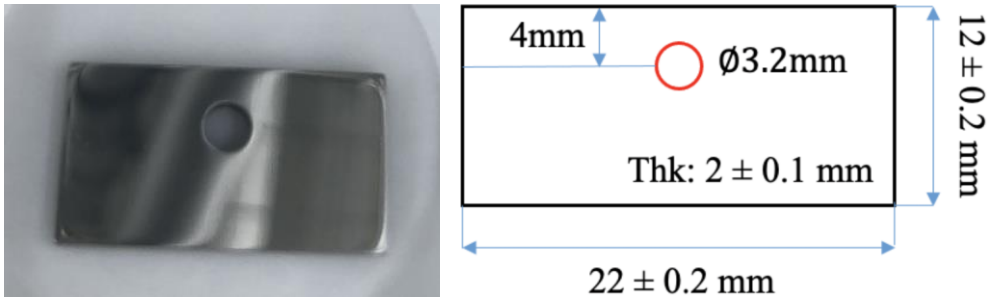

Figure 3-1 Specimen dimension used in the tests

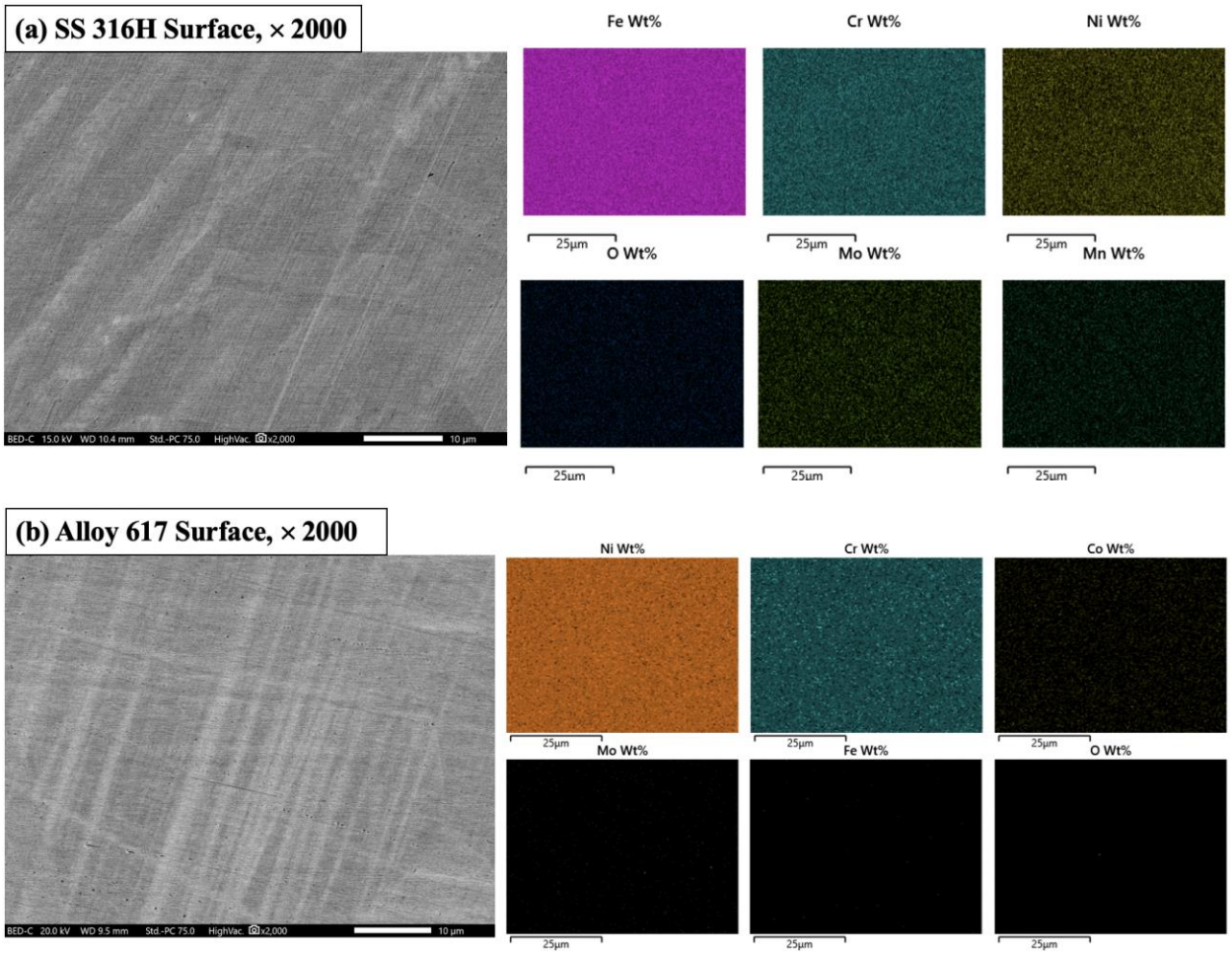

Figure 3-2 (a) Mapping scan on the surface of SS 316H; (b) Mapping scan on the surface of SS Alloy 617.

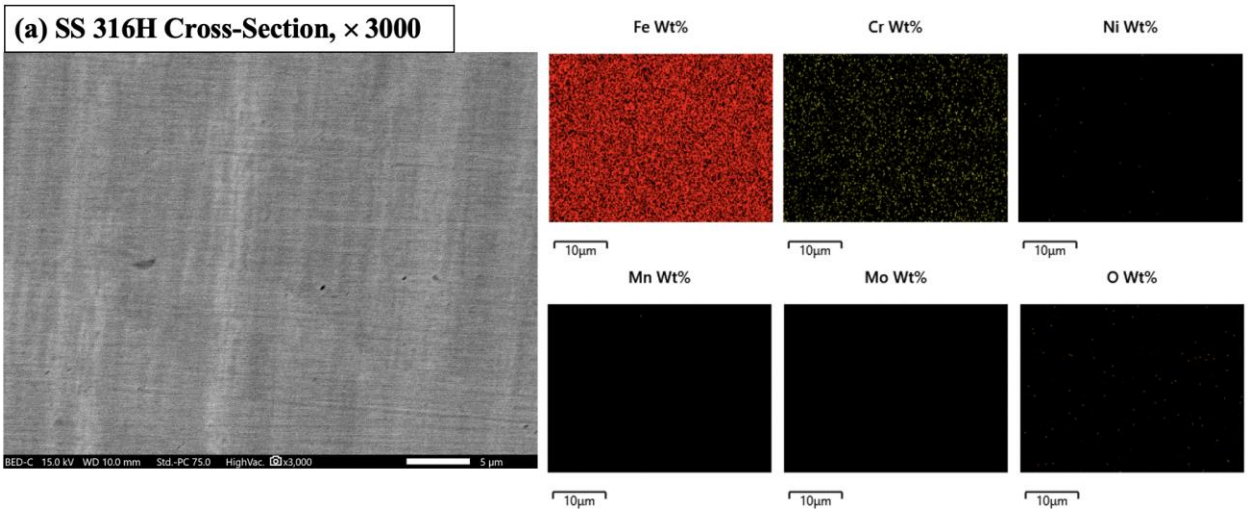

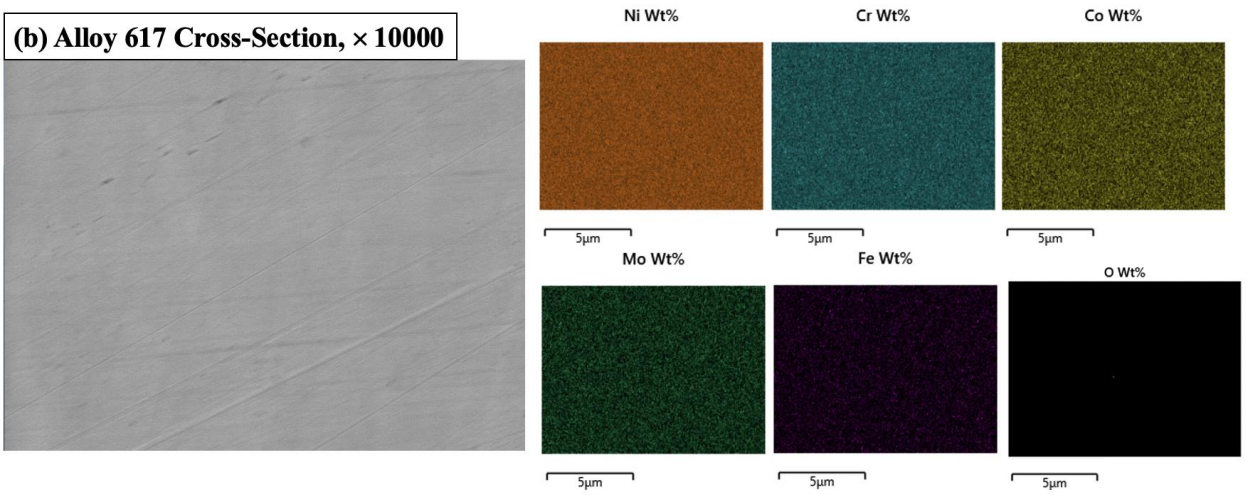

Figure 3-3 (a) Mapping scan on the cross-Section of SS 316H; (b) Mapping scan on the cross-section of Alloy 617.

3.1.1.2 NaF-KF-UF_4-UF_3 Salt Preparation

Before NaF-KF-UF_4-UF_3 salt fabrication, the purity check of NaF (Sigma Aldrich, 99%), KF (Sigma Aldrich, 99.5%), and UF_4 (Cameco, 85%) salt used in the tests were performed using Differential Scanning Calorimetry (DSC), ICP-MS, and XPS analysis, in which three salt samples were analyzed to ensure data reliability. DSC was used to measure the melting point and liquidus point of the salt. Before and after each sample analysis, aluminum powder (or wire, Sigma Aldrich, 99.999%) was used to verify the instrument condition, and the measured melting point of aluminum must be within 660.3 ± 5 ^{o}C. Otherwise, an instrument calibration was conducted. In the ICP-MS analysis, metal-based specie concentrations were obtained. To prepare ICP-MS samples, less than 10 mg salt samples were collected and dissolved into 20 ml 1M HNO_3 solution, which were placed on a shaking table for at least 12 hours to ensure all solid salt samples were dissolved. Before the analysis, the sample solution was diluted within 10 ppm. The recovery rate of ICP-MS instrument must be within 90% - 110 % at the end of analysis, otherwise, the data was invalidated. XPS analysis can give both metal and non-metal-based species concentration in the samples. In this study, XPS analysis was mainly used to measure the oxygen concentration in the samples through survey (SV) scans, and the UF_4/UF_3 ratio in the NaF-KF-UF_4-UF_3 salt through high resolution (HR) scans. Before analyzing samples, graphite and silicon dioxide were analyzed by SV and HR scans to ensure the instrument was in a good condition. HR scan data was fitted using MultiPak software[148]. Based on the NIST XPS database[149], UF_4, UF_3, UO_2 and K 2s (2s orbital of potassium) were included as shown in Figure 3-4. The UF_4/UF_3 ratio was calculated from the peak area ratio of UF_4 and UF_3. The fitting process were repeated three times, from which an average ratio was calculated to ensure data reliability. Detailed purity check analysis results of NaF, KF and UF_4 are given in Table 3-4.

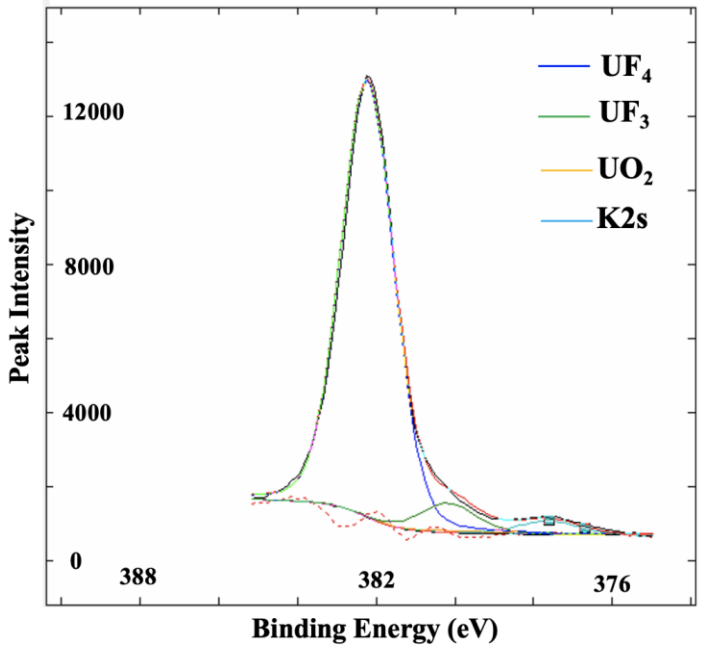

Figure 3-4 UF_4/UF_3 ratio fitting from the HR scan using XPS

NaF, KF and UF_4 were thermally purified separately before mixing together. An 80-mesh sieve was used to removed black clumps (UO_2) that may have been formed during fabrication, transportation and/or storage in UF_4. NaF, KF and UF_4 were mixed in a glassy carbon crucible and thermal purified in a glovebox following the temperature profile given in Table 2-1 to remove residual moisture in the salts. If black UO_2 precipitates were produced on the bottom of the glassy carbon crucible during the process, they were removed using a hammer after the salts cool down in a glovebox. The composition of the residual salts was adjusted accordingly to the target ranges. Finally, U metal, which was cleaned using diluted nitric acid solution to remove black uranium oxide on the surface, was added into the ternary salt at 750°C to produce UF_3 through the reaction of $U + 3UF_4 = 4UF_3$. The amount of U metal needed was calculated accordingly based on the target UF_4/UF_3 ratio, and the UF_4/UF_3 ratio was checked using XPS as shown in Figure 3-4. The measured UF_4/UF_3 ratio matched well with the target value after U metal was added as given in Table 3-5, which confirmed the quaternary salt fabrication method.

Table 3-4 Purity check results from ICP-MS and XPS analysis

Salt	Purity		Major Impurities	
	COA	ICP-MS (Metal basis, wt. %)	ICP-MS (Metal basis)	XPS
NaF	≥ 99%	99.12	S	I, K, C
KF	≥ 99.5%	99.11	Na, Al	C, O, Si, Na
UF_4	≥ 85%	99.7	Mg, Al, Ca	C, O

Table 3-5 UF_4/UF_3 Ratio check in pre-test NaF-KF-UF_4-UF_3 salts

Test ID	UF_4/UF_3 Ratio	
	Theoretical Value	Actual Value
1001	13.21	12.34 ± 1.23
1002		12.66 ± 2.53
1003		12.98 ± 1.25
2001		12.68 ± 1.28
S001		12.73 ± 2.67
S002		12.84 ± 1.18

3.1.2 Experimental Setup

In the corrosion tests, specimens were immersed in molten NaF-KF-UF_4-UF_3 salts and heated at 800 °C. For the 120-hour corrosion tests (test 1001, 1002, 1003 and 2001), ICP-MS and XPS salt samples were only collected before and after tests. The applied test setup is shown Figure 3-5. The whole test system was heated in a muffle furnace. A glassy carbon crucible was used as a salt container and a nickel crucible was used as a safety crucible. Ni wire was used to fixate the specimens to a Ni lid and hang the specimens in the salt. A boron nitride tube was applied to prevent galvanic corrosion between the specimen and Ni lid. For the two Alloy 617 tests that lasted for 72 and 32 hours, ICP-MS salt samples were collected periodically during tests by following the schedules shown in Table 3-6. Another test setup without a lid as shown in Figure 3-6 was used, which was more practical when it came to the salt sample collection at 800 ^{o}C.

At the end of each test, the specimens were removed from the furnace, and naturally cooled down to room temperature. Inductive coupled plasma mass spectroscopy analysis (ICP-MS) was applied

to measure the concentration of corrosion products such as Fe, Cr, Ni species, which was used to determine the weight change of specimens; thus, corrosion rate can be estimated accordingly. Scanning electron microscope (SEM) analysis was performed to study the corrosion behavior and attack depth. X-ray photoelectron spectroscopy (XPS) analysis was performed to check the UF_4/UF_3 ratio change before and after the tests.

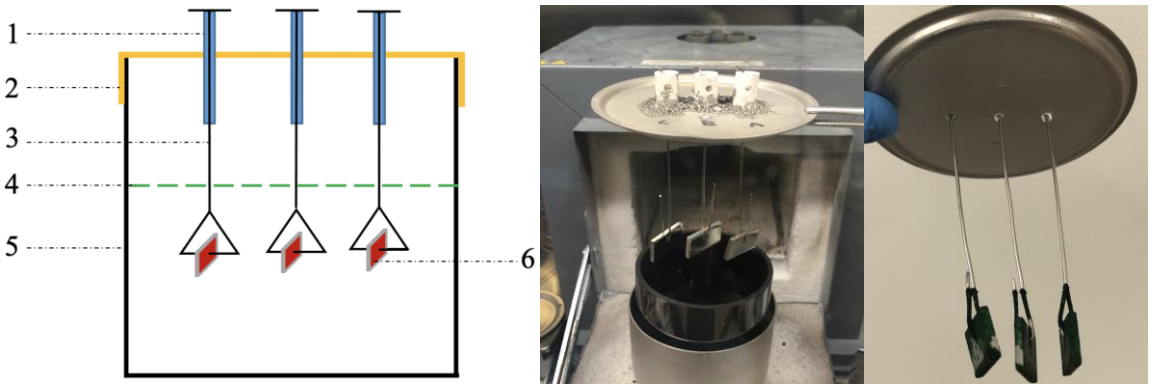

Figure 3-5 Static corrosion test Setup. 1: Boron nitride tube, 2: Nickel lid, 3. Nickel wire, 4: Molten salt liquid level, 5: Glassy carbon crucible, 6: Specimen.

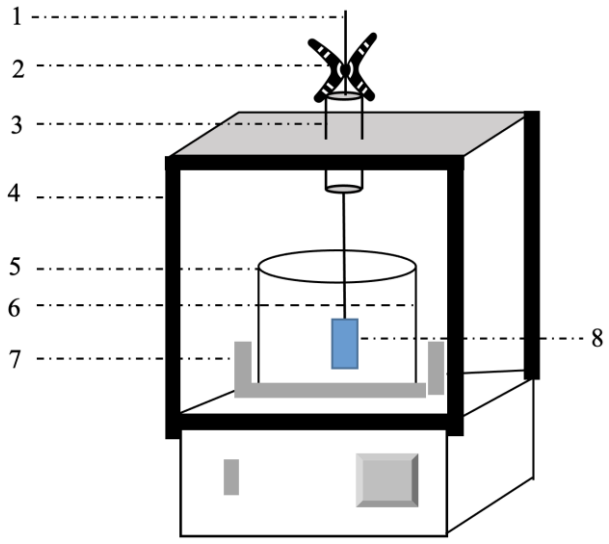

Figure 3-6 Alloy 617 corroison test setup: 1. Ni wire 2. Clip 3. Quartz tube 4. Furnace 5. Glassy carbon crucible 6. Liquid salt level 7. Nickel safety crucible 8. Alloy 617

Table 3-6 Salt samples collection schedule of test S001 and test S002

Test S001	Test S002
0 min	0 min
25 min	25 min
50 min	50 min
75 min	75 min
100 min	100 min
3 hours	140 min
7 hours	3 hours
10 hours	5 hours
14 hours	7 hours
24 hours	8.5 hours
32 hours	10 hours
44 hours	12 hours
56 hours	14 hours
72 hours	19 hours
/	24 hours
/	30 hours
/	32 hours

3.2 Results and Discussions

3.2.1 SS 316H Corrosion Study (120 hours)

3.2.1.1 Post-Test Salt Analysis

The post-test salts were broken into small pieces after cooling down in the glovebox, and their cross-section images are shown in Figure 3-7. This figure shows that more black uranium oxide precipitates (indicated by red arrow) were produced on the bottom of the salt in test 1001 and 1002 than in test 1003. There was no significant precipitate accumulation in test 1003. In test 1003, UF_4 was filtered using 80-mesh sieve to remove the majority of UO_2. However, the filtering procedure using an 80-mesh sieve was not applied in test 1001 and 1002, since we had not realized that the clumps in the salt could be a major issue in the early stage of salt fabrication as mentioned before.

Therefore, more oxides were introduced into the salt mixture, and precipitated onto the bottom of the salt during test 1001 and 1002.

Metal species, i.e., Fe, Cr and Mn, in addition to the salt matrix Na, K and U were identified in the post-test salt samples using ICP-MS. It indicates that Fe, Cr, and Mn are the major corrosion products. The measured concentration of metal species in the salts before and after corrosion are summarized in Table 3-7. Overall, the metal specie concentration of corrosion products descended in the order of C_{Fe}>C_{Cr}>C_{Mn} for all the three tests. The measured concentrations of Fe, Cr and Mn were similar in test 1001 and 1002, which were slightly higher than those for test 1003. This was due to the higher concentration of oxides in test 1001 and 1002, as previously discussed, which lead to salts becoming more corrosive[150].

XPS analysis was conducted to check the UF_4/UF_3 ratio in the post-test salt after the corrosion tests. The measured UF_4/UF_3 ratio in the three tests were summarized in Table 3-8. The measured values were consistent for all three tests. In this study, the UF_4/UF_3 ratio increased after corrosion tests, due to the presence of corrosive impurities, such as HF, which can oxidize UF_3 in the salts. The equilibrium reaction between UF_3 and corrosion products could happen in molten salts as well, which was expressed as CrF_2 (FeF_2) + UF_3 ⇌ Cr (Fe) + UF_4, T = 800 ℃, ΔG < 0. Some UF_3 was continuously consumed through the reaction with corrosion products CrF_2 or FeF_2 until reaching equilibrium, thus, resulting in the increasing of the UF_4/UF_3 ratio.

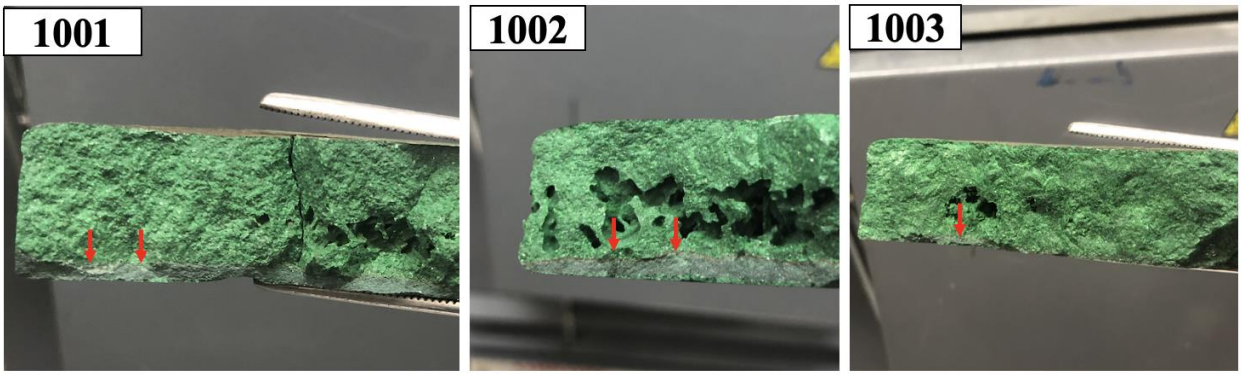

Figure 3-7 Cross-section of post-test salt

Table 3-7 Metal specie concentration in SS 316H-post-test salts measured using ICP-MS

Test ID			Cr	Mn	Fe
			mol %		
1001	Pre-Test	Avg.	0	0	0.012
		Std. Dev.	0	0	0.001
	Post-Test	Avg.	0.232	0.019	0.312
		Std. Dev.	0.001	0	0.007
1002	Pre-Test	Avg.	0	0	0.002
		Std. Dev.	0	0	0
	Post-Test	Avg.	0.267	0.021	0.443
		Std. Dev.	0.001	0	0.017
1003	Pre-Test	Avg.	0	0	0
		Std. Dev.	0	0	0
	Post-Test	Avg.	0.175	0.010	0.198
		Std. Dev.	0.001	0.001	0.009

Table 3-8 Measured UF_4/UF_3 ratio of SS 316H-post-test salt using XPS

Test ID	Post-Test-UF_4/UF_3 Ratio	
	Avg.	Std. Dev.
1001	47.16	4.04
1002	51.30	2.68
1003	46.62	4.11

3.2.1.2 Post-Test Specimen Analysis

At the end of the corrosion tests, specimens were removed from the molten salts. The post-test specimens are shown in Figure 3-8. The salt on the Ni wire indicated the original molten salt level at 800°C and there was no significant wicking phenomenon. In addition, salts were observed to adhere to the surface of specimens, which was difficult to remove. It meant that the weight change

of specimens between the pre-test and post-test can't be measured directly using a digital balance. Therefore, a new method was developed for the weight change measurement of specimens. In the present study, weight change was calculated using ICP-MS analysis results, since the metal specie concentration of corrosion products, such as Fe, Cr, and Mn, were measured as described in Section 3.2.1.1. It should be noted that the weight change was obtained without considering the possible reduction of corrosion products by UF_3 as discussed in Section 3.2.1.1. The corrosion rate was estimated using equation $CR_{Avg} = \frac{\Delta m}{At}$, where CR_{Avg} is the estimated average corrosion rate with a unit of $mg/cm^2 \cdot hour$, Δm is weight loss with a unit of mg and t is test time with a unit of $hours$. The calculated corrosion rate for SS 316H is given in Table 3-9. These values were consistent over the three tests with the corrosion rates of test 1001 and 1002 being slightly larger than that of test 1003. Corrosion in the molten salts is known to be mainly impurity driven. The fabricated salts in these two tests have more oxide impurities, thus, leading to more severe corrosion and producing more corrosion products compared with test 1003.

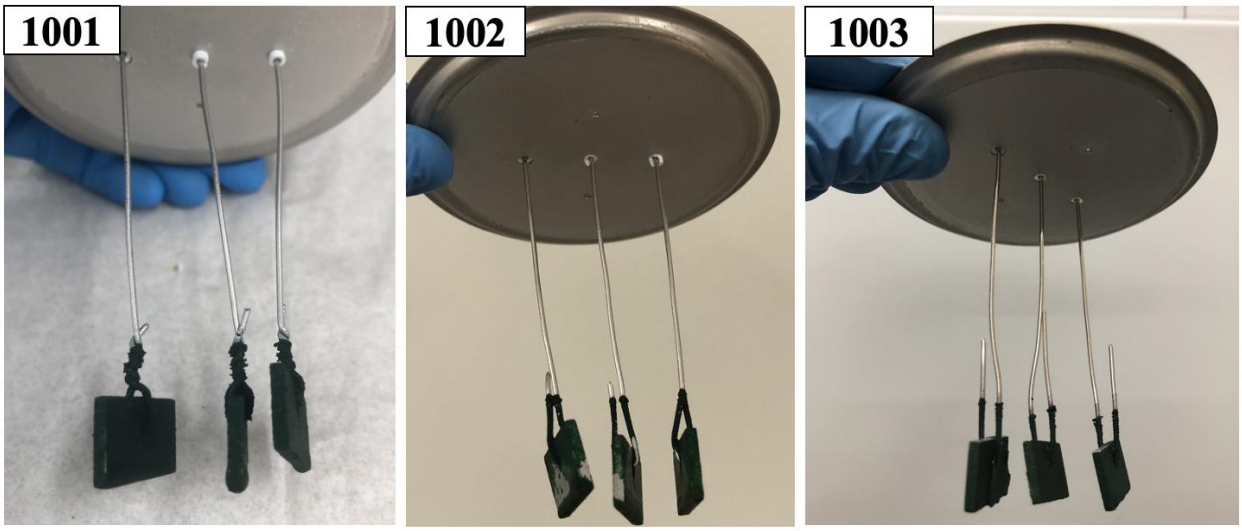

Figure 3-8 SS 316H-post-test-specimen overview

Table 3-9 Estimated corrosion rate of SS 316H in molten NaF-KF-UF_4-UF_3 salt

Test ID	Corrosion Rate ($mg/cm^2 \cdot hour$)
1001	33.66
1002	43.47
1003	22.49

SEM analyses were conducted on specimens to study corrosion behavior of SS 316H in molten NaF-KF-UF_4-UF_3 salt. The SEM analyses were conducted on the cross section of post-test specimen because the surface of the specimens was covered with salts. An overview of an SS 316H post-test specimen from Test 1003 is given in Figure 3-9. The whole specimen can be divided into

three parts: (1) salts on the surface, where bright particles were observed; (2) corroded area, where salts have been penetrated into the specimen through GBs, and black spots were observed along GBs; and (3) uncorroded area. To further understand the observed phenomenon, point, line and mapping scans were conducted accordingly in the three different areas.

Table 3-10 summarizes the point scan results of bright particles in salts on the specimen surface, which turned out to be uranium oxide. As for the corroded area, the attack depth and maximum attack depth of each specimen in tests were estimated using SEM. The thickness of specimens was measured using a caliper in the pre-tests and by SEM in the post-tests. The measured values are given in Table 3-11. The measured attack depth in the three tests was consistent. In test 1001 and 1002, the values were slightly larger than in test 1003, due to the higher impurity concentration as previously discussed. In the corroded area, mapping scans were conducted as given in Figure 3-10. Cr depletion was observed at GBs, due to the fact that Cr was the most easily attacked element compared with Fe and Ni. In addition, Cr enrichment was observed in specific areas in the mapping scan of Cr element, which matched with the study by Dai et al[77]. It has confirmed that the Cr enrichment was attributable to the low energy nature of low-Σ coincidence site lattice boundaries, primarily Σ_3 type GBs. Cr, O and Mn concentrations were enriched in the black spots observed along GBs as shown in Figure 3-10. SEM line scan was conducted as given in Figure 3-11. In the line scan, Cr, O and Mn counts increased in black spots, which validated that they were Cr/Mn oxides. The oxygen may come from the oxides that existed in the pre-test salt, or the oxygen in the glovebox, even though the oxygen level in the glovebox was maintained at less than 20 ppm during tests. Nevertheless, as for the black spot 3 shown in Figure 3-11, the C count has increased significantly, indicating that there are some carbides as well. Furthermore, many bright lines were observed as indicated by the red arrows in the SEM image (Figure 3-10). Based on the mapping scan result of the Mo element in Figure 3-10 , those bright lines were Mo-enriched phases. A line scan was conducted as well and is shown in Figure 3-12. Only the Mo count showed a significant increasing trend when the scan went across the bright line. Therefore, Mo enrichment occurred in the areas where bright spots were located, indicating Mo segregation. The driving force of Mo segregation is its lower partition coefficient compared with other elements such as Fe, Ni, and Mn[151,152,153]. Moreover, in both the corroded and uncorroded areas, GBs became visible after corrosion tests as shown in Figure 3-13 and Figure 3-14, respectively. In the uncorroded area, Cr/Mn carbides were confirmed to be produced at GBs by line scans due to heat treatment, which has been investigated in the study by Bandyopadhuay et al[154] and Bhuyan et al[155]. It's also believed that Cr/Mo-enriched carbides formed at the GBs was an extra driving force to Cr-depletion[86,156].

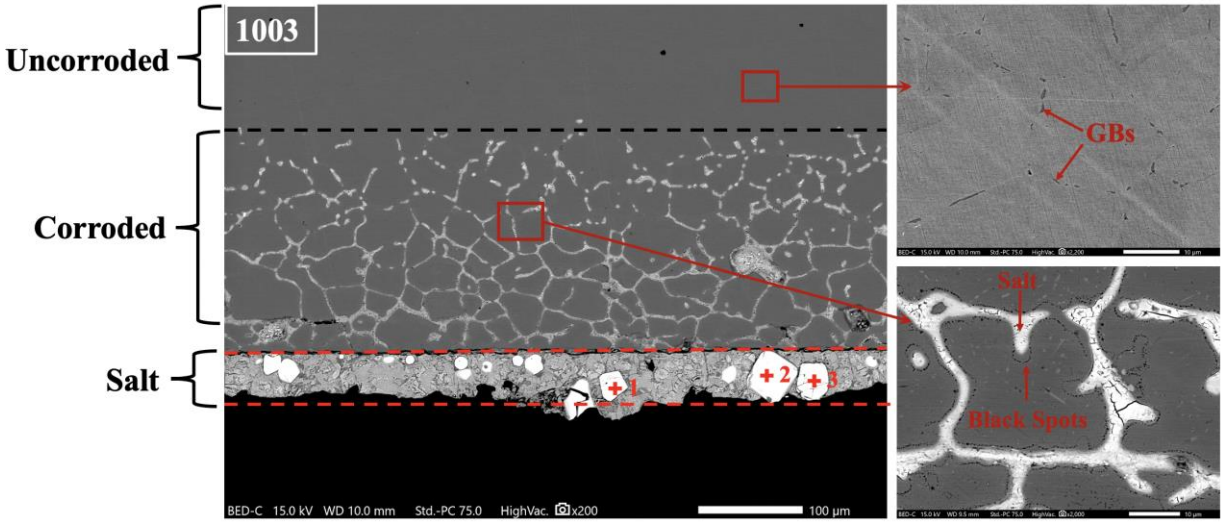

Figure 3-9 SEM image of 1003-post-test SS 316H specimen, Mag 200×

Table 3-10 SEM point scan on bright particles in salts, Mag 200×

Point	U (at. %)	O (at. %)
1	30.61	69.39
2	27.77	72.23
3	25.49	74.51
Avg (at. %)	27.96	72.04
Std. Dev. (at. %)	2.57	2.57

Table 3-11 Specimen attack depth in test 1001, 1002, 1003

SS 316H		Pre-Test		Post-Test				
		Thickness (Caliper) (mm)		Thickness (SEM) (mm)		Attack Depth (μm)		Max. Attack Depth (μm)
		Avg.	Std. Dev.	Avg.	Std. Dev.	Avg.	Std. Dev.	
1001	A	2.00	0.0058	2.0018	0.0053	264.50	31.15	405.90
	B	2.01	0.0058	2.0084	0.0067	279.83	20.42	388.70
	C	1.97	0.0058	1.9335	0.0067	284.70	61.33	504.10
1002	A	2.01	0.0058	2.0189	0.0089	292.31	35.03	375.70
	B	2.02	0.0058	2.0203	0.0094	296.70	58.70	367.90
	C	1.95	0.0000	1.9338	0.0121	294.40	50.79	491.50
1003	A	2.04	0.0058	2.0335	0.0096	225.50	41.30	498.80
	B	2.02	0.0058	2.0109	0.0168	228.62	40.37	398.40
	C	2.08	0.0058	2.0713	0.0108	235.52	29.28	385.40

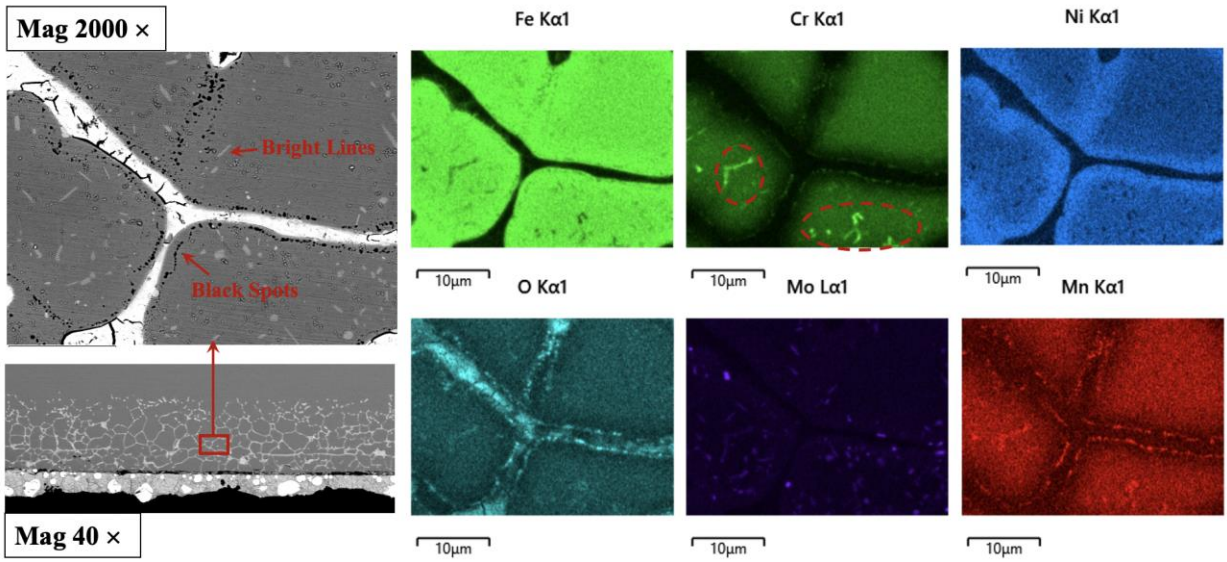

Figure 3-10 Mapping scan of corroded area of 1003-post-test SS 316H specimen, Mag 2000×

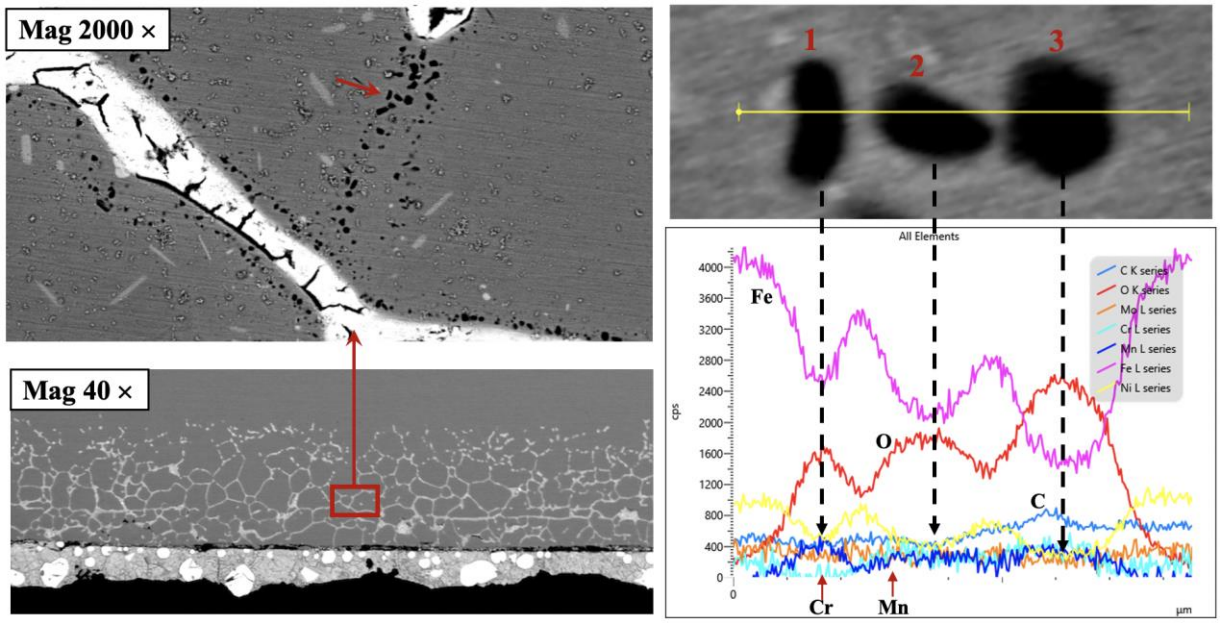

Figure 3-11 Line scan of black spots on the 1003-post-test SS 316H specimen, Mag 2000×

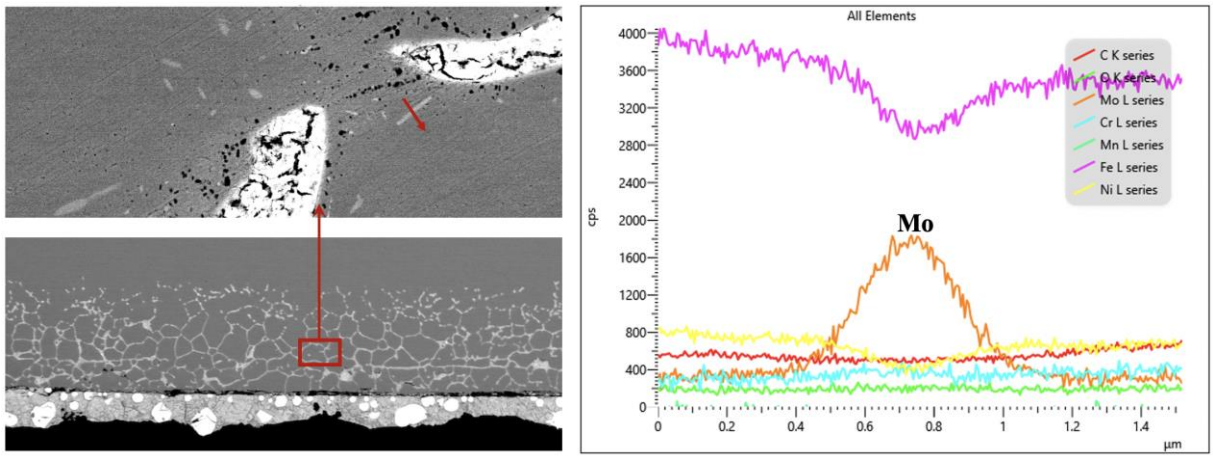

Figure 3-12 Line scan of bright line on the 1003-post-test SS 316H specimen, Mag 2000×

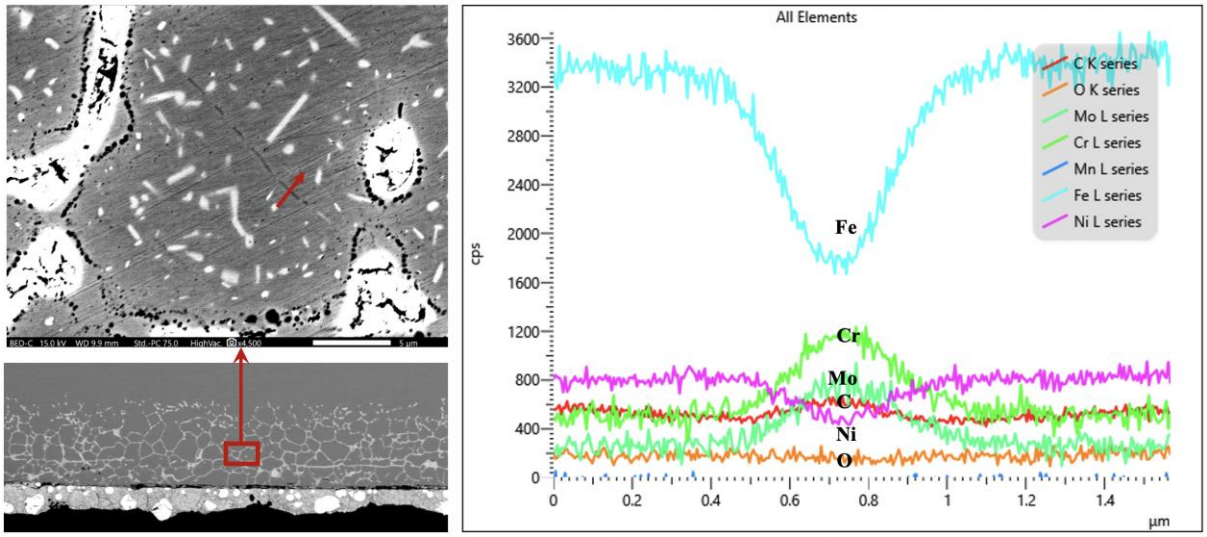

Figure 3-13 Line scan of GB of corroded area on the 1003-post-test SS 316H specimen, Mag 4500×

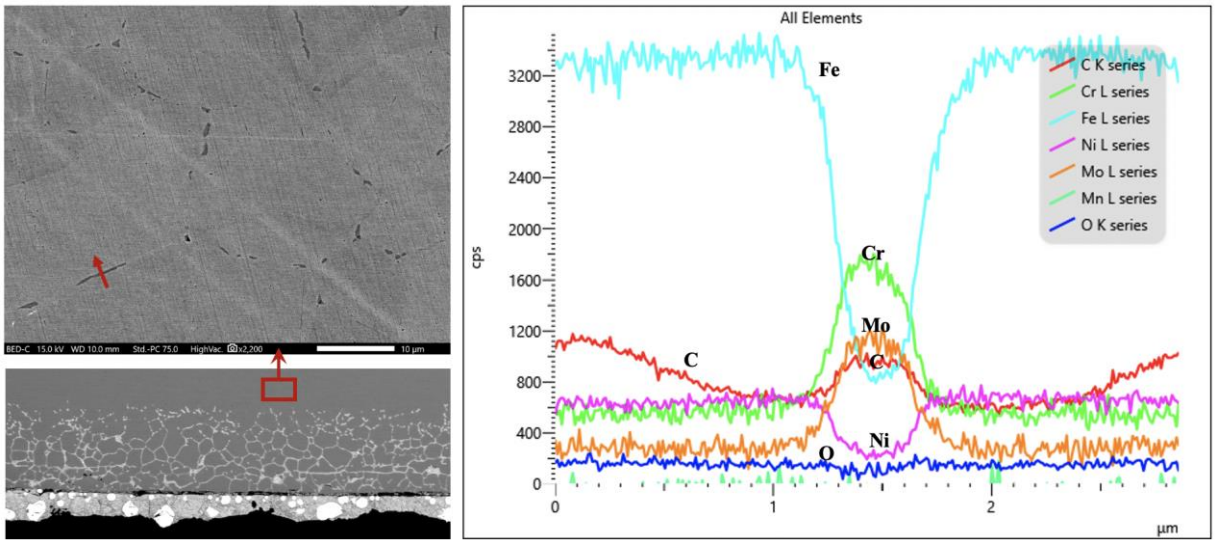

Figure 3-14 Line scan of GB of uncorroded area on the 1003-post-test SS 316H specimen, Mag 2200×

3.2.2 Alloy 617 Corrosion Study (120 hours)

3.2.2.1 Post-Test Salt Analysis

After the corrosion test, the post-test salt in test 2001 was cooled down to room temperature in the glovebox. The outside surface and cross-section of the salt are shown as given in Figure 3-15. Silver material was found to be deposited on the outside surface of salt (Figure 3-15 (a)), and there was no obvious black uranium oxides precipitated on the bottom of the salt (Figure 3-15 (b)), which was similar to that in Test 1003. SEM point scans were conducted to identify the silver material and the results are listed in Table 3-12. It was found that the silver material was Mo-

enriched; in other words, Mo was deposited in the salt during the corrosion test. Before discussing the Mo formation mechanism in the salts, it was necessary to study the major corrosion products of Alloy 617. Corrosion product metals species, i.e., Cr, Co, and Ni, were identified in the salt samples as given in Table 3-13. The measured concentrations of Cr, Co and Ni were in the order of C_{Cr}>C_{Ni}>C_{Co}. Once CrF_2 presented in the salt, the disproportionation reaction $3CrF_2 \rightleftharpoons 2CrF_3 + Cr$ may happen. After that, the chemical reactions between Cr and corrosion products of Mo in the salt occurred, which led to the deposition of Mo[157,158,159,160]. It explained how the Mo-enriched material formed at the interface between the salts and the glassy carbon crucible, where the nucleation of Mo happened. As a result of Mo deposition, the corrosion rate of Alloy 617 was not estimated in the test. XPS analysis was performed to determine the UF_4/UF_3 ratio in the post test salts. Similar to what was discussed in Section 3.2.1.1, the ratio increased from 12.68 ± 1.28 to 47.57 ± 3.86 after the corrosion tests since the majority of U^{3+} has been oxidized to U^{4+} by corrosive impurities, such as HF and moisture, or corrosion products, such as CrF_2 or FeF_2.

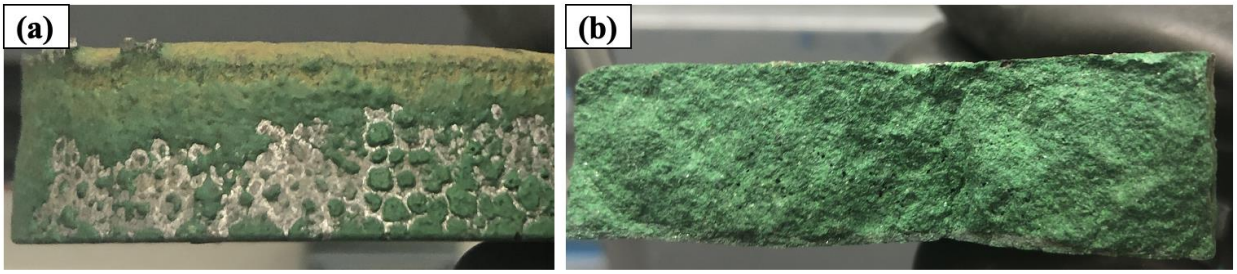

Figure 3-15 Outside surface and cross-section of post-test salt in test 2001

Table 3-12 Point scans of silver material in test 2001

Test	Point	Mo	Ni	Co	Fe
		wt %			
2001	1	73.1	18.2	6.4	2.4
	2	87.4	8.7	2.6	1.3
	3	63.2	24.0	9.0	3.8
	Avg.	74.6	16.9	6.0	2.5
	Std. Dev.	12.2	7.7	3.2	1.3

Table 3-13 Metal species concentration in the post-test salt of test 2001

Test ID			Cr	Co	Ni
			mol %		
2001	Pre-Test	Avg.	0	0	0
		Std. Dev.	0	0	0
	Post-Test	Avg.	0.260	0.003	0.057
		Std. Dev.	0.011	0.002	0.007

3.2.2.2 Post-Test Specimen Analysis

An overview of the Alloy 617 post-test specimens is given in Figure 3-16. Salts were observed on the surface of specimens and there was no obvious wicking phenomenon during the test. Some black material was found on the surface of the Ni lid, but the quantity of black material was extremely small, making it impossible to do further analyses to identify its composition. Considering the fact that no such material was observed on the Ni wire used to hang specimens, it is believed that this black material may be formed due to long-term heating at 800°C in the tests, since the Ni lid has been reused in four static corrosion tests.

An SEM image of the 2001-post-test specimen is shown in Figure 3-17. Similar to the 316H post-test specimens, salts penetrated into specimens in the corroded areas, and GBs became visible in the uncorroded areas after the corrosion test. A new phenomenon was also observed in the corroded area, where there were two significant different parts, i.e., the 1st and 2nd part, as shown in Figure 3-17. To understand the corrosion behavior of Alloy 617, the thicknesses of the pre-test and post-test specimens were measured using a caliper and SEM analysis, respectively. The results are given in Table 3-14, which indicates there is no significant thickness change in the pre-test and post-test specimens. The attack depth and maximum attack depth in the 1st and 2nd part were measured using SEM, as listed in Table 3-15. The measured attack depth and maximum attack depth of three specimens were consistent with one another in the test. SEM-EDS mapping and line scans were conducted to study the corrosion behavior in both the 1st and 2nd part. As demonstrated in Figure 3-5, the mapping scan results indicated that Cr had been almost completely depleted during the test in the 1st part. To further confirm this conclusion, four point scans were performed as well, and the result are summarized in Table 3-16. The measured average Cr concentration was 0.1 wt. %, confirming that almost all Cr was depleted in the 1st part, which matched well with the mapping scan result. A line scan, which started in the 2nd part and ended in the 1st part was performed as given in Figure 3-19. It's observed that Cr concentration became close to 0 once in the 1st part, which further confirmed the conclusion of complete Cr-depletion.

As for the 2nd part, a mapping scan was conducted as shown in, and Cr was partially depleted, similar to the SS316H specimens. In addition, Mo enrichment was observed at GBs in the mapping

scan. The line scan, as given in Figure 3-21, further confirmed this conclusion, since the Mo wt. % sharply increased and the Cr wt. % sharply decreased when crossing the GB. The Mo enrichment was due to Mo's lower partition coefficient, as discussed in Section 0. A black line-shaped material was observed in the metal matrix of the 2nd part, which was not observed in the SS 316H specimens. The line scan result, shown in Figure 3-22, indicates that the material is Cr/Mo-carbide, which were formed during the corrosion tests due to the heat treatment. Cr and Mo were found to be enriched and segregated at GBs in the uncorroded area as shown in Figure 3-23. The segregated Cr/Mo did not combine with C to form carbides at GBs in the Alloy 617 specimens, which was different from that of the SS 316H specimens. In the SS 316H specimens, Mo/Cr carbides were observed at GBs in the uncorroded area. The different phenomenon resulted from the different concentrations of C, Mo, and Cr in SS 316H and Alloy 617, which made the carbides formation at the GBs in Alloy 617 unfavorable. Thus, a lower driving force for Cr-depletion was presented in Alloy 617, and the attack depth was much smaller compared to that of in SS 316H, as discussed in 0. Moreover, the identified Mo/Cr carbides at GBs in the uncorroded area of the Alloy 617 specimens, have been present in the pre-test specimens before the corrosion tests, as shown in Figure 3-24, where the bright area has more Mo-carbides, and the dark area has more Cr-carbides[161].

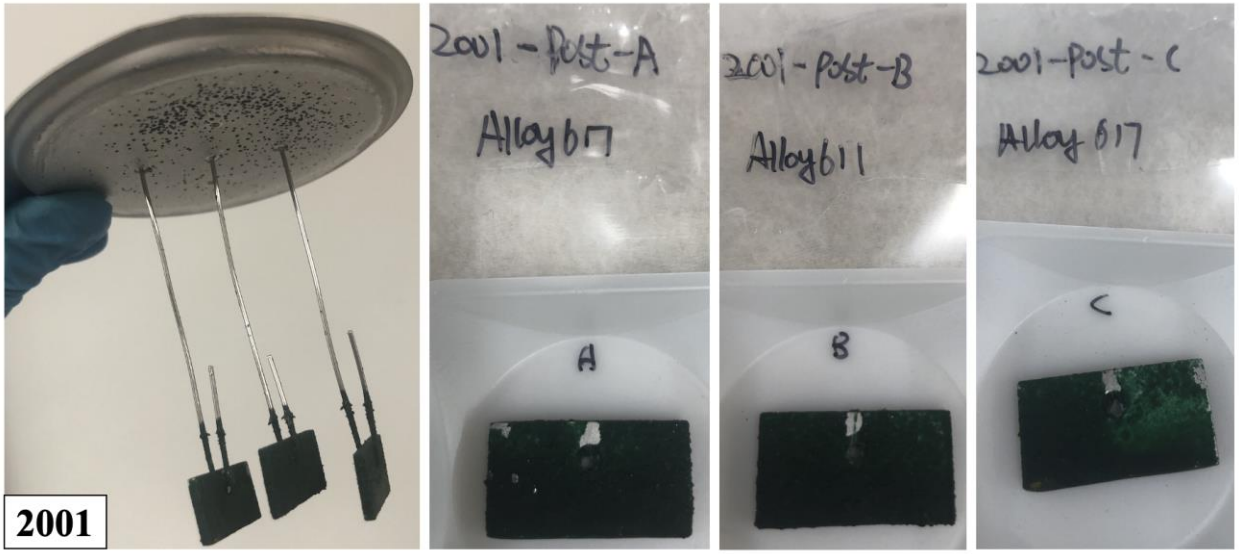

Figure 3-16 Overview of Alloy 617 post-test specimens in test 2001

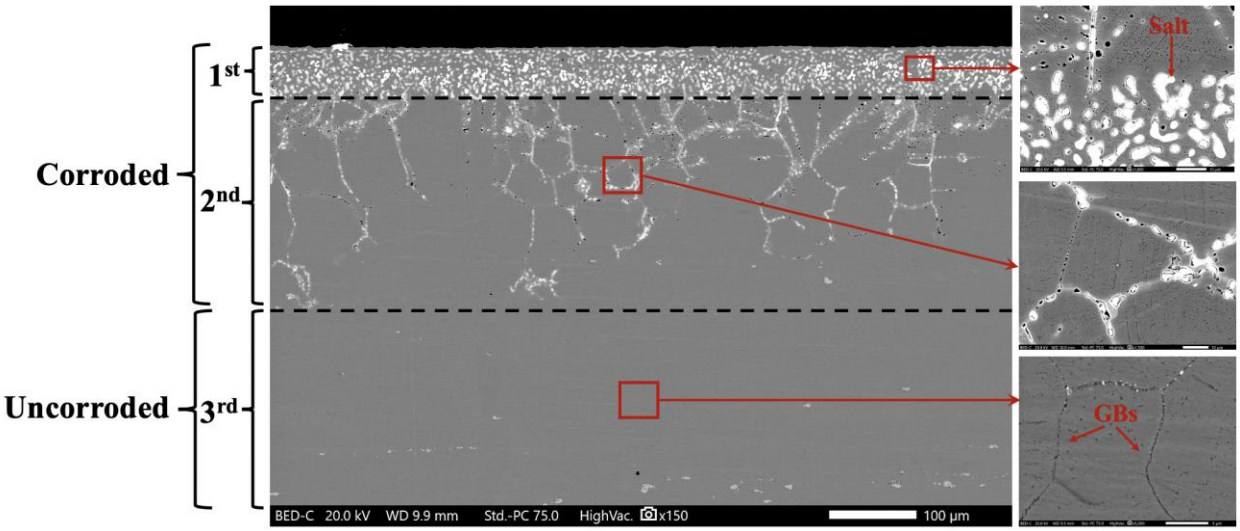

Figure 3-17 SEM image of 2001-post-test specimen cross-section

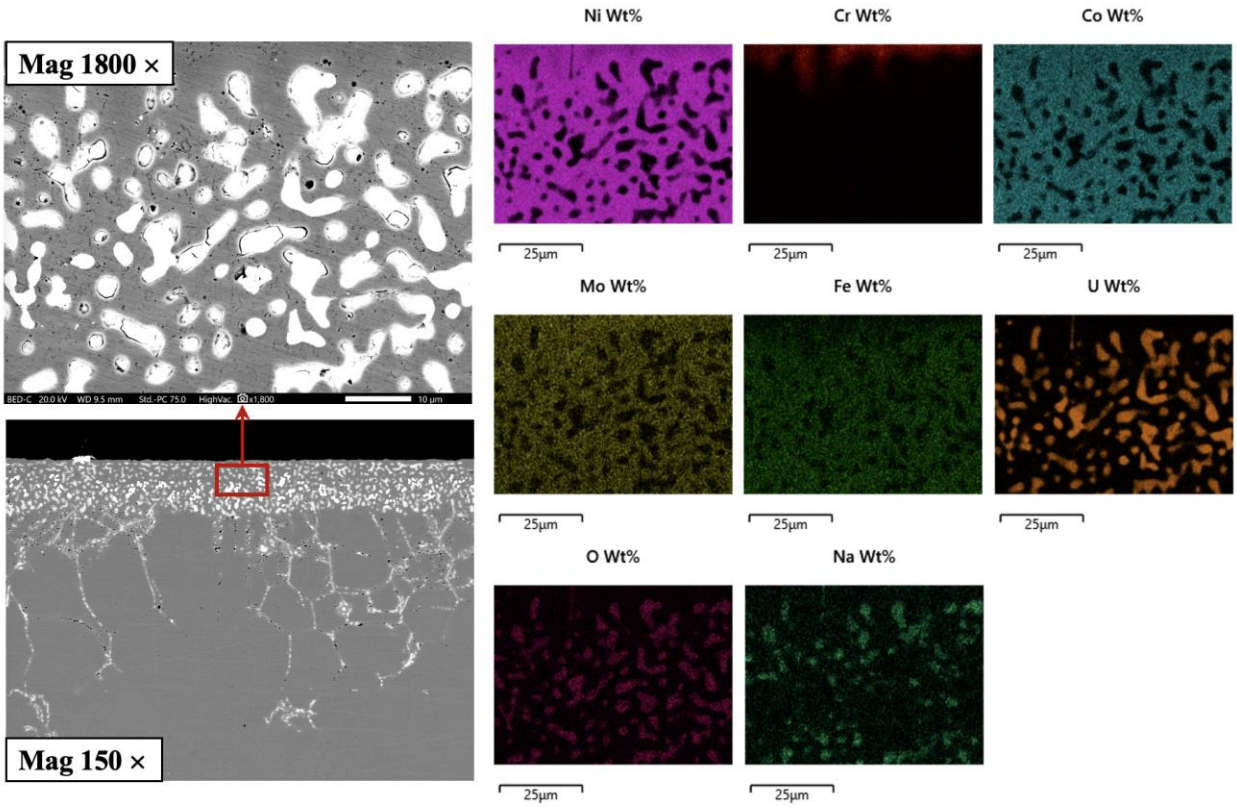

Figure 3-18 SEM mapping scan of 1st part on the 2001-post-test specimen cross-section

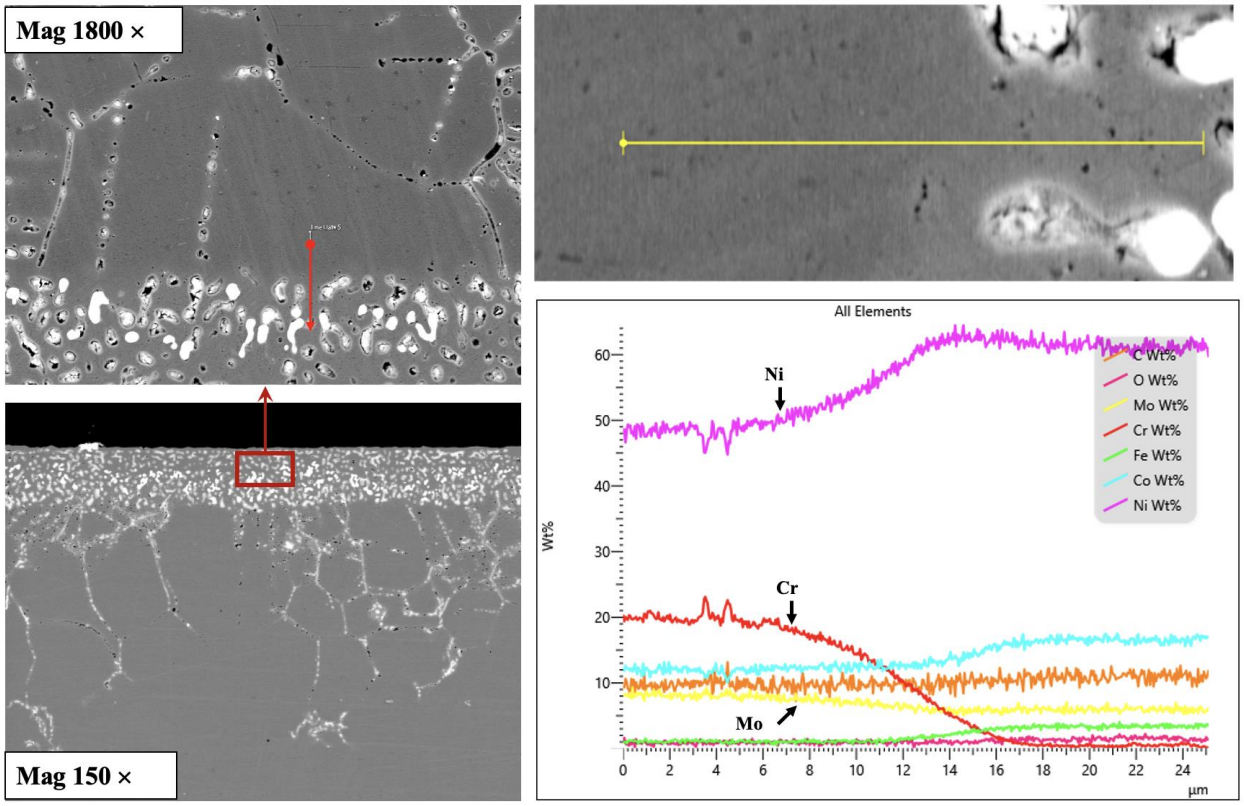

Figure 3-19 SEM line scan of 1st part on the 2001-post-test specimen cross-section

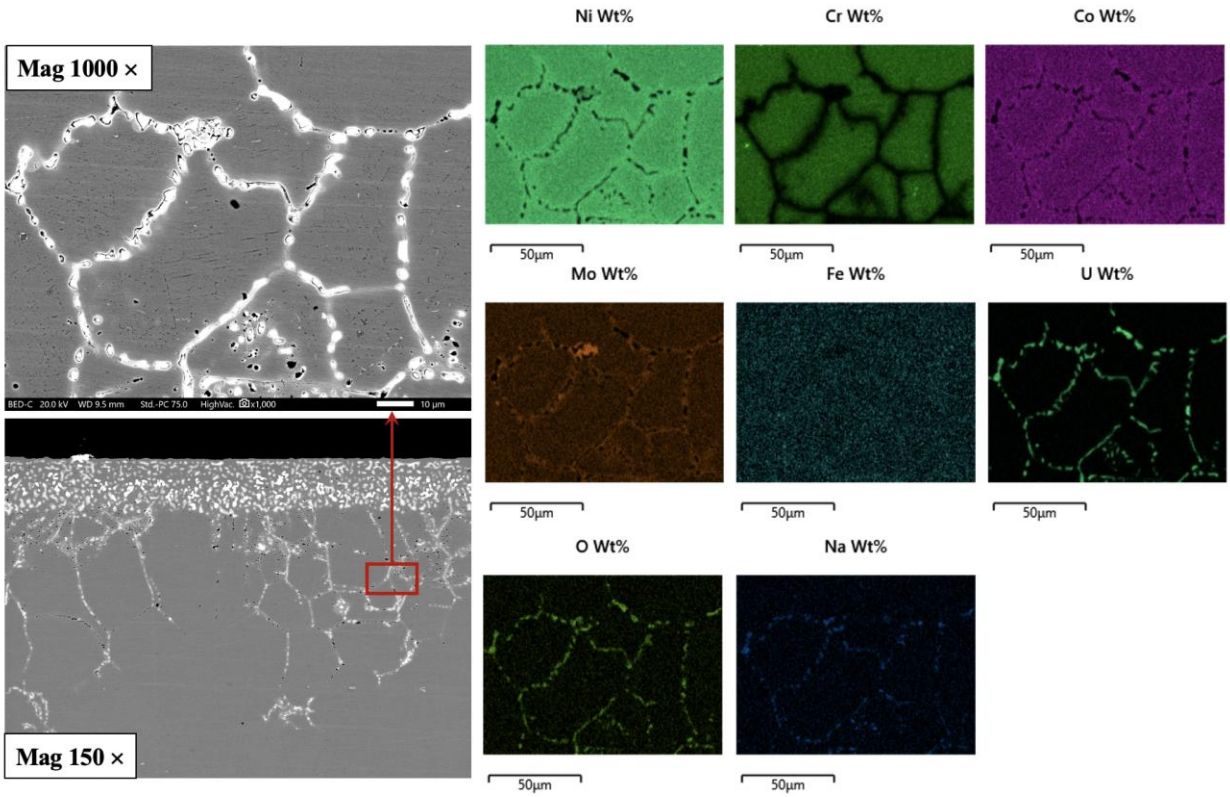

Figure 3-20 SEM mapping scan of 2nd part on the 2001-post-test specimen cross-section

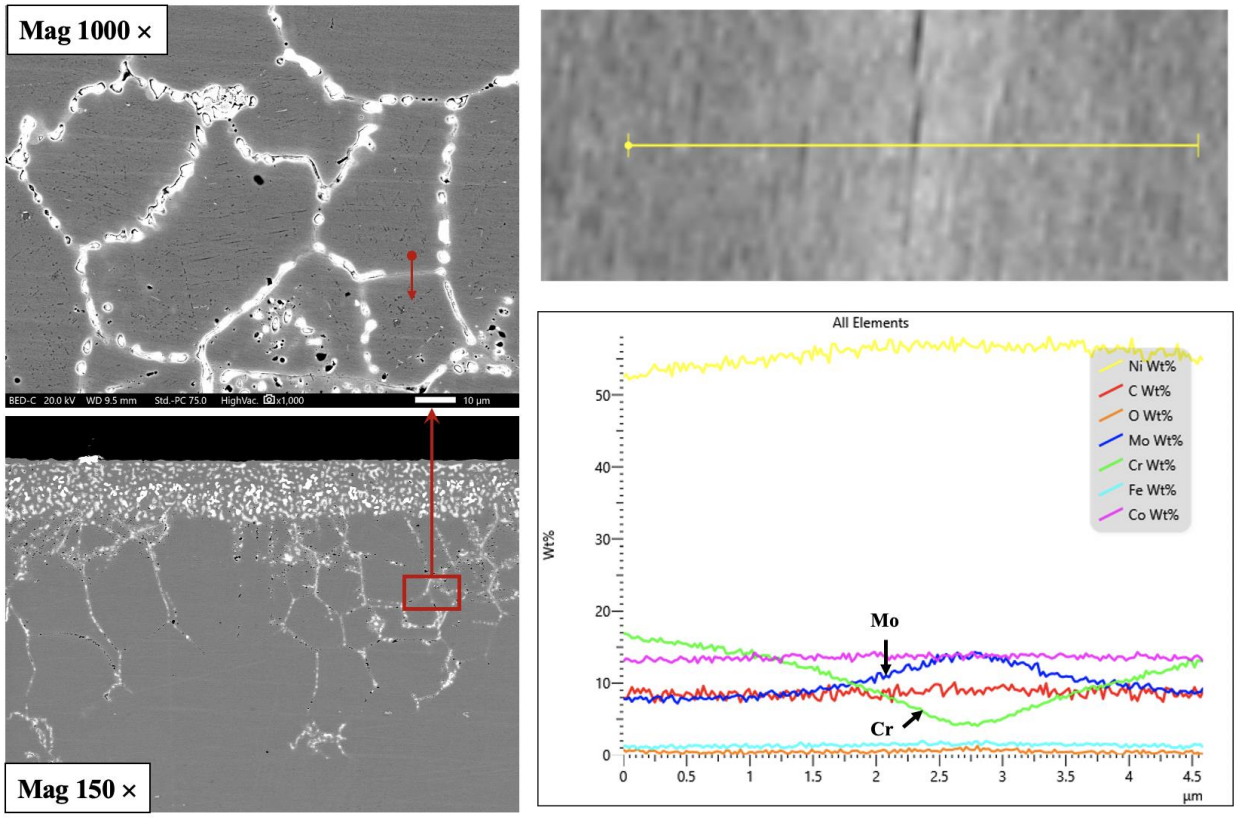

Figure 3-21 SEM line scan across GBs in the 2nd part on the 2001-post-test specimen cross-section

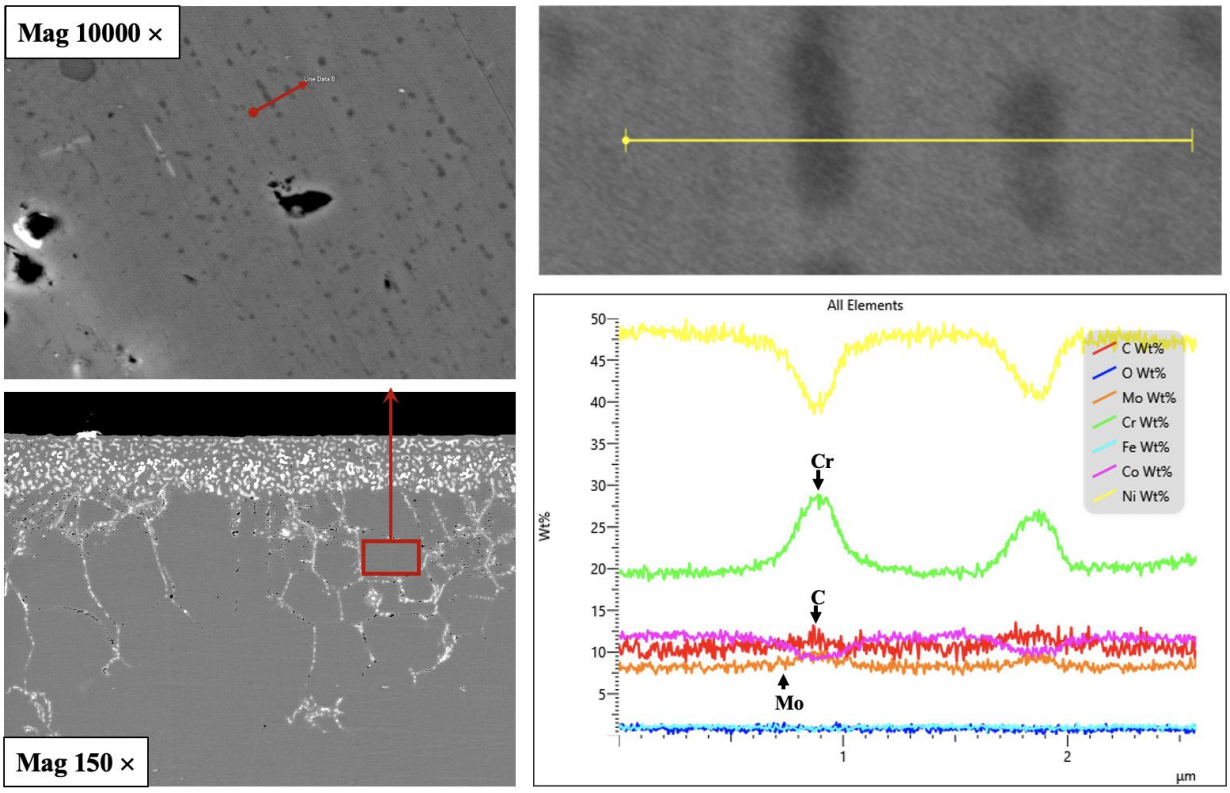

Figure 3-22 SEM line scan of black line-shaped material in the 2nd part on the 2001-post-test specimen cross-section

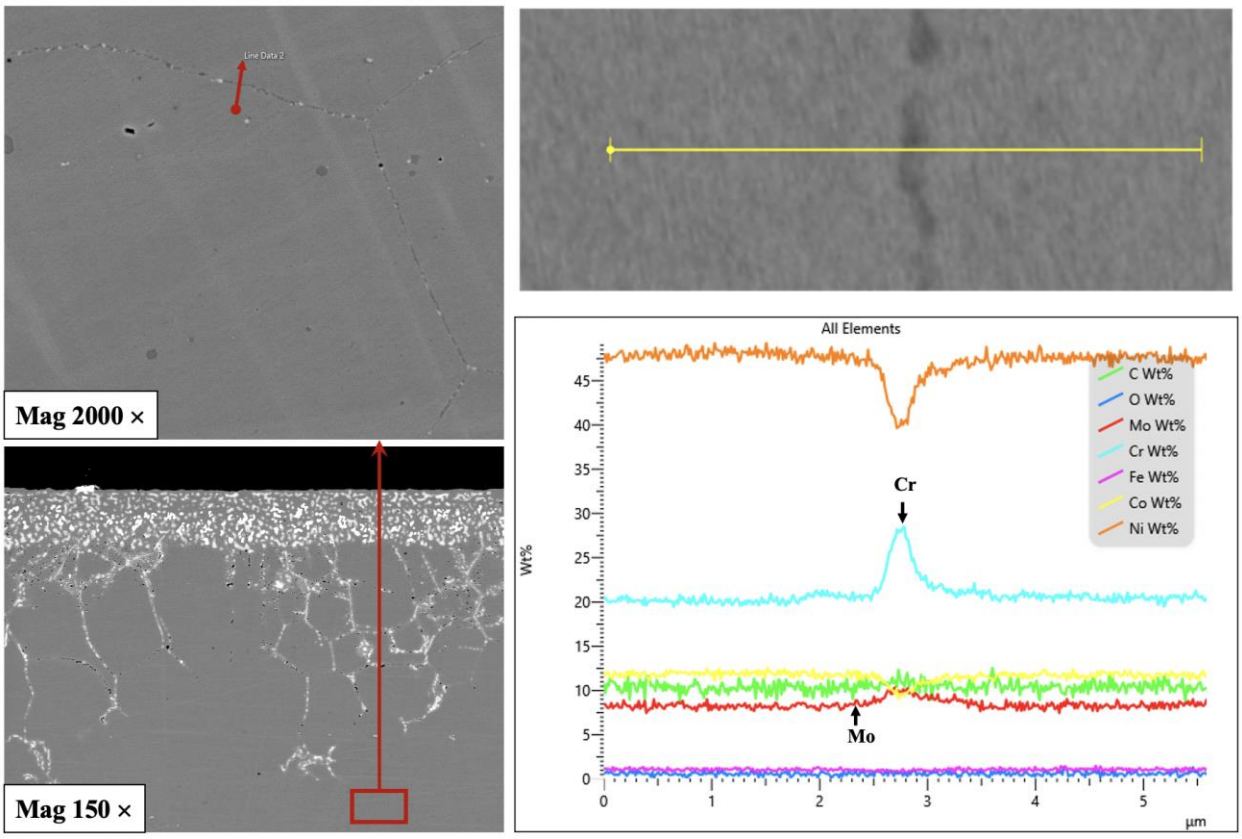

Figure 3-23 SEM line scan across GBs in the 3rd part on the 2001-post-test specimen cross-section

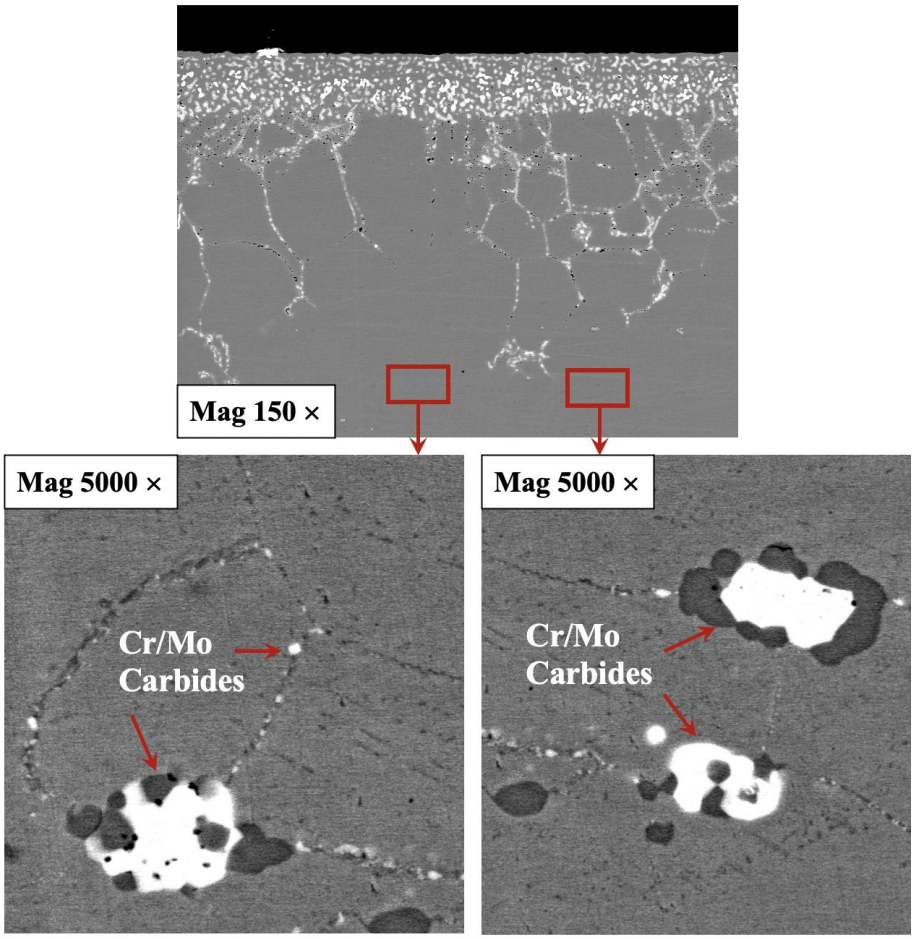

Figure 3-24 Carbides present at GBs in the 3rd part on the 2001-post-test specimen cross-section

Table 3-14 Thickness of Alloy 617 in the 2001-pre-test and 2001-post-test

Alloy 617		Pre-Test		Post-Test	
		Thickness (Caliper) (mm)		Thickness (SEM) (mm)	
		Avg.	Std. Dev.	Avg.	Std. Dev.
2001	A	2.00	0.01	1.9584	0.0185
	B	1.94	0.01	1.9447	0.0065
	C	1.91	0.01	1.9187	0.0089

Table 3-15 Attack depth and maximum attack depth of Alloy 617 in test 2001

Alloy 617		Attack Depth (μm)					
		1st Part			2nd Part		
		Avg.	Std. Dev.	Max.	Avg.	Std. Dev.	Max.
2001	A	50.22	5.93	66.09	189.47	43.85	320.60
	B	56.76	8.18	76.38	192.49	48.04	319.80
	C	58.23	6.63	72.57	192.37	35.21	319.70

Table 3-16 Point scans of 1st part on the 2001-post-test specimen cross-section

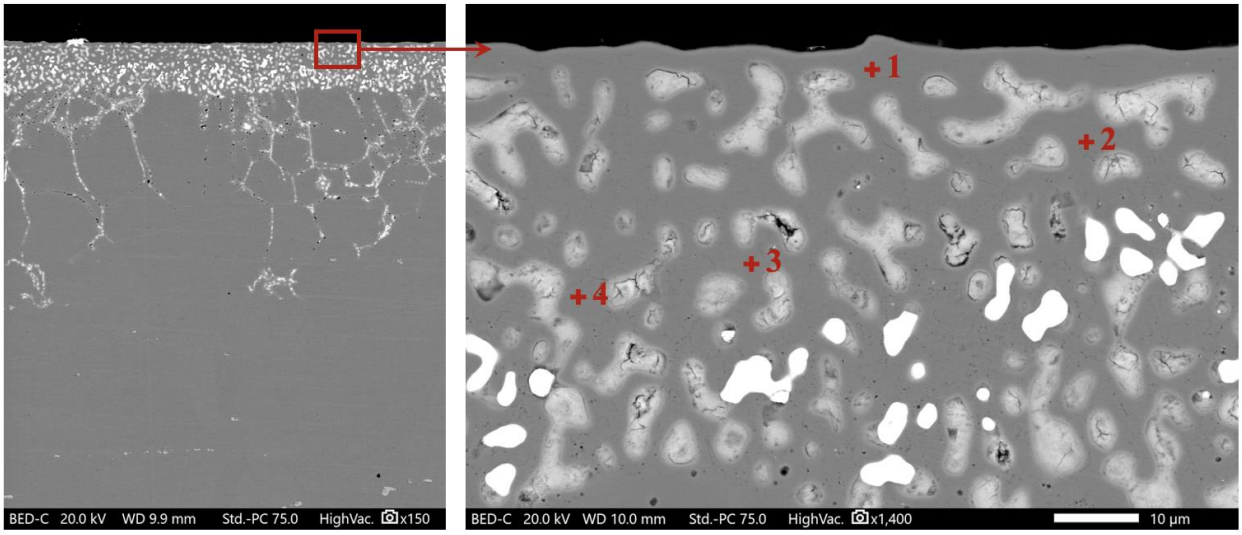

Point	Cr	Ni	Co	Mo	Fe	O	C
	wt. %						
1	0.1	62.3	16.5	5.2	3.7	0.5	11.7
2	0.1	62.6	16.3	5.7	3.7	0.5	11.1
3	0.1	64.0	16.1	6.4	3.7	0.4	9.3
4	0.1	63.9	15.6	6.6	3.6	0.6	9.6
Avg.	0.1	63.2	16.1	6.0	3.7	0.5	10.4
Std. Dev	0.00	0.88	0.39	0.64	0.05	0.08	1.16

3.2.3 Alloy 617 Corrosion Study with Time (72 hours & 32 hours)

3.2.3.1 Post-Test Salt Analysis

Salt sample collected periodically during the test S001 (72 hours) and S002 (32 hours) were analyzed using ICP-MS. Six major metal specie corrosion products, i.e., Cr, Fe, Co, Ni, Mo, and Al were identified. The concentration change trend of the metal species in both tests are shown in Figure 3-25. In both tests, the measured metal specie concentration has the similar trend. Cr specie has the largest concentration and increasing rate, because it is more easily attacked and has relatively higher concentration compared with other elements. In the first three hours, all corrosion products have a sharp increase which corresponds to the early stage of corrosion[162163,164]. Then, the Cr specie concentration continues to increase, as more and more Cr in the matrix is dissolved into the salt. However, the increasing rate of Cr in this stage is much slower as the Cr near the surface has been consumed, and it takes time for the Cr inside the matrix to diffuse outward[77]. Similarly, the concentration of Al increased slowly, then stabilizes around 0.25 at. % in the present study. However, Al species was not identified in the 2001 post-test salt. The cause of such difference was that the ICP-MS sample solution was diluted for ten times in the previous test, making the Al concentration beyond detection range. Moreover, the concentration of Fe, Co, Ni and Mo begins to go down slowly through the chemical reactions $Cr + MF_x \Leftrightarrow M + CrF_2$, T=800 °C, $\Delta G < 0$, where M is Mo, Fe, Co and/or Ni[126]. During the corrosion process, the oxidation (or corrosion) and reduction (chemical reaction between Cr and MF_x) of metal species, i.e., Mo, Fe, Co and/or Ni, happened at the same time. Over the initial corrosion stage, the oxidation reaction was dominant, thus, the concentration of corrosion products kept increasing. Once the corrosion products presented in the molten salts, the chemical reactions between Cr and MF_x begun, thus leading to the net corrosion rate, in other words, the MF_x concentration increasing rate becoming smaller. As the corrosion continues, the reduction reaction rate became larger than oxidation reaction rate, leading to the MF_x concentration decreasing. The Al concentration trend tended to be stable at the end of the tests in this work, which was mainly due to its low concentration in the metal matrix and more reactive property even than Cr.

Moreover, the Cr, Co, and Ni ion concentrations at the end of test 2001, S001 and S002 were given in Table 3-17. Around 0.003 mol % Co was identified in test 2001 and S002, and no Co ion presented in test S001. Ni ion was only identified in test 2001 with a value of 0.057 mol %. Cr ion concentration kept increasing but the concentration increase rate became smaller with the rise of test duration. The smaller Cr ion concentration increasing rate would result in the oxidation reaction of Co and Ni becoming dominant. Thus, Co and Ni ions presented again in test 2001.

The outside surfaces of S001 and S002 post-salt, as shown in Figure 3-26 (a) and (b), were analyzed using SEM. Similar to what previously discussed in Section 3.2.2, Mo-enriched silver material were identified, with an average composition of 90.6 wt.% Mo, 7.1 wt.% Ni, 1.9 wt.% Co, and 0.3 wt.% Fe. The Mo deposition attributed to the concentration decreasing of Mo metal specie in the molten salt as well. Moreover, it was observed that Mo quantity attached on the S002 post-test salt wall was much less than that of S001 test. Some silver material was found on the inner surface of glassy carbon, which was not observed in any other previous tests, and could be easily removed using polish paper. It was believed that the silver material was Mo-enriched

material same as that deposited in the salt but has been accumulated on the crucible temporally due to short test duration.

The measured UF_4/UF_3 ratio in the post-test salts is given in Table 3-18, which increased a lot since some U^{3+} could be oxidized by impurities, such as residual moisture in the salts. The orange UO_2F_2 formed on the inner surface of glassy carbon crucible further confirmed the presence of oxide impurity even after the thermal purification[165,166].

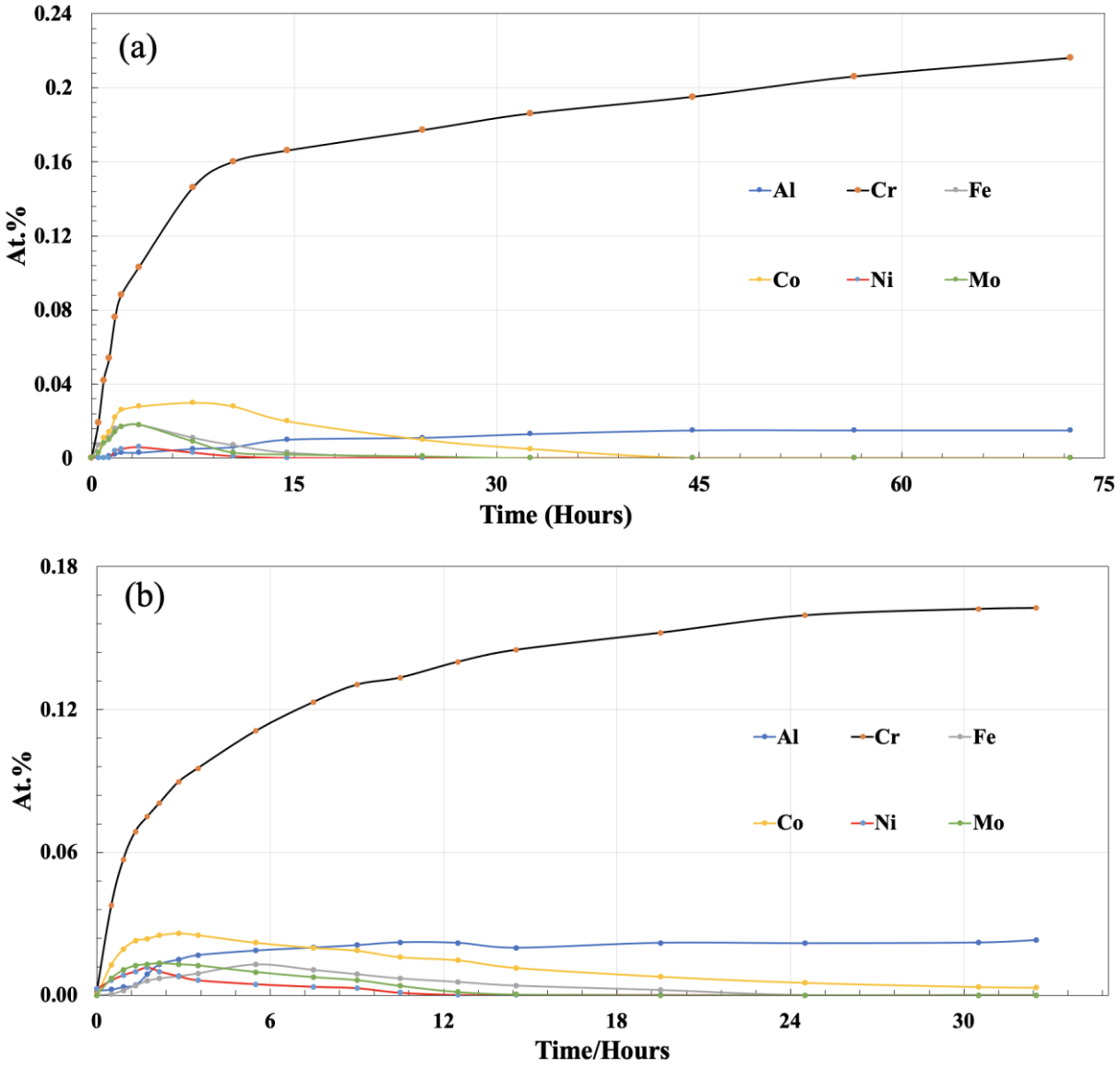

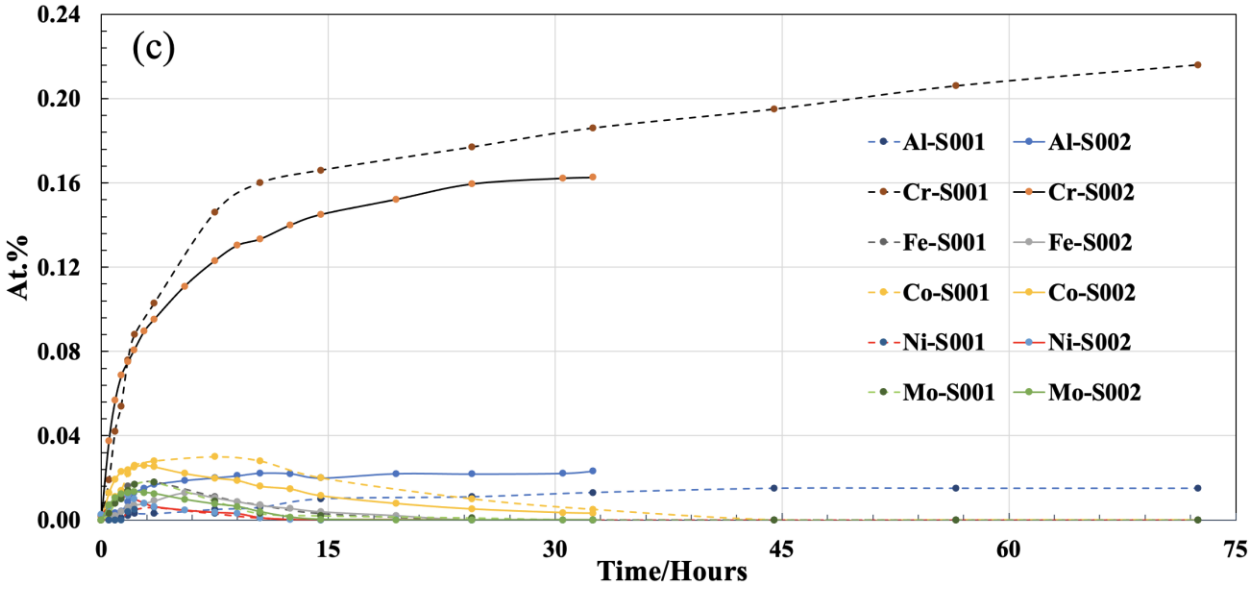

Figure 3-25 Metal specie corrosion products concentration change trend: (a) S001, (b) S002, (c) S001 & S002

Table 3-17 Cr, Co and Ni concentration at the end of test 2001, S001 and S002

Test ID			Cr	Co	Ni
			mol %		
2001	Post-Test	Avg.	0.260	0.003	0.057
		Std. Dev.	0.011	0.002	0.007
S001		Avg.	0.216	0.000	0.000
		Std. Dev.	0.001	0.000	0.000
S002		Avg.	0.163	0.003	0.000
		Std. Dev.	0.001	0.000	0.000

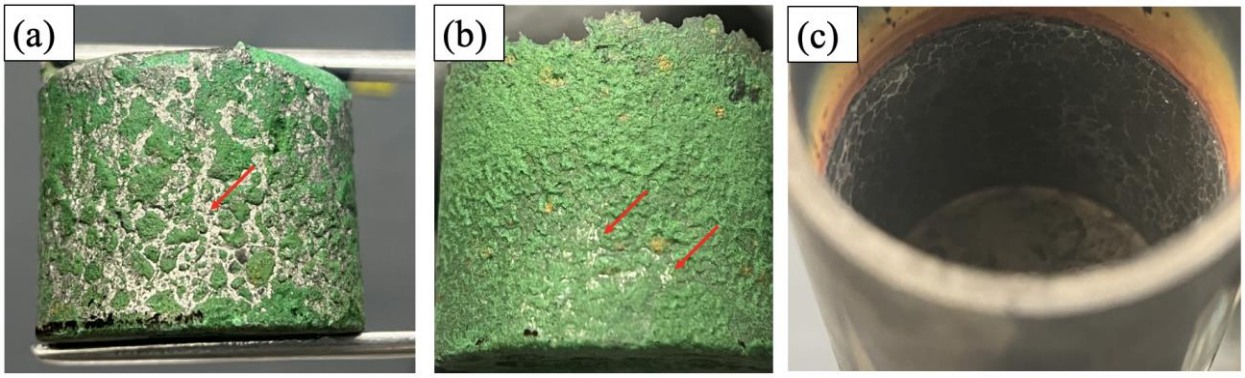

Figure 3-26 (a) Outside surface of S001-post-test salt, (b) Outside surface of S002-post-test salt, (c) Inner surface of glassy carbon crucible after S002 test

Table 3-18 UF_4/UF_3 ratio in the post-test salt of test S001 and S002

Test ID	Post-Test-UF_4/UF_3 Ratio	
	Avg.	Std. Dev.
S001	55.77	4.57
S002	52.14	1.97

3.2.3.2 Post-Test Specimen Analysis

Overall, the general corrosion behavior overserved in both tests (S001 and S002) were similar to that of previous Alloy 617 Test 2001. The corroded area was divided into two significant different parts, i.e., the 1st and 2nd part as shown in Figure 3-27. Salts were penetrated into the corroded areas of the specimen along the GBs. In the 1st part, Cr was completely depleted which was confirmed by the SEM point scan (Table 3-19), line scan (Figure 3-28) and mapping scan (Figure 3-29). In the 2nd part, Cr was depleted, and Mo was enriched at GBs as shown in Figure 3-29 (b) and Figure 3-30. Besides, new phenomenon was observed as well. As shown in Figure 3-29 (a), a thin Co layer was formed on the specimen surface. The line scans across the surface were conducted as shown in Figure 3-31. It was found that the composition of the deposition layer may vary at different positions, including Fe, Co, Ni and Mo. The thickness of deposition layer was also even at the specimen surface, which ranged from 1.2 μm to 3 μm. The formation of deposition layer was mainly due to the chemical reaction between Cr and corrosion products of Fe/Co/Ni/Mo at the surface, for which related studies have been conducted by Manly et al[167]. and Doniger et al[87]. No such layer was observed in the previous test 2001, perhaps because the deposition layer was formed over the early stage of the corrosion process, which might be re-dissolved into the salt and/or re-deposited at the interface between the salt and the glassy carbon crucible over the longer test duration. Moreover, Fe-enrichment and Mo-depletion were observed in the 1st part as shown in Figure 3-29 (a) and (b). The enriched-Fe may be diffused from those locations where Cr was

depleted completely and has not been corroded yet. As the salts penetrated into the specimen through the GBs, the reaction between Mo in the metal matrix and corrosion product of Fe in the penetrated salts, could further accelerate the depletion of Mo and the enrichment of Fe in the 1st part[168,169,170].

Many black spots randomly distributed in both corroded and uncorroded areas. Based on the SEM mapping scan and line scan shown in Figure 3-32 and Figure 3-33, the black spot areas were identified to be Cr/Mo enriched, not Cr/Mo carbides. It was known that long-term heat treatment was the major cause of carbides formation[171, 172,173]. 72 hours or 32 hours' test duration could lead to the Cr/Mo segregation, but not long enough for the carbides formation. In the uncorroded area, GBs became visible as shown in Figure 3-34, but there was no Cr/Mo enrichment at GBs due to short-term heat treatment.

There was no significant change on the thickness of specimens before and after tests as given in Table 3-20. The measured attacked depth in the 1st part and 2nd part was given in Table 3-21. The attack depth of the 1st part in test S001 was larger than that in test S002, which indicated a more severe corrosion. It was consistent with the ICP-MS results, in which the final Cr concentration in test S001 was larger than that in test S002.

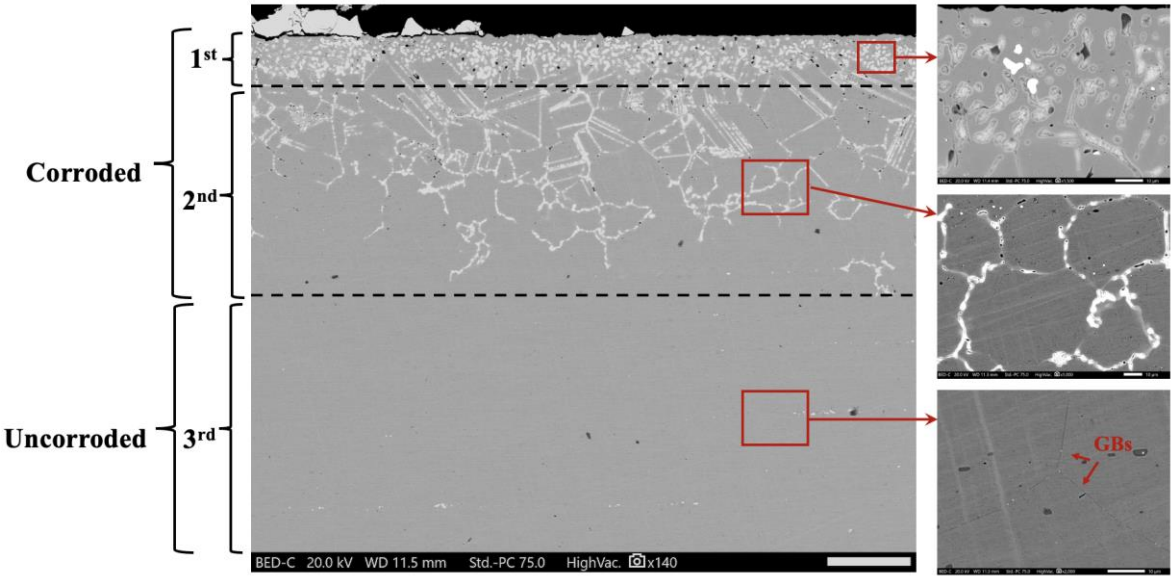

Figure 3-27 SEM image of S001 post-test specimen cross-section

Table 3-19 SEM point scan in the 1st part of test S001

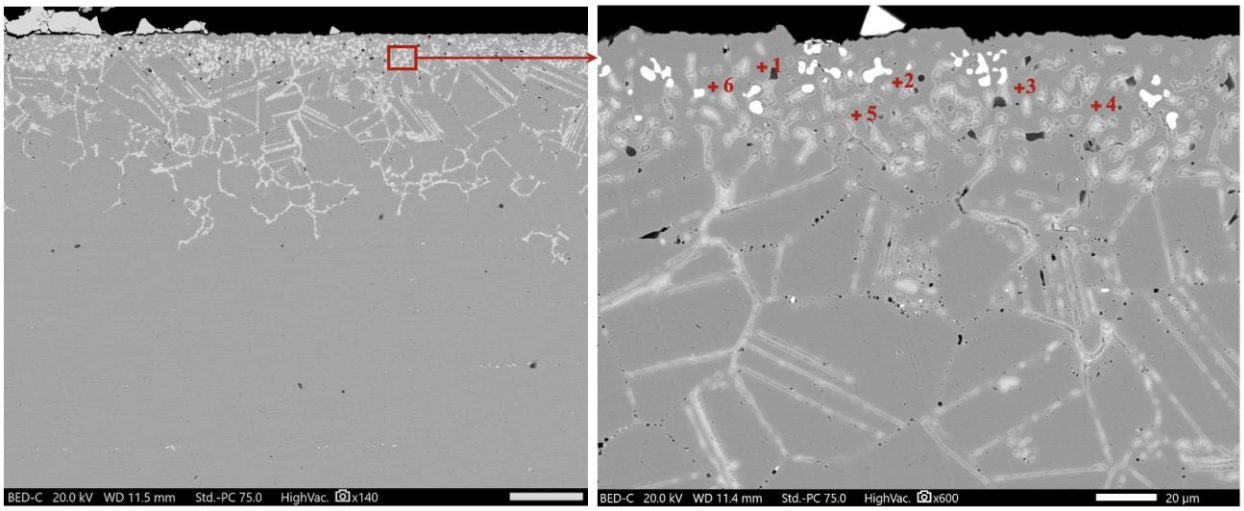

Point	Ni	Co	C	Mo	Fe	Cr	Al
	wt. %						
1	57.8	19.7	13.7	5.4	3.3	0	0
2	58.4	19.6	13.2	5.2	3.3	0.3	0.2
3	57.9	19.7	13.5	5.7	3.3	0	0
4	57.4	19.7	13.8	5.6	3.2	0.3	0
5	59.9	18.0	12.6	5.8	3.3	0.3	0.2
6	58.4	19.2	13.1	6.1	3.1	0.1	0
Avg.	58.3	19.3	13.3	5.6	3.3	0.2	0.1
Std. Dev	0.9	0.7	0.4	0.3	0.1	0.2	0.1

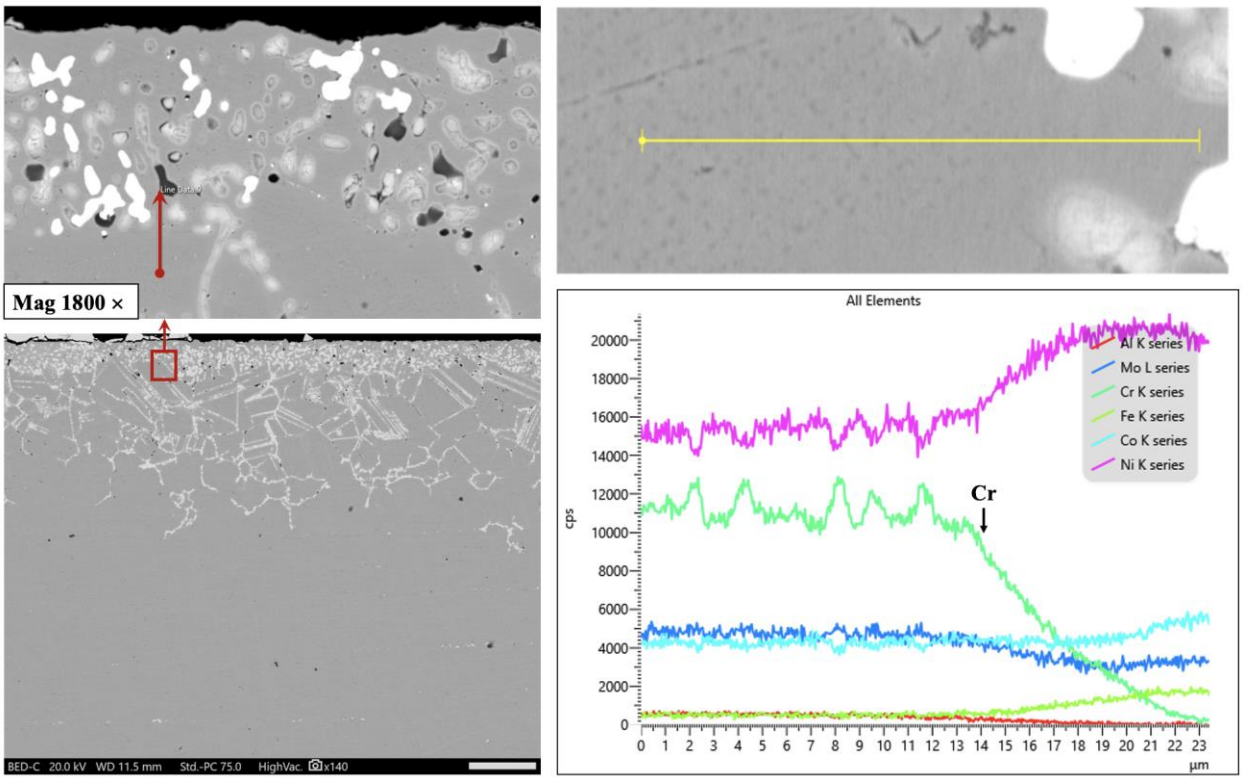

Figure 3-28 SEM line scan in the 1st part of test S001

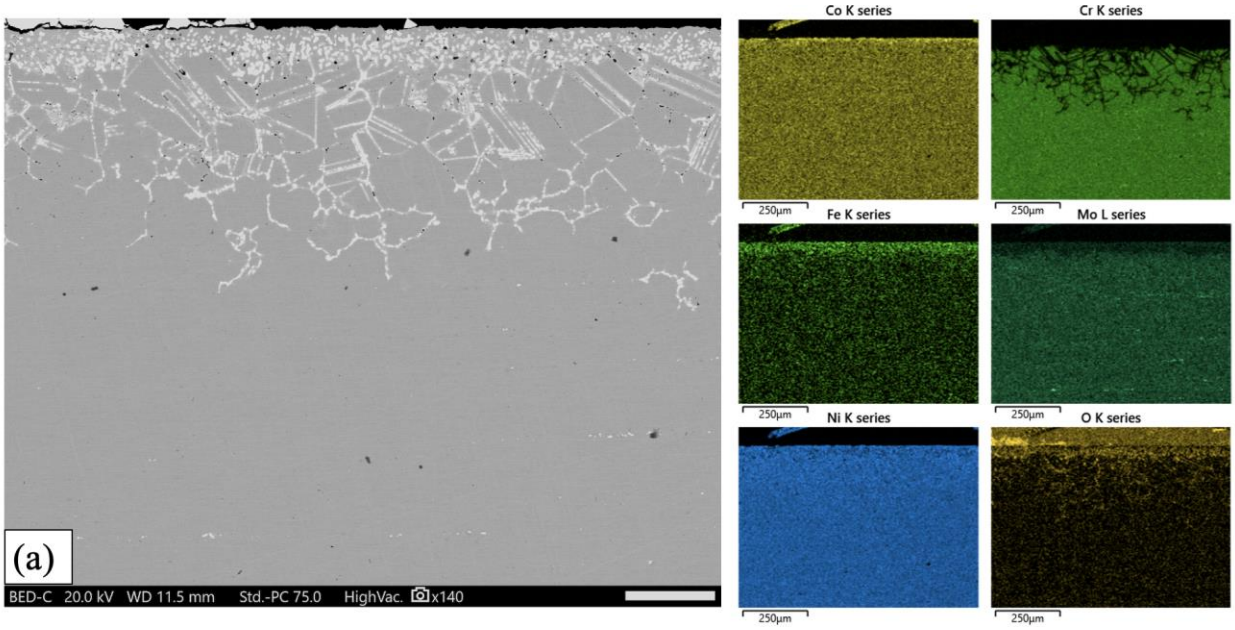

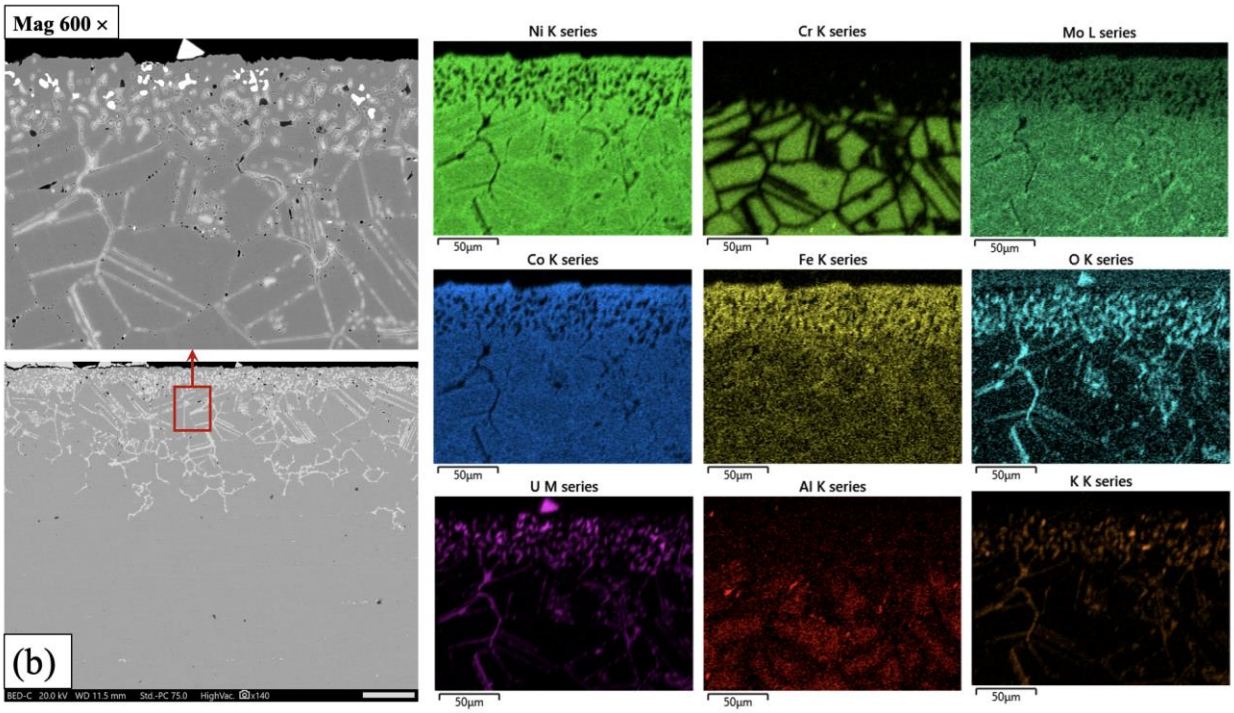

Figure 3-29 SEM mapping scan in the 1st part of test S001

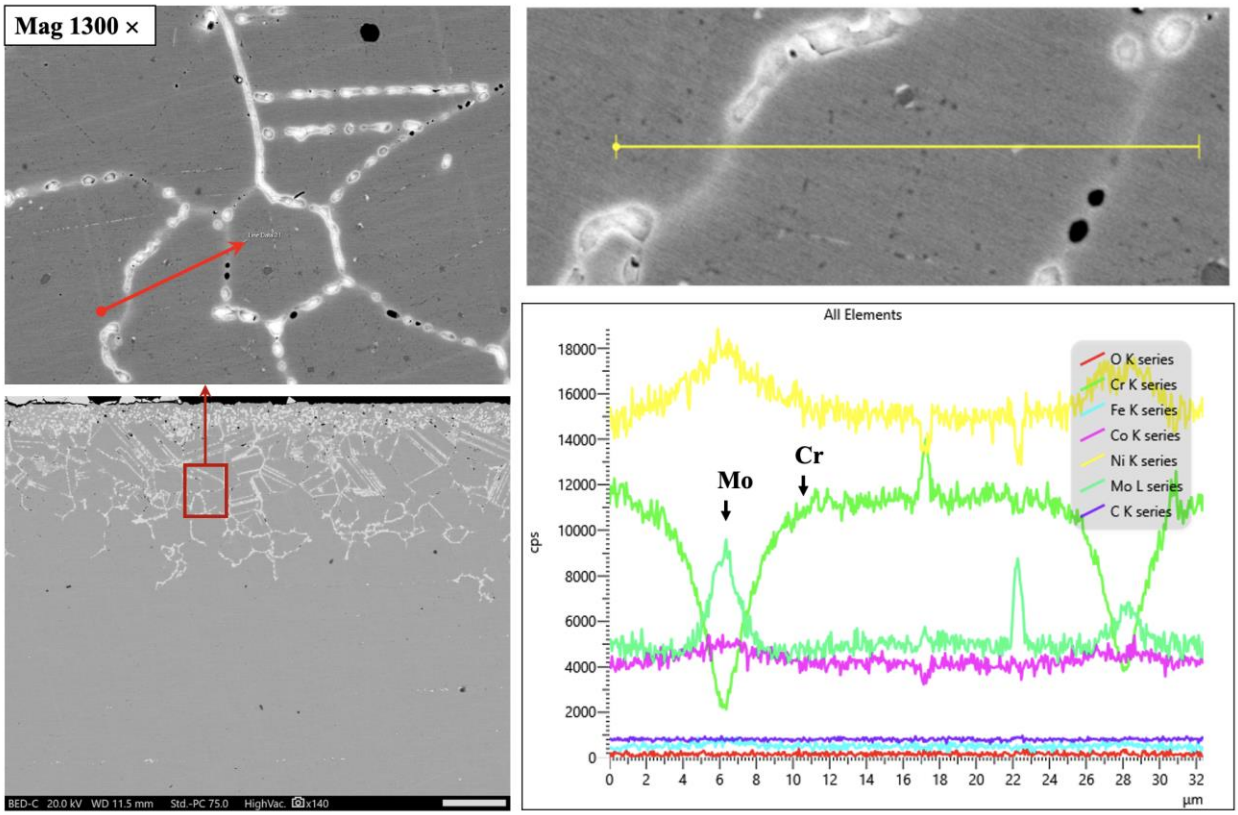

Figure 3-30 SEM line scan in the 2nd part of test S001

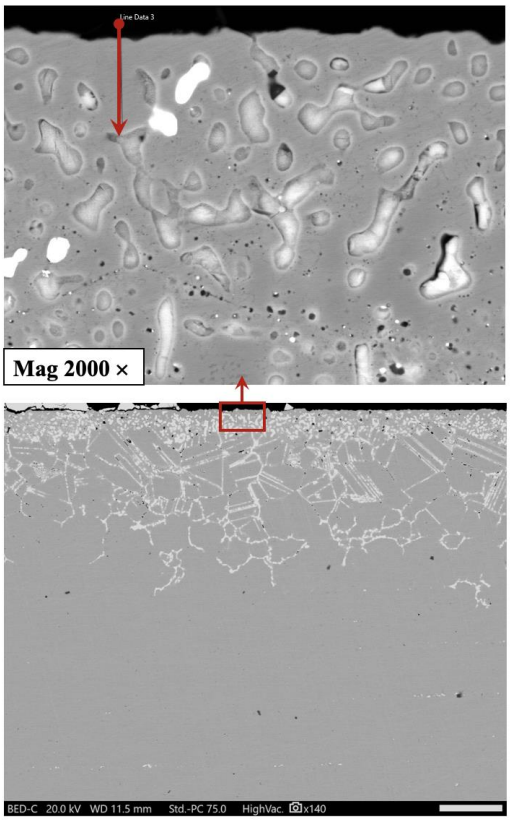
Mag 2000 ×
BED-C 20.0 kV WD 11.5 mm Std.-PC 75.0 HighVac. x140

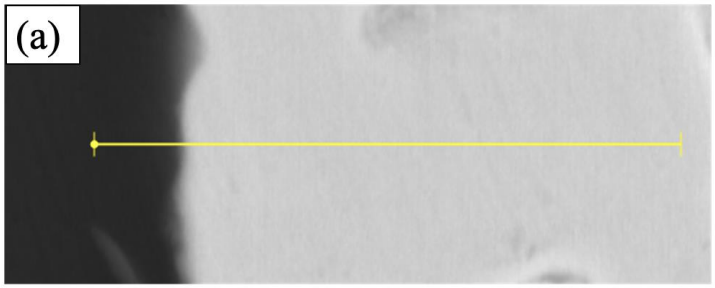
(a)

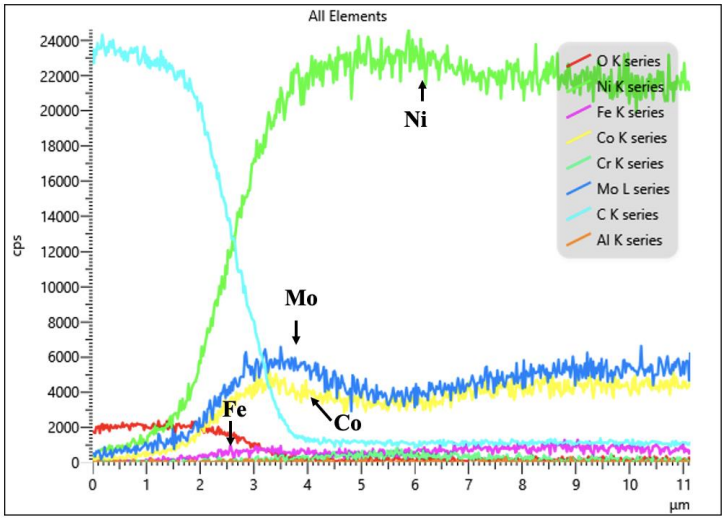
All Elements
cps
µm
O K series
Ni K series
Fe K series
Co K series
Cr K series
Mo L series
C K series
Al K series
Ni
Mo
Fe
Co

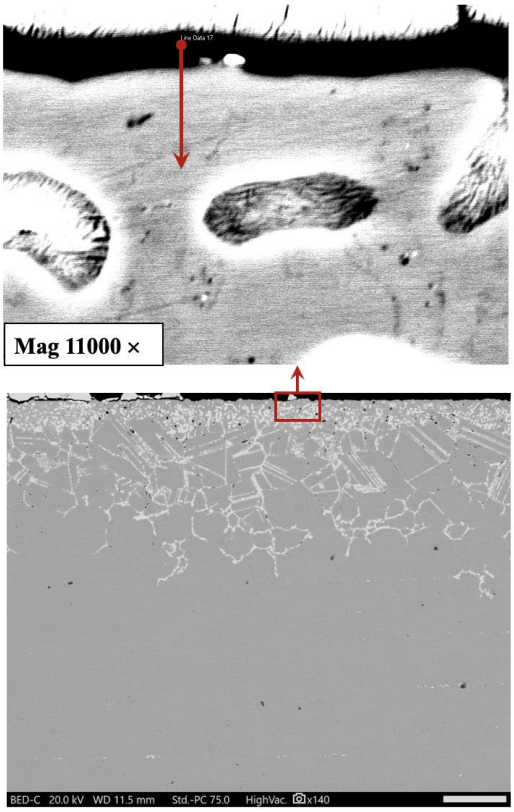
Mag 11000 ×
BED-C 20.0 kV WD 11.5 mm Std.-PC 75.0 HighVac. x140

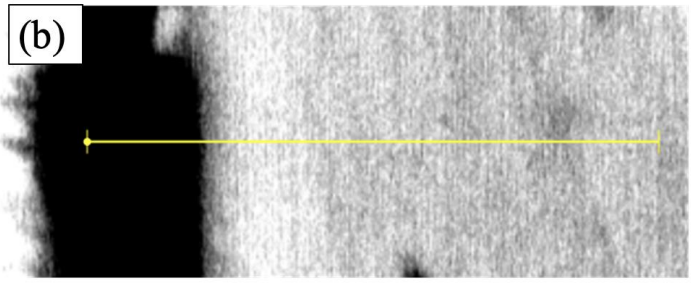
(b)

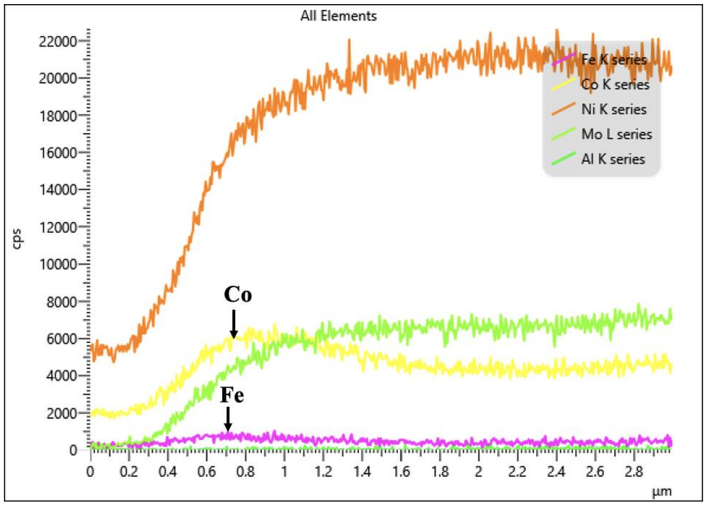
All Elements
cps
µm
Fe K series
Co K series
Ni K series
Mo L series
Al K series
Co
Fe

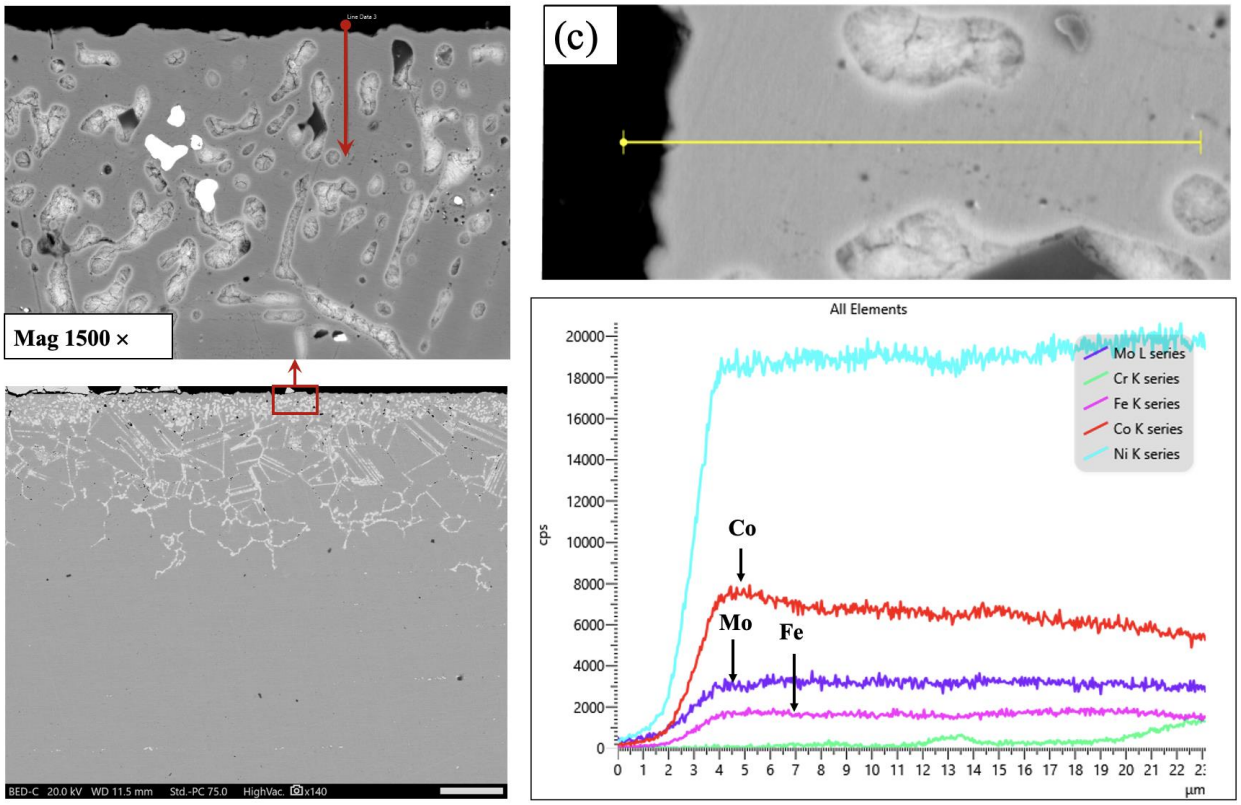

Figure 3-31 SEM line scan across the specimen surface in test S001

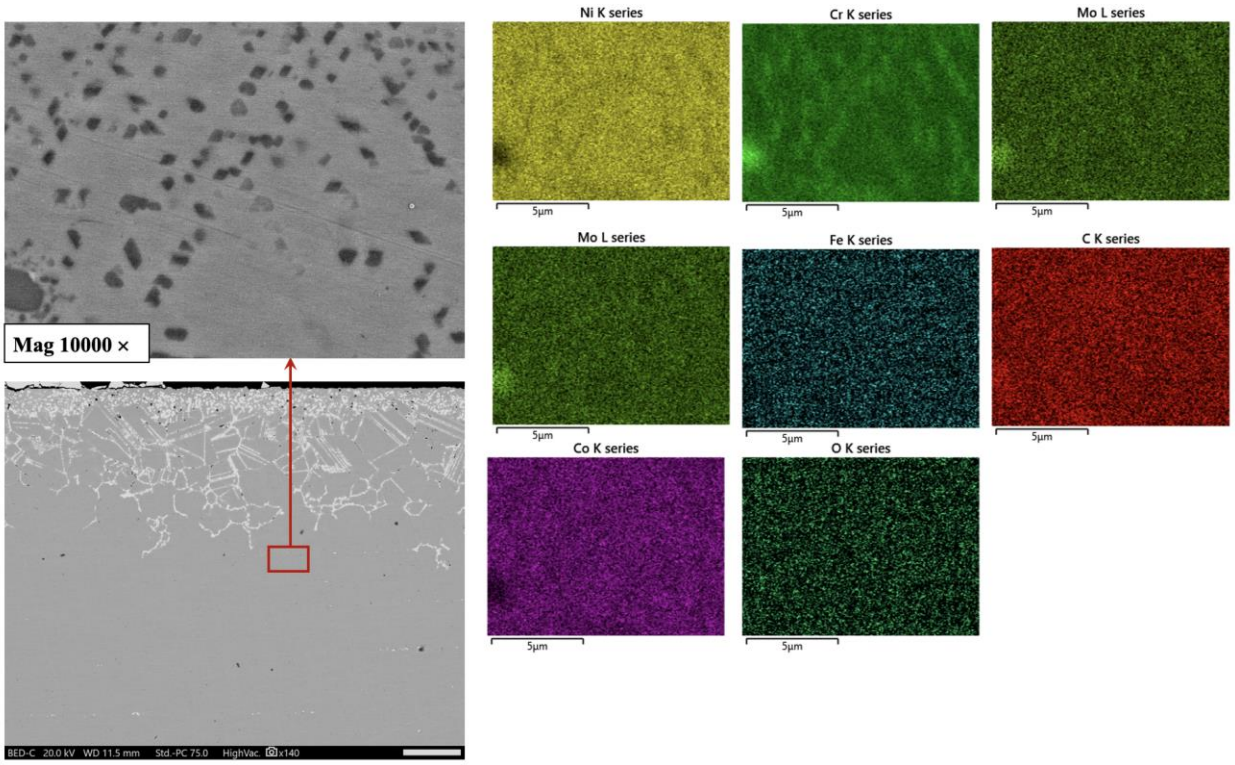

Figure 3-32 SEM mapping scan of black spots observed in test S001

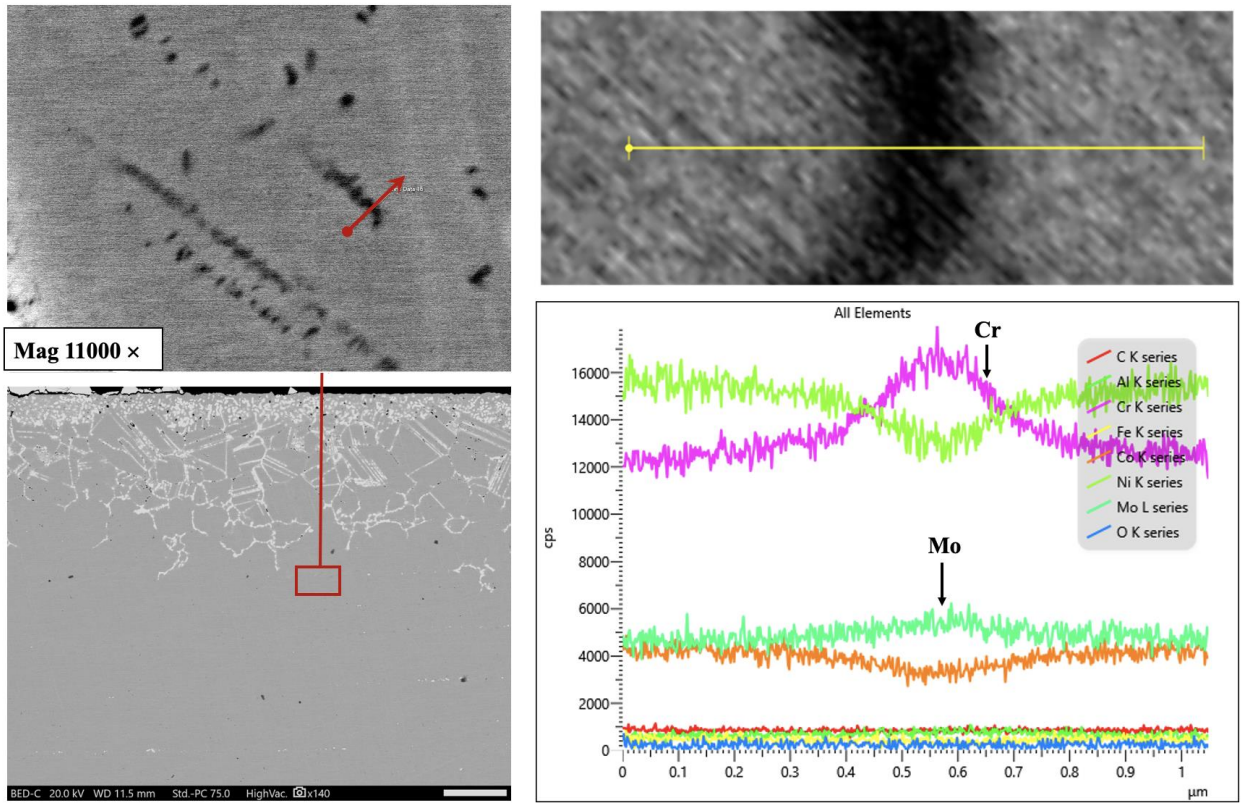

Figure 3-33 SEM line scan of black spots observed in test S001

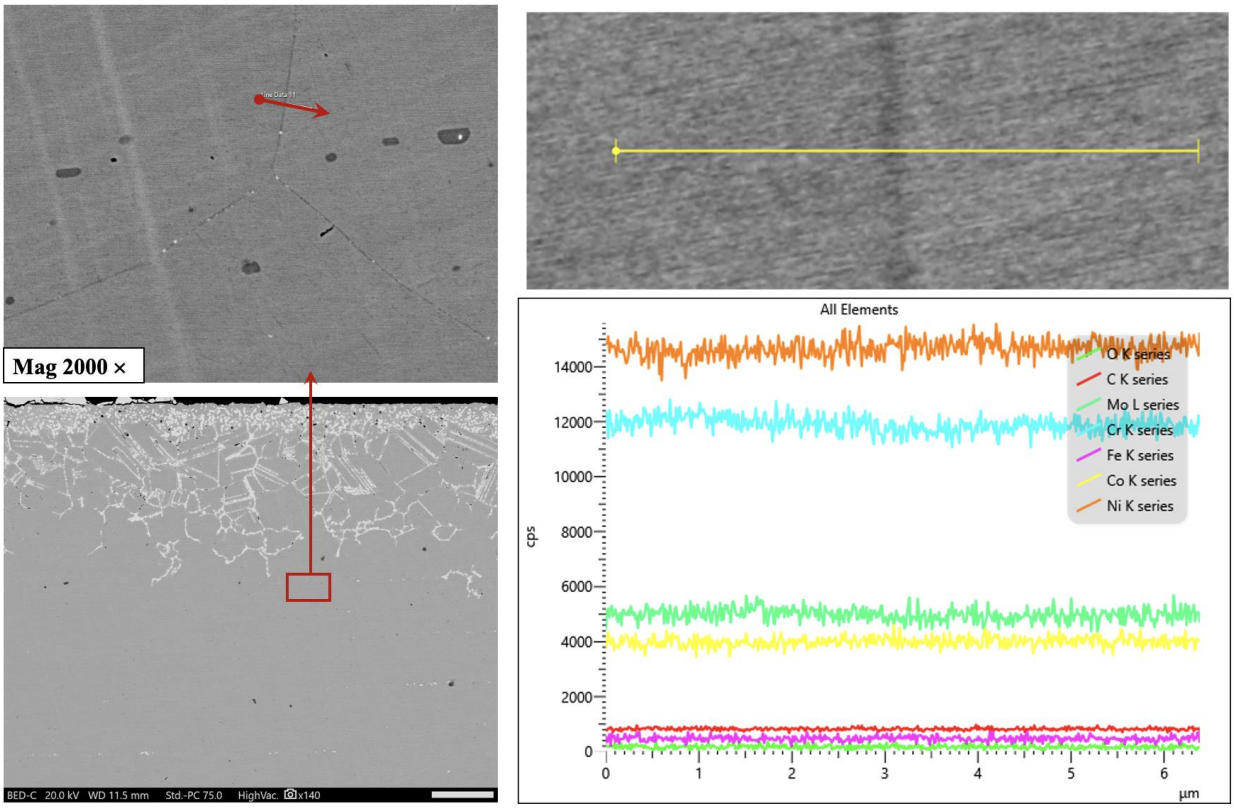

Figure 3-34 SEM line scan across GBs in the uncorroded area of test S001

Table 3-20 Thickness of pre-test and post-test Alloy 617 specimen in test S001 and S002

Test ID	Pre-Test		Post-Test	
	Thickness (Caliper) (mm)		Thickness (SEM) (mm)	
	Avg.	Std. Dev.	Avg.	Std. Dev.
S001	2.01	0.01	2.0157	0.0202
S002	1.96	0.01	1.9563	0.0217

Table 3-21 Attack depth of the 1st part and 2nd part in test S001 and S002

Test ID	Attack Depth (μm)					
	1st Part			2nd Part		
	Avg.	Std. Dev.	Max.	Avg.	Std. Dev.	Max.
S001	46.74	6.88	68.74	223.91	47.23	361.00
S002	34.75	5.35	46.64	120.02	31.70	193.00

3.3 Conclusions

Corrosion studies of SS 316H and Alloy 617 were conducted in thermally-purified molten NaF-KF-UF_4-UF_3 (UF_4/UF_3 with an initial value of 12~14) salts at 800°C.

In the 120-hour corrosion tests of SS 316H and Alloy 617:

- For SS 316H, Cr, Mn, and Fe were the major corroded species. The measured metal specie concentrations were consistent in the three tests, although the values tended to be larger in the first two tests (1001 & 1002), due to a higher oxide impurities level in the pre-test salts. For Alloy 617, Cr, Co, and Ni were the major corroded elements. In both the SS 316H and Alloy 617 tests, the UF_4/UF_3 ratio increased after the corrosion tests, since U^{3+} was consumed by corrosive impurities and/or corrosion products during the tests.
- For both SS 316H and Alloy 617, salt penetration and Cr-depletion were observed, and GBs became visible in the corroded and uncorroded areas after the corrosion tests. For the SS 316H corrosion specimens, Cr/Mn oxide, and carbide as well, were formed at the GBs in the corroded areas, while Cr/Mo carbides were formed at the visible GBs in the uncorroded areas. For the Alloy 617 corrosion specimens, the corroded areas were divided into two different parts: the 1st and 2nd part. In the 1st part, Cr was found to be completely depleted, and in the 2nd part, Cr was partially depleted. Mo-enrichment was observed at the GBs and Cr/Mo carbides were randomly distributed in the corroded areas. In the uncorroded areas, Cr and Mo were enriched at the GBs, and no significant carbides were identified, which was different from that in the SS 316H corrosion tests. Furthermore, Mo-enriched material was deposited at the salts and glassy carbon crucible interface, which was produced due to the disproportional reaction and chemical reactions between Cr and the Mo corrosion product. Based on the SEM results, the attack depth of Alloy 617 specimens was less than that of SS316H specimens.

In the 72- and 32-hour corrosion tests of Alloy 617:

- For both tests, Cr was depleted completely in the 1st part and partially depleted in the 2nd part. The concentration change trends of the corroded elements were similar. The Cr concertation has the largest value among the identified metal specie corrosion products and kept increasing during the tests. The other elements, Fe, Co, Ni and Mo

increased first, then decreased, due to the chemical reactions between Cr and the corrosion products of Fe, Co, Ni and Mo.

- A thin layer of Fe, Co, Ni and Mo was found on the surface of the specimen. Fe-enrichment and Mo-depletion were observed in the 1st part of the corroded areas. Cr/Mo-enrichment was observed in the black spots, which were randomly distributed in the matrix of the metal. The GBs were visible in the uncorroded areas, but there was no component concentration change at the GBs. The Cr/Mo enriched blackspots and visible GBs were due to the heat treatment, but not long enough for the formation of carbides.
- There was no significant change on the specimen thickness before and after the tests. The attack depth of the 1st part in the S001 test was larger than that of the S002, which indicated a more severe corrosion.

Based on the results of the present study, Alloy 617 is a better candidate compared with SS 316H, which can be used in the thermally-purified NaF-KF-UF_4-UF_3 salt. The corrosion of Alloy 617 becomes more severe with the rise of test duration in the studies system, which indicates that the corrosion reaction has not reached equilibrium.

4 Galvanic Corrosion Study of Alloy 617/Graphite in Molten NaF-KF-UF_4-UF_3 Salts

Galvanic corrosion tests of Alloy 617 and graphite were conducted in molten NaF-KF-UF_4-UF_3 salts at different temperatures for different test durations. It includes: (1) test GU001, which involves one test at 650 °C and one test at 750 °C for 2 hours, respectively, aiming at studying the temperature effect on the galvanic corrosion; (2) test GU002, which involves one test at 650 °C for 120 hours to study the galvanic corrosion development with time. ICP-MS analysis was conducted to measure the corrosion product concentration. SEM analysis was performed on the surface and cross-section of post-test specimens to study the corrosion behavior. Galvanic corrosion rate was calculated from the galvanic current.

4.1 Experiment

To accelerate the galvanic corrosion, salts used in test GU001 (650 & 750 °C) were from the corrosion test 1003, in which, some corrosion products of Cr (0.175 mol%) and Fe (0.198 mol%) existed, and salts used in test GU002 at 650 °C were from test GU001 at 650 °C. The surface area ratio of Alloy 617 and graphite specimens was 1, which were machined using EDM, with a dimension of 11.95 × 7.22 × 1.98mm, and 12.35 × 7.42 × 1.69mm, respectively. All the specimens were cleaned for 3 mins in an ultra-sonic machine to remove possible contamination and debris on the surface, then dried using a heating plate, transferred to a glovebox and sealed in a sample bag for future use.

A typical three-electrode electrochemical test setup was used as shown in Figure 4-1. Each specimen was fixed to a nickel wire, which was connected to a Gamry instrument to do the measurement. The more noble material graphite was used as a cathode, and the more active metal Alloy 617 acted as an anode. A platinum wire (diameter 1.0mm, Super Chemicals) was used as a reference electrode. A nickel crucible was used as a salt container, which was placed on an alumina safety dish. The specimens and salts were heated in a muffle furnace to a target temperature. During the electrochemical measurements in test GU001, an OCP scan was conducted for 1 hour before each galvanic corrosion (GC) measurement to ensure the system was stable. A GC measurement was performed for 2 hours using the ZRA technique, during which, the galvanic current and potential was recorded accordingly. For test GU002, the electrochemical measurements were conducted following the measurement profile which lasted for 120 hours as given in Table 4-1. During the galvanic corrosion tests, ICP-MS salt samples were collected before and after each test to measure the corrosion product concentration change. At the end of each test, specimens were removed from the salt and naturally cooled down to room temperature. SEM analysis was conducted on the surface and cross-section of the post-test specimen to check the galvanic corrosion effect.

Table 4-1 Electrochemical scan profile in test GU002 at 650 °C

Step	Electrochemical measurement	Duration (hour)
1st	OCP	24
2nd	GC	24
3rd	OCP	24
4th	GC	24
5th	OCP	24

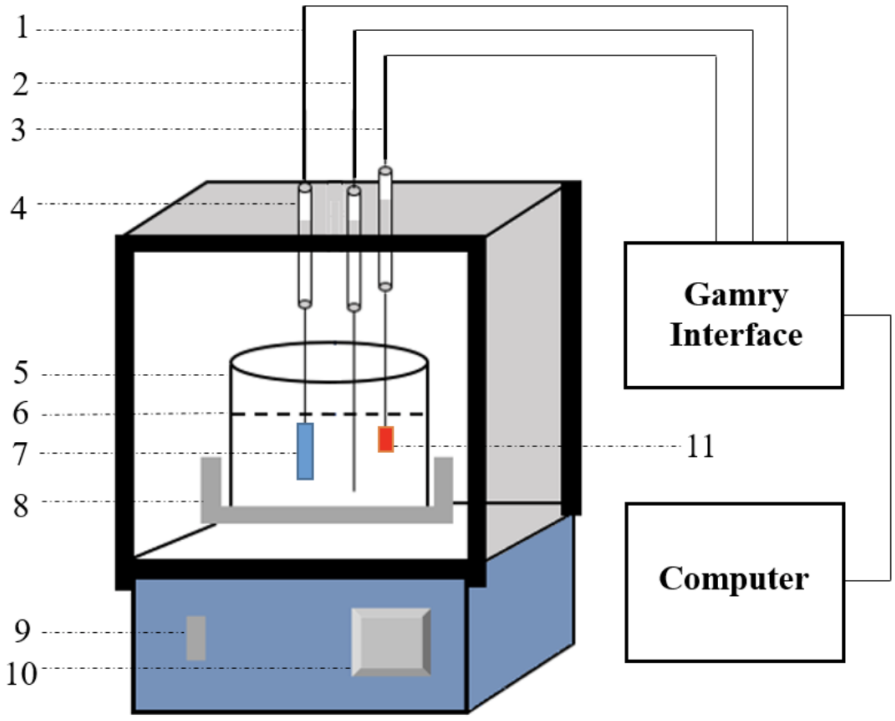

Figure 4-1 Alloy 617 Corroison test setup: 1. Ni wire working electrode 2. Pt wire reference electrode 3. Ni wire counter electrode 4. Quartz tube 5. Ni crucbile 6. Liquid salt level 7. Alloy 617 specimen 8. Alumina safety dish 9. Furnace power switch 10. Furnace display 11. Graphite Specimen

4.2 Results and Discussion

4.2.1 Alloy 617/Graphite Galvanic Corrosion Study (2 hours)

Figure 4-2 shows the galvanic current density i_g of Alloy 617/graphite couple in molten NaF-KF-UF_4-UF_3 salts at 650 and 750 °C. the positive value of galvanic current density further indicated that Alloy 617 acted as an anode, while the graphite was a cathode in the galvanic corrosion test. The galvanic current density significant increased with temperature. The i_g at 650 °C decreased

from 61 μA/cm^2 to 7.82 μA/cm^2 after exposure of 0.5 hours, and then stabilized at 5.63 μA/cm^2. At 750°C, the i_g shifted negatively from 115 μA/cm^2 to about 26.9 μA/cm^2 after exposure of 0.5 hours, and then stabilized at 23.5 μA/cm^2. The galvanic corrosion rate of Alloy 617 can be calculated using Eq. 1-8 and 1-10. According to the measured galvanic corrosion current density, the calculated galvanic corrosion rate was 0.0083 $mg/cm^2 \cdot hour$ for 650°C and 0.0320 $mg/cm^2 \cdot hour$ for 750 °C as listed in Table 4-2. The galvanic corrosion rate at 750 °C was about four times than that of 650°C. It indicated that the effect of temperature on the galvanic corrosion rate was significant, which were also reported by Qiu et al[117].

The SEM surface images of Alloy 617 specimens after the galvanic corrosion tests were shown in Figure 4-3. The specimen exhibited grain boundary attack, where clear grinding scratches can be observed. Compared to Figure 4-3 (a), the corrosion of Figure 4-3 (b) was much severe. The specimen surface at 750°C became rough and suffered more corrosion. The SEM cross-section images of Alloy 617 after the corrosion tests were shown in Figure 4-4, which further confirmed more roughness on the post-test Alloy 617 specimen at 750°C. In previous studies[81,174], the moisture in the molten fluoride salt could react with F^- and produce HF gas, which might dissolve into the molten salt and accelerate the material corrosion at higher temperatures. As discussed in Section 2, the measured kinetic data, such as diffusion coefficient and exchange current density, increased with a rise of the temperature, which could increase the corrosion reaction rate on the alloy surface. And the solubility of corrosion products was confirmed to increase at higher temperatures in previous studies[175,176], which further accelerated the corrosion rate.

ICP-MS analysis was conducted to measure quantity change of corrosion product metal species in the salts, from which the specimen weight change before and after the galvanic corrosion test was calculated. Thus, the average corrosion rate during the galvanic corrosion test was estimated. Based on ICP-MS results, the calculated average corrosion rate was 0.0108 $mg/cm^2 \cdot hour$ at 650 °C and 0.0505 $mg/cm^2 \cdot hour$ at 750 °C as listed in Table 4-2. The estimated average corrosion rate tended to be larger than the galvanic corrosion rate, because the metallic resistance from the anode surface to the cathode surface and solution resistance can influence the galvanic current measured as long as there was an appreciable distance between the coupled electrodes[101]. Moreover, before each GC measurement, an OCP scan was conducted, during which static corrosion could happen, and resulted in larger corrosion product concentrations.

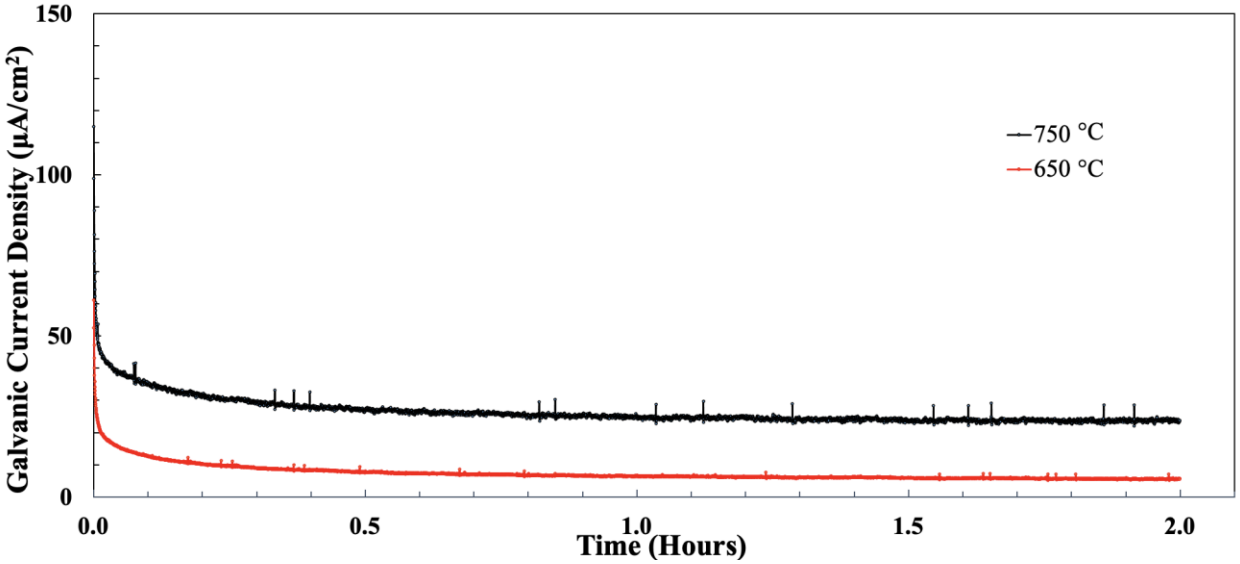

Figure 4-2 Galvanic current density of Alloy 617/graphite couple in molten NaF-KF-UF_4-UF_3 salts at 650 and 750 °C for 2 hours

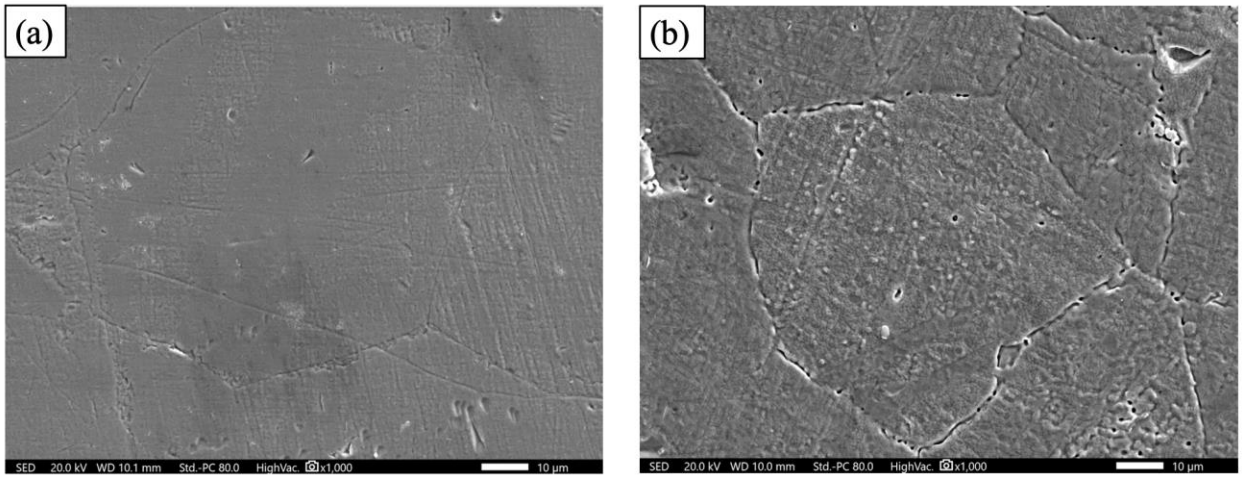

Figure 4-3 SEM surface images of the Alloy 617 specimen after the galvanic corrosion tests in the molten NaF-KF-UF_4-UF_3 salts, (a) 650 °C , and (b) 750 °C.

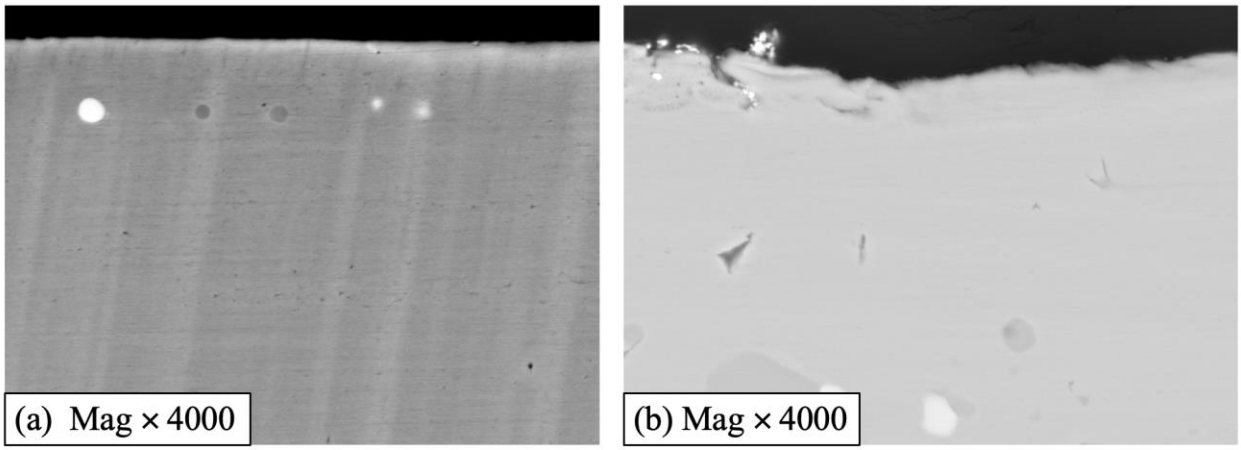

Figure 4-4 SEM cross-section images of the Alloy 617 specimen after the galvanic corrosion tests in the molten NaF-KF-UF_4-UF_3 salts, (a) 650 °C , and (b) 750 °C.

Table 4-2 Calcualted galvnic corroisn rate and average corrosion rate molten NaF-KF-UF_4-UF_3 salts at 650 and 750 °C

Temperature °C	Galvanic corrosion rate ($mg/cm^2 \cdot hour$)	Average corrosion rate ($mg/cm^2 \cdot hour$)
650	0.0083	0.0108
750	0.0320	0.0505

4.2.2 Alloy 617/Graphite Galvanic Corrosion Study (120 hours)

Figure 4-5 shows the galvanic current density i_g and OCP change trends during the 120 hours galvanic corrosion test in molten NaF-KF-UF_4-UF_3 salts at 650 °C. For the measured i_g of the 2nd and 4th day, they both had an initial decrease. In the early stage of galvanic corrosion, the Alloy 617 surface was clean, active, and uniform, therefore, the current flowing between the coupled metals was high. As the galvanic corrosion continued, a thin layer of corrosion products would be formed and accumulated on the surface of the Alloy 617. The accumulated corrosion products decreased the dissolution rate of Alloy 617, thus leading to the decreasing of galvanic current density. The measured i_g of the 4th day is finally stabilized at 27.5 μA/cm^2, which is larger compared with 20.7μA/cm^2 measured in the 2nd day. Moreover, the galvanic corrosion rate was calculated from the measured galvanic current. The calculated galvanic corrosion rate is 0.0227 $mg/cm^2 \cdot hour$ in the 4th day and 0.0329 $mg/cm^2 \cdot hour$ in the 2nd day. In the OCP curve as shown in Figure 4-5(b), the OCP value of Alloy 617 decreases with time, because of the consumption of oxidant impurities in the salts[177]. The lower OCP values of Alloy 617 in the 4th day could result in a larger potential difference of the Alloy 617/graphite couple, which is an

enhanced driving force for the galvanic corrosion, thus leading to a larger galvanic corrosion rate of the 4th day compared to that of the 2nd day in the present study.

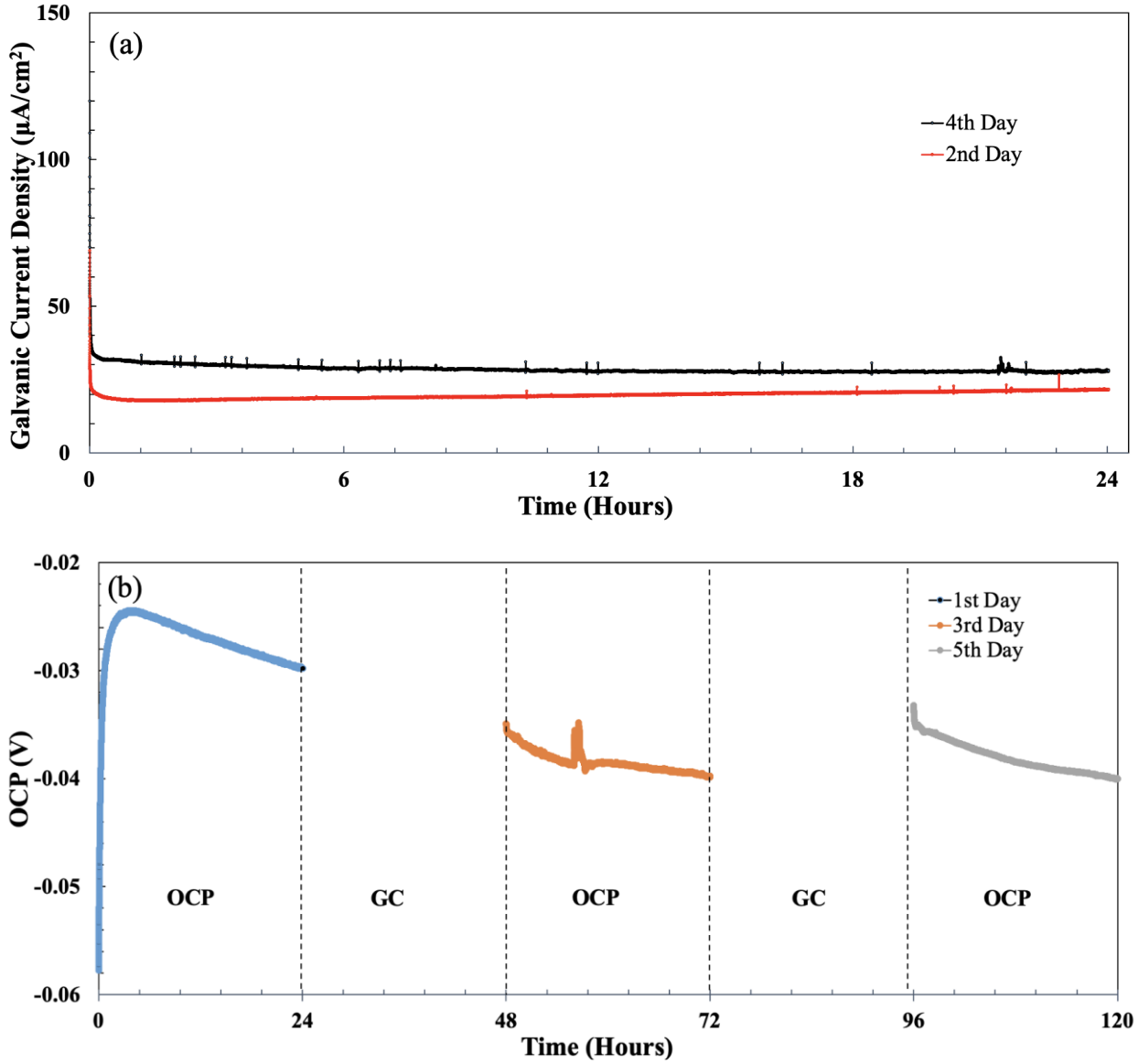

Figure 4-5 (a) Galvanic current density of Alloy 617/graphite couple (b) OCP of Alloy 617 in molten NaF-KF-UF_4-UF_3 salts at 650 and 750 °C over 120 hours test duration

An overview of SEM image on the cross-section of post-test specimen is shown in Figure 4-6. As observed in the previous Alloy 617 corrosion tests in Section 3, the corroded area is divided into two parts: the 1st part and the 2nd part as shown in Figure 4-6. In the 1st part, Cr has more severe depletion compared with the 2nd part as shown in the SEM mapping scan (Figure 4-7) and line scan (Figure 4-8). Cr is not completely depleted yet in the 1st part, which is different from previous Alloy 617 test. A line scan as given in Figure 4-10 was conducted in the 1st part to further study its corrosion behavior. Cr was observed to be under depletion at GBs. Assuming the corrosion products have not reached equilibrium in the molten salts, it indicated that more Cr would be

depleted with time and could result in complete Cr-depletion after longer test duration. Salts were penetrated into the specimen, in which uranium oxide was identified, and Cr was depleted along GBs in the 2nd part as shown in Figure 4-7. A very thin layer was formed on the surface of the specimen, due to the chemical reactions between the corrosion products in the salt and Cr near the specimen surface as previously discussed. The thin layer was composed of Fe, Mo and Ni, with a thickness around 0.8 μm as shown in the line scan (Figure 4-9). Due to the re-deposition of corrosion products on the specimen surface, the average corrosion rate of Alloy 617 was not calculated from ICP-MS analysis results.

The thickness of the specimen has no significant change before and after the test as given in Table 4-3. The average attack depth and maximum attack depth measured using SEM are given in Table 4-4. Compared with test 2001, the measured attack depth of the 1st and 2nd part are much smaller in test GU002, although the test duration is the same in both tests, and the galvanic effect can accelerate the corrosion of Alloy 617. This is due to the different oxide impurity level in the salts. Salts used in test 2001 is newly thermally-purified, in which a certain amount of oxides exist. While salts used in test GU002 have been used in the previous test 1003 at 800 °C and test GU001 at 650 °C, during which most of the oxide impurities have been consumed, thus making the salt less corrosive. In addition, no silver-colored Mo-enriched material was founded at the interface of the Ni crucible and the salt as shown in Figure 4-11. This was because the Ni crucible cannot support the disproportionation reaction of $CrF_2 = CrF_2 + Cr$, which made the chemical reaction between the Cr and corrosion product of Mo impossible. More studies are needed to further under these corrosion phenomena.

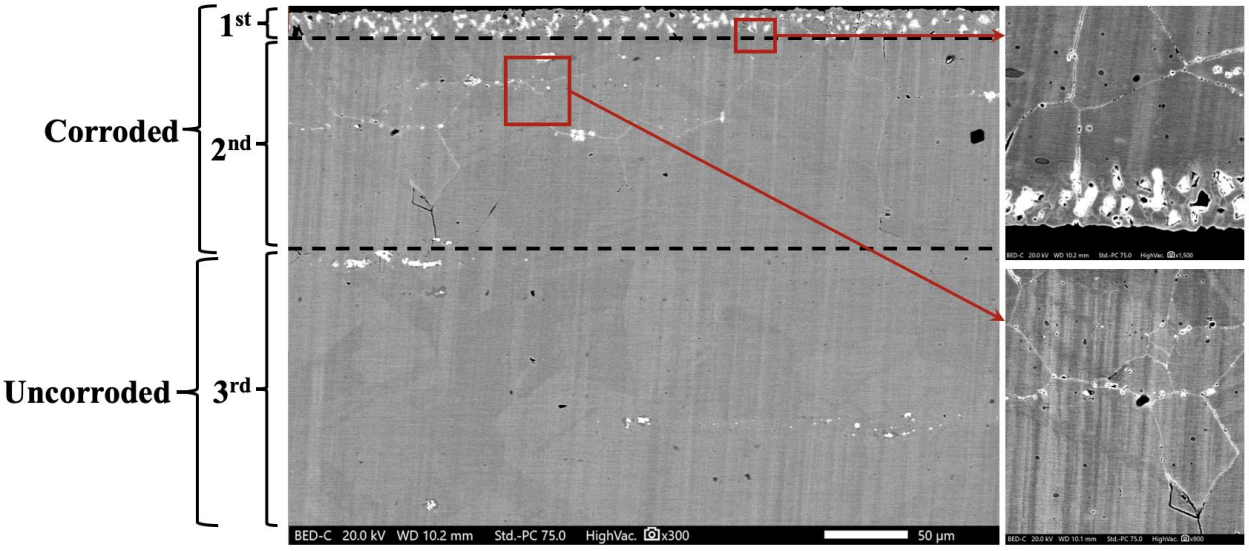

Figure 4-6 SEM image on the cross-section of post-test specimen in test GU002

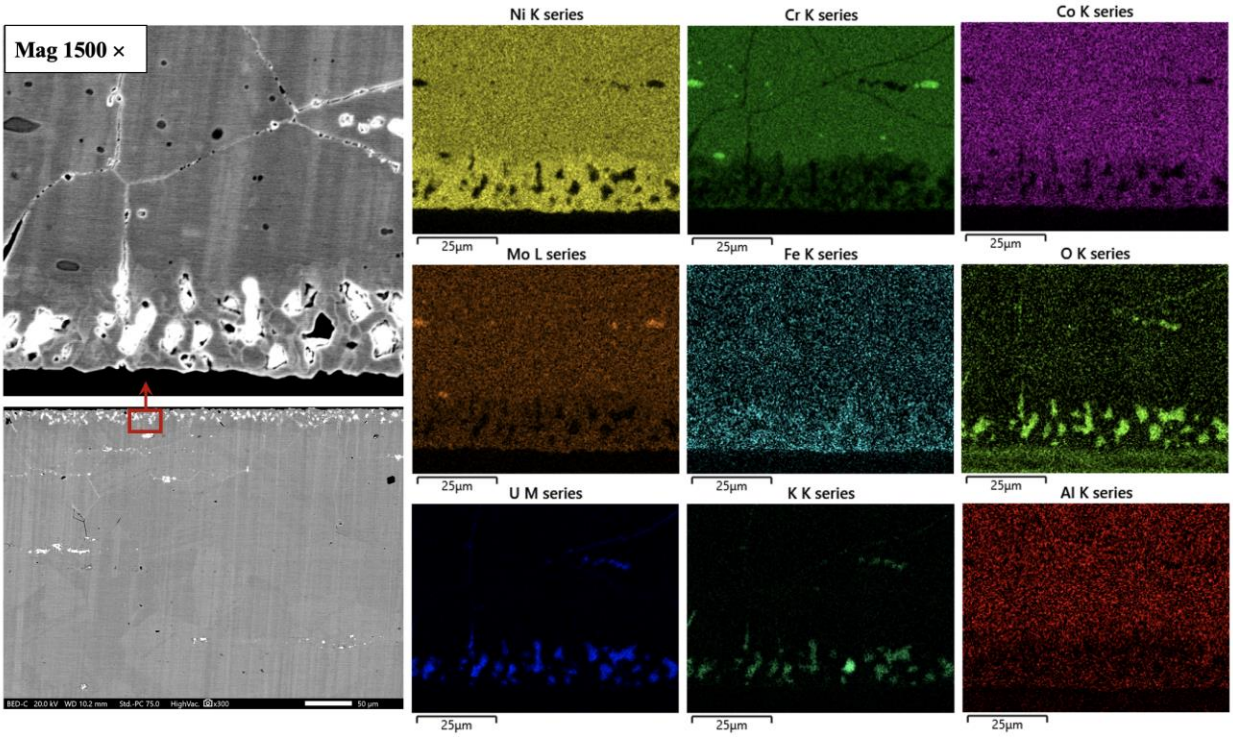

Figure 4-7 SEM mapping scan of the 1st part and 2nd part in test GU002

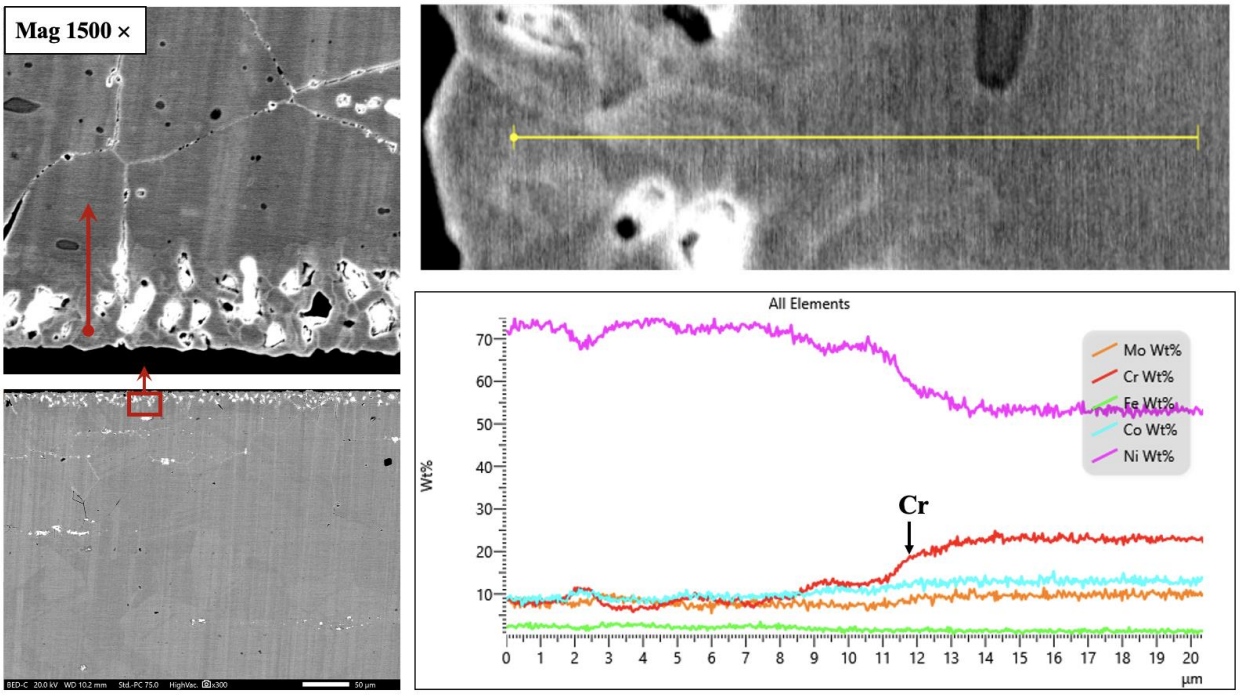

Figure 4-8 SEM line scan from the 1st part to the 2nd part in test GU002

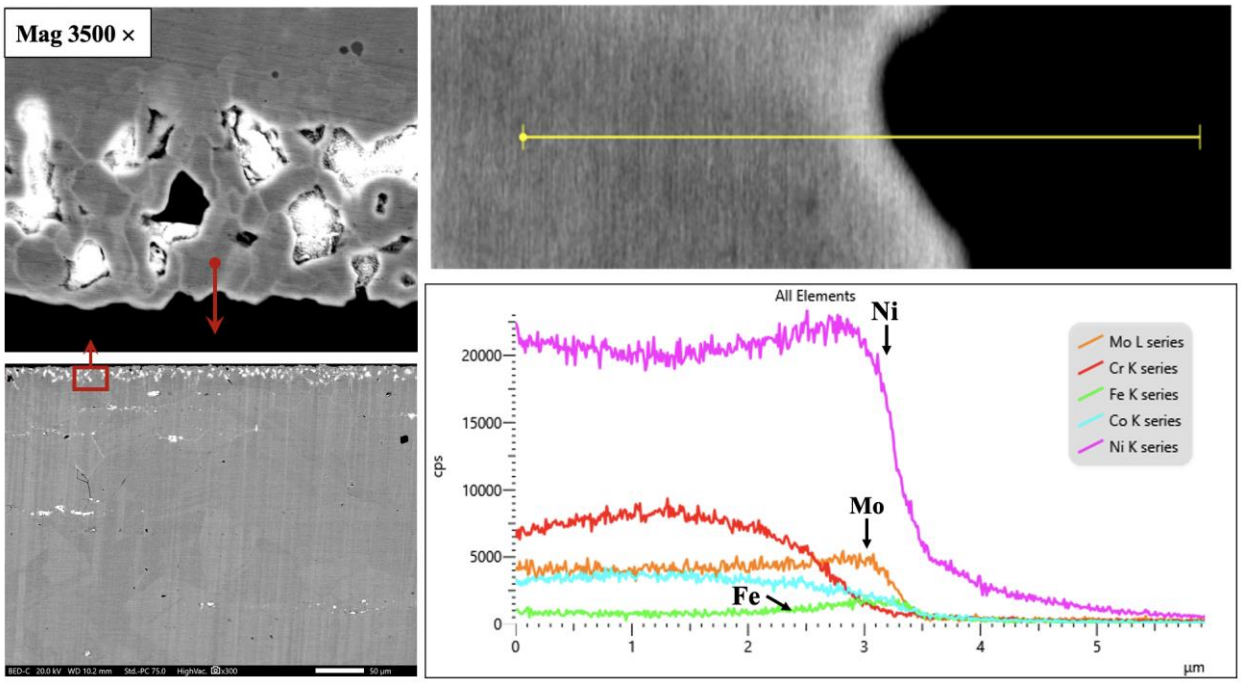

Figure 4-9 SEM line scan across the specimen surface in test GU002

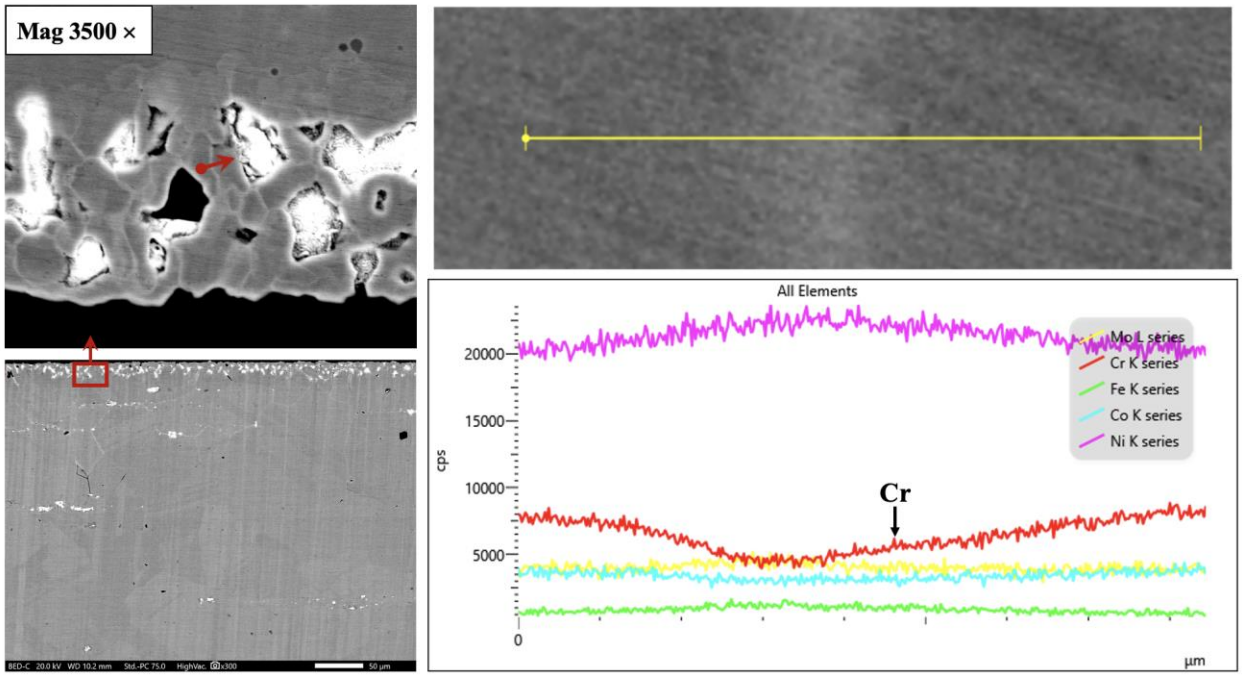

Figure 4-10 SEM line scan of the 1st part in test GU002

Table 4-3 Thickness of pre-test and post-test Alloy 617 specimen in test GU002

Test ID	Pre-Test		Post-Test	
	Thickness (Caliper) (mm)		Thickness (SEM) (mm)	
	Avg.	Std. Dev.	Avg.	Std. Dev.
GU002	2.01	0.01	2.0085	0.0092

Table 4-4 Attack depth of the 1st part and 2nd part in test GU002

Test ID	Attack Depth (μm)					
	1st Part			2nd Part		
	Avg.	Std. Dev.	Max.	Avg.	Std. Dev.	Max.
2001	55.07	4.26	76.38	191.44	42.37	320.60
GU002	13.25	3.04	22.89	93.65	33.75	164.50

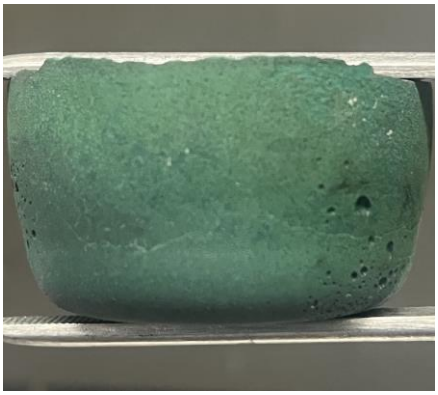

Figure 4-11 Outside surface of the post-test salt in test GU002

4.3 Conclusions

This chapter investigated the effect of temperature and exposure time on the galvanic corrosion of Alloy 617/graphite. For the 2-hour tests at 650 and 750 °C, it turns out that Alloy 617 acts as an anode and the graphite is the cathode in the galvanic corrosion test. The galvanic corrosion rate at 750 °C is much larger than that at 650 °C, which indicates that temperature is an important factor affecting the galvanic corrosion. The galvanic corrosion effect increases with temperature, which is further confirmed by SEM results, since the specimen surface is rougher at 750 °C. The measured average corrosion rate from ICP-MS is larger than that of galvanic corrosion rate, which is believed due to the static corrosion of Alloy 617 during the test.

For the 120-hour test at 650 °C, the measured galvanic corrosion rate of the 4th day is slightly larger than that of the 2nd day, which indicates that the galvanic corrosion increases with time in the present study. The increasing galvanic corrosion rate with time is because of the enhanced galvanic corrosion effect resulted from the larger potential difference between Alloy 617 and graphite. Moreover, the post-test specimen was analyzed using SEM. Cr depletion is more severe in the 1st part than that in the 2nd part. Although Cr in the 1st part is not completely depleted yet, more Cr is under depletion at GBs based on the SEM line scan, which make the complete Cr-depletion possible after a longer test duration if the corrosion reaction could continually happen and has not reached equilibrium in the studied system. A thin layer composed of Fe, Mo and Ni is formed due to the reactions between the corrosion products in the salts and Cr on the surface of Alloy 617 matrix. No Mo-enriched material was formed at the interface of the Ni crucible and the salt, because that the Ni crucible cannot support the disproportionation reaction of CrF_2 = Cr + CrF_3. Both the attack depth of the 1st part and 2nd part in the present test are smaller than that in test 2001, although the test duration is the same. It's due to the different oxide impurity concentrations in the salts.

5 Summary

In the present study, the kinetic properties, i.e., diffusion coefficient and exchange current density of the metal specie corrosion products (Fe, Cr and Ni ions) and non-metal species (OH^-), and corrosion studies of structural materials (SS 316H and Alloy 617), including static corrosion and galvanic corrosion, were investigated in molten $MgCl_2$-NaCl-KCl and/or NaF-KF-UF_4-UF_3 salts at temperatures ranging from 600 to 800 °C.

For the kinetic data measurements of metal and non-metal species:

- In both molten chloride and fluoride salts, the measured diffusion coefficient D of Fe^{2+}, Ni^{2+}, Cr^{2+}, Cr^{3+} and OH^- was independent of the ion concentration and followed the Arrhenius law, with values that descended in the order of $D_{OH^-} > D_{Cr^{2+}} > D_{Fe^{2+}} > D_{Ni^{2+}} > D_{Cr^{3+}}$. A non-linear curve fitting technique was applied to determine the i_0, α, i_L and k^0 values of Fe^{2+}, Ni^{2+}, Cr^{2+}, Cr^{3+} and OH^-. i_0 and k^0 followed the Arrhenius law, in which i_0 and k^0 of Cr^{2+} has the largest value followed by Fe^{2+}, Ni^{2+}, and Cr^{3+} at the same concentration and temperature.
- In molten $MgCl_2$-NaCl-KCl, a new method using ICP-MS analysis was developed to measure the actual OH^- concentration in the salt at different temperature, which also corresponded to the solubility of OH^- in the form of $Mg(OH)_2$ at each temperature. The measured C_{OH^-} value decreased from 4.11 to 2.84×10^{-6} mol cm^{-3} as temperature increased from 600 to 800ºC.
- In molten NaF-KF-UF_4-UF_3 salt, a new method – SD analysis – was applied to measure the diffusion coefficient in the multicomponent systems. It could eliminate the effect of the first reaction of Fe^{2+} on the second reaction of Cr^{2+}, which gave a more accurate result. The conventional CV method was also applied, in which the baseline of the second reaction was determined from the decay current of the first reaction. It turned out that there was no significant difference in the measured diffusion coefficient data, by using these two methods, because the low concentration of Fe^{2+} in the salts. The SD method was confirmed to perform well in the studied system. $D_{Cr^{2+}}$ was larger than $D_{Fe^{2+}}$ at the same temperature. In addition, the measured $D_{Fe^{2+}}$ and $D_{Cr^{2+}}$ values in molten NaF-KF-UF_4-UF_3 salts were slightly smaller than those obtained in molten $MgCl_2$-NaCl-KCl salts, because of larger density and molten salt viscosity of the molten NaF-KF-UF_4-UF_3 salts. In the measurements of i_0, an innovative method was also developed, which was successfully applied in the i_0, α and i_L measurements of Fe^{2+}, Cr^{2+} and Cr^{3+} in the multicomponent system. i_0 calculated in NaF-KF-UF_4-UF_3 salts tended to be smaller than that in $MgCl_2$-NaCl-KCl salts, which was due to the lower electrode reaction rate in molten NaF-KF-UF_4-UF_3 salts.
- A corrosion model was developed, which made corrosion rate prediction in a static system possible by using the measured kinetic parameter data in the experiments and would definitely provide further insight in the corrosion study of molten salts once applied in the field of corrosion.

For the corrosion study of SS 316H and Alloy 617:

- In the 120-hour corrosion tests of SS 316H and Alloy 617, the UF_4/UF_3 ratio increased after the corrosion tests, since U^{3+} was consumed by corrosive impurities and/or corrosion products during the tests. Cr, Mn, and Fe were the major corroded species for SS 316H, and Cr, Co, and Ni were the major corroded elements for Alloy 617. Mo-enriched material was deposited at the salts and glassy carbon crucible interface, which was produced due to the disproportionation reaction and chemical reactions between Cr and the Mo corrosion product in the corrosion test of Alloy 617. For both SS 316H and Alloy 617, salt penetration and Cr-depletion were observed, and GBs became visible in the corroded and uncorroded areas after the corrosion. For SS 316H, Cr/Mn oxide, and carbide as well, were formed at the GBs in the corroded areas, while Cr/Mo carbides were formed at the visible GBs in the uncorroded areas. For Alloy 617, the corroded areas were divided into two parts: the 1st and 2nd part. In the 1st part, Cr was completely depleted, and Cr was partially depleted in the 2nd part. Mo-enrichment was observed at the GBs and Cr/Mo carbides were randomly distributed in the corroded areas. In the uncorroded areas, Cr and Mo were enriched at the GBs, and no significant carbides were identified, which was different from that in the SS 316H corrosion tests. The attack depth of Alloy 617 specimens was less than that of SS316H specimens.
- In the 72- and 32-hour corrosion tests of Alloy 617, the concentration change trends of the corroded elements were similar. The concentration of Cr kept increasing though at different increasing rate during the tests. For the other identified corroded elements, i.e., Fe, Co, Ni and Mo, their concentrations increased first, then decreased. A thin layer of Fe, Co, Ni and Mo was found on the surface of the specimen, which was different from the previous 120-hour tests. Cr/Mo-enrichment was observed in the black spots, and GBs became visible in the uncorroded areas without component change when crossing the GBs, which were due to the heat treatment, but exposure period was not long enough for the formation of carbides.
- In the galvanic corrosion study of Alloy 617/graphite in NaF-KF-UF_4-UF_3 salts, Alloy 617 was used as an anode and the graphite was the cathode. In the 2-hour galvanic corrosion tests at 650 and 750 °C. The galvanic corrosion rate increased with the rise of temperature, in which, the galvanic corrosion rate at 750°C was about four times of that at 650°C. It indicated that temperature was an important factor affecting the galvanic corrosion. The SEM analysis of the post-test specimens further confirmed this conclusion, since the roughness of the post-test specimen surface at the higher temperature was larger. For the 120-hour galvanic corrosion test, the measured OCP tended to decrease with time, and the calculated galvanic corrosion rate has a slight increase with time, which was due to the enhanced driving force of the galvanic effect. Cr depletion and salt penetration were found at GBs, which was same to the Alloy 617 static corrosion tests results. A thin layer composed of Fe, Ni and Mo was formed on the post-test specimen surface due to the chemical reactions between the corrosion products and Cr near the surface of Alloy 617 specimen. No Mo-enriched material was observed at the interface of the Ni crucible and the salt after the galvanic corrosion test, because the Ni crucible cannot support the disproportionation reaction of CrF_2. In addition, the measured attack depth in the present test was much smaller than that in the previous Alloy 617 static corrosion test, although the test duration in both tests was 120 hours and the galvanic effect can accelerate the

corrosion in the salts. This was due to the different oxide impurity levels of salts used in the test, since the salt of 120-hour galvanic corrosion test was already used in the previous 120-hour static corrosion test and 2-hour galvanic corrosion test, during which most of the oxide impurities may have been consumed, making the salt much less corrosive.

The measured kinetic data in the present study have filled the gap of corrosion product and non-metal impurity's kinetic property data in molten salts. The newly-developed diffusion coefficient and exchange current density measurement method was successfully applied in the data measurements of a multicomponent system. And the developed corrosion model builds a connection between the experimental data (diffusion coefficient and exchange current density) and the corrosion rate. The corrosion studies of SS 316H and Alloy 617 gave us more insight into the corrosion behavior and mechanism in the molten salt at high temperatures. The corrosion of Alloy 617 with different test durations was also investigated, which shed light on the studies of how the corrosion was developed over the different corrosion stages. Moreover, in the galvanic corrosion studies of Alloy 617/graphite at different temperatures, it indicates that the galvanic corrosion is more severe at a higher temperature and the galvanic corrosion rate increases slightly with time. The galvanic effect on corrosion should be considered in the design and application of MSRs.

Nevertheless, more studies are needed in the future to further understand the material corrosion in molten salts as follows.

- The effect of oxide impurities on the salt penetration in molten NaF-KF-UF_4-UF_3 salts
- A comprehensive corrosion model that can be widely applied in MSRs
- The effects of moisture and anode/cathode surface area ratio on the galvanic corrosion in molten NaF-KF-UF_4-UF_3 salts
- The relation between static corrosion and galvanic corrosion in molten salts
- The galvanic corrosion of couples including three or more different materials

MSRs are the next generation advanced reactors, in which molten halide salts are applied to improve the reactors' efficiency and safety. As previously discussed, material corrosion is a challenge in the application of molten salts. This study will assist in creating a database of kinetic data for various commercial use in the corrosion field, such as corrosion rate prediction. It also cast light on the structural material corrosion study including static corrosion and galvanic corrosion in the molten salts. Hence, this collective information will assist in the evaluation of the structural material and accelerate the material selection process for critical components of the MSRs.

6 References

1. Wikipedia on the molten salts, https://en.wikipedia.org/wiki/Molten_salt.

2. Molten salt reactors, iaea.org/topics/molten-salt-reactors.

3. Y. Hirose, “Fast-spectrum fluoride molten salt reactor (FFMSR) with ultimately reduced radiotoxicity of nuclear wastes”, Intech Open, Nuclear power plants – processes in the nuclear fuel cycle, 2020.

4. K. Dodson, “Molten salt extraction (MSE) of Americium from Plutonium metal in CaCl2-KCl-PuCl3 and CaCl2-PuCl3 salt systems”, Master thesis, June 11th, 1992.

5. Bureau of Radiological Health, Radiological Health Handbook, U.S. Department of Health, Education, and Welfare, Rockville, Maryland 1970.

6. J. B. Knighton, R. G. Auge, and J.C. Brown, Production Tests of Single Contact Molten Salt Americium Extrction Process, CRDL 940501-002, December 1970.

7. Nuclear Engineering Department, Brookhaven National Laboratory, “Liquid metal fuel reactor systems, a collection of seven papers”, Nucleonics, 12(1954): 11-12.

8. M. Mehos et al., “Concentrating solar power Gen3 demonstration roadmap”, Technical report, NREL/TP-5500-67464, January 2017.

9. S. Fereres et al., “Molten carbonate salts for advanced solar thermal energy power plants: cover gas effect on fluid thermal stability”, Solar Energy Materials and Solar Cells, 118(2018): 119-126.

10. M. Mehos, C. Turchi, J. Vidal, M. Wangner, Z. Ma, C. Ho, W. Kolb, C. Andraka, A. M. Kruizenga. “Concentrating solar power Gen3 demonstration roadmap”. Technical report: NREL/TP-5500-67464. National renewable energy laboratory, Golden, CO(2017).

11. J. W. Kroger, “Fundamentals of High-temperature Corrosion in Molten Salts”, ASM Metals Handbook, Vol. 13, ASM International, PP 50-55.

12. C. Edeleanu, R. Littlewood, “Thermodynamics of Corrosion in Fused Chlorides”, Electrochim. Acta, 3, 195-207.

13. J. W. Ambrosek, “Molten Chloride Salts for Heat Transfer in Nuclear Systems”, Ph.D. Dissertation, University of Wisconsin, Madison, WI, 2011.

14. L. C. Olson, “Materials Corrosion in Molten LiF-NaF-KF Eutectic Salt”, Ph.D. Dissertation, University of Wisconsin, Madison, WI, 2009.

15. S. Guo, J. Zhang, W. Wu, W. Zhou, “Corrosion in the Molten Fluoride and Chloride Salts and Materials Development for Nuclear Applications”, Progress in Materials Science, 97, 448(2018).

16. J. W. Oldfield, ASTM STP 978, ASTM, West Conshohocken, PA, 1988, P5.

17. B. O. Okonkwo, H. Ming, F. Meng, J. Wang, X. Xu, E. Han, “Galvanic Corrosion Study between Low Alloy Steel A508 and 309/308 L Stainless Steel Dissimilar Metals: A Case Study of the Effects of Oxide Film and Exposure Time”, Journal of Nuclear Materials, 548(2021): 152853.

18. M. Nejedly, O. Matal, “Studies on Components for a Molten Salt Reactor”, Transactions of the 17th International Conference on Structural Mechanics in Reactor Technology (SMiRT 17), Prague, Czech Republic, August 17-22, 2003.

19. O. Matal et al., “Operating Experience with the Second Czechoslovak 30MW Steam Generator and Concept of Steam Generators with Double-Wall Heat Exchange Tubes”, Pro. Of Int. Symp. On Fast Breeder Reactors: Experience and Future Trends, Lyon, 22-26 July 1985, IAEA Viena 1986.

20. M. Koukolikova, P. Slama, Z. Novy, P. Svoboda, P. Toman, M. Marecek and J. Uhlir, “Research of Materials and Components for Molten Salt Reactors,” Transactions of the American Nuclear Society, 116 (2017): 523.

21. C. Forsberg, S. Lam, D. Carpenter, D. Whyte, R. Scarlat, C. Contescu, L. Wei, J. Stempien, E. Blandford, “Tritium Control and Capture in Salt-cooled Fission and Fusion Reactors: Status, Challenges, and Path Forward”, Nuclear Technology, 197(2017).

22. K. Sridharan, T. R. Allen, “Corrosion in Molten Salts”, Molten Salt Chemistry, 2013, 241-267.

23. S. Guo, J. Zhang, W. Wu, W. Zhou, “Corrosion in the Molten Fluoride and Chloride Salts and Materials Development for Nuclear Applications”, Progress in Materials Science, 97(2018): 448.

24. J. Serp, M. Allibert, O. Benes, S. Delpech, O. Feynberg, V. Ghetta, D. Heuer, D. Holcomb, V. Ignatiev, J. L. Kloosterman, L. Luzzi, E. Merle-Lucotte, J. Uhlir, R. Yoshioka and D. Zhimin, “The Molten Salt Reactor (MSR) in Generation IV: Overview and Perspectives”, Progress in Nuclear Energy, 77 (2014): 308.

25. J. R. Keiser, “Compatibility Studies of Potential Molten-Salt Breeder Reactor Materials in Molten Fluoride Salts”, ORNL/TM-5783, 1977.

26. H. E. McCoy, “Status of Materials Development for Molten Salt Reactors”, ORNL/TM-5920, 1978.

27. R. M. Boothby, Compendium of Nuclear Materials, R. Konings et al. eds, Elsevier, 4(2012): 23.

28. V. Vrchovinsky, J. Zrnik, T. Kvackaj and P. Wangyan, “Effect of Final Cold Rolled Microstructures on Creep Deformation Behavior in Ni Based Alloy,” Journal of Metals, Materials and Minerals 15 (2005): 57.

29. R. Wright, T. Sham, “Status of Metallic Structural Materials for Molten Salt Reactors”, INL/EXT-18-45171, May 2018.

30. H. J. Penkalla, J. Wosik, W. Fischer, F. Schubert: In Superalloys 718, 625, 706, and Various Derivatives, E. A. Loris, TMS, Warrendale, PA, 2001, PP 279-290.

31. W. Ren and R. W. Swindeman: Proc. PVP2006-ICPVT-11-93128, ASME, New York, NY, 2006, PP 1-12.

32. J. Randles, "A cathode ray polarograph, Part II: the current-voltage curves", Trans. Faraday Soc., 44(1948): 327.

33. A. Sevcik, "Oscillographic polarography with periodical triangular voltage", Collect. Chem. Commun., 13(1948): 349.

34. A. Ferrari, C. Foster, P. Kelly, D. Brownson, C. Banks, "Determination of the electrochemical area of screen-printed electrochemical sensing platforms", Biosensors, 8(2018): 53.

35. T. Berzins, P. Delahay, "Oscillographic polarographic waves for the reversible deposition of metals on solid electrodes", Journal of the American Chemistry Society, 75(1953): 555-559.

36. A. Bard, L. R. Faulkner, Electrochemical Methods: Fundamentals and Applications, John Wiley & Sons, N. Y. 1980.

37. H. Peng, M. Shen, C. Wang, Y. Zuo, L. Xie, "Electrochemical Investigation on the Stable Iron Species in Molten FLiNaK", Insights in Analytical Electrochemistry, 2(2016), 1:3.

38. B. Khalaghi, E. Kvalheim, M. Tokushige, L. Teng, S. Seetharaman, G. M. Haarberg, "Electrochemical Behavior of Dissolved Iron Chloride in KCl-LiCl-NaCl melt at 550°C", ECS Transaction, 64, 301 (2014).

39. D. Horvath, M. F. Simpson, "Electrochemical monitoring of Ni corrosion induced by water in eutectic LiCl-KCl", Journal of the Electrochemical Society, 165, C226 (2018).

40. D. Inman, J. C. Legey, R. Spencer, "The Electrochemistry of Chromium in Molten LiCl + KCl", Electroanalytical Chemistry and Interfacial Electrochemistry, 61, 289 (1975).

41. A. Cotarta, "Electrochemistry of Molten LiCl-KCl-CrCl3 and LiCl-KCl-CrCl2 Mixtures", J. Appl. Electrochem., 27, 651 (1997).

42. I. R. Elizarova, "Electrode Process in the Course of Cr (III) and Cr (II) Reduction/Oxidation in KCl Melt", Russian Journal of Electrochemistry, 45, 862 (2009).

43. Y. Inoue, K. Tanaka, I. Tago, "Linear Sweep Voltammetry of Nickel in Molten LiF-NaF-KF Eutectic", Journal of Nuclear Science and Technology, 24, 925(1987).

44. D. L. Manning, G. Mamantov, "Rapid Scan Voltammetry and Chronopotentiometric Studies of Iron in Molten Fluorides", J. Electroanal. Chem., 7(1964): 102.

45. W. Wu, S. Guo, J. Zhang, "Electrochemical Behavior of Cr3+ in Molten LiF-NaF-KF Eutectic", Int. J. Electrochem. Sci., 13(2018): 225-234.

46. W. Doniger, K. Sridharan, “Application of voltammetry for quantitative analysis of chromium in molten 2LiF-BeF_2 (FLiBe) salt”, Journal of Electroanalytical Chemistry, 838(2019): 73-81.

47. T. Yoko, R. Bailey, “Electrochemical studies of chromium in molten LiF-NaF-KF (FLiNaK)”, J. Electrochem. Soc., 131(1984): 2590.

48. L. Swain, S. Ghosh, G. Pakhui, B. Reddy, “Redox Behavior of Moisture in LiCl-KCl Eutectic Melts: A Cyclic Voltammetry Study”, Nuclear Technology, 207, 119(2021).

49. Y. Kanzaki, M. Takahashi, “The Hydrogen Electrode in Fused Lithium Chloride-Potassium Chloride Eutectic Containing Hydrogen Ion”, Electroanalytical Chemistry and Interfacial Electrochemistry, 58, 349(1975).

50. N. Minh, B. Welch, “The Cathodic Reduction of HCl Dissolved in LiCl-KCl-ZnCl2 Melts”, J. Electroanal. Chem., 92, 179(1978).

51. E. Littauer, K. Tsai, “Observations of the Diffusion Coefficient of the Hydroxyl Ion in Lithium Hydroxide Solutions”, Electrochimica Acta, 24, 351(1979).

52. Y. Kado, T, Goto, R. Hagiwara, “Oxygen Electrode Reaction in a LiCl-KCl Eutectic Melt”, Journal of the Electrochemical Society, 156, E167 (2009).

53. K. Xie, A. R. Kamali, “Electrochemical Production of Hydrogen in Molten Salt”, Energy Conversion and Management, 251(2022): 114980.

54. A. J. Bard, L. R. Faulkner, “Electrochemical Methods: Fundamentals and Applications”, 2nd Edition, John Wiley & Sons, Inc, 1944.

55. D. L. Manning, “Voltammetry of Iron in Molten Lithium Fluoride-Potassium Fluoride-Sodium Fluoride Salt”, Journal of Electroanalytical Chemistry, 6(1963): 227.

56. H. W. Jenkins, “Electrochemical Measurements in Molten Fluorides”, PhD Dissertation, University of Tennessee, Knoxville.

57. K. Lim, J. Yun, “Study on the Exchange Current Density of Lanthanide Chlorides in LiCl-KCl Molten Salt”, Electrochimica Acta, 295(2019): 577-583.

58. K. R. Kim, S. Y. Choi, J. G. Kim, S. Paek, W. I. Goh, “Electrochemical Investigation of Exchange Current Density of Uranium and Rare-Earths Couples (M^{3+}/M^0) in LiCl-KCl Eutectic Electrolyte”, Int. J. Electrochem. Sci., 10(2015): 7660

59. E. Wu, “Integrated Study on Rare Earth Drawdown by Electrolysis for Molten Salt Recycle”, Doctoral Dissertation, The Ohio State University, USA, 2017.

60. K. Lim, S. Park, J. Yun, “Study on Exchange Current Density and Transfer Coefficient of Uranium in LiCl-KCl Molten Salt”, Journal of The Electrochemical Society, 162(14): E334-337, 2015.

61. Yu. V. Stulov, S. A. Kuznetsov, “The Standard Rate Constant of Charge Transfer for the Cr^{3+}/Cr^{2+} Couple in NaCl-KCl-$CrCl_3$ and NaCl-KCl-K_3CrF_6 Molten Salts”, ECS Transactions, 33(7): 329-335 (2010).

62. D. Yoon, S. Phongikaroon, “Measurement and Analysis of Exchange Current Density for U/U3+ Reaction in LiCl-KCl Eutectic Salt via Various Electrochemical Techniques”, Electrochimica Acta, 227(2017): 170-179.

63. W. Wu, S. Guo, J. Zhang, “Exchange Current Densities and Charge-Transfer Coefficients of Chromium and Iron Dissolution in Molten LiF-NaF-KF Eutectic”, J. Electrochem. Sci., 164, C840 (2017).

64. S. Guo, E. Wu, J. Zhang, “Exchange Current Density of Gd (III)/ Gd Reaction in LiCl-KCl Eutectic and Analysis of Errors Caused by Various Methods”, Electrochim. Acta, 259, 253 (2018).

65. Osami Seri, “Estimation of Exchange Current Density for the Hydrogen Evolution Reaction of Titanium in Sulfuric Acid Solution”, J. Japan Inst. Met. Mater., 2018

66. J. A. Vega, S. Smith, W. E. Mustain, “Hydrogen and Methanol Oxidation Reaction in Hydroxide and Carbonate Alkaline Media”, Journal of the Electrochemical Society, 158(4): B349-B354, 2011.

67. D. Tang, J. Lu, L. Zhuang, P. Liu, “Calculation of the Exchange Current Density for Hydrogen Electrode Reactions: A Short Review and a New Equation”, Journal of Electroanalytical Chemistry, 644(2010): 144-149.

68. ASTM G31-72 . Annu. B. ASTM Stand.; 2004. Standard Practice for Laboratory Immersion Corrosion Testing of Metals. 2004.

69. ASTM G102-89. Annu. B. ASTM Stand.; 2015. Standard Practice for Calculation of Corrosion Rates and Related Information from Electrochemical Measurements; p. 1. 2015.

70. M. Groll, O. Brost, D. Heine, “Corrosion of Steels in Contact with Salt Eutectics as Latent Heat Storage Materials: Influence of Water and other Impurities” Heat Recovery Systems and CHP, 10 (1990): 567–572.

71. M. Uusitalo, P. Vuoristo, T. Mantyla, “High Temperature Corrosion of Coatings and Boiler Steels in Reducing Chlorine-containing Atmosphere”, Surface and Coatings Technology, 161 (2002): 275–285.

72. A. Schutz, M. Gunthner, G. Motz, O. Greibl, U. Glatzel, “High Temperature (Salt Melt) Corrosion Tests with Ceramic-Coated Steel”, Material Chemistry Physics, 159 (2015): 10-18.

73. M. Azzi, J. Rameau, “Corrosion in molten Na2CO3-K2CO3 at 800 °C — I. Effect of oxygen partial pressure on iron corrosion”, Corrosion Science, 24 (1984): 935–944.

74. T. Tzvetkoff, A. Girginov, M. Bojinov, “Corrosion of nickel, iron, cobalt and their alloys in molten salt electrolytes”, J. Mater. Sci. 30 (1995): 5561–5575.

75. D. Bankiewicz, P. Yrjas, M. Hupa, “High-temperature corrosion of superheater tube materials exposed to zinc salts”, Energy Fuels, 23 (2009) 3469–3474.

76. T. Yeh, H. Chang, M. Wang, T. Yuan, J. Kai, “Corrosion of Alloy 617 in high-temperature gas environments”, Nuclear Engineering and Design, 271(2014): 257-261.

77. Q. Dai, X. Ye, H. Ai, S. Chen, L. Jiang, J. Liang, K. Yu, B. Leng, Z. Li, X. Zhou, “Corrosion of Incoloy 800H Alloys with Nickel Cladding in FLiNaK Salts at 850 °C”, Corrosion Science, 133(2018): 349-357.

78. F. Ouyang, C. Chang, J. Kai, “Long-term corrosion behavior of Hastelloy-N and Hastelloy-B3 in Moisture-Containing Molten FLiNaK Salt Environments:, Journal of Nuclear Materials, 446(2014): 81-89.

79 A. Don, O. Muransky, I. Karatchevtseva, A. Zhang, Z. Li, N. Scales, J. J. Kruzic, L. Edwards, “Molten Salt Corrosion (FLiNaK) of Ni-Mo-Cr Alloy and its Welds for Appliation in Energy-Generation and Energy-Storage Systems”, Corrosion Science, 164(2020): 108306.

80. N.S. Patel, “Corrosion Behavior of Ni-based Superalloys in Molten FLiNaK Salts”, Corcon, 2017.

81. F. Ouyang, C. Chang, B. You, T. Yeh, J. Kai, “Effect of Moisture on Corrosion of Ni-based Alloy in Molten Alkali Fluoride FLiNaK salt Environments”, Journal of Nuclear Materials, 437(2013): 201.

82. Q. Lei, X. Zhang, M. Gao, W. Wen, Y. Jia, H. Liu, Y. Li, J. Liu, X. Zhou, “Inconel 617 Corrosion in FLiNaK Molten Salt: An in-situ X-ray Diffraction Study”, Corrosion Science, 182(2021): 109289.

83. X. Ye, H. Ai, Z. Guo, H. Huang, L. Jiang, J. Wang, Z. Li, X. Zhou, “The High-temperature Corrosion of Hastelloy N Alloy (UNS N10003) in Molten Fluoride Salts Analysed by STXM, XAS, XRD, SEM, EPMA, TEM/EDS”, Corrosion Science, 106(2016): 249-259.

84 M. Hofmeister, L. Klein, H. Miran, R. Retting, S. Virtanen, R.F. Singer, “Corrosion Behavior of Stainless Steels and a Single Crystal Superalloy in a Ternary LiCl-KCl-CsCl Molten Salt”, Corrosion Science, 90(2015): 46.

85. S. Ren, Y. Chen, X. Ye, L. Jiang, S. Yan, J. Liang, X. Yang, B. Leng, Z. Li, Z. Chen, Z. Dai, “Corrosion Behavior of Carburized 316 Stainless Steel in Molten Chloride Salts”, Solar Energy, 223(2022): 1-10.

86. G. Zheng, B. Kelleher, G. Cao, M. Anderson, T. Allen, K. Sridharan, “Corrosion of 316 Stainless Steel in High Temperature Molten Salt Li2BeF4”, Journal of Nuclear Materials, 416(2015): 143.

87. W. Doniger, C. Falconer, M. Elbakhshwan, K. British, A. Couet, K. Sridharan, “Investigation of Impurity Driven Corrosion Behavior in Molten 2LiF-BeF_2 Salt”, Corrosion Science, 174(2020): 108823.

88. M. Sarvghad, T.A. Steinberg, G. Will, “Corrosion of Stainless Steel 316 in Eutectic Molten Salts for Thermal Energy Storage”, Solar Energy, 172(2018): 198.

89. P. Deng, Q. Peng, E. Han, “Grain Boundary Oxidation of Proton-irradiated Nuclear Grade Stainless Steel in Simulated Primary Water of Pressurized Water Reactor”, 11(2021): 1371.

90. L. Yang, A. Yang, “Communication — On Zero Resistance Ammeter and Zero Voltage Ammeter”, Journal of The Electrochemical Society, 164(13): C819 – C821, 2017.

91. ASTM G71, “Standard Guide for Conducting and Evaluating Galvanic Cor- rosion Tests in Electrolytes”, ASTM, West Conshohocken, PA, 2014.

92. ASTM G199, “Standard Guide for Electrochemical Noise Measurement”, ASTM, West Conshohocken, PA (Reapproved 2014).

93. Kenneth L. Kaiser, Electromagnetic Compatibility Handbook, CRC Press. P13, 2004.

94. ASTM G217, “Standard Guidefor Corrosion Monitoring in Laboratories and Plants with Coupled Multielectrode Array Sensor Method”, ASTM, West Conshohocken, PA (Approved 2017).

95. AMETEK Scientific Instruments: Application of Galvanic Corrosion,

https://www.ameteksi.com/applications/corrosion/galvanic-corrosion

96. D. Jones, Principles and prevention of corrosion, Prentice-Hall, London, 1996, P75-86.

97. S. Dean, Handbook on corrosion testing and evaluation, Wiley, New York, 1971, P71.

98 .Standard Practice for Calculation of Corrosion Rates and Related Information from Electrochemical Measurements, ASTM-G102.

99. J. Yoo, Z. Park, J. Kim, L. Chung, “Developent of a Galvanic Sensor System for Detecting the Corrosion Damage of the Steel Embedded in Concrete Structures: Part 1. Laboratory Tests to Correlate Galvanic Current with Actual Damage”, Cement and Concrete Research, 33(2003): 2057.

100. F. Mansfeld, J.V. Kenkel, “Galvanic Corrosion of Al Alloy-III. The Effect of Area Ratio”, Corrosion Science, 15(1975): 239-250.

101. Z. Yin, M. Yan, Z. Bai, W. Zhao, W. Zhou, “Galvanic Corrosion Associated with SM 80SS Steel and Ni-based Alloy G3 Couples in NaCl Solution”, Electrochimica Acta, 53(2008): 6285-6292.

102. B. Okonkwo, H. Ming, F. Meng, J. Wang, X. Xu, E. Han, “Galvanic Corrosion Study between Low Alloy Steel A508 and 309/308L Stainless Steel Dissimilar Metals: A Case Study of the Effects of Oxide Film and Exposure Time”, Journal of Nuclear Materials, 548(2021): 152853.

103. S. Jeon, G. Song, D. Hur, “Galvanic Corrosion Between Alloy 690 and Mgnetite in Alkali Aqueous Solutions”, Metals, 2015, 2372-2382.

104. K. Fushimi, A. Naganuma, K. Azumi, Y. Kawahara, “Current Distribution During Galvanic Corrosion of Carbon Steel Welded with Type-309 Stainless Steel in NaCl Solution”, Corrosion Science, 50(2008):903-911.

105. Y. Wang, C. Zeng, W. Li, “The Influence of Temperature Gradient on the Corrosion of Materials in Molten Fluorides”, Corrosion Science, 136(2018): 180.

106. Y. Li, Z. Wang, X. Guo, G. Zhang, “Galvanic Corrosion between N80 Carbon Steel and 13Cr Stainless Steel under Supercritical CO_2 Conditions”, Corrosion Science, 147(2019): 260-272.

107. L. Gao, F. Han, S. Chen, X. Ye, B. Leng, “High-temperature Corrosion Behavior of Inconel 617 with Ni-Cladding in Molten FLiNaK Salt”, Materials and Corrosion, 73(2022): 486-496.

108. Y. Wang, J. Wu, C. Wang, S. Zhang, “Electrochemical Corrosion Behavior of 316L Stainless Steel in Molten Fluorides with a Temperature Gradient”, Electrochemistry Communications, 109(2019): 106612.

109. S. Choi, A. Strianese, O. Dale, M.Simpson, “Electrochemical Measurements for Assessing Corrosion of Metal Alloys in Molten LiF-NaF-KF and MgCl2-NaCl-KCl”, The Minerals, Metals & Materials Society, 73(2021): 3544.

110. R.S. Seller, W.J. Cheng, B.C. Kelleher, M.H. Anderson, K. Sridharan, C.J. Wang, T.R. Allen, “Corrosion of 316L Stainless Steel Alloy and Hastelloy-N Superalloy in Molten Eutectic LiF-NaF-KF Salt and Interaction with Graphite”, Nuclear Technology, 188, 192(2014).

111. Q. Liu, H. Sun, H. Yin, L. Guo, J. Qiu, J. Lin, Z. Tang, “Corrosion Behaviour of 316H stainless steel in molten FLiNaK eutectic salt containing graphite particles”, Corrosion Science, 160 (2019) 108174.

112. L. Olson, K. Sridharan, M. Anderson, T. Allen, “Nickel-plating for Active Metal Dissolution Resistance in Molten Fluoride Salts”, Journal of Nuclear Materials, 411(2011): 51–59.

113. G. Zheng, B. Kelleher, G. Cao, M. Anderson, T. Allen, K. Sridharan, “Corrosion of 316 Stainless Steel in High Temperature Molten Salt Li2BeF4”, Journal of Nuclear Materials, 416(2015): 143.

114. H. Ai, J. Hou, X. Ye, C. Zeng, H. Sun, X. Li, G. Yu, X. Zhou, J. Wang, “Influence of graphite-alloy interactions on corrosion of Ni-Mo-Cr alloy in molten fluorides”, Journal of Nuclear Materials, 503(2018): 116-123

115. J. Qiu, Y. Zou, G. Yu, H. Liu, Y. Jia, Z. Li, P. Huai, X. Zhou, H. Xu, “Compatibility of container materials with Cr in molten FLiNaK salt”, Journal of Fluorine Chemistry, 168 (2014): 69–74.

116. R. S. Seller, W. J. Cheng, M.H. Anderson, K. Sridharan, C.J. Wang, T.R. Allen, “Material Corrosion in Molten LiF-NaF-KF Eutectic Salt Under Different Reduction Oxidation Conditions”, Proceedings of ICAPP’ 12, Chicago, USA, June 24-28, 2021, 12189

117. J. Qiu, A. Wu, Y. Li, Y. Xu, R. Scarlat, D. Macdonald, “Galvanic Corrosion of Type 316L Stainless Steel and Graphite in Molten Fluoride Salt”, Corrosion Science, 170(2020): 108677.

118. J. C. Vidal and N. Klammer, “Molten chloride technology pathway to meet the U. S. DOE sunshot initiative with Gen3 CSP.” AIP Conf. Proc., 2216, 080006 (2019).

119. T. Yin, Y. Xue, Y. Yan, Y. Zheng, Y. Song, G. Wang, M. Zhang, M. Qiu, D. Hu, “Electrochemical Synthesis and Thermodynamic Properties of Pr-Ni Intermetallic Compounds in a LiCl-KCl-NiCl2-PrCl3 Melt”, ChemElectrochem, **6**, 876 (2019).

120. A. Valizadeh, P. Aleshkevych, M. Najafpour, “Role of Pt and PtO2 in the Oxygen-Evolution Reaction in the Presence of Iron uder Alkaline Conditions”, Inorganic Chemistry, 61(2022): 613-621.

121. Willsau, J.; Wolter, O.; Heitbaum, J. “Does the oxide layer take part in the oxygen evolution reaction on platinum: A DEMS study”, J. Electroanal. Chem. Interfacial Electrochem. 1985, 195 (2), 299−306.

122. R. Mom, L. Frevel, J. Velez, M. Plodinec, A. Gericke, R. Schlogl, “The Oxidation of Platinum under Wet Conditions Observed by Electrochemical X-ray Photoelectron Spectroscopy”, Journal of The American Chemical Society”, 141(2019): 6537-6544.

123. A. M. Keightley, J. C. Myland, K. B. Oldham, P. G. Symons, “Reversible Cyclic Voltammetry in the Presence of Product”, *J. Electroanal Chem.*, **322**, 25 (1992).

124. S. Guo, N. Shay, Y. Wang, W. Zhou, J. Zhang, “Measurement of Europium (III)/Europium (II) couple in Fluoride Molten Salt for Redox Control in a Molten Salt Reactor Concept”, *J. Nucl. Mater.*, **496**, 197 (2017).

125. W. Huang, L. Tian, C. She, F. Jiang, H. Zheng, W. Li, G. Wu, D. Long, Q. Li, “Electrochemical Behavior of Europium (III)-Europium (II) in LiF-NaF-KF Molten Salt”, *Electrochim. Acta*, **147**, 114 (2014).

126. HSC 10.0, Metso Outotec, Filand, OY.

127. “Chemical Reactions in Molten Salts: Stability of Structural Metal Fluorides,” section in series of Aircraft Nuclear Propulsion Project Quarterly Progress Reports: ORNL-1816, 1864, 1896, 1947, 2012, 2257, 2221, 2274, 2387, Oak Ridge National Laboratory, Oak Ridge, TN (1955–1958)

128. D. Williams, L. Toth, K. Clarno, “Assessment of Candidate Molten Salt Coolants for the Advanced High-Temperature Reactor (AHTR)”, ORNL/TM-2006/12, March 2006.

129. W. H. Jordan et al., Aircraft Nuclear Propulsion Project Quarterly Progress Report for period ending June 10, 1956, ORNL-2106, Oak Ridge National Laboratory, Oak Ridge, TN, p.95, (1956).

130. M. Korenko, M. Straka, L. Szatmary, M. Ambrova, J. Uhlir, “Electrochemical Separation of Uranium in the Molten System LiF-NaF-KF-UF4”, Journal of Nuclear Materials, 440(2013): 332.

131. V. Afonichkin, A. Bovet, V. Shishkin, “Salt Purification and Redox Potential Measurement for the Molten LiF-ThF_4-UF_4 Mixture”, Proceedings of the First ACSEPT International Worshop, 2010.

132. Y. Wang, J. Zhang, “Electrochemical Properties of CrF_2 in FLiNaK Molten Salt and the New Analytical Methods for their Determination”, Journal of The Electrochemical Society, 167(2020): 0806503.

133. M. Tylka et al., “Application of voltammetry for quantitative analysis of actinides in molten salts”, Journal of electrochemical society, 162(2015): H852.

134. J. Imbeaux, J. Saveant, “Convolutive potential sweep voltammetry: I. Introduction”, Journal of Electroanalytical Chemistry and Interfacial Electrochemistry”, 44(1973): 169.

135. K. Oldham, “New approach to the solution of electrochemical problems involving diffusion”, Analytical Chemistry, 41(1969): 1904.

136. K. Oldham, “Signal-independent electroanalytical method”, Analytical Chemistry, 44(1972): 196.

137. K. Oldham, “Semi-integral electroanalysis. Analog implementation”, Analytical Chemistry, 45(1973): 39.

138. K. Oldham, “Convolution: a general electrochemical procedure implemented by a universal algorithm”, Analytical Chemistry, 58(1986): 2296.

139. M. Goto, D. Ishii, “Semi-differential electroanalysis”, Journal of Electroanalytical Chemistry and Interfacial Electrochemistry, 61(1975): 361.

140. K. Oldham, J. Spanier, “The replacement of Fick’s laws by a formulation involving semi-differentiation”, 26(1970): 331.

141. K. Yoshida, N. Matubayasi, M. Nakahara, “Solvation shell dynamics studied by molecular dynamics simulation in relation to the translational and rotational dynamics of supercritical water and benzene”, J. Chem. Phys., 127(2007): 174509.

142. K. Yoshida, N. Matubayasi, M. Nakahara, “Self-diffusion coefficients for water and organic solvents at high temperatures along the coexistence curve”, J. Chem. Phys., 129(2008): 214501.

143. K. Krynicki, C. Green, D. Sawyer, “Pressure and temperature dependence of self-diffusion in water”, Faraday Discuss. Chem., 66(1978): 199-208.

144. K. Rah, S. Kwak, B. Eu, M. Lafleur, “Relation of tracer diffusion coefficient and solvent self-diffusion coefficient”, J. Phy. Chem., 106(2002): 11841-11845.

145. J. Wang, T. Hou, “Application of molecular dynamics simulations in molecular property prediction II: diffusion coefficient”, J. Comput. Chem., 32(2011): 3505-3519.

146. W. Zhou, J. Zhang, Y. Wang, “Review-modeling electrochemical processing for applications in pyroprocessing”, Journal of the Electrochemical Society, 165(2018): E712-724.

147. B. D’souza, “Material degradation studies in molten salts”, PhD. Dissertation, March 2021.

148. MultiPak 9.9.2, Physical Electronics, A Division of Ulvac-PHI

149. XPS database, distributed by the measurement services division of the national institute of standards and technology (NIST), U.S. Department of Commerce.

150. S. Guo, J. Zhang, W. Wu, W. Zhou, “Corrosion in the Molten Fluoride and Chloride Salts and Material Development for Nuclear Applications”, Progress in Material Science, 97(2018): 448-487

151. J. D. Defilippi et al., “Effect of chromium and molybdenum segregation on the ridging behavior of type 434 stainless steel”, Metallurgical Transactions, 1971(2): 3209

152. N. Li et al., “Intermediate temperature corrosion behavior of Fe-12Cr-6Al-2Mo-0.2Si-0.03Y alloy (C26M) at 300-600°C”, Corrosion Science, 157(2019): 274-283.

153. T. D. Anderson et al., “The influence of molybdenum on stainless steel weld microstructures”, Welding Journal, 2007(86): 281s.

154. N. Bandyopadhuay et al., “Carbide precipitation, grain boundary segregation, and temper embrittlement in NiCrMoV rotor steels”, Mettallurgical Transactions A, 1985(16A): 721.

155. P. Bhuyan et al., “Precipitate evolution during aging and its individual role on high-temperature hot corrosion response in Alloy 617”, Journal of Alloys and Compounds, 871(2021): 159499.

156. T. Thorvaldsson, G. L. Dunlop, “Grain Boundary Cr-depleted Zones in Ti and Nb Stabilized Austenitic Stainless Steels”, Journal of Materials Science, 18(1983), 793-803.

157. H. G. MacPherson, “Molten salt reactor program quarterly progress report for period ending October 31, 1958”, Oak Ridge National Laboratory

158. L. M. Toth, L. O. Gilpatrick, “The equilibrium of dilute UF3 solutions contained in graphite”, ORNL-TM-4056, Oak Ridge National Laboratory, 1972.

159. W. R. Grimes, “Molten salt chemistry”, Nuclear Application & Technology, 1970(8): 137.

160. Y. Liu et al., “Corrosion of Cr in molten salts with different fluoroacidity in the presence of CrF3”, Corrosion Science, 169(2020): 108636.

161. T. C. Totemeier, H. Tian, D. E. Clark, J. A. Simpson, “Microstructure and Strength Characteristics of Alloy 617 Welds”, INL/EXT-05-00488, June 2005.

162. Frankel, G.S., Vienna, J.D., Lian, J. et al., “A comparative review of the aqueous corrosion of glasses, crystalline ceramics, and metals”, npj Mater Degrad, 15 (2018):

163. S. Cong, G. Ran, Y. Li, S. Dong, X. Huang, “Early corrosion behavior of Al-based Gd2O3-W shielding composited in a simulated spent fuel wet storage environment”, Progress in Nuclear Energy, 137(2021): 103787.

164. Lu, Yongxin and Xu, Lianyong. "Early corrosion stage of welded carbon steel joints in CO2-saturated oilfield water" Materials Testing, 62(2020): 129-137.

165. D. Laycock, “Studies on inorganic oxide fluorides”, University of Leicester, Thesis, 1981.

166. Uranyl fluoride, IBILABS, https://ibilabs.com/uranium-uranyl-thorium-compounds/uranyl-compounds/uranyl-fluoride/

167. W.D. Manly, G.M. Adamson, J.H. Coobs, J.H. DeVan, D.A. Douglas, Aircraft Reactor Experiment-Metallurgical Aspects, Oak Ridge National Laboratory, Oak Ridge National Laboratory, Oak Ridge, Tennessee, 1957 AEC Research and Development Report ORNL-2349, Dec.

168. S. Lyon, “Corrosion of molybdenum and its alloys”, Shreir’s corrosion, 3(2010): 2157.

169. W. Acherman, J. Carter, C. Kenahan, D. Schlain, “Corrosion properties of molybdenum, tungsten, vanadium and their alloy”, Report investigations, US Bureau of Mines, 1966, P715.

170. C. Bishop, “Corrosion tests at elevated temperatures and pressures”, Corrosion, 19(1963): 308t-314t.

171. B. Singh, “Surface segregation of chromium carbide in stainless steel and its thermodynamic stability study by cyclic heat treatment”, International Journal of Mechanical Engineering and Technology, 8(2017): 1732-1738.

172. M. Htun, S. Kyaw, K. Lwin, “Effect of heat treatment on microstructural and mechanical properties of spring steel”, Journal of Metals, Materials and Minerals, 18(2008): 191-197.

173. T. Senthilkumar, T. Ajiboye, “Effect of heat treatment process on the mechanical properties of medium carbon steel”, Journal of minerals & materials characterization & engineering, 111(2): 142-152.

174. Y. Wang, Q. Wang, H. Liu, C. Zeng, Effects of the oxidants H_2O and CrF_3, on the corrosion of pure metals in molten (Li,Na,K)F, Corros. Sci. 103 (2016) 268–282.

175. J. Devan, R. Evans, “Corrosion Behavior of Reactor Materials in Fluoride Salt Mixtures”, ORNL-TM-328 (1962).

176. J. Yang, Y. Li, A. Xu, B. Fekete, D.D. Macdonald, “The electrochemical properties of alloy 690 in simulated pressurized water reactor primary water: effect of temperature”, J. Nucl. Mater. 518 (2019) 305–315.

177. S. Guo, W. Zhuo, Y. Wang, J. Zhang, “Europium induced alloy corrosion and cracking in molten chloride media for nuclear applications”, Corrosion Science, 163(2020): 108279.